Synthesis and Deposition of Directly Fused Porphyrin Tapes by Chemical Vapour Deposition Approach

Dissertation

Zur Erlangung des Grades
„Doktor der Naturwissenschaften“
im Promotionsfach Chemie

am Fachbereich Chemie, Pharmazie, Geographie
und Geowissenschaften
der Johannes Gutenberg-Universität Mainz

Giuseppe Bengasi
geboren in Leonforte

Mainz, 2020

The present studies have been conducted between October 2016 and December 2019 in the "Institut für Anorganische Chemie und Analytische Chemie der Johannes Gutenberg-Universität" of Mainz (Germany) and at the Luxembourg Institute of Science of Technology in Sanem (Luxembourg).

Esch sur Alzette, 17/02/2020

I, Giuseppe Bengasi, born in Leonforte (EN/Italy) in 31/07/1989, certify that I written my doctoral thesis independently and I have used no others than the specified written, electronic sources, as well as other tools. All the statements that were taken literally or analogously from other sources have been explicitly specified.

Date 17/02/2020 Signature _____

Day of the oral examination: 08-05-2020

CONTENTS

ABSTRACT

Porphyrins play a key role in biological processes such as photosynthesis and respiration. Inspired by their ubiquitous presence in natural systems, scientists have investigated their implementation in modern technological devices. In the last century, a wide series of studies have demonstrated the outstanding properties of this class of hybrid metal-organic compounds. In 2001, Osuka and co-workers reported for the first time the synthesis of directly fused polymeric porphyrin systems (porphyrin tapes). These systems possess impressive optoelectronic properties including electronic transitions occurring in the infrared, low attenuation factor and two-photon absorption. However, after twenty years from the discovery of porphyrin tapes, only few reports have investigated their use in the production of optoelectronic devices. This is mainly due to their complex synthesis and poor solubility, that reduce the industrial appeal and hinder the formation of smooth thin films required for device production.

In 2006, Gleason and co-workers reported the synthesis of conjugated polymers directly from the gas phase in a novel approach named oxidative chemical vapour deposition (oCVD). In oCVD, the delivery of the chemicals through the gas phase circumvents the problems related to the poor solubility of precursors and products and directly yields conjugated polymer thin films on a given substrate. The technique involves modest temperatures ($T \approx$ 300-500K) allowing the deposition of thin films on many thermostable substrates. Prior to this work, the oCVD technique was limited to the polymerization of small, purely organic monomers.

Inspired from these two ground breaking studies on porphyrin tapes and oCVD, this thesis aims to bridge the knowledge acquired in different scientific fields and to fill the technological gap required to integrate porphyrin tapes into devices. This thesis also aims to develop a deep understanding on the reactivity of porphyrins towards oxidative coupling in the gas phase. The use of metalloporphyrins as monomers in oCVD can be considered as improvement for both the oCVD and the porphyrin tapes synthesis fields. While the oCVD of metalloporphyrin would allow obtaining smooth thin films of porphyrin tapes with controlled thickness, the use of metal-containing monomers such as metalloporphyrins is unprecedented and would allow to introduce new functionalities in the films obtained by oCVD. In addition, the synthesis of

porphyrin thin films represents an important step towards the production of smart devices for catalysis, sensing and nonlinear optics.

A custom built oCVD reactor was built to tackle the challenge of using solid and poorly volatile monomers in oCVD. The reactor allowed the sublimation of metalloporphyrins with free *meso* and *beta* positions in the presence of $FeCl_3$ as oxidant to obtain porphyrin thin films on sensitive substrates. Both chemical and physical properties of the films were investigated. High Resolution Mass Spectrometry (HRMS), UV/Vis/NIR spectroscopy and Gel Permeation Chromatography (GPC), were used to characterize the chemical composition of the synthetized film. Two-point probe conductivity measurements, Conductive Atomic Force Microscopy (C-AFM) and Helium Ion Microscopy (HIM) probed the film morphology, topography and conductive properties. Density Functional Theory (DFT) and Electron Paramagnetic Resonance (EPR) spectroscopy unravelled a conceivable reaction mechanisms of nickel(II) porphyrins during the oxidative coupling. Secondary Ion Mass Spectrometry (SIMS) of the films prepared using different oxidants confirmed that $FeCl_3$ yields the best results for the oCVD of porphyrins.

The effect of the size of the porphyrin substituents on the film composition and properties was investigated. Since no solubilizing substituents are required on the porphyrin in oCVD, simple small phenyl substituents can be used for the synthesis of porphyrin tapes. This aspect represents the most important step forward in this work towards applications, as small substituents improve the electric properties of the films by decreasing the hindrance between different polymer chains.

Different metal cations such as Fe^{III}, Co^{II}, Ni^{II}, Cu^{II}, Zn^{II}, Pd^{II} in the porphyrin core during the oCVD and in the film show, as in solution based studies, that the metal center influences the regioselectivity of the oxidative coupling steps. Thanks to cyclic voltammetry and DFT, information on the position and symmetry of the frontier orbitals were obtained and related to the regioselectivity of the reaction. Finally, the metal center appears to be crucial, since it helps avoiding acid-base reactions which stop the oxidative coupling and hence the polymerization.

ABBREVIATIONS

CVD	Chemical Vapour Deposition
PVD	Physical Vapour Deposition
oCVD	Oxidative Chemical Vapour Deposition
iPECVD	initiated Plasma Enhanced Chemical Vapour Deposition
HRMS	High Resolution Mass Spectrometry
GPC	Gel Permeation Chromatography
C-AFM	Conductive Atomic Force Microscopy
STM	Scanning Tunneling Microscopy
HIM	Helium Ion Microscopy
DFT	Density Functional Theory
EPR	Electron Paramagnetic Resonance
ESR	Electron Spin Resonance
SIMS	Secondary Ion Mass Spectrometry
CV	Cyclic Voltammetry
HOMO	Highest Occupied Molecular Orbital
LUMO	Lowest Unoccupied Molecular Orbital
SOMO	Singly Occupied Molecular Orbital
BAHA	(4-bromophenyl) aminium hexachloroanimonate
DDQ	2,3-dichloro-5,6-dicyano *p*-benzoquinone
$Sc(OTf)_3$	Scandium triflate
TBPO	Di-*tert*-butyl-peroxide
NIR	Near Infrared

ECL	Effective Conjugation Length
FcH	Ferrocene
CB	Conduction Band
VB	Valence Band
EDOT	3,4-Ethylenedioxythiphene
PEDOT	Poly-3,4-ethylenedioxythiphene
OLED	Organic Light Emitting Diode
PANI	Polyaniline
PDA	Polydopamine
PPy	Polypyrrole

1 PORPHYRINS AND PORPHYRIN TAPES

1.1 Porphyrins

Porphyrins are organic compounds composed of four pyrrolic rings bridged by methine groups (**Figure 1**). Porphryins and porphyrin-derived compounds (chlorins, bacteriochlorins i.e.) are widely present in nature and play a key role in several biological processes such as cellular respiration and photosynthesis. This is related to the special nature of porphyrinoids conferring to them their interesting chemical-physical properties. On one hand, their highly conjugated electronic system gives high molar extinction coefficients necessary for effective light harvesting photosynthesis and allows the occurrence of redox chemistry in absence of metal centers. On the other hand, the metal center allows the uptake and release of small molecules such as O_2 and CO_2 in haemoglobin, and can provide catalytic activity to porphyrinoids.[1–4] For these reasons, porphyrins attracted broad attention in the scientific community which is interested in their use for light harvesting[5,6], artificial photosynthesis[7], mimicking/understanding natural processes and development of new catalysts.[2,8–10] Porphyrins represent an extremely versatile molecular platform containing electronic and optical properties that can easily be modified and tuned.[11–13] In fact, the chemical-physical properties of the molecule can be modified through complexation with different metal cations and through introduction of organic groups on the *meso* and/or *β* position **(Figure 1)**. [13]

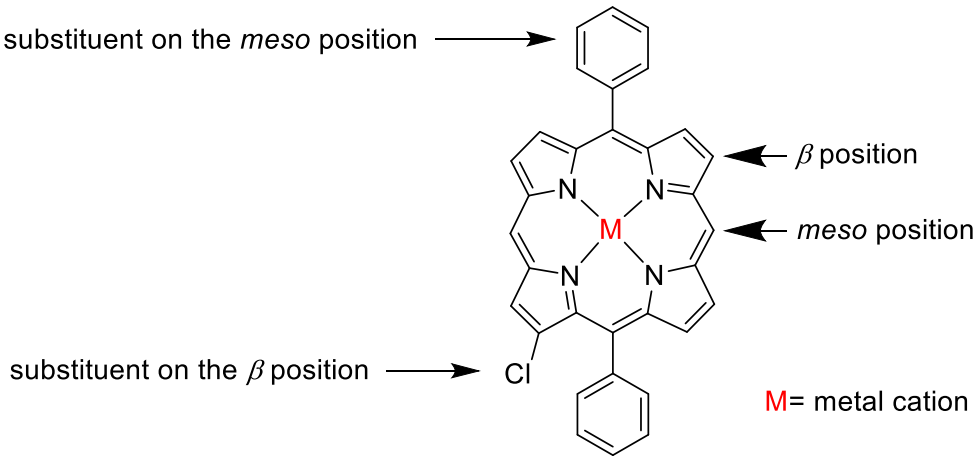

***Figure 1**. Schematic of the structure of a porphyrin, positions on the porphyrin and examples of substituents.*

1.2 Gouterman four orbitals model for porphyrins

The name porphyrin arise from the Greek word "πορφύρα" (porphyra), meaning purple, in reason of the intense colour characterizing this class of compounds. One of the main characteristics of porphyrins is their highly conjugated electronic structure leading to their remarkable optical properties. The colour of porphyrins relates to their UV-Vis absorption spectrum. Porphyrins possess very characteristic absorption spectra presenting two main features ascribed to π–π* transitions. (**Figure 2)**:

- The **B band** (or Soret band) is the most intense absorption in the spectra, usually placed around 400 nm ($\varepsilon \approx 10^5$ $M^{-1} \cdot cm^{-1}$).
- The **Q bands** are the less intense absorptions in the spectra, usually placed between 500 and 800 nm ($\varepsilon \approx 10^4$ $M^{-1} \cdot cm^{-1}$).

Martin Gouterman was one of the most active researchers interested in the physical nature of these absorptions.[14] During his pioneering studies in the early 60's, he developed the "*four orbital model*" to explain the intensity and position of the absorption bands finding the relationship between the number of Q bands and the molecular symmetry.[14]

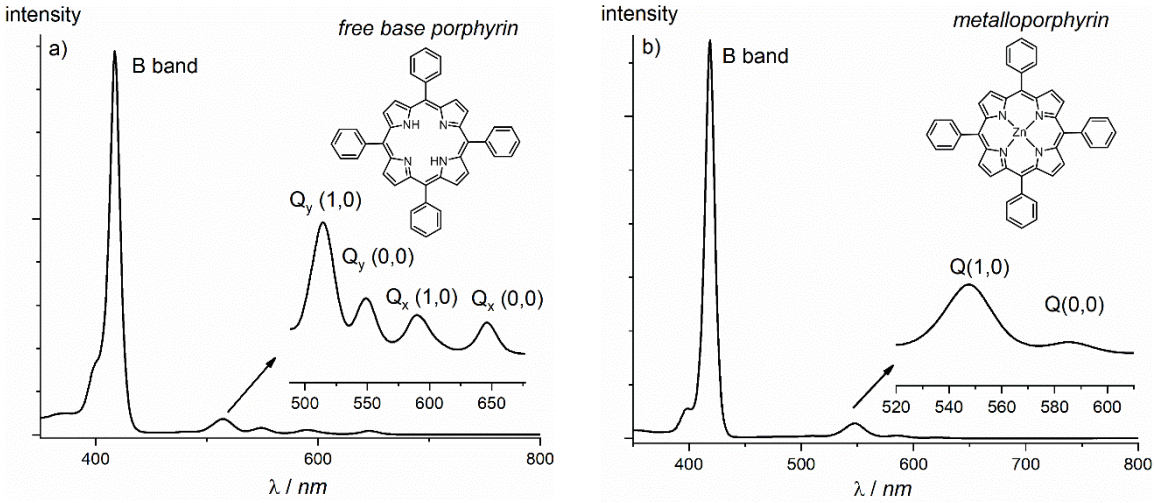

Figure 2. *UV/Vis absorption spectra of a) 5,10,15,20 tetraphenyl porphyrin (inset) and b) 5,10,15,20 tetraphenyl porphyrinato zinc(II) (inset) in dichlorometane. The Q bands are associated to different vibrational states indicated as $Q_{x,y}(a,b)$ in the graphs.*

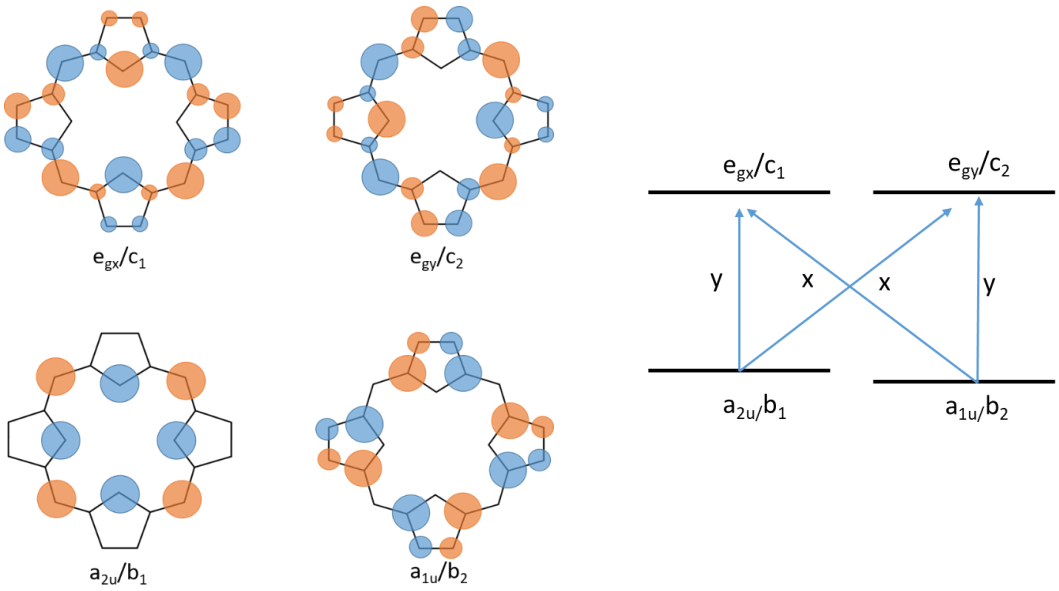

Figure 3. *(Left) HOMOs (b1, b2) and LUMOs (c1, c2) of the porphyrins derived from molecular orbital calculations. (Right) Schematic of the HOMO-LUMO transitions occurring in porphyrins and their respective transition polarization.*

According to his model, metalloporphyrins possess D_{4h} symmetry, that can be described using a simplified model based on a polyene ring of 16-members possessing filled frontier orbitals. The molecular orbitals of the porphyrins are obtained by molecular orbital calculations. According to the model, the molecule possess two almost accidentally degenerate HOMOs with a_{2u} and a_{1u} symmetry respectively and two degenerate LUMOs with e_g symmetry and different orientation in the space (e_{gx}, e_{gy}) (**Figure 3**). Group theory predicts two singlet states belonging to E_u symmetry arising from these transitions (**Figure 4**). The transitions originate from the excitation of electrons between the HOMOs (a_{2u} and a_{1u}) and the LUMOs (e_{gx} and e_{gy}) (**Figure 3** right). Based on the polyene model, Gouterman hypothesised the near

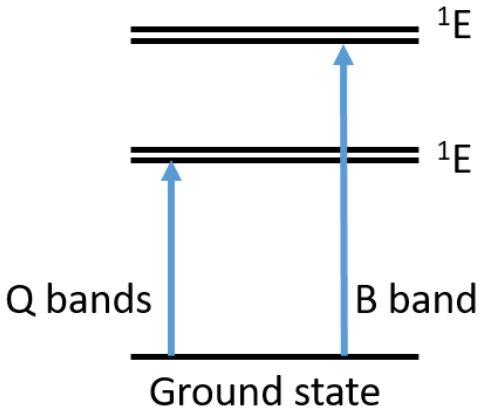

Figure 4. *Schematic of the transition from the ground state to the first and second excited states yielding the Q and B bands respectively.*

degeneracy of the a_{1u} and a_{2u} orbitals suggesting that only in case of similar energy of these orbitals, the visible range transitions (Q bands) would be forbidden. This hypothesis is confirmed in the intrinsic low absorption of the Q bands related to their forbidden transition nature. However, this simple representation would suggest a single Q band in the spectra of metalloporphyrins while f**igure 2b** clearly shows the existence of two Q bands. The multiplicity of the transition in the visible range is rationalized considering accessible vibrational levels, yielding multiple Q bands in the UV-Vis spectra of metalloporphyrins (**Figure 2b**). This hypothesis is also confirmed in experimental data showing constant distance and intensity between the Q bands.[14]

The model can also extended to porphyrins without metal center (**Figure 2a inset**). Porphyrins without metal cation in the core, are called *free base* porphyrins. In *free base* porphyrins, two protons facing each other on nitrogen atoms replace the metal center, (**Figure 2a**) lowering the symmetry to D_{2h}. The nomenclature adopted for metalloporphyrins' orbitals is no longer valid since it is strictly related to D_{4h} symmetry. To generalize the model, "b_1" and "b_2" labels replace the a_{2u} and a_{1u} labels while "c_1", "c_2" replace the e_{gx} and e_{gy} labels (**Figure 3**). In *free base* porphyrins, the presence of the two hydrogens in the core modifies the relative energy of the c_1, c_2 orbitals. The new electronic structure can be better described with an 18-membered polyene ring model. According to the 18 membered polyene ring model, the Q band ^1E_u state splits in two new states $^1B_{1u}$ and $^1B_{2u}$ (**Figure 5**). Once again, this aspect is confirmed in the *free base* porphyrin's UV-Vis absorption spectra (**Figure 2a**) exhibiting four Q bands. While two

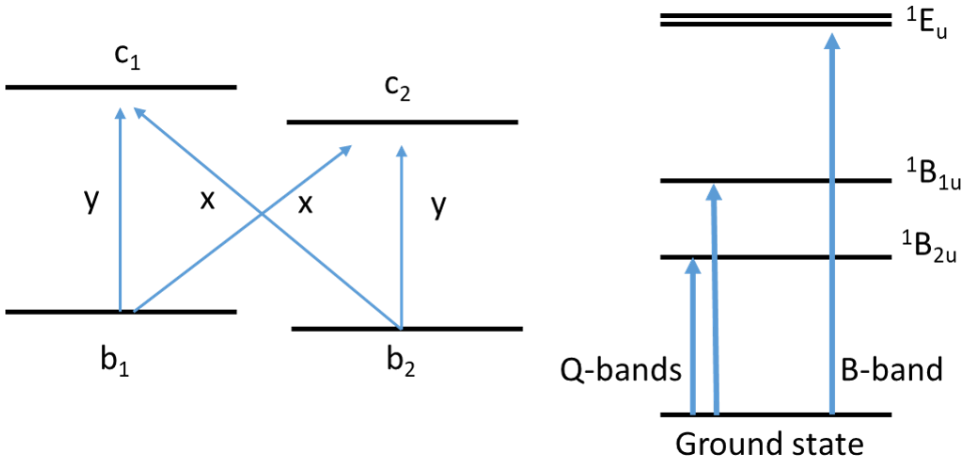

***Figure 5**. Schematic representation of the transition occurring in a D_{2h} symmetry porphyrin. The hydrogen atoms will remove the degeneracy between the c_1 and c_2 orbitals. The lower symmetry will split the ^1E_u transition in two new transitions ($^1B_{1u}$ and $^1B_{2u}$), thus increasing the number of Q bands.*

bands are related to transitions from the ground state to the $^1B_{1u}$ and $^1B_{2u}$ states (**Figure 5)**, the other two bands arise from the accessibility of vibrational states.

1.3 π-extended porphyrins

An interesting aspect of porphyrinoids is the possibility to tune their optical, electronic and chemical properties by introducing different substituents. Substituents can be introduced both at the *meso* and *β*–position of the macrocycle. According to the frontier molecular orbitals and their model structure calculated for porphyrins (See **chapter 1.2**), chemical modification on the *β*–positions will mainly affect the position of the a_{1u}/b_2 orbitals while modification on the meso position will affect the position of the a_{2u}/b_1 orbitals.[14] Through the introduction of conjugated substituents onto the porphyrin macrocycle, it is possible to extend the π-system conjugation. This extension generally increases the electron density on the frontier orbitals rising the energy of the HOMO. The result is a reduction of the HOMO-LUMO gap corresponding to a redshift in the absorption bands.[15–18] Extension of the porphyrin π–system easily yield absorption in the near infrared region.[13] This aspect is of particular interest in applications such as dye sensitised solar cells, and bulk heterojunction solar cells, since extending the absorption to the near infrared region improves the devices' performance.[5,6] Extension of the π–system provides further interesting properties such as low conductivity attenuation factors [12,19,20] and two-photon absorption[21,22]. Generally, the extension of the π–system is achieved by fusion of aromatic rings on the porphyrin core (**Figure 6a)** using a strong oxidant or introducing conjugated bridges through cross coupling reactions on the meso

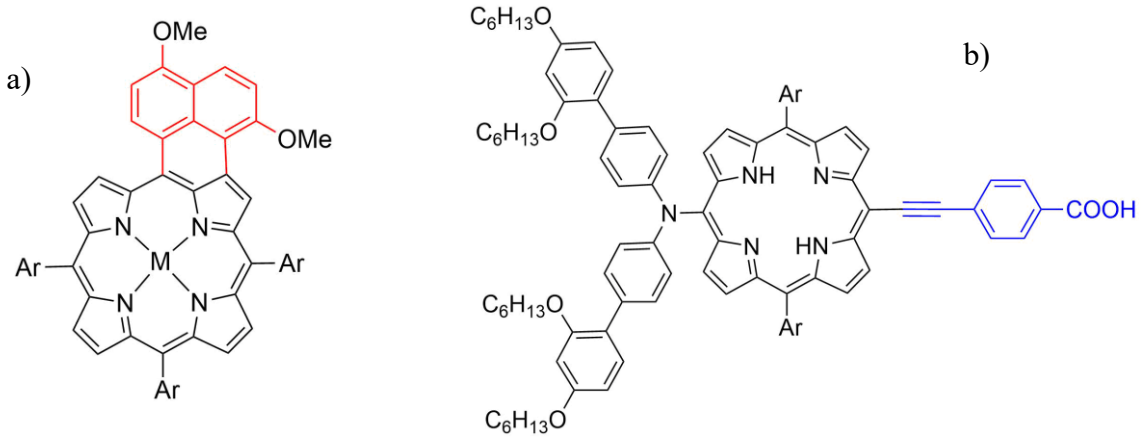

Figure 6*.Examples of π–extended porphyrins. The most common methods in the extension of the π–system consist in the fusion of aromatic rings on the molecule (a) or in the conjugation through triple bond bridge (b).*

position (**Figure 6b**). Both these extension processes possess synthetic drawbacks such as multiple steps and complex synthesis. Besides, the resulting redshift in the absorption is generally modest. Literature provides numerous examples of these reactions showing conjugation of the porphyrin core with anthracene,[15,16] naphthalene (**Figure 6a**),[17,23] phenyl rings,[24,25] pyridine[12] and several other aromatic systems.[13]

1.4 Singly linked fused porphyrins

An alternative to the traditional methods for the π-system extension, was proposed by Osuka and co-workers in 1997.[26] Osuka's group achieved the extension of the porphyrin π-system forming conjugated porphyrin polymers. This approach present several advantages:

- one step synthesis,
- use of a single compound to extend the π–system,
- commercially available starting materials,
- reaction time lower than 30 minutes.

The synthesis of singly linked porphyrins can be achieved mixing zinc porphyrins with available *meso* positions in presence of Ag^+ salts. The synthesis is remarkably regiospecific yielding only *meso-meso* linked porphyrins (**Figure 7**).

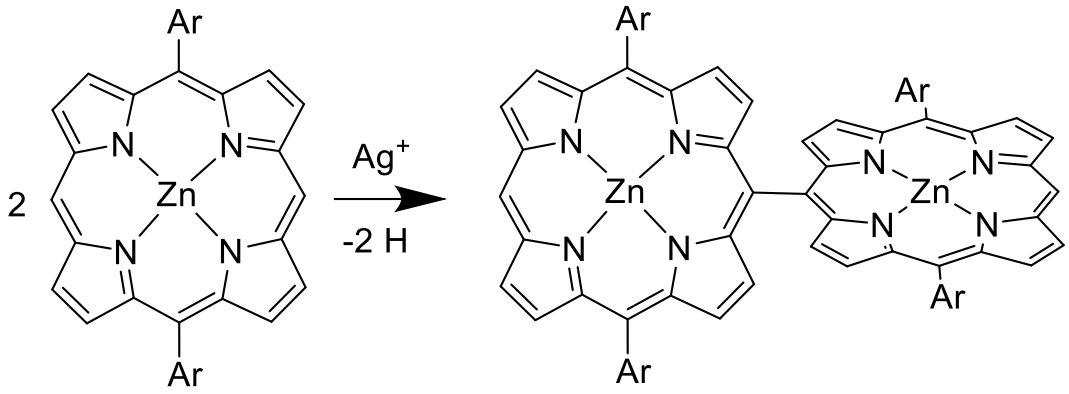

***Figure** 7. Extension of the porphyrin π–system. The extension occurs through conjugation to another porphyrin with the formation of a meso-meso bond.*

Employing $AgPF_6$ as oxidant avoids the termination of the polymerization via halogenation of the *meso* and *β*-positions. Consequently, the use of $AgPF_6$ provides a route towards the synthesis of polymeric chains containing up to 1024 monomeric units.[27] Although simply synthesized with extremely high regioselectivity, linking the porphyrins only on the *meso*-position mainly induces a nearly perpendicular orientation between the two porphyrinic units (**Figure 7**). In this conformation, the π–systems on the two porphyrins are almost perpendicular hindering an optimal conjugation. This perpendicular arrangement also affects the conductive properties of the compounds providing to singly linked porphyrin tapes higher attenuation factors compared to the respective triply linked planar structures (see below).[12] Furthermore, the distribution of dihedral angles between the units of the singly linked porphyrins polymer varies with temperature. As a result, the conductivity in singly linked porphyrin polymers strongly depends on the temperature.[28]

1.5 Doubly linked fused porphyrins

To improve the π–conjugation, a modification to the original reaction was achieved few years later.[29] The reaction takes advantage of the difference in reactivity of nickel(II) and palladium(II) porphyrins leading to the formation of *meso–β/β–meso* doubly linked porphyrins (**Figure 8**). The presence of double linkages forces the co-planarity between the units improving the electronic connection between the two porphyrins. Because of its flat structure, polymers of this class of compound were named porphyrin tapes. To synthesize doubly linked porphyrin tapes, $AgPF_6$ was replaced with stronger oxidants such as (4-bromophenyl) aminium hexachloroantimonate (BAHA) or with a mixture of 2,3-dichloro-5,6-dicyano-p-benzoquinone (DDQ) and scandium triflate $Sc(OTf)_3$. The improved conjugation affects the UV/Vis/NIR absorption spectra of these compounds, exhibiting a marked bathochromic effect towards the NIR region (**Figure 9**). Every monomer unit added to the tape increases the π–conjugation causing an additional redshift of the absorption bands. Doubly linked porphyrins are subject to the Effective Conjugation Length (ECL) effect. The ECL is described as the number of uninterrupted π–bonds at which the optical absorption onset saturates in the conjugated system. Although the number of units that can be added to the porphyrin tape is virtually infinite, the ECL effect limits the maximum conjugation of the system. Osuka and co-workers estimated that the ECL effect for doubly linked tapes is reached around 1500 nm.[30] Cyclic voltammetry measurements demonstrated that increasing the number of conjugated units reduces the potential required for the first electron oxidation in the polymer (**Figure 9**). This can be rationalized by the increase in the energy of the HOMO, when the porphyrin undergoes

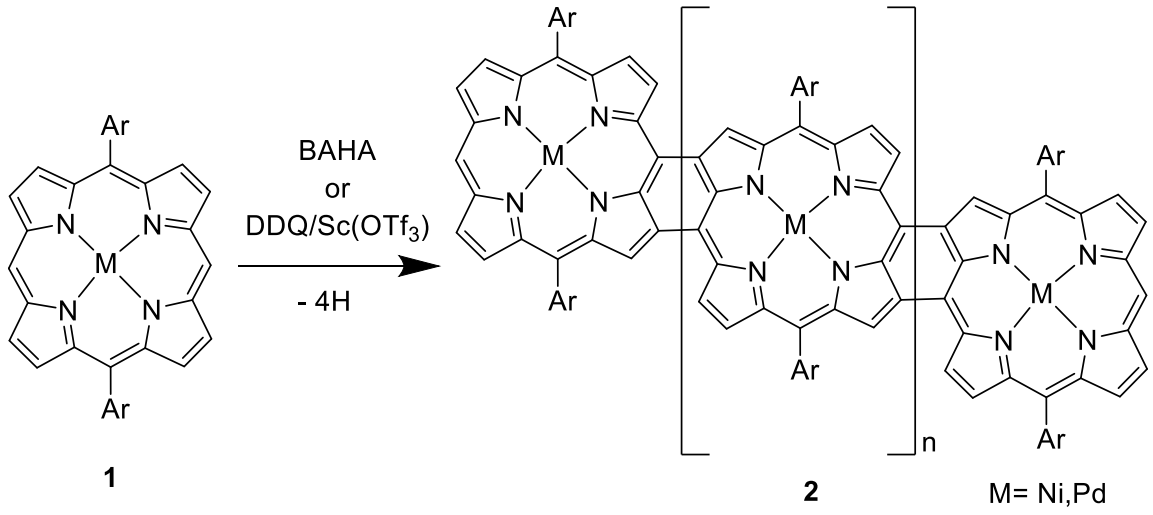

***Figure 8**. Reaction for the synthesis of doubly linked porphyrin tapes*

π–extension. This synthesis presents several drawbacks including small conversion of the monomers into final products and, when the tapes are composed of more than five units, insolubility in the case of phenyl *meso*-substituents.

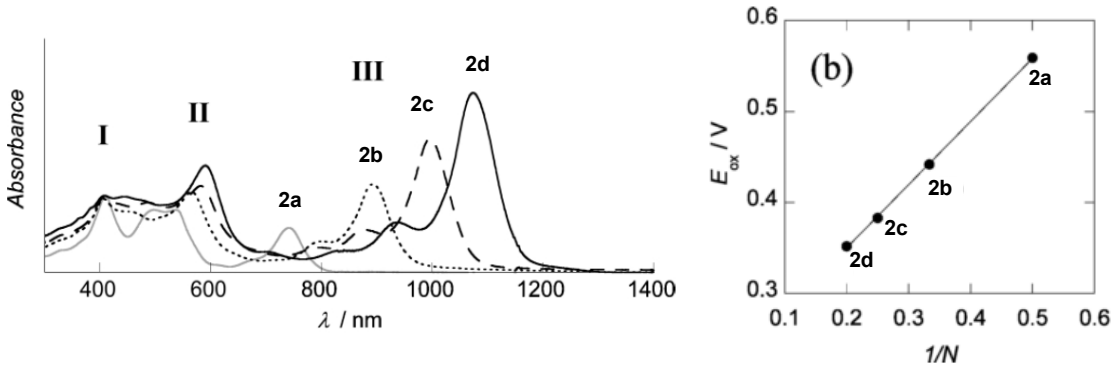

Figure 9. *(Left) UV/Vis/NIR absorption spectra of doubly linked nickel porphyrin tapes. (Right) First oxidation potential (Vs AgClO4/Ag in CHCl3) for doubly linked nickel(II) porphyrin tapes. Number of porphyrins in the doubly linked tape: 2a (n=0) 2b (n=1) 2c (n=2) 2d (n=3). Republished with permission of Chem. Commun., From [A.Tsuda, Y. Nakamura, A.Osuka, Chem. Commun,* ***2003****, 1096-1097]. Permission conveyed through Copyright Clearance Center, Inc.*

1.6 Triply linked porphyrin tapes

The synthesis of triply linked zinc porphyrin tapes was achieved in 2001.[31] The synthesis was performed in two steps (**Figure 10**):

- reaction of zinc(II) porphyrins with Ag^+ oxidants to obtain polymeric *meso*−*meso* singly linked porphyrins,
- second oxidation with DDQ and $Sc(OTf)_3$ converting *meso*−*meso* into *β*–*β*/*meso*−*meso*/*β*–*β* linked porphyrins.

The first step of the reaction consists in the formation of *meso-meso* singly linked porphyrin tapes using Ag^+ salts as reported by Osuka in 1997.[26] The second oxidation step induces a complete co-planarization of the molecule, finally exhibiting an exceptionally high level of

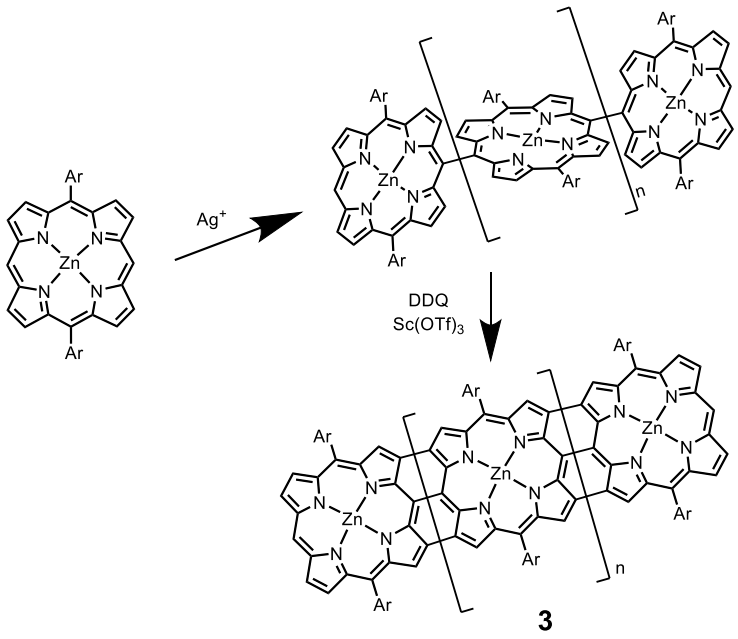

***Figure 10**. Synthesis of triply linked porphyrin tapes. The reaction evolves in two steps. Firstly, meso-meso connections between the units are formed by of Ag^+ salts. In a second oxidation step triply linked porphyrins tapes are formed adding a mixture of DDQ and $Sc(OTf)_3$.*

conjugation of the π–system through new bonds between the *β*–positions. This increased conjugation strongly affects the UV-Vis-NIR absorption spectrum of the molecule. A new unit added to the polymeric chain shifts the absorption bands towards the NIR region. If a sufficient number of units is added to the polymer (around 6), the porphyrin tape exhibits absorption bands reaching the IR region (**Figure 11**).[31] Thanks to the extension of the π–system, the HOMO-LUMO gap is reduced, yielding absorption bands at 3500 cm^{-1} / 2800 nm for dodecamers. Cyclic voltammetry measurements of the first oxidation of the porphyrin tapes confirm (similarly to doubly linked tapes) that the reduction of the HOMO-LUMO gap is related to an increase in the energy of the HOMO orbitals (**Figure 12**).[32] Other studies showed

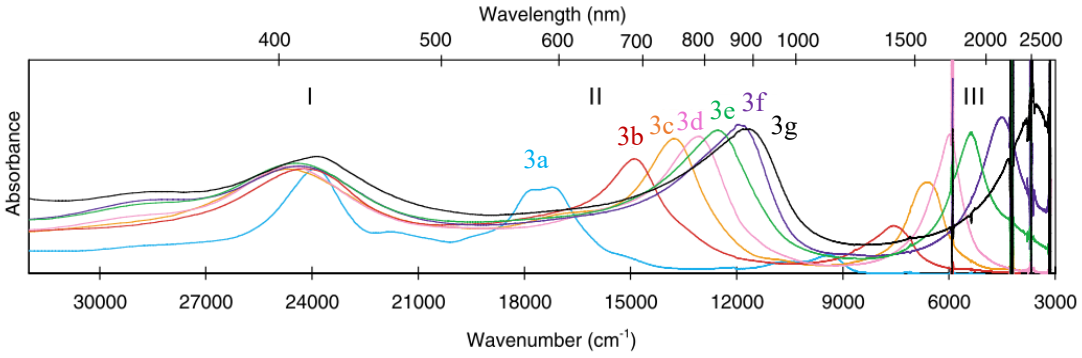

***Figure 11.** UV/Vis/NIR absorption spectra of triply linked zinc(II) porphyrin tapes. Number of porphyrins in the triply linked tape (**n**): 3a (n=0), 3b (n=1), 3c (n=2), 3d (n=3), 3e (n=4), 3f (n=5), and 3g (n=10). From [A.Tsuda, A.Osuka, Science, **2001**, 293, 79–82]. Reprinted with permission from AAAS.*

an ECL of 14 porphyrin units, corresponding to an ECL of *ca.* 12 nm. Triply linked porphyrin tapes present high nonlinear optical response[22,33] and improved electric performances compared to orthogonal singly linked porphyrins[12,28] Recently, it was shown that triply linked porphyrins exhibit an increase of the molecular conductance with length.[20] It was suggested that this behaviour is related to the reduction of the HOMO-LUMO gap increasing the chain length of the tape. This compensates the increased tunnelling distance.[19]

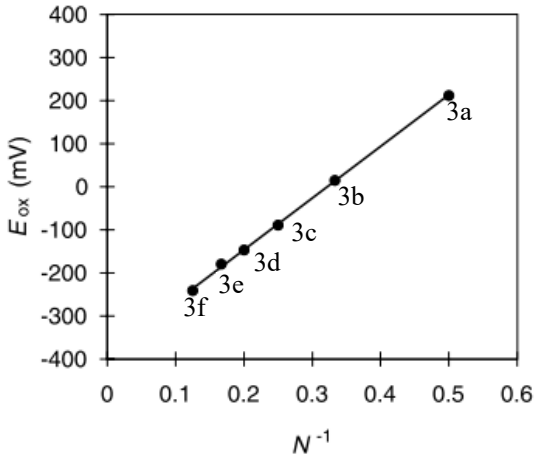

Figure 12. First oxidation potential for triply linked zinc porphyrin tapes. *Number of porphyrins in the tape (**n**): 3a (n=0), 3b (n=1), 3c (n=2), 3d (n=3), 3e (n=4), 3f (n=5), and 3g (n=10). From [A.Tsuda, A.Osuka, Science, **2001**, 293, 79–82]. Reprinted with permission from AAAS.*

1.7 UV-VIS (Band I/II/III)

Due to the strong modification of the electronic structure of porphyrin tapes, the classic division of the UV/Vis spectrum of porphyrin in B and Q bands is inadequate to describe the absorption spectra of porphyrin tapes. For this reason it was proposed to divide the spectra of porphyrin tapes in three parts, namely bands I, II and III (**Figure 9** and **Figure 11**). The **band I** *region* corresponds to the region between 400 and 500 nm where B bands are usually observed. This band usually broadens instensely when compared to the monomeric porphyrins. The **band II** region covers the range usually occupied by the Q bands. It corresponds to the region between 500 and 600 nm for doubly linked tapes, and between 600 and 1000 nm for triply linked porphyrins tapes. Finally, the **band III** region corresponds to the region over 800 nm in doubly linked tapes and over 1000 nm in triply linked porphyrins.

1.8 Reaction mechanism

The details of the reaction mechanism behind the formation of fused porphyrins are still debated. According to the most accredited proposed mechanism, the reaction starts when the porphyrin is oxidized to form a radical cation (**Figure 13**). The π-radical cation (electron-deficient/electrophile) can readily react with a neutral porphyrin (electron-rich/nucleophile) yielding intermediate adducts. A second oxidation and the elimination of two H^+ from the intermediate yields the products of the reaction i.e. *meso-meso, β-meso*, or *β-β* coupled porphyrins (**Figure 13**). Lastly, further oxidation and deprotonation of the dimer yields doubly and triply linked porphyrins. The reaction mechanism highlights the importance of the first C-C formation, which dictates the regioselectivity of the overall coupling reaction. Interestingly, the *β–β* coupling has been reported only as a side reaction during coupling of palladium(II) porphyrins.[34] This is probably related to the significant electronegativity of the palladium(II) cation, able to partially move the electron density of the neutral porphyrin from the *meso* to the *β* position.

1.9 Regioselectivity of the porphyrin coupling

Doubly and triply linked porphyrins exhibit different optical and electronic properties.[30,31] As a result, the regioselectivity towards the formation of doubly or triply linked porphyrin tapes plays a key role in defining the properties of optoelectronic devices produced using porphyrin tapes. Osuka and Tsuda observed for the first time the high regioselectivity of zinc(II) porphyrins in their oxidative coupling.[31] Unlike other metallo-porphyrins, zinc(II) 5,15-di-(aryl) porphyrins form exclusively *meso-meso* links in the presence of Ag^+ oxidants.[26]

Osuka also reported the high regioselectivity of nickel(II) di-phenyl porphyrins towards the formation of doubly linked porphyrin tapes.[29] Similarly, tri-phenyl palladium(II) porphyrins, and porphyrins bearing strong electron-withdrawing groups on the *meso* position form mainly doubly linked porphyrin tapes.[35] In the other cases, both doubly and triply linked porphyrins are usually obtained.[35–37]

It is clear that the regioselectivity between the doubly or triply linked porphyrins highly depends on the central metal ion and on the substituent pattern.[31,35–37] In almost all cases, the *meso*-position is involved in the oxidative coupling. This is attributed to the high electron density at the *meso*-position of the neutral porphyrin, which acts as nucleophile in the coupling reaction.[26,34,38] The significant electron density is related to the phenyl rings at the *meso* positions acting as electron donors and thereby raising the a_{2u} orbital energy level compared to the a_{1u} orbital. As described in **chapter 1.2**, the a_{2u} orbital possesses significant orbital coefficient at the *meso*-positions and a node at the *β*–positions. As a result, in porphyrins with a_{2u} orbital higher than a_{1u}, the *meso*-positions possess nucleophilic behaviour. Since higher energy a_{2u} orbitals are typical for neutral 5,15-di-(aryl) porphyrins, regioselectivity in oxidative coupling reactions is associated with the electrophilic site after the formation of the radical cation (**Figure 14**):[26,34,38]

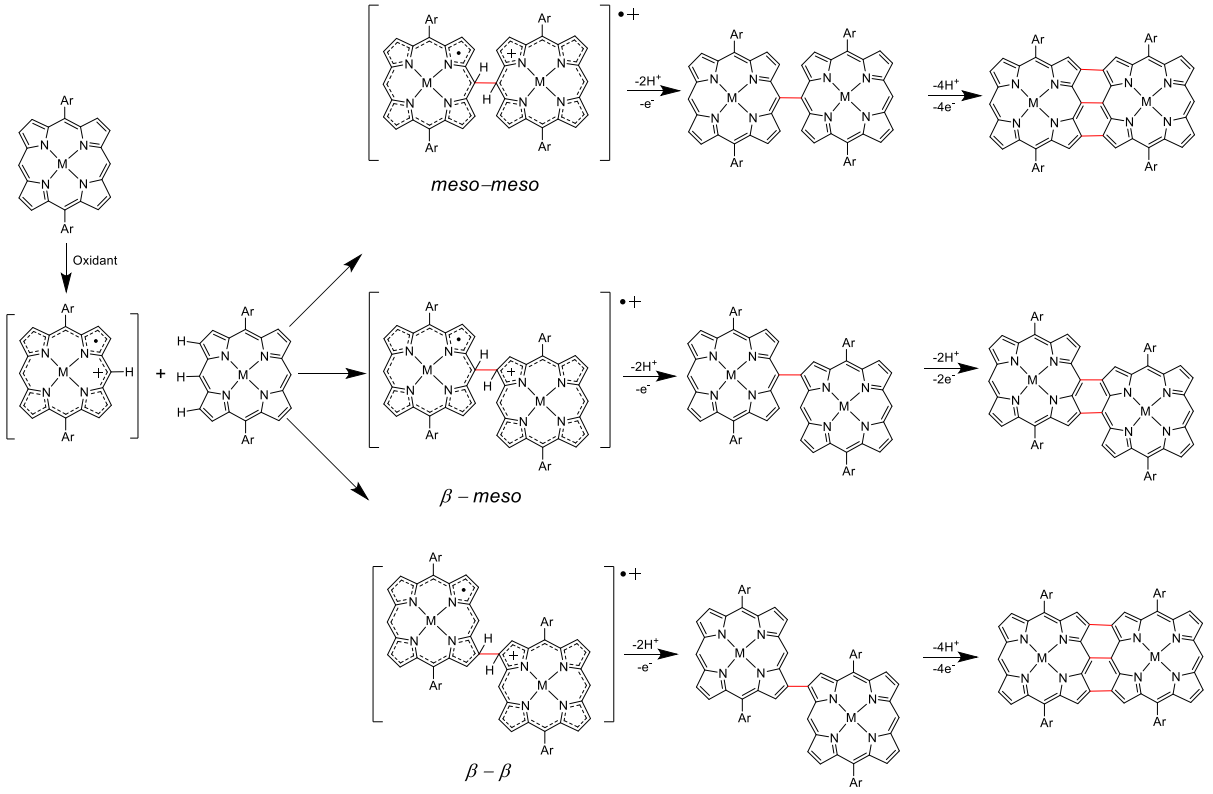

- Electrophilic site at the *meso*-position will yield triply linked porphyrins,
- Electrophilic site at the *β*-position will yield the doubly linked porphyrins.

The electrophilic site of the porphyrin π-radical cation is related to the orbital hosting the unpaired electron. In fact, while the a_{2u} radical cation character has node at the *β* positions, the a_{1u} orbitals have nodes at the *meso*-positions (**Figure 15**).

Furthermore, the oxidation of the porphyrin often induces changes to the porphyrins' electron distribution and to the molecular structure. As a result, the order of the frontier orbitals of the porphyrin π-radical cation, can be different compared to the respective neutral porphyrin. Finally, molecular distortions can also cause a mixing of the porphyrins' states inducing mixed (a_{1u}/a_{2u}) character of the radical cation orbitals.[39]

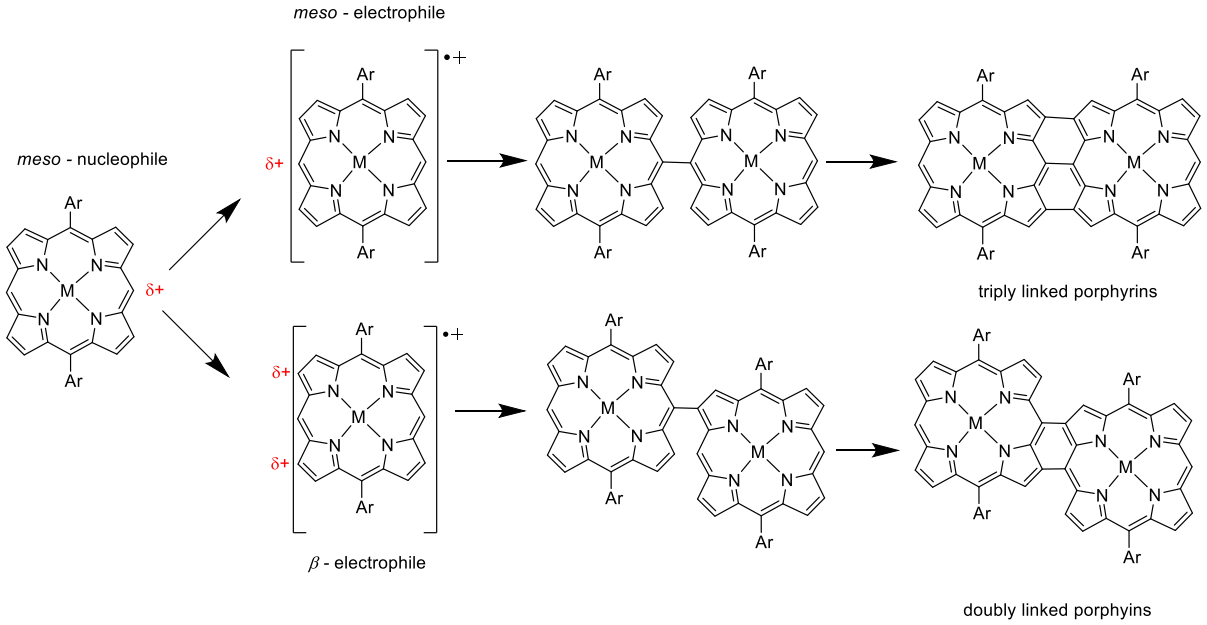

Figure 14. *Synthesis of triply or doubly linked fused porphyrins as a function of the electrophilic site.*

Figure 13*. Schematic of the formation of the porphyrin-porphyrin adducts and following formation of fused porphyrins*

1.10 The position of the frontier orbitals

An elegant way to estimate the nature of the π-radical cation symmetry is to perform electron spin resonance (ESR) experiments on the oxidized porphyrins. The experiment provides insight into the symmetry of the frontier orbital (a_{1u} vs a_{u2}) responsible for the electrophilic behaviour of the molecule. The ESR spectra of oxidized zinc(II) porphyrins exhibit a characteristic signal splitting resulting from the coupling of the unpaired electron with the four nitrogen on the molecule.[40] This suggests that the unpaired electron in zinc(II) 5,15-di-(aryl) porphyrins radical cation is placed in an a_{2u} orbital since a_{1u} orbital contain nodes on the four nitrogen atoms. On the contrary copper(II), palladium(II) and nickel(II) 5,15-di-(aryl) porphyrins have been attributed a_{1u} frontier orbitals.[40] The attribution of the nature of the frontier orbitals for a metalloporphyrin radical cation is often complex and highly debated in literature.[39] For example, Spiro and co-workers observed by resonant Raman spectroscopy that oxidized tetraphenyl porphyrins can undergo molecular structural distortions. This deformation, is due to pseudo Jahn-Teller distortions, and causes changes in the molecular symmetry allowing molecular states mixing. As a result of mixing, the predominant A_{2u} state of tetraphenyl porphyrins mixes with the A_{1u} state. If the porphyrin's π-radical cation exhibits a mixed character, both doubly and triply linked porphyrin tapes will be formed.[41] The mix however

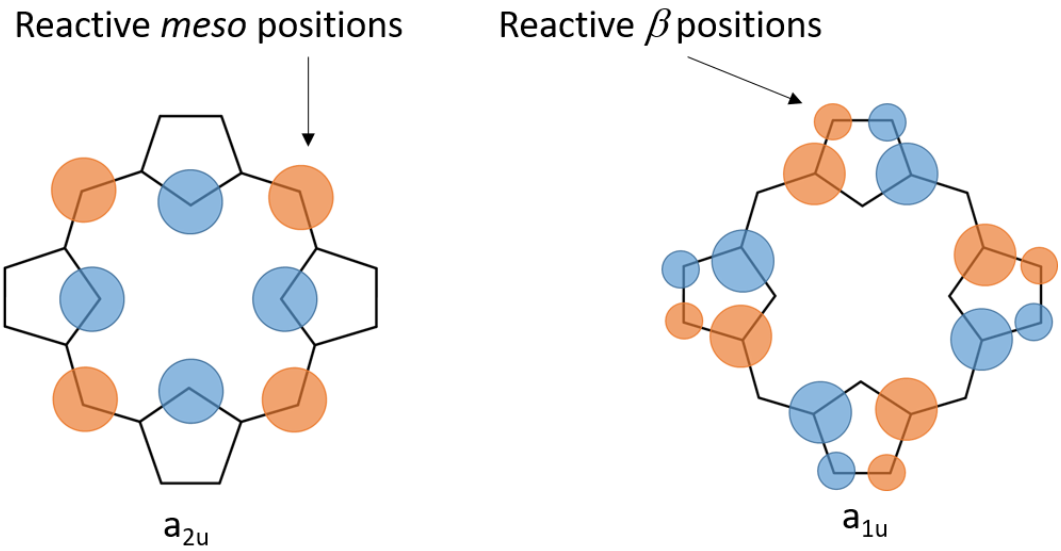

Figure 15. *Schematic of the porphyrin a_{2u} and a_{1u} frontier orbitals*

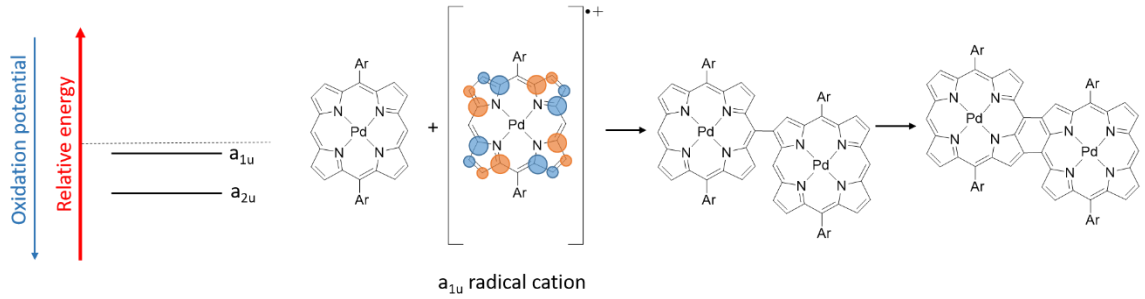

Figure 16. *Schematic of the orbitals relative energy, radical cation character and oxidation potential of the palladium(II) 5,15 di-(aryl) porphyrins.*

requires both the reduction of the molecular symmetry upon oxidation, and proximity of the A_{1u} and A_{2u} states. Another method to indirectly estimate the relative position of the frontier orbitals is cyclic voltammetry. With the substituent pattern on the porphyrin fixed, the relative position of the a_{2u} and a_{1u} orbitals depends exclusively on the metal center. As a result of the node on the nitrogen for the a_{1u} orbitals, the metal center will affect mainly the position of the a_{2u} orbitals.[35]

In the case of highly electronegative ions, such as palladium(II) (d^8 configuration) the electron density in the a_{2u} orbitals will be reduced resulting in a lowering of energy of these orbitals and thus higher oxidation potential (**Figure 16**).[34,42]

The opposite occurs in zinc(II) porphyrins. Zinc (II) possess a d^{10} configuration involving completely filled *d* orbitals. This electronic configuration increases the electron density on the a_{2u} orbitals resulting in higher energy a_{2u} orbitals and thus a lower oxidation potential (**Figure 17**).[42]

Finally, nickel(II) 5,15 di-(phenyl) porphyrins exhibit intermediate electronegativity. This leads to an intermediate oxidation potential with the a_{1u} and a_{2u} orbitals closer in energy. Oxidation of the porphyrin is also suggested to cause pseudo Jahn-Teller distortions leading to

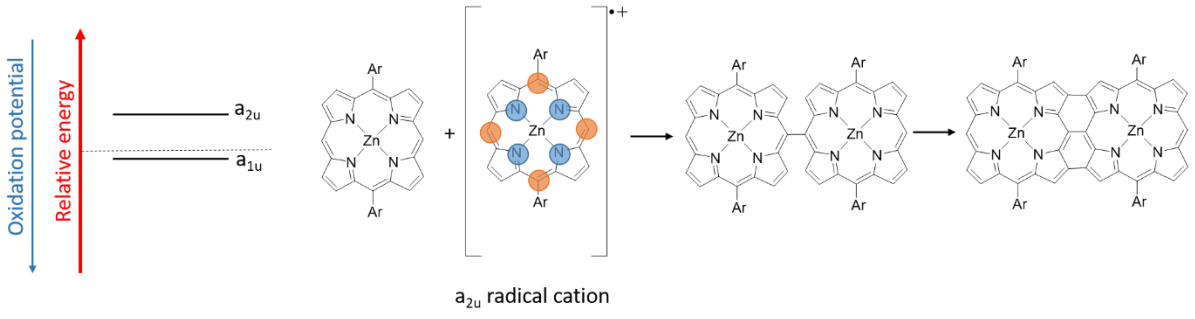

Figure 17. *Schematic of the orbitals' relative energy, radical cation character and oxidation potential of the zinc(II) 5,15 di- (phenyl) porphyrins.*

saddle arrangements. This arrangement decrease the symmetry of the molecule, thus allowing the mixing of the A_{1u} and A_{2u} states (**Figure 18**).

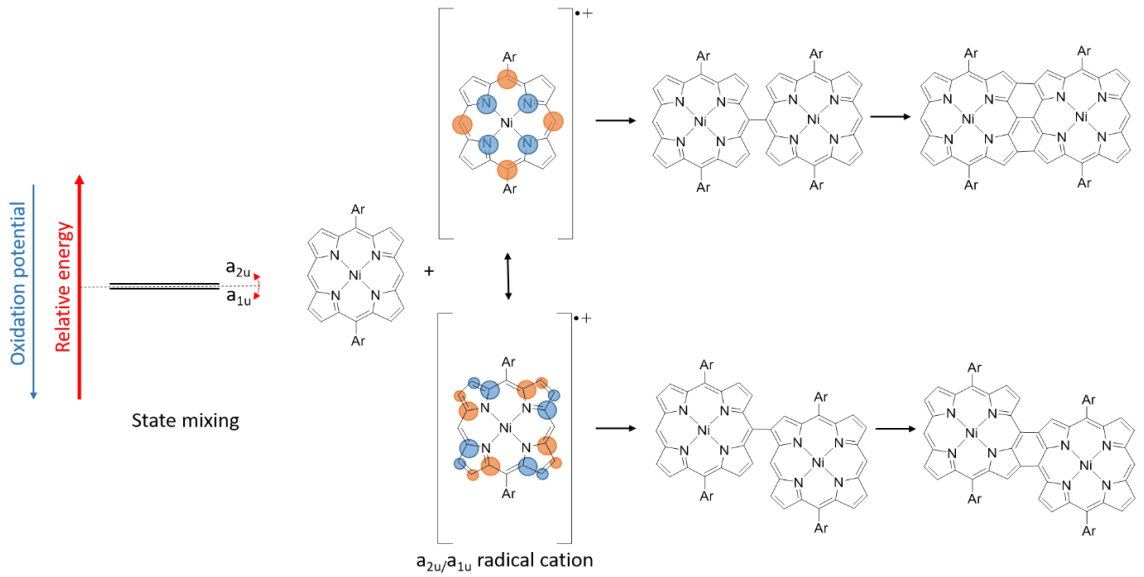

***Figure 18**. Schematic of the orbitals' relative energy, radical cation character and oxidation potential of the nickel(II) 5,15 di-phenyl porphyrins.*

1.11 The oxidant for the synthesis of porphyrin tapes

The oxidant type plays a key role in the synthesis of porphyrin tapes. There are several aspects to evaluate while choosing the correct oxidant. Firstly, the oxidant must be strong enough to reach the first oxidation of the porphyrin. This highly dependent on the metal-center and on the substituent on the porphyrin.[42–45] The solvent also plays a key role since it can modify the oxidant strength. For example, Ag^+ formal potential varies between 0.04 V in acetonitrile and 0.65 V in dichloromethane (values vs FcH).[46] Thus, finding the appropriate porphyrin/solvent/oxidant combination is not trivial, since the oxidant should also be able to yield the desired compound in a single step. Although this is already possible for doubly linked porphyrin tapes[30] using a mixture of DDQ/$Sc(OTf)_3$ (**chapter 1.6**), no oxidant has worked yet to exclusively yield triply linked porphyrin tapes in a single step.

Another problem related to the choice of the oxidant is the presence of undesired side-reactions. For example, while $AgBF_4$, $AgClO_4$ and $AgPF_6$ yield singly linked porphyrin arrays, $AgNO_2$ has been shown to cause *meso*-nitration of the porphyrin hindering the growth of porphyrin tapes.[26] Oxidants containing halogen atoms in their structure can cause halogenation of the

porphyrin tapes hindering the growth of long chains.[30,35] Finally, the industrial scale up of technologies is highly related to its final cost. Therefore, the ideal oxidant should be earth abundant and cheap, to lower the costs of the device production. Unfortunately, the synthesis proposed for triply linked porphyrin tapes requires Ag^+ oxidants which are neither cheap nor earth abundant.

For these reasons, several working groups have aimed to achieve one-step synthesis starting from cheap earth abundant oxidants limiting possible side reactions. Particularly, Zheng, Zhu and co-workers who found that iron(III) salts, such as $Fe(ClO_4)_3$ and $Fe(OTf)_3$, provide a straightforward synthesis of doubly and triply linked porphyrins tapes in one-step.[35] Brennan and co-workers discovered that also copper(II) salts in acetonitrile, such as $Cu(BF_4)_2$ and $Cu(ClO_4)_2$, yields similar results.[36,37] However, the proposed iron and copper oxidants never achieved high regioselectivity towards the synthesis of triply linked porphyrin tapes. [30,31,35–37] Although iron(III) and copper(II) salts are suitable for a wide range of metallo-porphyrins such as Cu^{2+},[36,37] Pd^{2+}[35]and Ni^{2+}[35], all the proposed syntheses exhibit the formation of a mixture of doubly and triply linked porphyrin tapes. It should be noted that none of the findings on the different oxidants report the synthesis on zinc porphyrin, which is likely related to zinc porphyrin's demetalation in the presence of acids produced during the oxidative coupling. It is likely that silver(I) salts produce weaker acids during the oxidative coupling. The moderate cost and abundance of these iron and copper oxidants make them appealing alternatives to the Ag^+/DDQ/$Sc(OTf)_3$ oxidant mixture in case of upscaling.

1.12 Solubility of porphyrins tapes

Porphyrins are known to aggregate in solution due to strong π–π interactions leading to poor solubility. The solubility however can be tuned modifying the peripheral groups of the porphyrin, thus achieving even water solubility.[47,48] As a result of their relatively simple synthesis, the most common substituents are phenyl rings, that lead to the formation of tetraphenyl porphyrins. The phenyl rings are twisted around 75° with respect to the porphyrin macrocycle hindering the π–π aggregation and improving the solubility. The introduction of a long polar chain, such as polyethylene glycol, allows water solubility by retaining a neutral porphyrin structure.[47] Solubility can also be improved introducing charged substituents, such as sulfonic acid groups, allowing retaining solubility even when supramolecular aggregates are

formed.[49] The peripheral group also affects how a porphyrin aggregates in solution and on substrates.[48,50]

The solubility of porphyrins is decreased in porphyrin tapes where the highly planar structure induces strong aggregation causing precipitation of the molecule.[30] The solubility also hinders the growth of long porphyrin tapes since the precipitation stops the polymerization process.[30,51] To increase the solubility of the porphyrin tapes and achieve higher degrees of polymerization alkyl groups have been introduced in the structure such as 3,5-*tert*-butyl or 3,5-dioctyloxyphenyl groups.[26,27,31] This allows synthesis of extremely long porphyrin tapes up to 24 units and singly linked porphyrin wires with 1024 units.[27,32] The poor solubility of porphyrin tapes represents an obstacle towards their integration in technological devices. Modern devices are mainly based on thin film technology and the insolubility of porphyrin tapes hinders control over the production of smooth thin films from solution-based approaches. Furthermore, the large substituents required to achieve extended structures, limit the interactions between the π-systems of different porphyrin chains. This affects the performance of optoelectronic devices where the charge carrier is required to move along the material between polymer chains.[5]

2 CVD OF CONJUGATED POLYMERS

2.1 Polymers

Polymers are macromolecules characterized by large molecular mass. Because of their structural properties and versatility, polymers are present ubiquitously in natural systems. In biological systems, polymers cover an impressive variety of roles such as in fundamental biological processes (proteins), genetic information storage (DNA) and structural function (lignin and collagen). However, their role is not limited to natural science. The coexistence high mechanical properties and light weight allows macromolecules to cover a fundamental role in material science, with a market estimated in $611.9 billion in 2017.[52]

The term “polymers” derives from two Greek words “polýs” and “meros” meaning “composed of multiple parts”. Indeed, similar to a chain made of multiple rings, polymers are also composed of multiple smaller components known as monomers. This idea of molecules made of smaller components, was theorized for the first time only in 1920. The German chemist Hermann Staudinger was awarded with the Nobel prize in 1953 for this theory.

Polymerization reactions affects both the special distribution of the molecules and the chemical-physical properties. For example, while acetylene is a gas, polyacetylene is a transparent solid. Several factors influence the properties of polymers such as conformation, interactions between chains and degree of crystallinity.[53–56] Thus, having a strict control over the organization of a polymeric structure is crucial for the design of materials with improved mechanical properties. The synthesis of stereotactic polymers with outstanding mechanical properties possible today thanks to the discovery of the Ziegler-Natta catalysts for olefin polymerization.[57,58] The discovery of this catalyst is so significant that Giulio Natta and Karl Ziegler were awarded with the Nobel Prize in 1963 for their pioneering studies.

2.2 Conductive polymers

After the Zigler and Natta invention, polymers had an increasing role everyday life. Polymers replaced paper in packaging, metals in structural functions, and they are widely used for their insulating properties. However, polymers did not cover a key role in electronics until recent years with the invention of flexible electronics. The foundation for the development of organic electronics was laid in the late '70s when Alan MacDiarmid, Hideki Shirakawa and Alan Heeger discovered the metallic behaviour of doped polyacetylene.[59] They showed the intrinsic conductivity of polyacetylene to increase from 10^{-5} Ω•cm^{-1} to 10^{3} Ω•cm^{-1} when exposed to an oxidizing agent. This discovery earned MacDiarmid, Shirakawa and Heeger the Nobel prize later in years 2000. Before the discovery of metallic polymers, high conductivity was an exclusive prerogative of metal containing materials. Unlike metals, polymers are flexible, cheap and allow the introduction of other functionalities thanks to the versatility of the organic compounds. Organic polymers today have a key role in the development of new technological devices with advanced functionalities.[60–62] A wide numbers of monomers is been employed for the synthesis of conjugated polymers such as polyacetylene,[63] polyaniline[64] and polythiophene[65] (**Figure 19)**. The synthesis of conductive polymers containing aromatic or heterocyclic building blocks is usually achieved employing Lewis acid catalysts. In addition, electrochemical polymerization is widely used for synthesis of metallic polymers due to its simple applicability, low cost and the possibility to tune the counter ion in the doping process. Conductivity in conductive polymers is strictly related to the conjugation of double bonds, allowing electron flow in the material. However, the conductive properties of the pristine polymers are generally poor. Similar to polyacetylene, a strong increase up to a metallic behaviour can be achieved upon doping in all the conjugated polymers.

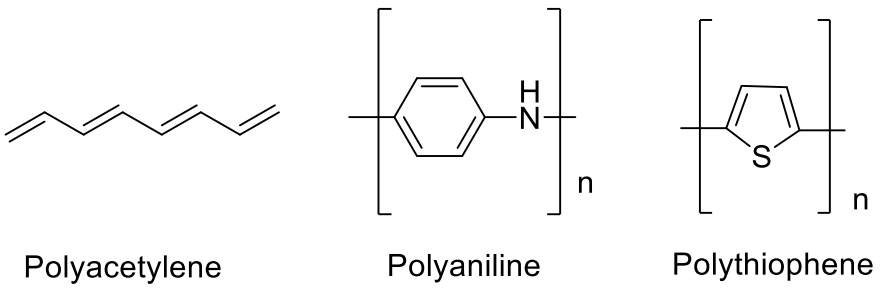

Figure 19. *Chemical structure of some of the most common conjugated polymers.*

2.3 Conductivity in polymers

Conductivity in polymers can be explained by considering the formation of electronic bands upon the mixing the molecular orbitals of the monomeric units. The band formed by the HOMOs will act similar to a valence band (**VB**) in inorganic conductors, while the band formed by the LUMOs behave as a conduction band (**CB**). Unlike inorganic materials, the extraction of one electron from the **VB** will not lead to hole in the **VB**, rather to the formation of new levels between **VB** and **CB** (**Figure 20b)**. These new levels arise from the distortion of the polymeric structure. The distortion of the ionized level causes a relaxation of the ionized state

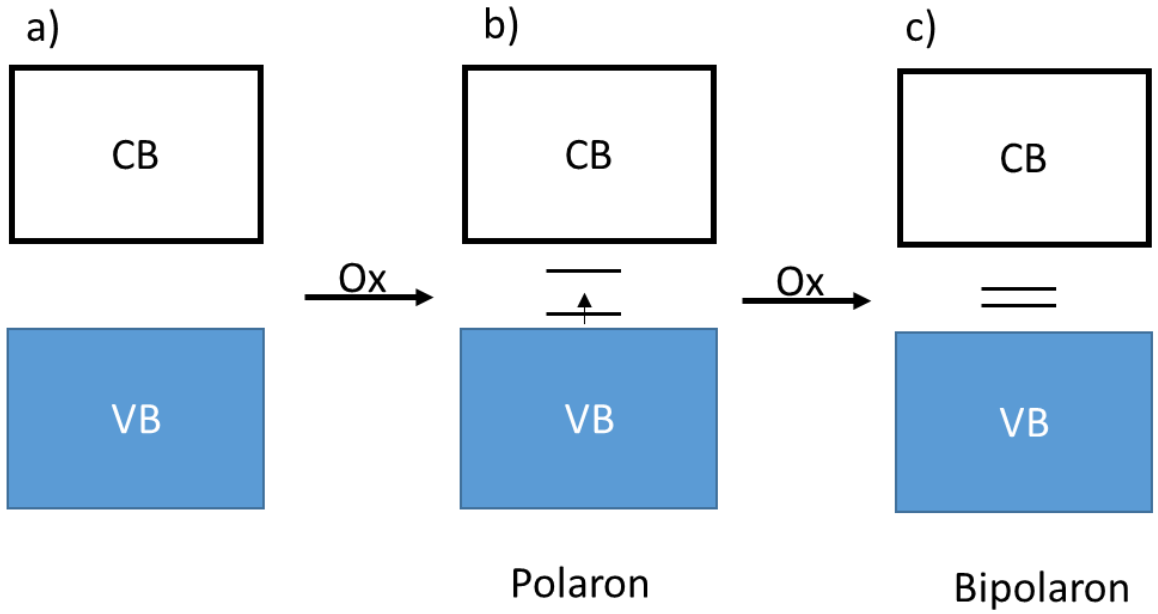

Figure 20. *Formation of polarons and bipolarons in conductive polymers.*

(stabilization of the LUMO) and a distortion of the structure in the ground state (destabilization of the HOMO) leading to two new levels between **VB** and **CB (Figure 20b**). The result of this chemical process will be a new radical cation associated to a lattice distortion called polaron. Further oxidation can lead to both the formation of new polarons or the extraction of the electron from the existing polaronic levels. The removal of the electron from the polaronic level will induce a new distortion of the polymeric chain and the formation of doubly charged species. The formation of a pair of charges associated to a strong lattice distortion is called bipolaron. This new distortion causes bipolaron levels get closer in energy (**Figure 20c**). In the case of high level of doping, bipolaron levels will merge forming new bands between the **VB** and the **CB (Figure 21a).** It has been shown that polythiophene is characterized from a small bandgap between **VB** and **CB.** At high level of doping, the bipolaronic bands formed will

merge with the **VB** and with the **CB** causing a metallic behaviour in the polymer (**Figure 21b**).[66]

A similar model can be applied to n-doped polymers. In this case the polymer will be negatively charged and the electrons will fill the π* orbitals of the macromolecule resulting in partially filled **CB**.[66] Generally, the doping process occurs through oxidants (p-doping) or reductants (n-doping). Better results are usually achieved by p-doping using oxidants such as I_2, Br_2 or AsF_5.[67,68] Examples of n-doped polymers are rare, since p-doping usually achieves better performance.

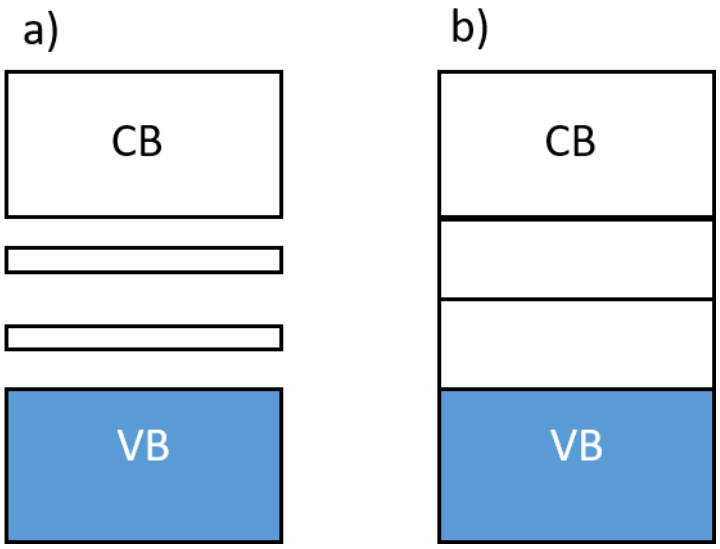

***Figure 21**. a) Structure of the bipolaron in conjugated polymers. If the bipolaronic bands are close to the **VB** and **CB,** a new electronic structure will result in a metal like structure with a partially filled **VB**.*

2.4 Vapour deposition

Modern technology moves towards the integration of multiple functionalities in single devices. Smartphones are a perfect example of this principle by integrating in a single device multiple sensors, GPS, telecommunications and OLED screens. Consequently, the production of new devices requires the invention of new technologies and the miniaturization of existing technologies. Consequently, the market has increased the demands for organic and inorganic thin films with controlled thickness and functional properties. Several methods exist for the formation of thin films from solution such as spin coating and dip coating. However, solution based technologies present several drawbacks including

- inhomogeneous films due to dewetting,
- incompatibility of substrates with some solvents,
- poor control over film thickness.

Furthermore, to deposit a chemical compound it must be prepared separately and be soluble in the solvent used for the process. Vapour deposition techniques overcome these drawbacks. In vapour deposition the absence of solvent avoids dewetting effects and solvent incompatibility with the substrate. Furthermore, film thickness can be easily controlled. Several techniques have been developed in the last decades allowing simultaneous synthesis and deposition of organic (as poly-acrylates[69]), inorganic (as metals,[70] oxides[71] and fluorides[72]) and hybrid films[73] on virtually any substrate. It is possible to discriminate between Physical Vapour Deposition (PVD) and Chemical Vapour Deposition (CVD). In PVD no chemical reaction occurs during the film deposition, while CVD techniques are characterized by a chemical

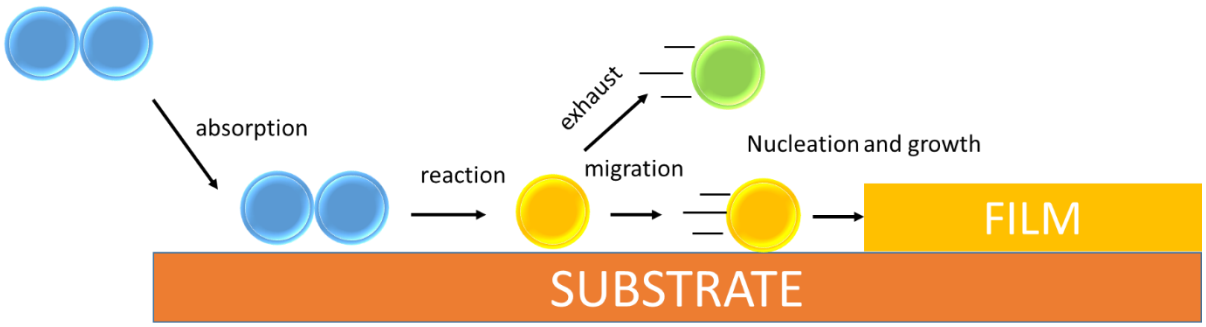

***Figure 22**. Schematic of the CVD process. The precursor reachs the surface where it can react, migrate, sublime and grow as film.*

reaction yielding the desired compounds (**Figure 22)**. CVD represents one of the most common solutions in industry for the synthesis of thin films because of its up-scalability and high control of the film properties. The main advantage of CVD techniques is the chemical reaction occurring in the gas phase, yielding the desired compounds deposited on the substrate. However, as a drawback this demands the volatility of the precursor.

The most simple CVD technique is the thermal CVD where the chemical reaction is triggered by high substrate temperature. This approach is used in the production of oxides and fluorides such as TiO_2[74], Cu_2O[71] and CaF_2[72]. One drawback is the temperature required to trigger the chemical reaction. As a result, substrates and precursors choice is limited by the temperature. Thermal sensitive substrates (i.e. paper and polymers) and precursors (such as organic compounds) show obvious poor compatibility with thermal CVD.

2.5 CVD of polymers

In order to increase the number of usable precursors and substrates, several other CVD approaches have been developed in the last decades aimed at reducing the temperature involved in the process. The main difference between such techniques lies in the event initiating the chemical reaction. The most common alternatives to thermal CVD rely on plasma (plasma enhanced CVD[75]), light (photo-assisted CVD[76]) or chemical initiation (initiated CVD[77]/molecular layer deposition[78]). Although the main application of CVD is the synthesis of inorganic thin films, the development of these new techniques allows the production of organic and polymeric thin films. Lastly, several parameters such as pressure, injection system and chemical initiators can also be adapted to the use organic precursors.

Organic precursors generally suffer from poor volatility demanding low pressure CVD set-up to obtain thin films.[78–81] In this case, the precursor is usually provided as a vapour (e.g. 3,4-ethylenedioxythiophene (EDOT) and aniline).[79] In low pressure set-ups, the precursor can be introduced as a solid and sublimed towards the substrate as in the case of $FeCl_3$ used as initiator for the oxidative polymerization of EDOT. One drawback of the low pressure CVD, is the expensive equipment required such as pumps and reactors compatible with high vacuum levels. An alternative to the use of low pressure set-ups, is to introduce the precursors as an aerosol, allowing the use of atmospheric pressure set-ups.[82] The synthesis of polymeric layers by CVD still represents a challenge for modern material science. Lastly, to date oxidative CVD is the

only vapour deposition technique allowing the synthesis of conjugated polymers retaining control over the chemical reaction.

2.6 The oxidative chemical vapour deposition (oCVD)

The invention of conductive polymers revolutionized the production of electronic and optoelectronic devices. However, the integration of conductive polymers in devices is complex due to their poor solubility, representing a serious limitation to their application. Modification of the chemical structure of the monomer is required to achieve the solubility necessary to process the polymers as thin films. An example is the modification of the pending groups on thiophene (e.g. ethanesulfonate and butanesulfonate), allowing its water solubility in industrial applications.[83] However, the modification of the monomer requires a significant synthetic effort. A solution to the insolubility of the polymer was proposed in 2006 by Karen Gleason, who implemented oxidative polymerization in CVD, thus providing the first example of oxidative CVD (oCVD) .[84] The oCVD consists of simultaneous vaporization of an oxidant (e.g. $FeCl_3$) and a suitable monomer (e.g. EDOT). The oxidant allows the oxidative coupling of the monomers directly yielding conjugated polymers thin films. Relying on the gas phase, the oCVD cuts the need of solubility of monomers and products. Furthermore, the oxidant acts simultaneously as coupling and doping agent, yielding doped films. As a result of condensing synthesis, deposition and doping in a single step, the final cost of the device production is reduced. Another advantage of oCVD, is represented by the low temperature required for the process, allowing deposition on sensitive substrates such as textiles or polymers.[79] However, to ensure the sublimation of monomer and oxidant, the process requires reduced pressure.

In oCVD, the substrate is usually placed on a heated stage at the top of the reactor facing downwards (**Figure 23a)**. In case of liquid or high-to-moderate vapour pressure monomers, injection in the reaction chamber occurs from the vapour phase. The oxidant is usually solid (i.e. $FeCl_3$) and, therefore, is provided using a heated crucible (**Figure 23a**). In case of liquid oxidant, the oxidant can be introduced in the chamber directly as vapour (**Figure 23b)**.

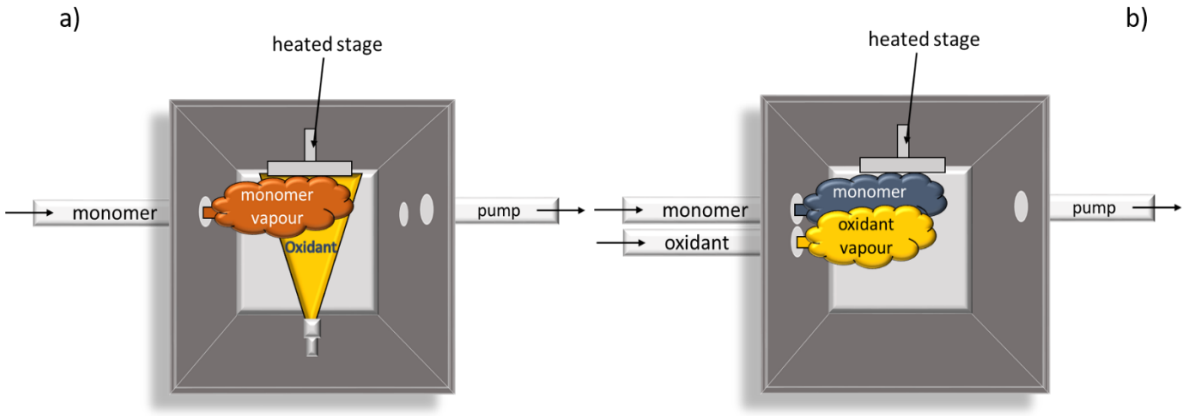

Figure 23*. Typical layouts of oCVD reactors. a) Monomer injected as vapour and oxidant sublimed in the chamber, b) monomer and oxidant injected as vapour in the chamber*

2.7 Monomers and oxidants in oCVD

To be used in oCVD, precursors should be highly volatile to be delivered towards the substrate. As a result, the monomers employed in oCVD are generally small molecules with a simple chemical structure. This aspect clearly limits the functionality that can be provided to the thin film. The first and most studied monomer in oCVD is 3,4 ethylenedioxythiophene (EDOT), yielding poly 3,4 ethylenedioxythiophene (PEDOT). Interest in this material is driven by its numerous potential applications ranging from OLED to photovoltaics. Furthermore, PEDOT is transparent and highly conductive. Other polymers have been synthesized by oCVD such as polyaniline (PANI),[64] polydopamine (PDA),[85,86] or polypyrrole (PPy)(**Figure 24**).[87,88] In addition, multiple monomers can be used simultaneously in the chamber to obtain co-polymers.[89]

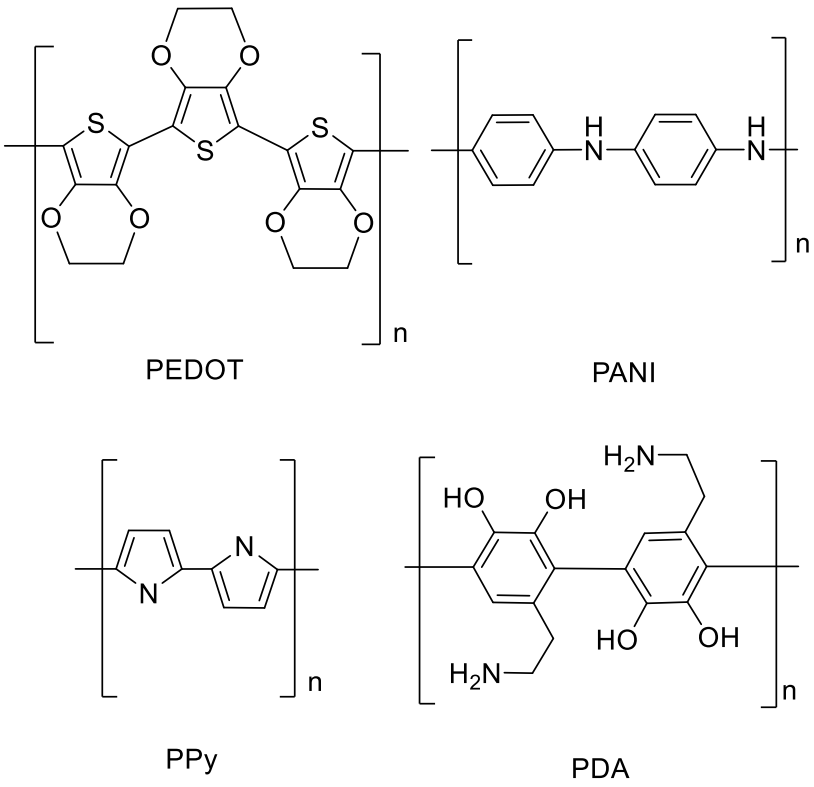

***Figure 24**. Structure of the most common polymers synthetized by oCVD.*

Significant effort has been made also in finding more suitable oxidants for the oCVD process. $FeCl_3$ is the most common oxidant in oCVD. However, at the end of the deposition traces of unreacted $FeCl_3$ remain in the formed film, which require further rinsing step to be eliminated.

The oxidant also influences the morphology and conformality of the film. For example, Br_2 was reported to yield more conformal coatings compared to $FeCl_3$. However, its practical use is limited by its high toxicity and because of its corrosives nature damaging the reactors.[79] $CuCl_2$ also increases the conformality of oCVD films compared to $FeCl_3$. It also induce higher level of porosity due to the slower formation of gaseous by-products.[90] More recently $VOCl_3$[65] and $SbCl_5$[91] , which are liquid under standard conditions, have been used as oxidants in oCVD. The high volatility of liquid oxidants cuts the need for rinsing steps. Lastly, liquid oxidants provide an easier control over the oxidant delivery rate through the control of its flowrate.[64]

Lastly, sublimation/evaporation can affect the oxidant strength. As an example, the sublimation of $FeCl_3$ yields among other products the synthesis of Cl_2, which is characterized from a higher standard oxidation potential.[92,93]. Unfortunately, literature lacks of studies on the oxidant strength in the gas phase, thus hindering a more accurate selection of the oxidant in oCVD.

3 PVD AND CVD OF PORPHYRINS

3.1 Sublimation of porphyrins

Although an impressive number of publications is being released every year regarding porphyrinoids, only few of them are related to porphyrins in the vapour phase. This is mainly related to the high temperature and vacuum typically required for sublimation of the porphyrins, and to the simplicity of other solution-based approaches. Several techniques have been employed for the sublimation such as thermal evaporation,[94] pulse-injection,[95] and glow discharge[96]. Due to its simplicity, thermal evaporation is more often used to deposit thin and sub-monolayer films. However, heat can induce the oxidative degradation of the macrocycle through the elimination of one of the methine bridges in the porphyrin yielding linear oligopyrroles.[97] The high temperature required for the sublimation of porphyrins is probably a consequence of the strong π–π interactions between porphyrins in the solid state. As a result, reduced pressure (often ultra high vacuum) must be used to achieve the sublimation of intact porphyrinoids. Even at reduced pressure, the temperature required for the sublimation of porphyrins can be greater than 300°C.[97] Nonetheless, sublimation still represents a valuable method for the purification of porphyrins from the by-products of the reaction.[98]

3.2 Surface assisted reactions of porphyrins

Several groups studied the self-organization of porphyrin monolayers by Scanning Tunneling Microscopy (STM) through sublimation of porphyrins on metallic substrates.[99–102] These studies rely on the thermal stability of the porphyrin core up to 300°C. For example, Yokoyama and co-workers showed cyanophenyl porphyrin's substituent sublimed on Au(111) substrates, are able to spontaneously form supramolecular structures on gold surface.[50] Similar studies showed that porphyrins and porphines sublimed on metallic substrates can form covalent bonds and polymers via surface assisted reactions.[103–106]

Interestingly, Auwärter and co-workers demonstrated that porphines undergo oxidative coupling on Ag(111) surface upon heating at 300K.[107] The reaction yields directly fused porphines similar to the porphyrin tapes obtained by Osuka. On one hand, these reactions exhibit extreme simplicity since the only requirement is the sublimation of the porphyrin under

vacuum, on a heated metallic stage. On the other hand, they all rely on surface reactions limiting the synthesis to sub-monolayers. Furthermore, the syntheses are highly substrate dependent hindering the application in technological devices.

3.3 CVD of porphyrins

Literature on the synthesis of porphyrin based materials from a solution based approach is extremely rich with examples. Contrarily, the preparation of porphyrin based materials from the gas phase offers only few isolated examples. In 1999 Yoshida and co-workers performed a pioneering study in this field exploring the plasma polymerization of cobalt tetraphenyl porphyrin.[108] This study showed that highly reactive species formed in the plasma are able to yield polymeric structures containing porphyrins. However, due to the non-specificity of plasma reactions, the porphyrins macrocycle is poorly retained in the final film. Other groups developed different methods to synthesize porphyrin containing materials from the gas phase. Particularly, Tonezzer, Maggioni and co-workers showed the use glow discharge induced sublimation to form cobalt tetraphenyl porphyrin thin films[96] or to immobilize porphyrins in polyimide films through co-sublimation with polyimide precursors.[109] More recently, Boscher, Heinze and co-workers showed that it is possible to immobilize intact zinc(II) tetraphenyl porphyrins in a polydimethylsiloxane matrix through co-injection of the precursors in atmospheric pressure dielectric barrier discharge. Contrarily to Yoshida's example, these works do not involve any reaction of the porphyrin. Consequently, they cannot be strictly considered as chemical vapour depositions of porphyrins.

The first example of a controlled chemical vapour deposition of porphyrins was published only in 2016. Boscher, Heinze, Gleason and co-workers showed the possibility to obtain polymeric porphyrin thin films by initiated Plasma Enhanced Chemical Vapour Deposition (iPECVD).[81] The technique relies on the radical polymerization of the porphyrin's pyrrolic ring (**Figure 25)** and consists in delivering the sublimed porphyrin towards the substrate while *tert*-butyl-peroxide (TBPO) is used as initiator cleaved by the plasma. The material exhibits outstanding gas-separating performances when deposited on permeable membranes. The technique yields extremely smooth and pinhole-free polymeric porphyrin films. It was shown that the gas-separation properties arises from the compact arrangement of the porphyrin units in the polymer. In fact, the polymeric structure lead to a dense structure with small holes with a comparable size to the kinetic diameter of small gas molecules such as H_2 and O_2 or CO_2.[75]

The properties of this material were further improved by co-polymerization in the presence of divinylbenzene.[110] The study also showed that via reduced plasma power it was possible to improve the retention of the porphyrin macrocycle. However, the radical polymerization yields poly-chlorins (reduced porphyrins) instead of conjugated poly-porphyrins. As a result, the polymerization does not increase the conjugation of the aromatic system, hindering its use in optoelectronic devices.[81]

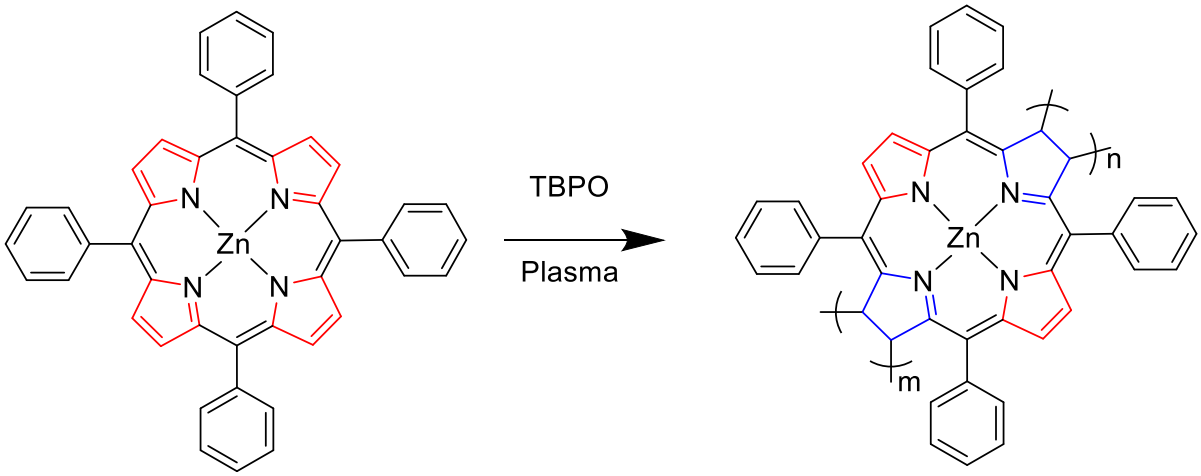

Figure 25. S*chematic of the polymerization of tetraphenyl porphyrins by iPECVD. The conjugation of the system is lost due to the formation of chlorins (Blue pyrrolic rings).*

4 AIM OF THE WORK

Since Osuka's first publication in 2000 on porphyrin tapes, several studies have been conducted on this class of compounds. These studies showed intense NIR absorption, two-photon absorption properties and unique electrical properties including low conductance attenuation factors. However, the low solubility of porphyrin tapes and their complex synthesis hinder their integration in optoelectronic devices. In fact, the most common modern devices rely on smooth thin films, which cannot be obtained in the absence of acceptable solvent solubility. This PhD thesis aims to fill the gap between the fused porphyrin tapes and CVD of conjugated polymers, thus circumventing the low processability of porphyrin tapes and allowing their integration into optoelectronic devices. The main goal of the present work is to develop a straightforward synthesis and deposition of porphyrin tapes thin films directly from the gas phase. The gas phase approach circumvents the limitation of the poor solubility of porphyrin tapes yielding smooth thin films. In order to reach this goal, the oCVD ability to form conjugated C-C bonds was exploited.

The PhD project was divided in 5 different key-points:

- Firstly, the possibility to obtain porphyrin tapes by oCVD of nickel(II) 5,15 diphenyl porphyrin with $FeCl_3$ was proven. A systematic study of the chemical composition, optical, electric and morphological properties of the obtained film was proposed aiming to provide a full representation of the properties of the film.
- In a second phase, the role of the oxidant in the oCVD of porphyrins was studied. The replacement of $FeCl_3$ with copper(II) salts such as $CuCl_2$ and $Cu(ClO_4)_2$ was investigated. It was also shown that the conductivity of the porphyrin tapes obtained by oCVD is highly dependent on the oxidant's sublimation temperature.
- In a third phase, the reaction mechanism of the oCVD of porphyrins was investigated and compared to the results reported by solution based approaches to obtain porphyrin tapes. Several differences have been observed between the reactivity of porphyrins in oCVD and solution based approaches. To explain these differences, a representation of the electronic structure of nickel(II) 5,15 diphenyl, 5,10,15 triphenyl and 5,10,15,20 tetraphenyl porphyrins and of their radical cations was derived via DFT and EPR studies.
- In a fourth phase, the possibility of obtaining porphyrin tapes with different of the *meso*-substituents was investigated, and the effect of substituents on the electric properties of the thin

film was evaluated. Differences in the electric performances were correlated to the intermolecular distances thanks to DFT calculations and Gel Permeation Chromatography experiments. The intermolecular distances could be tuned by the size of the substituents and their orientation in the space, which favoured or hindered the π–π interactions.

- Finally, the effect of the metal center was investigated. The porphyrins bearing iron(III), cobalt(II), nickel(II), copper(II), zinc(II) and palladium(II) metal cations were tested in oCVD and the obtained films were characterized. The effect of the metal ion on the regioselectivity of the reaction was investigated and related to the reaction mechanism.

5 RESULTS AND DISCUSSION

The outcomes of this work have been published (or submitted for section 5,5) as scientific articles in peer-reviewed chemistry journals. All the articles have been published in an open access format.

The article in the section 5.1, published with the title "Conductive fused porphyrin tapes on sensitive substrates by a chemical vapour deposition approach", discusses the synthesis and deposition of nickel(II) 5,15-di-(phenyl)-porphyrin tapes by oCVD. $FeCl_3$ was selected as the oxidant due to its well known use in oCVD. The deposition yields thin films with conductivities in the order of 10^{-2} S/cm and ohmic behaviour. The occurrence of oxidative polymerization was evidenced by high resolution mass spectrometry (HRMS). The HRMS showed the cyclization of the phenyl ring on the porphyrin macrocycle, which will be further described in the following studies. Modifying the porphyrin monomer in nickel(II) 5,15 di(3,5-*tert*-butylphenyl) porphyrins improved the solubility of the polymer, allowing to confirm the polymerization through GPC analysis.

The use of different oxidants and the effect of different amount of oxidant delivered to the substrate were investigated in an article entitled "Conductive directly fused poly(porphyrin) coatings by oxidative chemical vapour deposition – from single to triple fused"(chapter 5.2). While $FeCl_3$ was confirmed to be the most effective oxidant of the series, a change of the conductivity of the film with the amount of oxidant delivered was observed by C-AFM. This effect was related to the enhanced planarization of the molecule due to the increased number of bonds between the monomeric units.

The reaction mechanism was investigated in the article published with the title "Reactivity of Nickel(II) Porphyrins in oCVD Processes—Polymerisation, Intramolecular Cyclisation and Chlorination"(chapter 5.3). The study highlights the importance of the SOMO in the regioselectivity. Furthermore, the necessity of free *meso* positions to allow the nucleophilic attack starting the oxidative coupling was confirmed. The SOMO was investigated by means of density functional theory and EPR spectroscopy suggesting that in nickel(II) porphyrins the SOMO has a mixed a_{1u}/a_{2u} character.

The role of the *meso*-substituent on the film properties was investigated in the paper published with the title: "Molecular Flattening Effect to Enhance the Conductivity of Fused Porphyrin

Tapes Thin Films"(chapter 5.4). The study showed that increasing the size of the substituents (phenyl < mesityl < di-*tert*-butylphenyl < dodecyl-oxyphenyl) affects the π–π stacking, the intermolecular distance and, consequently, the conductivity of the films. The intramolecular cyclization between the phenyl ring and the porphyrin macrocycle forces the planarity of the molecule and improves the π–π stacking. This planarization reduces the intermolecular distance and improves the conductivity of the film with an effect that was called "molecular flattening effect".

Finally, the effect of the metal center was investigated in a manuscript submitted with the title "Metal Ion Effect on Regioselectivity in the Synthesis of Porphyrin Tapes in oCVD" (chapter 5.5). The study confirmed that the metal center highly affects the regioselectivity of porphyrins in oxidative coupling reactions. Particularly, zinc(II) porphyrins yield only triply linked porphyrin tapes while palladium(II) porphyrins form doubly linked porphyrin tapes. For the first time cobalt, porphyrin tapes have been synthesized. The absence of a metal center allows acid-base reactions, which hinders the polymerization reaction.

5.1 Conductive Fused Porphyrin Tapes on Sensitive Substrates by a Chemical Vapor Deposition Approach

Giuseppe Bengasi, Kamal Baba, Gilles Frache, Jessica Desport, Paul Gratia, Katja Heinze, and Nicolas D. Boscher

Angew. Chem. Int. Ed. **2019**, *58*, 2103 –2108

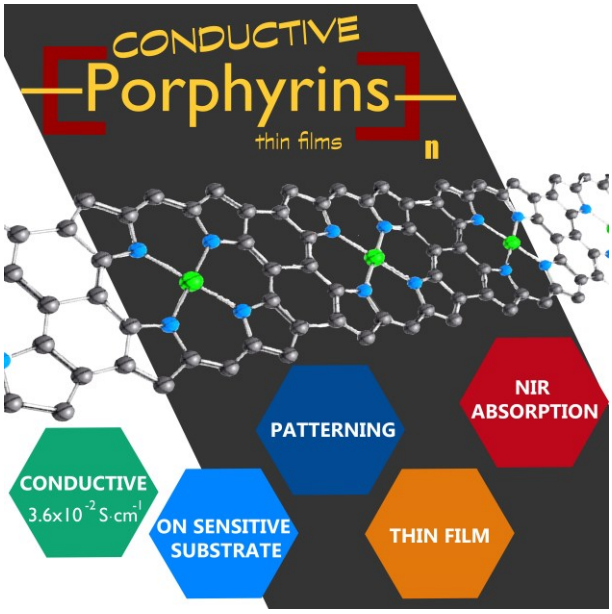

Directly fused metalloporphyrin tapes were simultaneously synthesized and deposited in a thin film form by scalable and substrate-independent chemical vapor deposition (CVD). Patterned and conductive (3.6×10^{-2} S cm^{-1}) conjugated poly(porphyrin) thin films are formed. Mass spectrometry provides insight into the oxidative polymerization reaction and two side reactions (metalloporphyrin chlorination and π extension via intramolecular ring fusion).

Author Contribution

The synthesis and deposition of the porphyrin tape, UV/Vis/NIR characterization were performed by Giuseppe Bengasi with contribution from Kamal Baba. Giuseppe Bengasi and Paul Gratia performed the electrical characterization. Gilles Frache performed the mass spectrometry analysis. Jessica Desport performed the GPC analysis. Giuseppe Bengasi made the interpretation of the results with contributions of all co-authors. Giuseppe Bengasi, Nicolas Boscher and Katja Heinze contributed equally in writing the manuscript.

Supporting Information

Supporting information can be found at page 96.

Reprinted from permission from:

Giuseppe Bengasi, Kamal Baba, Gilles Frache, Jessica Desport, Paul Gratia, Katja Heinze, and Nicolas D. Boscher; *Angew. Chem. Int. Ed.* **2019**, *58*, 2103 –2108

Thin Films

International Edition: DOI: 10.1002/anie.201814034
German Edition: DOI: 10.1002/ange.201814034

Conductive Fused Porphyrin Tapes on Sensitive Substrates by a Chemical Vapor Deposition Approach

*Giuseppe Bengasi, Kamal Baba, Gilles Frache, Jessica Desport, Paul Gratia, Katja Heinze, and Nicolas D. Boscher**

Abstract: *Oxidative polymerization of nickel(II) 5,15-diphenyl porphyrin and nickel(II) 5,15-bis(di-3,5-tert-butylphenyl) porphyrin by oxidative chemical vapor deposition (oCVD) yields multiply fused porphyrin oligomers in thin film form. The oCVD technique enables one-step formation, deposition, and p-doping of conjugated poly(porphyrins) coatings without solvents or post-treatments. The decisive reactions and side reactions during the oCVD process are shown by high-resolution mass spectrometry. Owing to the highly conjugated structure of the fused tapes, the thin films exhibit an electrical conductivity of* $3.6\times10^{-2}\,S\,cm^{-1}$ *and strong absorption in the visible to near-infrared spectral region. The formation of smooth conjugated poly(porphyrins) coatings, even on sensitive substrates, is demonstrated by deposition and patterning on glass, silicon, and paper. Formation of conductive poly(porphyrins) thin films could enable the design of new optoelectronic devices using the oCVD approach.*

The exceptional properties of porphyrins are well-known in the scientific community, which has thoroughly investigated this class of compounds and its possible applications in functional devices such as solar cells,[1,2] sensors,[3,4] or catalysts.[5,6] The key features of interest of these compounds lay in their optical and optoelectronic properties that are intrinsically related to the chemical structure of the porphyrin macrocycle and its substituents. Similar to other compound classes,[7] the optical absorbance of porphyrins can be drastically shifted to the near-infrared (NIR) by conjugating the porphyrin core to further aromatic systems such as naphthalene.[8,9] Another way to obtain NIR absorbing porphyrins consists in the direct fusion of porphyrin rings. Osuka's group successfully demonstrated the formation of *meso-meso*/β-β/β-β triply fused porphyrin polymers using oxidative coupling reactions in solution. The very small band gaps of these tapes lead to absorptions in the NIR spectral region.[10] The most important fusion reaction employed zinc(II) porphyrins as monomers and silver(I) salts as oxidants, forming singly linked linear poly(porphyrins). Further oxidation using a combination of 2,3-dichloro-5,6-dicyano-1,4-benzoquinone and $Sc(OTf)_3$ increases the degree of conjugation.[11] Following these seminal works, the scientific community tried to improve the process employing different metalloporphyrins and more efficient oxidants enabling the formation of doubly or triply fused porphyrins in one-step reactions in solution.[12–16] Although these materials exhibit very interesting properties such as NIR and two-photon absorption, their very poor solubility and infusibility render their integration into devices very challenging or even impossible. To increase the solubility of directly fused porphyrins, solubilizing organic side chains were attached with the drawback of requiring tedious syntheses of the porphyrin monomers.[17] Bulky pendant groups, employed to prepare the bulk heterojunction blends, dilute the functional porphyrin macrocycle and hinder intermolecular π–π stacking, yielding relatively poor photovoltaic performances.[18] Furthermore, the solution-based approaches developed so far are limited to a small range of suitable substrates restricting possible applications of directly fused porphyrins. Several studies have also reported the formation of fused porphyrins from the sublimation under ultra-high vacuum onto oriented metal surfaces, for example, Ag(111),[19] or their fusion with graphene nanostructures.[20] However, in the latter approaches, the direct coupling of porphyrins at a surface is fully dependent on the supporting substrate.

Oxidative chemical vapor deposition (oCVD) is an elegant method for the simultaneous synthesis and deposition of conjugated polymer thin films on a wide variety of substrates.[21] oCVD relies on the vapor phase delivery of a monomer and an oxidant to a surface. Conjugated doped polymers then form directly on the substrate. The technique is successfully used for the production of doped poly(3,4-ethylenedioxythiophene) (PEDOT)[22] or polyaniline thin films from the respective thiophene and aniline monomers.[23] To date, oCVD involves chemically rather simple monomers such as pyrroles, thiophenes, or selenophenes. Yet, these monomers alone are incompetent to confer highly advanced optical and optoelectronic properties to the obtained thin films.

[*] G. Bengasi, Dr. K. Baba, Dr. G. Frache, Dr. J. Desport, Dr. P. Gratia, Dr. N. D. Boscher
Materials Research and Technology
Luxembourg Institute of Science and Technology (LIST)
5 Avenue des Hauts-Fourneaux, 4362 Esch/Alzette (Luxembourg)
E-mail: nicolas.boscher@list.lu
G. Bengasi, Prof. Dr. K. Heinze
Institute of Inorganic Chemistry and Analytical Chemistry
Johannes Gutenberg University of Mainz
Duesbergweg 10–14, 55128 Mainz (Germany)
Supporting information and the ORCID identification number(s) for the author(s) of this article can be found under: https://doi.org/10.1002/anie.201814034.

Herein we report the simultaneous synthesis, deposition, and p-doping of fused porphyrin thin films by an oCVD approach. As specific functionalization of the porphyrin monomer is not required, commercially available or easy-to-prepare inexpensive porphyrins are employed. The oxidative polymerization of these porphyrins is evidenced by ultraviolet-visible-near infrared (UV/Vis-NIR) spectroscopy, laser desorption ionization high-resolution mass spectrometry (LDI-HRMS), and gel permeation chromatography (GPC). Our study corroborates the decisive C–C bond-forming reactions and side reactions occurring during the oCVD reaction of porphyrins. The morphology of the fused porphyrin thin films is assessed by scanning electron microscopy (SEM) and atomic force microscopy (AFM). The electrical properties of the resulting fused porphyrin thin films are evaluated by conductivity measurements. Finally, the oCVD approach is used to form patterned conductive fused porphyrin thin films on a variety of substrates, namely silicon, glass, and printer paper.

Based on its hydrolytic stability even in the presence of acids formed in the oxidative polymerization process and the availability of unsubstituted *meso* and β positions for polymerization, we selected nickel(II) 5,15-diphenyl porphyrin (NiDPP) as suitable monomer for oCVD (Scheme 1). As

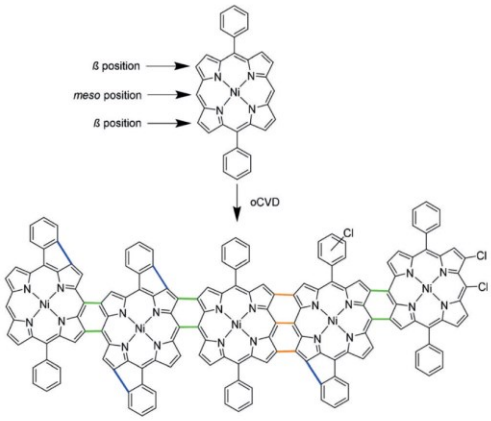

Scheme 1. The oxidative coupling reaction of NiDPP with $FeCl_3$. The reaction leads to coupling of the monomers thanks to the unsubstituted *meso* and β positions of NiDPP. NiDPP allows formation of β-*meso* bonds (green bonds) and β-*meso*-β triply linked porphyrin units (orange bonds). Chlorination is observed but the reactive site is not identified and only example positions are depicted. Blue bonds indicate a possible intramolecular cyclization between the phenyl substituent and a pyrrole.

oxidant we chose iron(III) chloride owing to its proven high suitability for oCVD processes[24] and owing to the ability of Fe^{3+} species to promote the synthesis of directly fused porphyrins in solution chemistry approaches.[12] The oCVD reaction was performed under reduced pressure (10^{-3} mbar) in a customized stainless steel reaction chamber equipped with two crucibles used to simultaneously sublime NiDPP

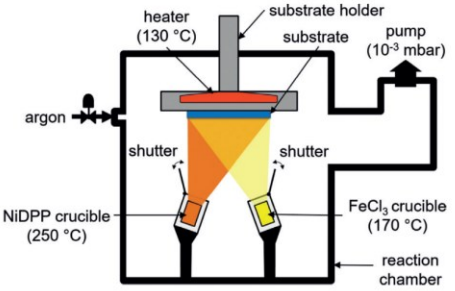

Figure 1. The oCVD reactor. The heated substrate is placed above two heated crucibles containing the oxidant and the metalloporphyrin, respectively. The pressure of the chamber is reduced to 10^{-3} mbar to ensure sublimation of the monomers and oxidants at reasonable temperatures.

(250 °C) and $FeCl_3$ (170 °C) (Figure 1). Printer paper sheets, microscope glass slides, silicon wafers, and commercial organic field-effect transistor chips were used as substrates to demonstrate the versatility and potential of the oCVD approach. The substrates were placed on a heated stage placed 20 cm above the two crucibles. The oCVD reaction of NiDPP with $FeCl_3$ yields 200 nm thick and strongly colored dark green coatings. Such a dark green coloration contrasts with the orange color of the reference NiDPP coating prepared from the sublimation of NiDPP in the absence of an oxidant (Figure 2).

Figure 2. Optical image of the sublimed NiDPP coating (orange, left) and patterned oCVD NiDPP coating (green, right) deposited on paper. The green oCVD NiDPP coating displays electrical conductivity.

UV/Vis-NIR spectroscopic analysis, performed on coated glass substrates, reveals significant differences in the absorption spectrum of the dark green oCVD NiDPP coating with respect to the orange sublimed NiDPP coating. The absorption around 360 nm increases, the Soret band broadens, the red-shifted Q bands collapse to a new broad band around 668 nm and, importantly, broad absorptions appear in the NIR region up to 2200 nm (Figure 3). These observations are in full agreement with the formation of multiply fused porphyrins that typically exhibit broad absorptions that can reach the NIR spectral region, while singly linked porphyrins only yield absorption in the UV/Vis region.[14,17]

In contrast to the soluble sublimed NiDPP coating, the oCVD NiDPP coating is almost insoluble in common organic

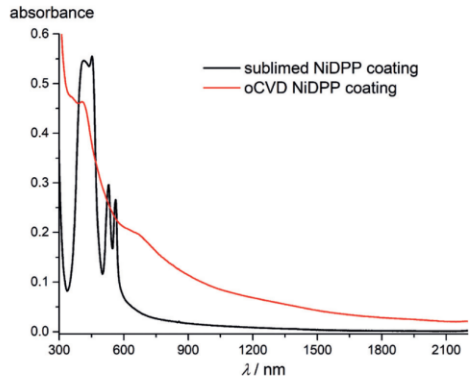

Figure 3. Comparison of the UV/Vis-NIR absorption spectra of the sublimed (black) and oCVD (red) NiDPP coatings formed on glass substrates.

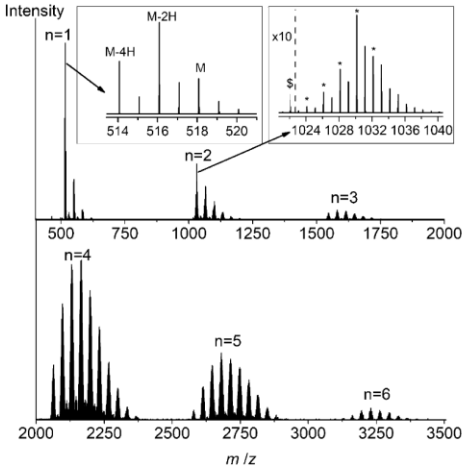

Figure 4. LDI-HRMS spectra of the oCVD NiDPP coating. The spectra reveal the presence of monomeric to hexameric species ($n = 1$–6) and peak distributions owing to exchange of hydrogen by chlorine atoms deriving from the oxidant. The left inset shows the loss of hydrogens likely due to an intramolecular cyclization reaction ($n = 1$). The same reaction occurs in the dimer region ($n = 2$), where the signals overlap with the isobaric formation of new bonds between the monomeric units (right inset, "*"). The spectrum shows the presence of a triply linked porphyrin dimer with four phenyl rings fused on the porphyrin core ("$").

solvents such as THF, acetone, dichloromethane, or hexafluoroisopropanol (Supporting Information, Figure S1). UV/Vis-NIR analysis of the acetone-soluble phase ascertains the presence of unreacted $FeCl_3$ and NiDPP monomer derivatives (Supporting Information, Figure S2). Although red-shifted, the Soret and Q bands still appear clearly in the absorption spectrum of the acetone solution. This indicates that the porphyrin core is essentially intact, yet reactions able to modify the HOMO–LUMO gap of the porphyrin must have occurred. Compared to the pristine NiDPP monomer, the number of the Q bands increased in the soluble part of the oCVD NiDPP coating pointing to a different symmetry of some macrocyclic species (Supporting Information, Figure S3). This spectral evidence, along with the partial solubility of the oCVD NiDPP coating, confirm the presence of a variety of chain lengths that yield both soluble and insoluble fractions and side reactions that modify the porphyrin symmetry. However, the absence of NIR absorption in the soluble fraction of the oCVD NiDPP coating suggests that the highly conjugated poly(porphyrins) are insoluble and stick to the glass substrate even upon rinsing.

The relative atomic compositions of the oCVD NiDPP coating, obtained by XPS, are rather close to the theoretical ones of NiDPP and fused NiDPP oligomers (Supporting Information, Table S1). The slight decrease of the nickel, nitrogen, and carbon element concentrations is associated to the expected incorporation of iron (3%) and chlorine (2%) into the oCVD NiDPP coating. Analysis of the Cl 1s XPS spectrum reveals the presence of two chlorine environments. The first contribution at lower binding energies is associated to residues of unreacted $FeCl_3$ or $FeCl_2$ by-products in the oCVD NiDPP coating (Supporting Information, Figure S4). The second chlorine environment at higher binding energies is attributed to organic chloride, most probably related to the chlorination of the porphyrin macrocycles, which is a well-known side reaction when fusing porphyrins in presence of $FeCl_3$.[8]

LDI-HRMS analysis directly acquired from the oCVD NiDPP coating reveals the presence of NiDPP oligomers confirming the successful oxidative polymerization of NiDPP (Figure 4). The signal related to the presence of the free-base porphyrin H_2DPP is negligibly weak, confirming that NiDPP effectively retains the nickel ion in the porphyrin core during the deposition and polymerization. Up to hexameric oligomers are observed in the mass spectrum (Figure 4), which corresponds to the instrumental limit (4000 m/z). Although LDI-HRMS analysis does not provide an exhaustive view into the mass distribution and the intensities related to the different species detected are not directly related to their abundance, the high resolution of the technique (up to 0.003 amu) represents a valuable tool for the unambiguous characterization of the sample. Moreover, the formation of even longer oligomers, with masses outside the instrumental limit, is conceivable. Unfortunately, the insolubility of the oCVD NiDPP coating prohibits GPC analysis and consequently the detailed mass distribution of the oCVD NiDPP coating remains elusive. Nonetheless, the absorptions up to 2200 nm in the UV/Vis-NIR absorption spectrum (Figure 3) strongly suggest the presence of highly conjugated poly(porphyrins), since singly linked porphyrins are NIR-transparent.[25]

With the aim to perform a GPC analysis and undoubtedly demonstrate the direct fusion of porphyrin in oCVD, we investigated the oCVD reaction of nickel(II) 5,15-bis(di-3,5-*tert*-butylphenyl) porphyrin (NiDD*t*-BuPP). The introduction

of the *tert*-butyl groups to the pendant phenyl substituents should reduce the intermolecular π–π stacking and ensure a better solubility of the formed fused porphyrins.[26] Moreover, with the aim to produce shorter and THF-soluble fused porphyrin oligomers that can be characterized by GPC, a lower temperature (150 °C) was employed to sublimate the oxidant limiting the oxidant delivered to the substrate. The UV/Vis-NIR (Supporting Information, Figure S5) and LDI-HRMS spectra (Supporting Information, Figure S6) of the oCVD NiDD*t*-BuPP coating evidence a highly similar behaviour between NiDD*t*-BuPP and NiDPP with an absorbance in the NIR region and the detection of multiply fused oligomers. Furthermore, the structure and deposition conditions of the oCVD NiDD*t*-BuPP coating allows its GPC analysis. The GPC analysis of the oCVD NiDD*t*-BuPP coating confirms the formation of polymeric species (Supporting Information, Figure S7). UV detection confirms the presence of monomeric units together with a broad polymer distribution, exhibiting masses up to 5000 g mol^{-1} (relative to polystyrene standards), in good agreement with LDI-HRMS data. The far lower solubility of the NiDPP oCVD coating and its oligomers intensities ratio in the LDI-HRMS spectra suggest that NiDPP could possess an even higher chain length.

The mass spectrometric analysis of the two oCVD NiDD*t*-BuPP and oCVD NiDPP coatings confirms the formation of one to three C–C bonds between the porphyrin units (Scheme 1). The LDI-HRMS spectra display signals related to the formation of triply linked β-β/*meso*-*meso*/β-β porphyrins for NiDPP (Figure 4). This is in contrast to solution-based oxidative polymerization processes delivering only double *meso*-β/*meso*-β linkages between the porphyrin units.[14,27] LDI-HRMS reveals another unexpected difference between the oCVD approach and the reported solution-based methods. For the peak distributions related to both the porphyrin monomer and oligomers, the LDI-HRMS spectrum exhibits signals suggesting the simultaneous elimination of two hydrogen atoms 2H (Figure 4; Supporting Information, Figure S6). Since the maximum number of hydrogen pairs eliminated is proportional to the number of phenyl rings in the detected monomeric and oligomeric species, we attribute these signals to dehydrogenated species. As a hypothesis, we suggest that these species could have formed by intramolecular cyclization reactions between the phenyl substituents and the porphyrin pyrrole β positions. Possibly, this intra-porphyrin dehydrogenation could also assist in the formation of triply linked porphyrins, since porphyrin π extension via ring fusion should modify the electron distribution and the reactivity of the porphyrin β positions towards the oxidative coupling.

Furthermore, the LDI-HRMS spectra exhibits peak distributions showing multiple chlorine incorporation. In fact, the distance between the peaks equals the exchange of a hydrogen atom by chlorine. Partial chlorination could also account for the very low solubility of the present oCVD NiDPP coating, since chlorination is known to decrease porphyrin solubility.[28] Both these side reactions are related to the use of $FeCl_3$ as oxidant, as $FeCl_3$ is competent to cause chlorination of porphyrins (especially in presence of Cl_2 that could be produced during the sublimation of the oxidant) and cyclization of aromatic rings on the porphyrin core.[8,29,30] Furthermore, both chlorination and extension of the π conjugation owing to the phenyl cyclization should modify the HOMO–LUMO gaps and modify the orbital symmetry. This is in agreement with the LDI-HRMS analysis of the poorly soluble fraction of oCVD NiDPP coating in acetone that confirms the presence of chlorinated and dehydrogenated compounds (Supporting Information, Figure S8).

Since we expected fused porphyrins being electrically conductive, basic charge transport properties of the oCVD NiDPP and oCVD NiDD*t*-BuPP coatings were investigated. The electrical conductivity of the oCVD coatings deposited onto commercial OFET chips was measured without applying any gate voltage and recording the current–voltage scans with a two-point probe to extract the conductivity using Ohm's law. Gratifyingly, the oCVD NiDPP coating displays an electrical ohmic conductivity with a value of 3.6×10^{-2} S cm^{-1} (Figure 5c). Although the obtained value is several orders of magnitude lower than the record reported for oCVD synthesized PEDOT films (6300 S cm^{-1}),[31] such a conductivity value is outstanding for a poly(porphyrin) thin film and may be useful for organic photonic and optoelectronic applications. Moreover, the room for improvement is vast since no optimization of the process was performed so far. The measured conductivity suggests that the oCVD NiDPP coating is a p-doped semiconducting material owing to the

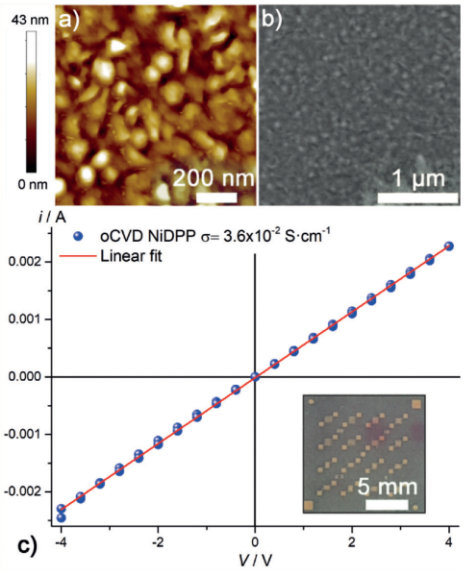

Figure 5. a) Atomic force microscopy and b) scanning electron microscopy images of a 200 nm thick oCVD NiDPP coating deposited on a silicon wafer. c) Lateral electrical conductivity measurement of the oCVD NiDPP coating deposited on OFET chips used to determine the conductivity (inset).

excess of $FeCl_3$ that is known to act as doping agent during the oCVD process.[22] Unfortunately, determining the hole mobility via field-effect measurements was impossible owing to the high conductivity of the oCVD NiDPP coating (p-doped), which results in the channel being ON already at zero gate voltage. Interestingly, the oCVD NiDD*t*-BuPP coating, polymerized from a reduced amount of $FeCl_3$ compared to the oCVD NiDPP coating, exhibits a drastically reduced conductivity (2.5×10^{-7} S cm^{-1}; Supporting Information, Figure S9). The large discrepancy between the conductivity of the oCVD NiDPP and oCVD NiDD*t*-BuPP coatings likely arises from 1) the presumably lower polymerisation length of the fused NiDD*t*-BuPP oligomers and 2) the reduced dopant concentration due to the lower oxidant reactant amount employed for in the oCVD reaction as well as from 3) a reduced intermolecular π–π stacking of the oligomers in the oCVD NiDD*t*-BuPP coatings. The reduction of the intermolecular π–π stacking by bulky substituents is a strong limitation to the photovoltaic performances of fused porphyrins.[18] Thus, the ability to directly fused porphyrins irrespective of their substituents should rapidly improve the photovoltaic performances of these visible-NIR light absorbent materials.

Finally, to demonstrate the potential of the oCVD of porphyrins for direct integration of conjugated poly(porphyrins) into optoelectronic devices, such as LEDs or hole-transporting materials in solar cells, we employed masks to coat and pattern various substrates. In particular, we readily deposited the oCVD NiDPP coating on printer paper using masks (Figure 2). The patterned film perfectly resembles the used mask with conjugated poly(porphyrin) lines as thin as one millimetre. Interestingly, electrical conductivity was even observed for the oCVD NiDPP coating deposited on printer paper. Scanning electron microscopy (SEM) and atomic force microscopy (AFM) analyses made on a 200 nm thick oCVD NiDPP coating deposited on a silicon wafer reveal the formation of a rather smooth (Sa = 4.6 nm) granular morphology composed of ca. 50 nm particles (Figure 5a,b). The oCVD NiDPP coating is only slightly rougher that its sublimed counterpart (Supporting Information, Figures S10, S11). The ability to readily synthesize fused porphyrins and deposit them as smooth and dense thickness-controlled thin films represent a breakthrough in a field limited so far by low synthetic yields and the impossibility to process the produced materials in thin film form. The exceptional porphyrin and fused-porphyrin functionalities coupled to a substrate independent CVD approach suitable for patterning offers many strong advantages in the design of devices, including solar cells,[18] multi-charge storage systems,[32] sensors, and catalytic[33] and photocatalytic systems.[34]

In summary, the one-step synthesis, deposition and doping of multiply fused porphyrin oligomers, was achieved from a substrate independent and up-scalable oxidative chemical vapor deposition approach using simple metalloporphyrins and inexpensive oxidants. The oCVD reaction of NiDD*t*-BuPP yields up to pentamers for the investigated reaction conditions. On the other hand, the oCVD reaction of NiDPP likely forms slightly longer oligomers as assumed from the large increase of the conductivity. However, the insolubility of the oCVD NiDPP coating prevents GPC analysis and the limited range of observation of LDI-HRMS (up to NiDPP hexamers detected) does not allow to assess any polymerization length. Along the targeted oxidative polymerization of porphyrins, two side reactions, namely porphyrin chlorination and porphyrin π extension via intramolecular ring fusion, occur in the oCVD process. These side reactions, which initially might be seen as limitations of the oCVD process, may also be used as an asset to 1) decrease the solubility of the formed conjugated poly(porphyrins) and hence to stabilize the film and to 2) further increase the π conjugation. Further studies to gain a deeper understanding on the role of the metal center of the porphyrin, of the porphyrin substituents, and of the employed oxidant are currently ongoing in our laboratories. Finally, oCVD allowed the deposition of the conjugated poly(porphyrins) as thin films that can be exploited for the fabrication of optoelectronic devices thanks to the high electrical conductivity of the oCVD NiDPP coating of 3.6×10^{-2} S cm^{-1}. The versatility of this approach and its ability to pattern and deposit conjugated poly(porphyrins) thin films on sensitive and flexible substrates, such as paper, may pave the way to a plethora of future applications.

Acknowledgements

We gratefully acknowledge the financial support of the Luxembourg National Research Fund (fnr.lu) through the POLYPORPH project (C15/MS/10340560/POLYPORH/Boscher). D. El Assad, J. L. Biagi, Dr. J. Guillot, and P. Grysan from LIST are acknowledged for data collection and insightful discussions. We thank M. Gerard from LIST for the design and development of the oCVD reactor.

Conflict of interest

The authors declare no conflict of interest.

Keywords: chemical vapor deposition · oxidative coupling · polymerization · porphyrins · thin films

How to cite: *Angew. Chem. Int. Ed.* **2019**, *58*, 2103–2108
Angew. Chem. **2019**, *131*, 2125–2130

[1] S. Mathew, A. Yella, P. Gao, R. Humphry-Baker, B. F. E. Curchod, N. Ashari-Astani, I. Tavernelli, U. Rothlisberger, M. K. Nazeeruddin, M. Grätzel, *Nat. Chem.* **2014**, *6*, 242–247.
[2] L.-L. Li, E. Wei-Guang Diau, *Chem. Soc. Rev.* **2013**, *42*, 291–304.
[3] C. H. A. Esteves, B. A. Iglesias, R. W. C. Li, T. Ogawa, K. Araki, J. Gruber, *Sens. Actuators B* **2014**, *193*, 136–141.
[4] P. Heier, N. D. Boscher, T. Bohn, K. Heinze, P. Choquet, *J. Mater. Chem. A* **2014**, *2*, 1560–1570.
[5] K. Rybicka-Jasińska, W. Shan, K. Zawada, K. M. Kadish, D. Gryko, *J. Am. Chem. Soc.* **2016**, *138*, 15451–15458.
[6] S. Lin, C. S. Diercks, Y.-B. Zhang, N. Kornienko, E. M. Nichols, Y. Zhao, A. R. Paris, D. Kim, P. Yang, O. M. Yaghi, C. J. Chang, *Science* **2015**, *349*, 1208–1213.

[7] Y. Jiang, X. Zheng, Y. Deng, H. Tian, J. Ding, Z. Xie, Y. Geng, F. Wang, *Angew. Chem. Int. Ed.* **2018**, *57*, 10283 – 10287; *Angew. Chem.* **2018**, *130*, 10440 – 10444.
[8] J. P. Lewtak, D. Gryko, D. Bao, E. Sebai, O. Vakuliuk, M. Ścigaj, D. T. Gryko, *Org. Biomol. Chem.* **2011**, *9*, 8178 – 8181.
[9] L. Dou, Y. Liu, Z. Hong, G. Li, Y. Yang, *Chem. Rev.* **2015**, *115*, 12633 – 12665.
[10] A. Tsuda, A. Osuka, *Adv. Mater.* **2002**, *14*, 75 – 79.
[11] A. Tsuda, A. Osuka, *Science* **2001**, *293*, 79 – 82.
[12] C.-M. Feng, Y.-Z. Zhu, S.-C. Zhang, Y. Zang, J.-Y. Zheng, *Org. Biomol. Chem.* **2015**, *13*, 2566 – 2569.
[13] B. J. Brennan, M. J. Kenney, P. A. Liddell, B. R. Cherry, J. Li, A. L. Moore, T. A. Moore, D. Gust, *Chem. Commun.* **2011**, *47*, 10034 – 10036.
[14] A. Tsuda, Y. Nakamura, A. Osuka, *Chem. Commun.* **2003**, 1096 – 1097.
[15] B. J. Brennan, J. Arero, P. A. Liddell, T. A. Moore, A. L. Moore, D. Gust, *J. Porphyrins Phthalocyanines* **2013**, *17*, 247 – 251.
[16] A. A. Ryan, M. O. Senge, *Eur. J. Org. Chem.* **2013**, 3700 – 3711.
[17] N. Yoshida, N. Aratani, A. Osuka, *Chem. Commun.* **2000**, 197 – 198.
[18] J. Kesters, P. Verstappen, M. Kelchtermans, L. Lutsen, D. Vanderzande, W. Maes, *Adv. Energy Mater.* **2015**, *5*, 1500218.
[19] A. Wiengarten, K. Seufert, W. Auwärter, D. Ecija, K. Diller, F. Allegretti, F. Bischo, S. Fischer, D. A. Duncan, A. C. Papageorgiou, et al., *J. Am. Chem. Soc.* **2014**, *136*, 9346 – 9354.
[20] Y. He, M. Garnica, F. Bischoff, J. Ducke, M. Bocquet, M. Batzill, W. Auwärter, J. V. Barth, *Nat. Chem.* **2016**, *9*, 33 – 38.
[21] M. Wang, X. Wang, P. Moni, A. Liu, D. H. Kim, W. J. Jo, H. Sojoudi, K. K. Gleason, *Adv. Mater.* **2017**, *29*, 1604606.
[22] W. E. Tenhaeff, K. K. Gleason, *Adv. Funct. Mater.* **2008**, *18*, 979 – 992.
[23] Y. Y. Smolin, M. Soroush, K. K. S. Lau, *Beilstein J. Nanotechnol.* **2017**, *8*, 1266 – 1276.
[24] H. Goktas, X. Wang, N. D. Boscher, S. Torosian, K. K. Gleason, *J. Mater. Chem. C* **2016**, *4*, 3403 – 3414.
[25] A. Osuka, H. Shimidzu, *Angew. Chem. Int. Ed. Engl.* **1997**, *36*, 135 – 137; *Angew. Chem.* **1997**, *109*, 93 – 95.
[26] T. Tanaka, A. Osuka, *Chem. Soc. Rev.* **2015**, *44*, 943 – 969.
[27] A. Tsuda, A. Nakano, H. Furuta, H. Yamochi, A. Osuka, *Angew. Chem. Int. Ed.* **2000**, *39*, 558 – 561; *Angew. Chem.* **2000**, *112*, 572 – 575.
[28] M. O. Senge, O. Flögel, K. Ruhlandt-Senge, *J. Porphyrins Phthalocyanines* **2001**, *5*, 503 – 506.
[29] T. Wijesekera, A. Matsumoto, D. Dolphin, D. Lexa, *Angew. Chem. Int. Ed. Engl.* **1990**, *29*, 1028 – 1030; *Angew. Chem.* **1990**, *102*, 1073 – 1074.
[30] L. E. Wilson, N. W. Gregory, *J. Phys. Chem.* **1958**, *62*, 433 – 437.
[31] X. Wang, X. Zhang, L. Sun, D. Lee, S. Lee, M. Wang, J. Zhao, Y. Shao-horn, M. Dinc, T. Palacios, K. K. Gleason, *Sci. Adv.* **2018**, *4*, eaat5780.
[32] D. Bonifazi, M. Scholl, F. Song, L. Echegoyen, G. Accorsi, N. Armaroli, *Angew. Chem. Int. Ed.* **2003**, *42*, 4966 – 4970; *Angew. Chem.* **2003**, *115*, 5116 – 5120.
[33] D. Khusnutdinova, B. L. Wadsworth, M. Flores, A. M. Beiler, E. A. R. Cruz, Y. Zenkov, G. F. Moore, *ACS Catal.* **2018**, *8*, 9888 – 9898.
[34] A. Fateeva, P. A. Chater, C. P. Ireland, A. A. Tahir, Y. Z. Khimyak, P. V. Wiper, J. R. Darwent, M. J. Rosseinsky, *Angew. Chem. Int. Ed.* **2012**, *51*, 7440 – 7444; *Angew. Chem.* **2012**, *124*, 7558 – 7562.

Manuscript received: December 10, 2018
Accepted manuscript online: December 17, 2018
Version of record online: January 21, 2019

5.2 Conductive Directly Fused Poly(Porphyrin) Coatings by Oxidative Chemical Vapour Deposition – From Single- to Triple- Fused

Kamal Baba, Giuseppe Bengasi, Dana El Assad, Patrick Grysan, Esther Lentzen, Katja Heinze, Gilles Frache and Nicolas D. Boscher.

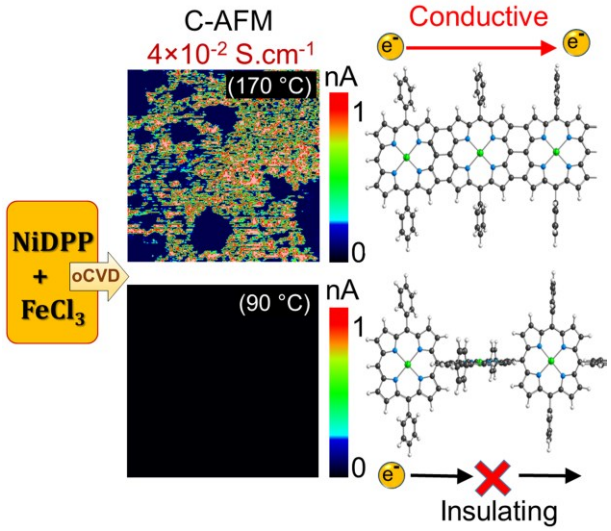

Conductive fused metalloporphyrin thin films are simultaneously synthesised and deposited by using a straightforward chemical vapour deposition approach. The dependence of the fusion reaction and side mechanisms on the oxidant is evidenced.

Authors Contributions

Kamal Baba performed the experiments with contributions from Giuseppe Bengasi. Dana El Assad and Gilles Frache performed the Mass Spectrometry analyses, Patrick Grysan performed the C-AFM measurements and Esther Lentzen performed the nano-SIMS analyses. Kamal Baba, Giuseppe Bengasi and Nicolas Boscher made the interpretation of the results with contributions of all co-authors. Nicolas Boscher and Kamal Baba finalized the manuscript with contribution from Giuseppe Bengasi and Katja Heinze.

Supporting Information

Supporting information can be found on page 110.

Reprinted from permission from:

Kamal Baba, Giuseppe Bengasi, Dana El Assad, Patrick Grysan, Esther Lentzen, Katja Heinze, Gilles Frache, and Nicolas D. Boscher, *Eur. J. Org. Chem.* **2019**, 2368–2375.

ChemPubSoc Europe

DOI: 10.1002/ejoc.201900045

EurJOC European Journal of Organic Chemistry

Full Paper

Fused Porphyrin

Conductive Directly Fused Poly(Porphyrin) Coatings by Oxidative Chemical Vapour Deposition – From Single- to Triple-Fused

Kamal Baba,[a] Giuseppe Bengasi,[a,b] Dana El Assad,[a] Patrick Grysan,[a] Esther Lentzen,[a] Katja Heinze,[b] Gilles Frache,[a] and Nicolas D. Boscher*[a]

Abstract: While the solution-phase synthesis of directly fused porphyrin tapes has been successfully developed in recent years, the deposition of these promising compounds in thin film form has remained a challenge. In this study, we report the simultaneous synthesis and deposition of conductive directly fused poly(porphyrin) coatings based on a substrate independent and up-scalable oxidative chemical vapor deposition (oCVD) approach. A particular emphasis is given to the selection and sublimation conditions of the oxidant. The direct fusion of nickel(II) 5,15-(diphenyl)porphyrin (NiDPP) is successfully achieved using three different oxidants, namely iron(III) chloride ($FeCl_3$), copper(II) chloride ($CuCl_2$) and copper(II) perchlorate hexahydrate ($Cu(ClO_4)_2{\cdot}6H_2O$). $FeCl_3$ is demonstrated as the most suitable oxidant, allowing the formation of mainly singly-fused poly(NiDPP) or conductive mainly doubly or triply-fused poly(NiDPP) that strongly absorb in the NIR. High-resolution mass spectrometry evidences the chlorination of the formed compounds as a side reaction. This chlorination can either be considered as a drawback by preventing the formation of large directly fused NiDPP oligomers or as an asset when targeting the formation of fully insoluble directly fused poly(NiDPP) coatings. Overall, the described oCVD approach opened up the possibility to tune the band gap, conductivity, and solubility of directly fused P(NiDPP) coatings.

Introduction

Porphyrins, whose central structure is composed of four pyrrole units joined by four methine bridges, have been selected by nature to fulfil some of the most important biological processes, i.e. photosynthesis and respiration.[1] Their remarkable functional properties led to the development of numerous porphyrinic compounds for various technological applications, including photovoltaic,[2] catalysis,[3–6] gas detection[7–9] or separation[10] and medical applications.[11] Porphyrin's properties can be adjusted by tuning the central metal ion[3] or/and the pendant groups located at the *meso* or/and *beta* positions.[5,12] The properties of porphyrin-based devices are also greatly dependent on their integration mode since porphyrins may be directly used dissolved in a liquid medium,[4,5,11] covalently grafted onto a surface,[2,6] embedded in a matrix[8] or polymerized.[9,13]

Conjugated porphyrin polymers, including directly fused porphyrins,[4,14–17] possess fascinating electronic and optoelectronic properties that may yield electronic noses[18] or organic solar cells[19] with enhanced performances. However, the two main synthetic routes towards conjugated poly(porphyrins), (i) oxidative polymerization using a suitable oxidant[15–17] or (ii) electrodeposition,[20] are a major drawback to their integration into devices. Indeed, the weak solubility of porphyrin monomers, oligomers and polymers requires the introduction of bulky pendant groups to form conjugated poly(porphyrins) in which the tetrapyrrole moieties responsible for the targeted properties end-up diluted.[19,21]

Very recently, we reported the simultaneous synthesis and deposition of conjugated poly(porphyrin) coatings from the oxidative chemical vapor deposition (oCVD) of simple and commercially available porphyrins,[22] i.e. nickel(II) 5,15-(diphenyl)porphyrin (NiDPP) and nickel(II) 5,15-bis(di-3,5-*tert*-butylphenyl) porphyrin (NiDD*t*BuPP). In oCVD, the monomer and the oxidant are both delivered through the vapor phase towards a substrate on which they adsorb and react to form conjugated polymer coatings.[23] Such an approach considerably simplified the integration of conjugated polymers into devices and cease the need for soluble monomers. On the other hand, oCVD reduces the range of suitable oxidants that often decompose prior to sublimation. Iron(III) chloride ($FeCl_3$) has been the candidate of choice in oCVD.[23] Indeed, when performed from the gas phase, the reaction of $FeCl_3$ with NiDPP or NiDD*t*BuPP readily produces directly fused porphyrin tapes in thin film form on various substrates,[22] including dielectric substrates such as paper or glass. Interestingly, double- and triple-fused porphyrin tapes were formed (Figure 1), intensifying and red-shifting the Soret band and the Q-bands deeply

[a] *Materials Research and Technology Department, Luxembourg Institute of Science and Technology, 5 Avenue des Hauts-Fourneaux, 4362 Esch-sur-Alzette, Luxembourg*
E-mail: nicolas.boscher@list.lu
https://www.list.lu/en/mrt/
[b] *Institute of Inorganic Chemistry and Analytical Chemistry, Johannes Gutenberg University of Mainz, Duesbergweg 10-14, 55128 Mainz, Germany*
https://www.ak-heinze.chemie.uni-mainz.de/
Supporting information and ORCID(s) from the author(s) for this article are available on the WWW under https://doi.org/10.1002/ejoc.201900045.

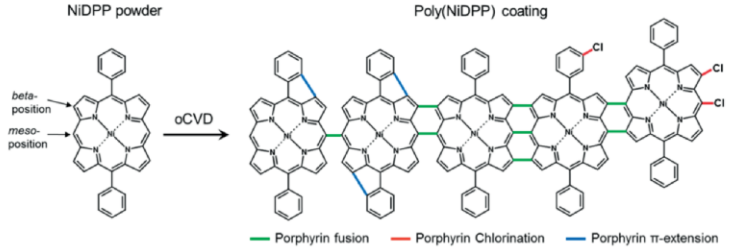

Figure 1. Scheme illustrating the diverse reactions occurring during the oCVD reaction of NiDPP. Alongside the targeted oxidative fusion of NiDPP, which can be singly, doubly or triply-fused, chlorination of NiDPP and π-extension of NiDPP via ring fusion have also been reported.[22]

into the near infrared (NIR) region, i.e. above 2000 nm. Aside from the oxidative fusion of the porphyrin monomers, their chlorination was also evidenced using mass spectrometry. Chlorination of the porphyrins, also reported for the solution-phase synthesis of directly fused porphyrins,[24,25] may partly hinder the oxidative fusion of porphyrins.[21] Indeed, chloride is known to be a bad-leaving group for aromatic rings[26] and one can assume that chlorination of *meso* and *beta* positions prevents the formation of large directly fused porphyrin oligomers (Figure 1).

With the aim to tune the degree of fusion, which strongly impacts the band gap,[27,28] conductivity and solubility of fused porphyrin tapes,[21] we now investigate three different oxidants for the oCVD reaction of NiDPP. The oxidative fusion of the NiDPP monomers, yielding NIR absorption when triply fused, is demonstrated by ultraviolet-visible near infrared (UV/Vis-NIR) spectroscopy and laser desorption/ionization high-resolution mass spectrometry (LDI-HRMS). Besides, the chlorination of the porphyrin monomers and directly fused porphyrin polymers is evidenced by LDI-HRMS, supported by X-ray photoelectron spectroscopy (XPS) and secondary-ion mass spectrometry (SIMS) analyses. The mechanisms driving the oxidative fusion of porphyrins with respect to the type of oxidant as well as the impact on the porphyrin-based thin films' chemistry, morphology, and conductivity inspected by conductive atomic force microscopy (C-AFM) are discussed.

Results and Discussion

Due to the extremely low volatility of porphyrins,[29] their use in CVD processes has always been a challenge[30,31] and considerably restrained the exploitation of their remarkable properties. Sublimation under low-pressure conditions can allow the delivery of porphyrins to a surface.[32] Under certain deposition conditions, we have recently demonstrated that the vapor phase transport of porphyrins can be coupled to a free-radical chain-growth polymerization[10,13] or an oxidative polymerization reaction[22] to form functional poly(porphyrin) coatings. Nevertheless, unlike most of the other monomers investigated in initiated CVD (iCVD) or oCVD,[33] the very high sticking coefficient of porphyrins implies that they readily deposit on a surface to form thin films irrespective of their polymerization.[10,13,22] Thus, in addition to the importance of the oxidant selection, one may pay particular attention to its delivery rate to ensure the oxidative fusion of porphyrins, as well as control their degree of fusion.

Based on the oCVD method depicted in Figure S1, we deposited three series of uniform NiDPP-based thin films using $FeCl_3$, copper(II) chloride ($CuCl_2$) or copper(II) perchlorate ($Cu(ClO_4)_2$). For each of the investigated oxidants, a minimum of three different sublimation temperatures of the oxidant was investigated to study the influence of their delivery rate on the degree of fusion of the formed fused porphyrin tapes. The NiDPP-based thin films, with a thicknesses close to 200 nm, exhibited a color that ranged from vivid orange (for the NiDPP-based thin films grown without or with small amount of oxidant, i.e. lower sublimation temperatures) to dark green (for the NiDPP-based thin films grown from the highest oxidant delivery rates, i.e. higher sublimation temperatures) (Figure 2a & Figure S2). Qualitatively, the colors indicate the occurrence of the reactions depicted in Figure 1, i.e. oxidative fusion, chlorination, and π-extension via ring fusion.

The UV/Vis-NIR absorption spectra of the NiDPP-based thin films grown from the oCVD reaction of NiDPP with $FeCl_3$, $CuCl_2$ or $Cu(ClO_4)_2$ confirm the color changes described above (Figure 2b–e & Figure S3). Notably, the spectra reveal a progressive broadening and disappearance of the Soret (412 nm) and Q bands (530 and 562 nm) upon increasing the oxidant delivery rates. The alteration of the absorption bands related to the NiDPP monomer is coupled to an increase of the absorbance at higher wavelengths, which is consistent with the formation of directly fused porphyrin tapes.[16] Notably, the absorption of the NiDPP-based thin films extends deeply into the NIR region up to 2500 nm, when prepared from higher $FeCl_3$ and $Cu(ClO_4)_2$ delivery rates (Figure 2b and Figure 2e). This indicates the formation of multiple-fused porphyrin tapes, which typically exhibit broad absorptions that can reach the NIR spectral region, while singly fused porphyrins only yield absorption in the UV/Vis region.[27,28] In the case of $CuCl_2$, the near infrared absorption of the NiDPP-based thin films remained almost negligible for all the deposition conditions (Figure 2c), suggesting that $CuCl_2$ is most probably less suitable than $FeCl_3$ and $Cu(ClO_4)_2$ for the synthesis of multiple-fused NiDPP tapes.

Expectedly, the solubility of the NiDPP-based thin films greatly depends on the deposition conditions. The NiDPP-based thin films elaborated from the highest oxidant sublimation tem-

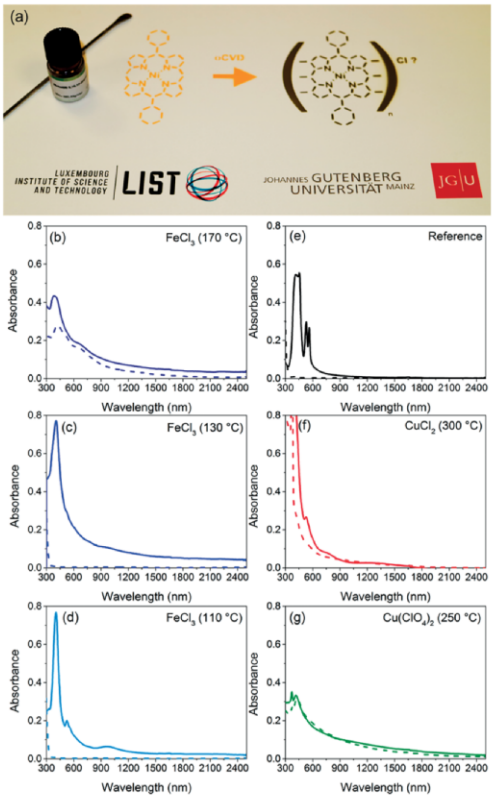

Figure 2. (a) Photograph of an A4 sheet of printer paper coated by (left) the reddish reference NiDPP coating (evaporated) and (right) the greenish poly(NiDPP) coating prepared from the oCVD reaction of NiDPP with $FeCl_3$ (170 °C) using a patterned mask. The photograph illustrates the ability of oCVD to both coat temperature sensitive substrates and to allow patterning for device fabrication. (b–g) UV/Vis-NIR absorption spectra of the as-deposited (solid line) and acetone-rinsed (dashed line) NiDPP-based thin films deposited on glass using different oxidants sublimed at different temperatures: (b) $FeCl_3$ (170 °C), (c) $FeCl_3$ (130 °C), (d) $FeCl_3$ (110 °C), (f) $CuCl_2$ (300 °C) and (g) $Cu(ClO_4)_2$ (250 °C). (e) The UV/Vis-NIR absorption spectrum of the reference NiDPP coating (sublimed in the absence of oxidant) is provided for comparison. The sharp and intense peak at 370 nm observed on (f) is related to the presence of the $Cu(ClO_4)_2$ in the NiDPP-based thin films.

peratures, i.e. above 150 °C, 300 °C and 250 °C for $FeCl_3$, $CuCl_2$ and $Cu(ClO_4)_2$, respectively, are insoluble or weakly soluble in several non-polar (chloroform), polar protic (methanol, hexafluoro2-propanol) and aprotic organic solvents (acetone, dichloromethane), while the NiDPP-based thin films elaborated from lower oxidant sublimation temperatures are fully soluble in acetone (Figure 2b–e). Such behavior results from the combination of the three reactions, namely direct fusion (from single to triple), chlorination and π-extension of porphyrins via ring fusion, occurring during the oCVD reaction. Due to the low solubility in acetone of the NiDPP-based thin film formed from $CuCl_2$ at 300 °C, which might be only composed of short and mainly singly fused porphyrin oligomers in view of its UV/Vis-NIR absorption spectra (Figure 2c), chlorination and π-extension of the porphyrins possibly play a significant role in the solubility of the NiDPP-based thin films.[34,35]

Similarly to the UV/Vis-NIR absorption data, the high-resolution mass spectrometry (HRMS) analyses of the NiDPP-based thin films are strongly influenced by the deposition conditions (Figure 3). Depending on the selected oxidant and its sublimation temperature, direct fusion of the porphyrins, chlorination of the porphyrins and π-extension of the porphyrins via ring fusion (Figure 1) are detected. Demetalation of the NiDPP monomer is also observed for several conditions, i.e. $FeCl_3$ (90 °C to 130 °C) and $Cu(ClO_4)_2$ (250 °C). Interestingly, NiDPP demetalation is not observed for the formed dimers. This is consistent with the reported influence of the central metal ion on the porphyrin oxidation potential and the difficulties to directly fuse free-base porphyrins.[21] LDI-HRMS does not provide a complete representation of all the oligomer/polymer chains formed. Indeed, the LDI-HRMS instrument only detects *m/z* values lower than 4000. Moreover, the ionization and desorption of larger molecules are far less probable, making their detection more challenging. In other words, the lower intensity of the dimeric and trimeric over the monomeric species is not indicative of their lower abundance. Nevertheless, the different LDI-HRMS spectra provide several informative trends. First, the signal of the monomer ion $NiDPP^+$ ($C_{32}H_{20}N_4Ni^+$, *m/z* = 518.104) decreases upon addition of an oxidant (Figure 3), indirectly suggesting the formation of compounds from the porphyrin monomer, such as large oligomers or polymers. In particular, the base peak (i.e. the most abundant ion), decreases by three to four orders of magnitude between reference NiDPP coating and the NiDPP-based thin films obtained from $FeCl_3$ sublimed above 110 °C (Figure 3a).

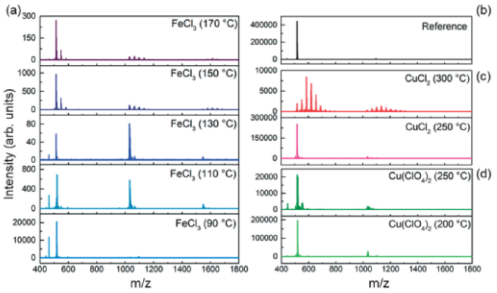

Figure 3. LDI-HRMS spectra of the NiDPP-based thin films obtained using (a) $FeCl_3$, (c) $CuCl_2$ and (d) $Cu(ClO_4)_2$ for different oxidant sublimation temperatures. (b) The LDI-HRMS spectrum of the reference NiDPP coating is provided for comparison.

Moreover, the different trends observed by LDI-HRMS may be informative on the degree of occurrence of the different reactions, i.e. direct fusion of porphyrin, chlorination of porphyrin and π-extension of porphyrin. As an example, the NiDPP-based thin film produced from $FeCl_3$ sublimed at 130 °C exhibits intense peaks related to the NiDPP dimers ($[(NiDPP)_2 - H_6]^+$ at

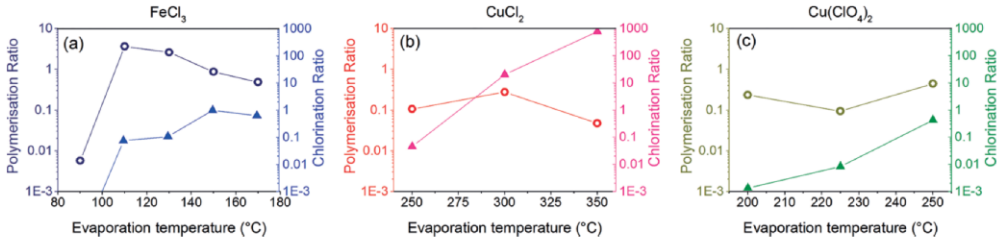

Figure 4. Calculated polymerization and chlorination ratios for the NiDPP-based thin films formed using (a) $FeCl_3$, (b) $CuCl_2$ and (c) $Cu(ClO_4)_2$ for different oxidant sublimation temperatures. The polymerization ratio is calculated from the sums of the oligomer peak intensities over the sums of the monomer peak intensities from the LDI-HRMS spectra, while the chlorination ratio is calculated from the sums of the chlorinated compound peak intensities over the non-chlorinated compound peak intensities from the LDI-HRMS spectra.

m/z 1030.161, $[(NiDPP)_2\text{-}H_4]^+$ at *m/z* 1032.176, $[(NiDPP)_2\text{-}H_2]^+$ at 1034.192) (Figure 3a). On the other hand, the NiDPP-based thin film produced from $CuCl_2$ sublimed at 300 °C exhibits a large number of chlorinated NiDPP monomeric and dimeric species (Figure 3c).

In an attempt to determine the oCVD conditions favouring oxidative fusion of NiDPP over chlorination, we calculated for each of the investigated conditions (i) the ratios of the sums of the oligomer peak intensities over the sums of the monomer peak intensities (later called the polymerization ratio) and (ii) the ratios of the sums of the chlorinated compound peak intensities over the non-chlorinated compound peak intensities (later called the chlorination ratio) (Figure 4). Such as presumed from the LDI-HRMS spectra, $FeCl_3$ sublimed at intermediate temperatures (i.e. 110 °C and 130 °C) yields the highest polymerization ratios (Figure 4a). Below 110 °C, the lack of $FeCl_3$ does not ensure the oxidative fusion of NiDPP for the reported oCVD conditions. On the other hand, increase of the sublimation temperature of $FeCl_3$ above 110 °C decreases the polymerization ratio. This correlates with an increasing chlorination ratio (Figure 1), which hinders the oxidative fusion of NiDPP when chlorine occupies the *beta* or/and *meso* positions (Figure 1). Chlorination of NiDPP may be promoted by the formation of Cl_2 while heating $FeCl_3$ under vacuum. Indeed, the decomposition temperature of $FeCl_3$ to give $FeCl_2$ and Cl_2 decreases from 375 °C to 275 °C when reducing the pressure from atmospheric to low vacuum.[36,37] Since our oCVD approach operates under high vacuum, one may assume that decomposition of $FeCl_3$ to the stronger oxidant Cl_2 occurs already well below 275 °C.[38]

A similar behavior is observed for the two other oxidants $CuCl_2$ and $Cu(ClO_4)_2$ with the chlorination ratio increasing with higher oxidant sublimation temperature (Figure 4b & c), while the polymerization ratio first increases with an increase of the oxidant sublimation temperature before to decay when chlorination become excessive (Figure 4b). However, in both cases, the polymerization ratio remains always lower than the best values obtained using $FeCl_3$ (Figure 4a).

Consequently, $FeCl_3$ appears as the best oxidant for the oxidative fusion of NiDPP among the three oxidants studied in the present work. Conversely, $CuCl_2$ appears as a poorly suitable candidate for the oxidative fusion of NiDPP as it leads to excessive chlorination and rather poor polymerization rates (Figure 4c).

This conclusion is supported by the UV/Vis-NIR observations that display a rather weak extension of the absorption to higher wavelengths for the thin films obtained from $CuCl_2$ (Figure 2c), which indicates the formation of mainly singly fused NiDPP oligomers. This poor yield of polymerization is not related to a lack of $CuCl_2$ oxidant since XPS analysis of the NiDPP-based thin films deposited from $CuCl_2$ revealed rather large amounts of copper (ca. 21 %) and chlorine (ca. 29 %). Moreover, the XPS Cl 2p core level, strongly dominated by the metal chloride environment (Cl $2p_{3/2}$ = 198.7 eV and Cl $2p_{1/2}$ = 200.3 eV), indicates that most of the $CuCl_2$ contained in the NiDPP-based thin films remains unreacted (Figure 5b). This contrasts with the XPS Cl 2p core levels for the NiDPP-based thin films deposited from $FeCl_3$ (Figure 5a) and $Cu(ClO_4)_2$ (Figure 5c), which are composed of significant organic chloride contributions (Cl $2p_{3/2}$ = 200.8 eV and Cl $2p_{1/2}$ = 202.4 eV) alongside metal chloride (Cl $2p_{3/2}$ = 198.7 eV and Cl $2p_{1/2}$ = 200.3 eV) and perchlorate environments (Cl 2p 3/2 = 208.5 eV and Cl $2p_{1/2}$ = 210.1 eV) (Table S2). Nevertheless, the conclusions made in this work are only applicable

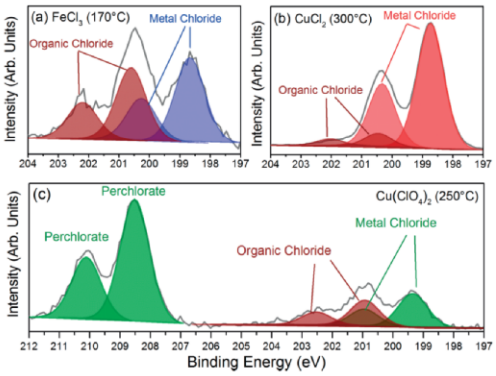

Figure 5. XPS curve-fitting of the Cl 2p core level for the NiDPP-based thin films formed using (a) $FeCl_3$, (b) $CuCl_2$ and (c) $Cu(ClO_4)_2$ sublimed at 170 °C, 300 °C and 250 °C, respectively.

to the case of NiDPP since $CuCl_2$ has already been reported as a suitable candidate for the oCVD of PEDOT.[39] Thus, $CuCl_2$ might even be a more suitable oxidant for the oCVD of metalloporphyrins with a lower oxidation potential.

XPS highlighted that a significant amount of oxidant is incorporated into the thin films grown by oCVD. Thus, beyond our chemical investigations, we performed SIMS mapping in order to investigate the homogeneity of the NiDPP-based thin films and document the oxidant integration. The reference NiDPP coating provides a smooth and homogeneous coverage of the silicon substrate, such as illustrated by the secondary electron image and SIMS image of the $^{12}C^{14}N$ clusters (Figure 6a). In contrast, the secondary electron images of the NiDPP-based thin films deposited in the presence of an oxidant all display a heterogeneous morphology with particles and islands disseminated across the surfaces (Figure 6b-d). SIMS imaging highlights hot spots for the $^{12}C^{14}N$, ^{35}Cl, $^{56}Fe^{16}O$ and ^{63}Cu elements that match the observed morphology. Noticeably, ^{35}Cl hot spots match with the hot spots of $^{56}Fe^{16}O$ and ^{63}Cu for the NiDPP-based thin films formed using $FeCl_3$, $CuCl_2$ and $Cu(ClO_4)_2$, respectively. Strikingly, the ^{35}Cl, $^{56}Fe^{16}O$ and ^{63}Cu images, highlighting the strong heterogeneities in the oxidant repartition, are the exact negative of the $^{12}C^{14}N$ elements from the directly fused porphyrin tapes.

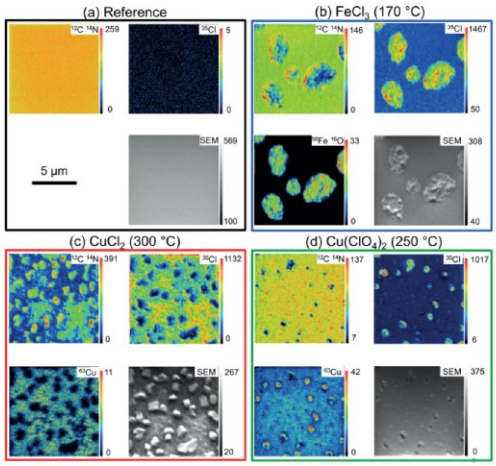

Figure 6. Elemental distribution of $^{12}C^{14}N$, ^{35}Cl, ^{63}Cu, $^{56}Fe^{16}O$ and secondary electron images on (a) the reference NiDPP coating and the NiDPP-based thin films formed using (b) $FeCl_3$, (c) $CuCl_2$ and (d) $Cu(ClO_4)_2$ sublimed at 170 °C, 300 °C and 250 °C, respectively. Field of view is 10 × 10 µm².

Unsurprisingly in view of the LDI-HRMS investigations (Figure 4), the NiDPP-based thin films obtained from $FeCl_3$ reach the highest conductivities. On the other hand, the maximum conductivity (i.e. 4×10^{-2} S·cm^{-1} for $FeCl_3$ sublimed at 170 °C) is not reached for the $FeCl_3$ sublimation temperature yielding to the highest polymerization ratio (110 °C). With the objective to assess the conductivity of the directly fused NiDPP tapes independently from the heterogeneities related to the films morphology and the large oxidant inclusions (Figure 6b), conductive atomic force microscopy (C-AFM) was employed to evaluate the local electron-current distribution, i.e. conductivity, of the poly(porphyrins) coatings produced from $FeCl_3$.

In accordance with the LDI-HRMS investigations, no electron-current could be measured for the NiDPP-based thin films formed from $FeCl_3$ sublimed at 90 °C (Figure 7b). Increase of the $FeCl_3$ delivery rate, i.e. raising the sublimation temperature, yields to progressive increase of the electron-current to several picoamperes for the NiDPP-based thin films formed from $FeCl_3$ sublimed at 110 °C and several nanoamperes for the NiDPP-based thin films formed from $FeCl_3$ sublimed at 130 °C and 170 °C (Figure 7b). Such a result, which may first sound as contradictory when compared to the calculated polymerization ratios, correlates with the higher degree of unsaturation of the NiDPP-based thin films formed from $FeCl_3$ sublimed above

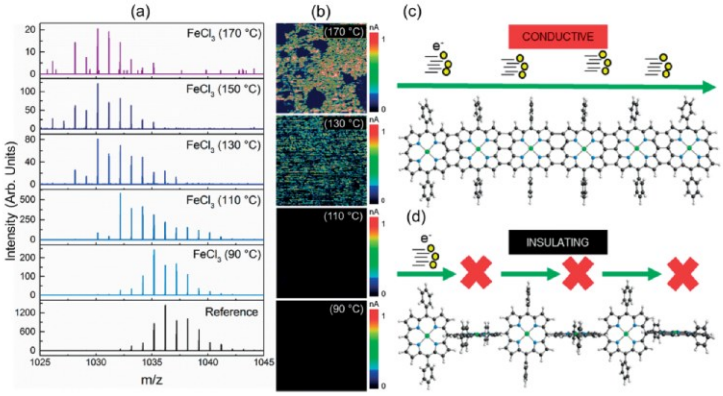

Figure 7. (a) Dimer region of the LDI-HRMS spectra in the mass range *m/z* 1020 to 1050 of the NiDPP-based thin films obtained using $FeCl_3$ sublimed at different temperatures. (b) C-AFM electron-current images (2 × 2 µm²) of the NiDPP-based thin films elaborated from $FeCl_3$ sublimed at 90 °C, 110 °C, 130 °C and 170 °C. Schematics of (c) a flat and tape-shaped triply-fused poly(NiDPP) and (d) a singly-fused poly(NiDPP), which arranged with an orthogonal conformation between the neighbouring NiDPP unit.

130 °C. This is notably expressed by a –2H shift of the maximum intensity for the dimeric peaks observed by LDI-HRMS (Figure 7a), hinting on a transition from mostly singly-fused poly(NiDPP) formed for 110 °C $FeCl_3$ sublimation temperature to more double- and triple-fused poly(NiDPP) formed for $FeCl_3$ sublimation temperatures greater than 130 °C. This result is consistent with the work by Osuka et al. that reported higher conductivities for flat and tape-shaped triply-fused porphyrin tapes (Figure 7c) in comparison to singly-fused porphyrins,[40] which arranged with an orthogonal conformation between the neighboring porphyrin units (Figure 7d). This underlines the importance of controlling the oxidant delivery rate when performing the oxidative fusion of porphyrins, which in addition of readily depositing on the substrate irrespective of their polymerization due to their very high sticking coefficient can form singly, doubly and triply-fused poly(porphyrins).

Higher oxidant delivery rates also favor the chlorination of the formed compounds (Figure 4) and can even be considered as an asset when targeting the simultaneous synthesis and deposition of insoluble directly fused poly(porphyrin) coatings (Figure 2) since halogenation of porphyrins reduces their solubility.[34] Nevertheless, one should highlight that above a $FeCl_3$ sublimation temperature of 130 °C, the electron-current of the NiDPP-based thin films reached several nanoamperes and any further incorporation of oxidant may even reduce the conductivity of the resulting thin film. Indeed, the inclusion of oxidant agglomerates evidenced by SIMS (Figure 6b), is also observed from the electron-current images (Figure 7b), which revealed a very similar morphology for the NiDPP-based thin film formed from $FeCl_3$ sublimed at 170 °C.

The micrometric and low electron-current flow regions correspond to the $FeCl_3$ islands observed by SIMS (Figure 6b). In the perspective to promote the formation of directly fused poly(porphyrin) coatings with a higher degree of polymerization/fusion and a better homogeneity, both adjusted oxidant delivery modes and different types of oxidants may be investigated. In particular, other successful oCVD and vapour phase polymerization (VPP) oxidants, which can be solid, e.g. iron(III) tosylate,[41] or liquid under ambient conditions, e.g. bromine[42,43] (Br_2), vanadium oxytrichloride[44] ($VOCl_3$) and antimony pentachloride[45] ($SbCl_5$), are under investigation.

Conclusions

The importance of the oxidant selection and delivery rate when performing the oCVD of porphyrins is evidenced. In the case of nickel(II) 5,15-(diphenyl)porphyrin, $FeCl_3$ is demonstrated as the most suitable oxidant, allowing the formation of mainly singly-fused poly(NiDPP) or conductive mainly multiply-fused poly(NiDPP) with absorption in the NIR region. Supply of $FeCl_3$ at a controlled rate is essential to promote direct fusion of NiDPP over undesired chlorination. Indeed, chlorination occurring at the free *beta* and *meso* positions of NiDPP monomer hinders the step-growth polymerization reaction. This side reaction is enhanced by an excess of oxidant, as well as by the use of an inappropriate oxidant that may directly induce chlorination or form chlorine that further chlorinates the porphyrin. Nevertheless, chlorination of the poly(NiDPP) is also demonstrated to yield fully insoluble NiDPP-based thin films, which might be useful for several applications, including electrocatalysis. In conclusion, the careful selection and delivery of the oxidant, i.e. $FeCl_3$, allows the oCVD of conductive directly fused poly(NiDPP) coatings on various substrates, e.g. printer paper, glass, and silicon. The described oCVD approach opened the way to the practical use of conductive poly(porphyrins) that have a great potential for gas sensing,[18] catalysis,[4] photovoltaic[19] and optoelectronic applications.[21]

Experimental Section

Oxidative Chemical Vapour Deposition.

The oCVD experiments described in this paper were performed in a custom-built oCVD reactor (Figure S1). The reactor body is a stainless steel cube of 41 cm on each side (Kurt J. Lesker Co.) equipped with a dry scroll pump (Varian) and a turbomolecular pump (Agilent) to achieve high vacuum. A butterfly-type throttling valve (VAT) and a microleak valve fed with argon (Air Liquide, 99.999 %) were used to maintain the pressure to 10^{-3} mbar for all the deposition experiments. The pressure was monitored by means of a baratron vacuum gauge (MKS). The porphyrin and oxidant are placed in two low-temperature evaporation (LTE) point sources (Kurt J. Lesker Co.) at the bottom of the chamber and oriented upward at the inverted temperature-controlled substrate holder (Thermocoax) located approximately 20 cm above. In the present study, the porphyrin and oxidant evaporators were loaded with 10 mg of nickel(II) 5,15-(diphenyl)porphyrin (NiDPP) and 150 mg of iron(III) chloride ($FeCl_3$, 97 %), 250 mg of copper(II) chloride ($CuCl_2$, 97 %) and 300 mg of copper(II) perchlorate ($Cu(ClO_4)_2$, 98 %), respectively. Porphyrin's evaporator temperature was kept at 250 °C when oxidant's evaporator temperature was varied differently for each oxidant (from 90 °C to 170 °C for $FeCl_3$, 250 °C to 350 °C for $CuCl_2$ and 200 °C to 250 °C for $Cu(ClO_4)_2$) (Table S1) to sublime the solid oxidants at different rates as confirmed by weight measurements. Microscope glass slides, pristine and platinum-coated silicon wafers and printer paper sheets were used as substrates. The substrate holder was maintained at 130 °C for the deposition experiments on glass and silicon substrates and at 50 °C for the deposition experiments on printer paper. The deposition time was set to 30 minutes for all experiments. The NiDPP monomer was prepared from the metalation of 5,15-(diphenyl)porphyrin (PorphyChem, 98 %) with $Ni(OAc)_2{\cdot}4H_2O$.[46] The oxidants were obtained from Sigma-Aldrich and used without further purification. Although we have not experienced any problems in handling the perchlorate salts, all materials should be handled with extreme care.

Thin Film Characterization.

The optical absorbance of the NiDPP-based thin films was measured in the range of 250–2500 nm using a UV/Vis-NIR spectrophotometer (Perkin Elmer, Lambda 950) equipped with an integrating sphere. The optical absorbance of the as-deposited and acetone-rinsed NiDPP-based thin films was measured directly on glass substrates. The absorbance of the dissolved or partly dissolved NiDPP-based thin films in acetone (99.5 %) was measured in 3.5 mL quartz cuvettes with a 1 cm light path. Atmospheric pressure laser desorption/ionization coupled with a high-resolution mass spectrometer (AP-LDI-HRMS) was employed for the characterization and identification of the oligomers produced by the oCVD reaction of NiDPP

with the different oxidants, namely $FeCl_3$, $CuCl_2$ or $Cu(ClO_4)_2$. HRMS analyses were performed with an LTQ/Orbitrap Elite™ Hybrid Linear Ion Trap-Orbitrap Mass Spectrometer from Thermo Scientific (San Jose, CA) coupled with an AP-LDI (ng) UHR source from MassTech Inc (Columbia, MA) with a 355 nm Nd:YAG laser. The as-deposited NiDPP-based thin films were directly probed, without any matrix deposition, by the laser following a spiral motion during 30 seconds per sample. An in-source decay (ISD) of 70 V was applied to the samples in order to prevent any formation of non-covalent NiDPP clusters that could interfere with the distribution of the NiDPP oligomers. A maximum injection time of 800 ms and a resolving power of 240,000 at *m/z* 400 within the normal mass range (*m/z* 300–2000) and the high mass range (*m/z* 1800–4000) were employed for the HRMS analyses. With the aim to establish trends and qualitative information on the oxidative fusion and chlorination of NiDPP, the signal intensity of the *m/z* values of the various monomers and oligomers species were extracted and integrated for all ions of interest with a tolerance of ±3 ppm from the ion chromatogram. A polymerization ratio was calculated from the sum of the areas corresponding to the extracted ions of NiDPP-derived oligomers over the sum of the areas corresponding to extracted ions of the NiDPP-derived monomers from the mass chromatogram, while a chlorination ratio was calculated from the sum of the areas of the extracted ions corresponding to chlorinated NiDPP-derived compounds over the extracted ions corresponding to non-chlorinated NiDPP-derived compounds from the mass chromatogram. X-ray photoelectron spectroscopy (XPS) analyses were performed on a Kratos Axis Ultra DLD instrument using a monochromatic Al K_α X-ray source ($h\upsilon$ = 1486.6 eV) at a power of 105 W. Charge calibration was accomplished by fixing the binding energy of carbon (C 1s) to 285.0 eV. Secondary ion mass spectrometry (SIMS) measurements were performed on a Cameca NanoSIMS50 using a Cs^+ primary ion beam with an impact energy of 16 keV and a current of around 1.5 pA on the sample surface. The masses studied simultaneously in the multicollection mode were $^{12}C^{14}N$, ^{35}Cl, ^{63}Cu and $^{56}Fe^{16}O$. Images were acquired at a size of 10 x 10 μm^2 and 256 × 256 pixels. Secondary electron images were recorded using the same SIMS instrument. C-AFM was used to simultaneously map the topography and local electrical conductivity of the samples' surface. The measurements were performed with an Innova AFM (Bruker, Santa Barbara) coupled with a DLPCA 200 current amplifier (Femto, Germany). The conductive AFM tips are SCM-PIC (Bruker, Santa Barbara) coated with a 20 nm layer of Pt/Ir, and with a nominal spring constant of 0.2 $N{\cdot}m^{-1}$. The topography was obtained by maintaining the tip deflection constant via the feedback loop of the AFM acting on the piezo Z direction. A 4 V bias is applied via the gold back electrode of the samples, then the grounded conductive tip was collecting electrons to the current amplifier. A 10^9 $V{\cdot}A^{-1}$ amplification was used and the signal output was then transmitted to the AFM electronic and recorded. The thickness of the different samples were all in the same range, ca. 50 nm, to ensure the comparison of the results. For each new tip, a check of the system was done with a 10 MΩ resist.

Acknowledgments

Authors gratefully acknowledge the financial support of the Luxembourg National Research Fund (FNR.lu) through the POLYPORPH project (C15-MS-10340560-POLYPORPH-Boscher). Dr. N. Valle, Dr. J. Guillot, C. Vergne, B. Marcolini and R. Vaudemont from LIST are acknowledged for the SIMS, XPS and TGA measurements.

Keywords: Porphyrinoids · Conjugation · Polymerization · Chemical vapor deposition · Thin films

[1] A. R. Battersby, *Nat. Prod. Rep.* **2000**, *17*, 507.
[2] S. Mathew, A. Yella, P. Gao, R. Humphry-Baker, B. F. E. Curchod, N. Ashari-Astani, I. Tavernelli, U. Rothlisberger, M. K. Nazeeruddin, M. Grätzel, *Nat. Chem.* **2014**, *6*, 242.
[3] W. Zhang, W. Lai, R. Cao, *Chem. Rev.* **2017**, *117*, 3717.
[4] D. Khusnutdinova, B. L. Wadsworth, M. Flores, A. M. Beiler, E. A. Reyes Cruz, Y. Zenkov, G. F. Moore, *ACS Catal.* **2018**, *8*, 9888.
[5] C. H. Lee, D. K. Dogutan, D. G. Nocera, *J. Am. Chem. Soc.* **2011**, *133*, 8775.
[6] B. Shan, A. Nayak, R. N. Sampaio, M. S. Eberhart, L. Troian-Gautier, M. K. Brennaman, G. J. Meyer, T. J. Meyer, *Energy Environ. Sci.* **2018**, *11*, 447.
[7] N. A. Rakow, K. S. Suslick, *Nature* **2000**, *406*, 710.
[8] N. D. Boscher, T. Bohn, P. Heier, F. Moisy, B. Untereiner, K. Heinze, P. Choquet, *Sens. Actuat. B* **2014**, *191*, 553.
[9] R. Paolesse, S. Nardis, D. Monti, M. Stefanelli, C. Di Natale, *Chem. Rev.* **2017**, *117*, 2517.
[10] N. D. Boscher, M. Wang, A. Perrotta, K. Heinze, M. Creatore, K. K. Gleason, *Adv. Mater.* **2016**, *28*, 7479.
[11] S. Singh, A. Aggarwal, N. V. S. D. K. Bhupathiraju, G. Arianna, K. Tiwari, C. M. Drain, *Chem. Rev.* **2015**, *115*, 10261.
[12] P. Heier, C. Förster, D. Schollmeyer, N. Boscher, P. Choquet, K. Heinze, *Dalton Trans.* **2013**, *42*, 906.
[13] N. D. Boscher, M. Wang, K. K. Gleason, *J. Mater. Chem. A* **2016**, *4*, 18144.
[14] R. Paolesse, L. Jaquinod, F. D. Sala, D. J. Nurco, L. Prodi, M. Montalti, C. Di Natale, A. D'Amico, A. Di Carlo, P. Lugli, K. M. Smith, *J. Am. Chem. Soc.* **2000**, *122*, 11295.
[15] A. Tsuda, H. Furuta, A. Osuka, *Angew. Chem. Int. Ed.* **2000**, *39*, 2549; *Angew. Chem.* **2000**, *112*, 2649.
[16] A. Tsuda, A. Osuka, *Science* **2001**, *293*, 79.
[17] A. A. Ryan, M. O. Senge, *Eur. J. Org. Chem.* **2013**, *2013*, 3700.
[18] C. H. A. Esteves, B. A. Iglesias, R. W. C. Li, T. Ogawa, K. Araki, J. Gruber, *Sens. Actuat. B* **2014**, *193*, 136.
[19] J. Kesters, P. Verstappen, M. Kelchtermans, L. Lutsen, D. Vanderzande, W. Maes, *Adv. Energy Mater.* **2015**, *5*, 1500218.
[20] M. A. Vorotyntsev, D. V. Konev, C. H. Devillers, I. Bezverkhyy, O. Heintz, *Electrochim. Acta* **2010**, *55*, 6703.
[21] T. Tanaka, A. Osuka, *Chem. Soc. Rev.* **2015**, *44*, 943.
[22] G. Bengasi, K. Baba, P. Gratia, K. Heinze, N. D. Boscher, *Angew. Chem. Int. Ed.* **2019**, *58*, 2103; *Angew. Chem.* **2019**, *131*, 2121.
[23] H. Goktas, X. Wang, N. D. Boscher, S. Torosian, K. K. Gleason, *J. Mater. Chem. C* **2016**, *4*, 3403.
[24] A. K. Sahoo, Y. Nakamura, N. Aratani, K. S. Kim, S. B. Noh, H. Shinokubo, D. Kim, A. Osuka, *Org. Lett.* **2006**, *8*, 4141.
[25] J. P. Lewtak, D. Gryko, D. Bao, E. Sebai, O. Vakuliuk, M. Ścigaj, D. T. Gryko, *Org. Biomol. Chem.* **2011**, *9*, 8178.
[26] N. A. Senger, B. Bo, Q. Cheng, J. R. Kee, S. Gronert, W. Wu, *J. Org. Chem.* **2012**, *77*, 9535.
[27] A. Tsuda, Y. Nakamura, A. Osuka, *Chem. Commun.* **2003**, 1096.
[28] N. Yoshida, N. Aratani, A. Osuka, *Chem. Commun.* **2000**, 197.
[29] G. L. Perlovich, O. A. Golubchikov, M. E. Klueva, *J. Porphyrins Phthalocyanines* **2000**, *4*, 699.
[30] N. D. Boscher, D. Duday, P. Heier, K. Heinze, F. Hilt, P. Choquet, *Plasma Process Polym.* **2013**, *10*, 336.
[31] M. Tonezzer, G. Maggioni, E. Dalcanale, *J. Mater. Chem.* **2012**, *22*, 5647.
[32] W. Auwärter, D. Écija, F. Klappenberger, J. V. Barth, *Nat. Chem.* **2015**, *7*, 105.
[33] M. Wang, X. Wang, P. Moni, A. Liu, D. H. Kim, W. J. Jo, H. Sojoudi, K. K. Gleason, *Adv. Mater.* **2017**, *29*, 1604606.
[34] M. O. Senge, O. Flögel, K. Rhulandt-Senge, *J. Porphyrins Phthalocyanines* **2001**, *5*, 503.
[35] Y. Saegusa, T. Ishizuka, K. Kommamura, S. Shimizu, H. Kotani, N. Kobayashi, T. Kojima, *Phys. Chem. Chem. Phys.* **2015**, *17*, 15001.
[36] J. G. Hooley, M. Bartlett, *Carbon* **1967**, *5*, 417.
[37] J. G. Hooley, J. R. Sams, B. V. Liengmet, *Carbon* **1970**, *8*, 467.
[38] T. Wijesekera, A. Matsumoto, D. Dolphin, D. Lexa, *Angew. Chem. Int. Ed. Engl.* **1990**, *29*, 1028; *Angew. Chem.* **1990**, *102*, 1073.

[39] N. J. Trujillo, M. C. Barr, S. G. Im, K. K. Gleason, *J. Mater. Chem.* **2010**, *20*, 3968.
[40] B. Keun, N. Aratani, J. Kuk, D. Kim, A. Osuka, K. Yoo, **2005**, *412*, 303.
[41] M. Fabretto, M. Müller, K. Zuber, P. Murphy, *Macromol. Rapid Commun.* **2009**, *30*, 1846.
[42] H. Chelawat, S. Vaddiraju, K. Gleason, *Chem. Mater.* **2010**, *22*, 2864.
[43] D. Bhattacharyya, K. K. Gleason, *Chem. Mater.* **2011**, *23*, 2600.
[44] S. Nejati, K. K. S. Lau, *Langmuir* **2011**, *27*, 15223.
[45] Y. Y. Smolin, M. Soroush, K. K. S. Lau, *Beilstein J. Nanotechnol.* **2017**, *8*, 1266.
[46] S. A. Yao, C. B. Hansen, J. F. Berry, *Polyhedron* **2013**, *58*, 2.

Received: January 10, 2019

5.3 Reactivity of Nickel(II) Porphyrins in oCVD Processes— Polymerisation, Intramolecular Cyclisation and Chlorination

Giuseppe Bengasi, Kamal Baba, Oliver Back, Gilles Frache, Katja Heinze, and Nicolas D. Boscher

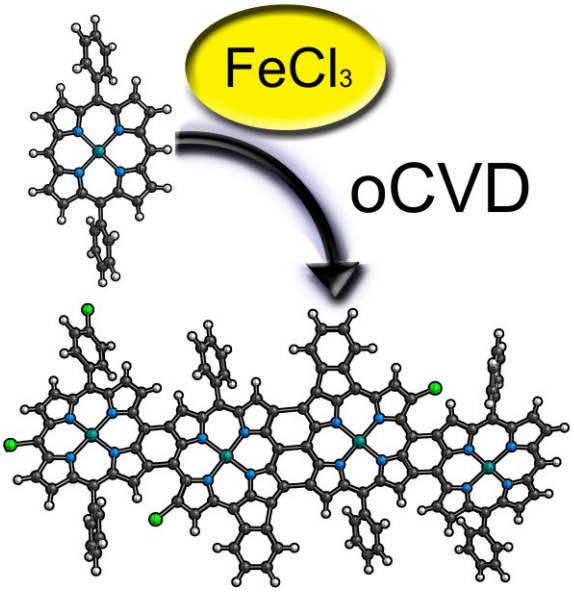

Oxidative chemical vapour deposition of (5,15-diphenylporphyrinato)nickel(II) with $FeCl_3$ as the oxidant yielded a conjugated polymetalloporphyrin as a highly coloured thin film on glass and plastic substrates. The initial steps of the oxidative coupling were elucidated by means of spectroscopic, mass spectrometric and quantum chemical studies.

Author contributions

Giuseppe Bengasi performed the experimental section with contributions from Kamal Baba and Oliver Back. Giuseppe Bengasi performed the quantum chemical study. Gilles Frache performed the mass spectrometric analysis. Giuseppe Bengasi made the interpretation of the results with contributions of all co-authors. Giuseppe Bengasi, Katja Heinze and Nicolas D. Boscher contributed equally to write the manuscript.

Supporting information

Supporting information can be found at page 116.

Reprinted from permission from:

Giuseppe Bengasi, Kamal Baba, Oliver Back, Gilles Frache, Katja Heinze, and Nicolas D. Boscher; *Chem. Eur. J.* **2019**, *25*, 8313 – 8320

ChemPubSoc Europe

DOI: 10.1002/chem.201900793

CHEMISTRY
A European Journal
Full Paper

Chemical Vapor Deposition | *Hot Paper*

Reactivity of Nickel(II) Porphyrins in oCVD Processes—Polymerisation, Intramolecular Cyclisation and Chlorination

Giuseppe Bengasi,[a, b] Kamal Baba,[b] Oliver Back,[a] Gilles Frache,[b] Katja Heinze,*[a] and Nicolas D. Boscher*[b]

Abstract: Oxidative chemical vapour deposition of (5,15-diphenylporphyrinato)nickel(II) (NiDPP) with iron(III) chloride as oxidant yielded a conjugated poly(metalloporphyrin) as a highly coloured thin film, which is potentially useful for optoelectronic applications. This study clarified the reactive sites of the porphyrin monomer NiDPP by HRMS, UV/Vis/NIR spectroscopy, cyclic voltammetry and EPR spectroscopy in combination with quantum chemical calculations. Unsubstituted *meso* positions are essential for successful polymerisation, as demonstrated by varying the porphyrin *meso* substituent pattern from di- to tri- and tetraphenyl substitution. DFT calculations support the proposed radical oxidative coupling mechanism and explain the regioselectivity of the C–C coupling processes. Depositing the conjugated polymer on glass slides and on thermoplastic transparent polyethylene naphthalate demonstrated the suitability of the porphyrin material for flexible optoelectronic devices.

Introduction

Porphyrins and porphyrinic compounds experience widespread and growing interest due to their remarkable electronic and optoelectronic properties,[1] which enable applications in photovoltaics,[2] electro- and photocatalysis[3,4] and chemical sensing.[5,6] Particular interest focuses on directly fused metalloporphyrins, which have an extended π system, fascinating optical properties such as near-infrared (NIR) absorption,[7] two-photon absorption,[8] nonlinear optical properties[9] and enhanced electrocatalytic activity.[10] Although the current synthetic routes to directly fused metalloporphyrins consist of treating a metalloporphyrin having free *meso* and β positions (Scheme 1) with a suitable oxidant in solution, the poor solubility of metalloporphyrin monomers, oligomers and polymers requires the introduction of solubilising pendant groups to achieve high chain lengths.[11]

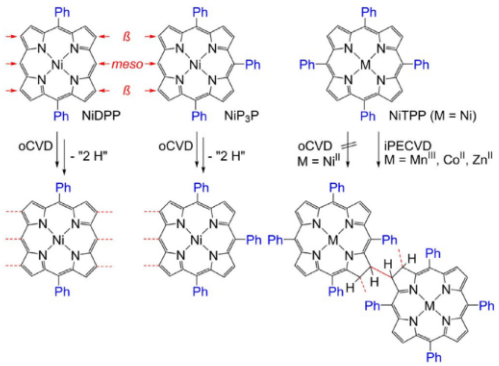

Scheme 1. Molecular structures of the porphyrins investigated in this work. NiDPP can form linear polymers with up to three linkages between monomers. NiP_3P should merely form dimers and MTPP should not readily polymerise in an oCVD process, but can form sterically congested β–β-linked polychlorins by iPECVD.

The best results are obtained by dehydrogenative coupling of zinc(II) porphyrins with silver(I) salts followed by a second oxidation step to obtain β–β/*meso*–*meso*/β–β triply fused metalloporphyrins.[7] Inspired by these seminal studies, alternatives for the formation of directly fused metalloporphyrins have been developed.[11–17] However, fused metalloporphyrins are generally poorly soluble and infusible, and hence straightforward integration into devices is prevented.[18,19] On the other hand, introduction of solubilising agents on the porphyrins hinders the π–π interactions that are required for electronically conducting materials.[1,20]

[a] G. Bengasi, O. Back, Prof. Dr. K. Heinze
Institute of Inorganic Chemistry and Analytical Chemistry
Johannes Gutenberg University of Mainz
Duesbergweg 10-14, 55128 Mainz (Germany)
E-mail: katja.heinze@uni-mainz.de

[b] G. Bengasi, Dr. K. Baba, Dr. G. Frache, Dr. N. D. Boscher
Materials Research and Technology Department
Luxembourg Institute of Science and Technology
5 Avenue des Hauts-Fourneaux, L-4362 Esch-sur-Alzette (Luxembourg)
E-mail: nicolas.boscher@list.lu

Supporting information and the ORCID identification number(s) for the author(s) of this article can be found under: https://doi.org/10.1002/chem.201900793.

Chemical vapour deposition (CVD) processes enable simultaneous synthesis and deposition of a plethora of thin-film compositions directly from the vapour phase. In particular, CVD circumvents the challenges related to the poor solubility of the starting monomers and resulting polymers, since no solvents are required in this process.[21] Recent ground-breaking studies also demonstrated successful free-radical polymerisation and oxidative polymerisation of porphyrins in CVD processes (Scheme 1).[20,22]

Initiated plasma-enhanced CVD (iPECVD) of free-base, manganese(III), cobalt(II) and zinc(II) 5,10,15,20-tetraphenylporphyrins[22] yielded polymeric films by free-radical polymerisation of one of the *exo*-pyrrole double bonds of the monomers (Scheme 1).[23] The propagation reaction occurs at the β position of the porphyrin (22 π electrons) and leads to a reduced porphyrin (chlorin with 20 π electrons). In these polychlorin thin films the monomers are covalently connected through β–β linkages, yet π conjugation is absent (Scheme 1).[22]

On the other hand, the oxidative chemical vapour deposition (oCVD) reaction of (5,15-diphenylporphyrinato)nickel(II) (NiDPP, Scheme 1) with $FeCl_3$ furnished π-conjugated poly(-NiDPP) thin films by dehydrogenative C–C coupling. These films show a remarkably high conductivity of $3.6\times10^{-2}\,S\,cm^{-1}$.[20] Moreover, patterned conductive poly(NiDPP) thin films were readily formed even on printer paper owing to the potential of oCVD to form conjugated polymer thin films directly from the vapour phase without the need for solvents.[20] In addition, the oxidative coupling of the NiDPP monomer in oCVD yielded NIR-absorbing coatings consistent with the formation of directly fused metalloporphyrins.

Although thin film preparation by oCVD is rather straightforward, mechanistic details and the side reactions occurring in the oCVD process are not yet fully understood. Herein, we report insights into the dehydrogenative fusion sites for di-, tri- and tetraphenyl *meso*-substituted nickel(II) porphyrins (Scheme 1). Laser desorption ionisation (LDI) HRMS and UV/Vis/NIR spectroscopy were used to probe the direct fusion of di- and triphenyl-substituted nickel(II) porphyrins to form conjugated oligomers and polymers. Characterisation of the thin films was complemented by studies on the monomers and monomer radical cations as the active species by cyclic voltammetry (CV), EPR spectroscopy and DFT calculations to provide insights into the initial steps in oCVD of nickel(II) porphyrins.

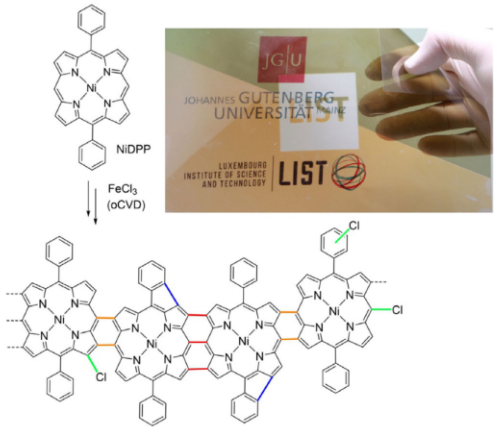

Scheme 2. The oCVD reaction of NiDPP yields a conjugated fused metalloporphyrin polymer with *meso*–β/β–*meso* (orange bonds) or β–β/*meso*–*meso*/β-β (red bonds) links between the monomer units. Potential side reactions, namely, cyclisation between a phenyl substituent and the porphyrin macrocycle (blue bonds) and chlorination of the porphyrin (green bonds), are indicated. The location of cyclisation and chlorination is not clear and merely representative. The inset shows an optical image of a bent transparent PEN foil coated by the greenish oCVD NiDPP film (top area of the foil) and the orange reference NiDPP film (bottom area of the foil).

Results and Discussion

Preparation of thin films by oCVD and film characterisation

Nickel(II) 5,15-diphenylporphyrins form linear polymers both in solution and in oCVD-based approaches with suitable oxidants (Scheme 2).[18,20] Nickel(II) as central metal ion is inert towards demetallation by acids, which can be produced during the coupling reactions. Consequently, all oCVD processes in this study were performed with the respective stable nickel(II) porphyrins.[24] $FeCl_3$ is quite volatile[25] and its oxidation potential is sufficiently high to make it an ideal oxidant for oCVD processes[20,26] and for the dehydrogenative coupling of porphyrins in solution-based approaches.[14]

With the aim of identifying the sites involved in the oxidative coupling of 5,15-diphenyl-substituted porphyrins during the oCVD process, we selectively blocked the remaining *meso* sites by phenyl substituents and investigated the oCVD reaction of tri- and tetra-*meso*-substituted nickel(II) 5,10,15-triphenylporphyrin (NiP_3P) and nickel(II) 5,10,15,20-tetraphenylporphyrin (NiTPP), respectively (Scheme 1). NiTPP should be unable to form linkages at its *meso* positions. On the other hand, NiP_3P should mainly form dimers and trimers through its single free *meso* position (Scheme 1).

The oCVD reaction of NiDPP and NiP_3P with $FeCl_3$ as oxidant under the reported conditions (see Experimental Section)[20] yielded greenish coatings on glass and on polyethylene naphthalate (PEN) foils, in contrast to the reddish colour of the respective reference NiDPP and NiP_3P coatings formed in the absence of oxidant (Scheme 2; Supporting Information, Figure S1). On the other hand, the oCVD reaction of NiTPP with $FeCl_3$ has a far less pronounced impact on the colour of the coatings, which only turned from reddish for the reference NiTPP coating to orange for the oCVD NiTPP coating (Supporting Information, Figure S1 c).

All films produced by oCVD covered the substrates homogeneously with thicknesses determined by profilometry of 200, 120 and about 10 nm for NiDPP, NiP_3P and NiTPP, respectively. The decreasing film thickness in this series suggests a relation between the number of phenyl rings and the evaporation rate of the phenyl-substituted porphyrins in the oCVD process.

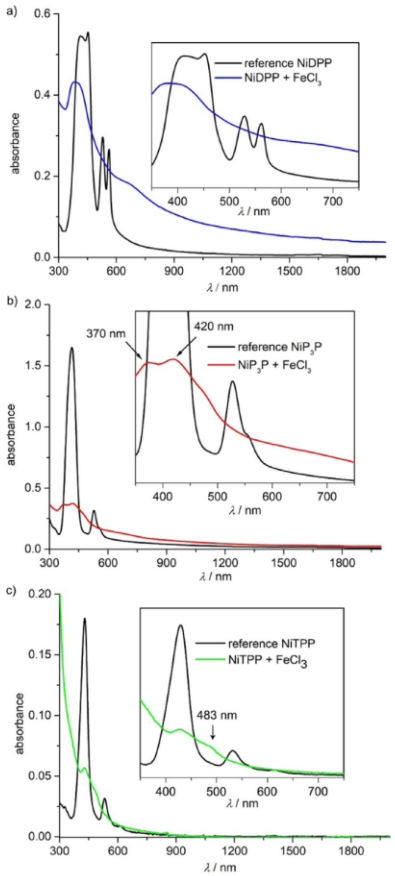

Figure 1. UV/Vis/NIR absorption spectra of the oCVD coatings grown from a) NiDPP (blue line), b) NiP_3P (red line) and c) NiTPP (green line) on glass slides. UV/Vis/NIR absorption spectra of the respective sublimed porphyrins are provided for comparison (black lines).

UV/Vis/NIR absorption spectroscopy revealed broader absorption of the oCVD coatings compared to the reference coatings obtained by sublimation of the respective porphyrin. The absorption of the oCVD NiP_3P and NiDPP coatings even tails significantly into the NIR region (Figure 1a and b). In particular, the oCVD NiDPP coating appreciably absorbs up to 2000 nm (Figure 1a). According to reports of Osuka et al.,[7,18] these observations suggest the formation of oligomers with higher conjugation lengths.

In addition, the oCVD NiDPP coating is almost insoluble in many common nonpolar, polar aprotic and protic organic solvents (e.g., chloroform, dichloromethane, acetone, methanol, hexafluoro-2-propanol), whereas the oCVD NiP_3P and NiTPP coatings are partly and fully soluble in these solvents, respectively (Supporting Information, Figure S2). Clearly, the solubility of the coating decreases on reducing the number of phenyl rings attached to the porphyrins from four to two. This is consistent with the proposed polymerisation through the *meso* positions (*meso*–β, *meso*–*meso*), which is impossible for NiTPP, while NiP_3P may yield less soluble dimers and possibly short oligomers. On the other hand, NiDPP essentially forms insoluble coatings. As expected, all reference coatings formed by sublimation, that is, porphyrin monomers, are completely soluble in the aforementioned solvents.

UV/Vis/NIR spectroscopic analysis of the acetone- and dichloromethane-soluble phases of all oCVD coatings revealed broadened and bathochromically shifted Soret and Q bands (Supporting Information, Figure S3 and Table S1) together with unconsumed $FeCl_3$ showing an absorption band at 350 nm in acetone. The characteristic changes of the Soret bands of the soluble, low molecular weight fractions of the NiP_3P and NiTPP oCVD coatings are very similar to those observed for the NiDPP films. We had attributed these absorption changes to dehydrogenative intramolecular cyclisation reactions between the phenyl rings and the β position of the porphyrin and/or chlorination of the porphyrins (Scheme 2).[20] Both reactions modify the porphyrin symmetry and the HOMO–LUMO energy gap, which results in red shifts and different numbers of Q bands compared with the respective starting materials.[27–29]

These two side reactions are particularly noticeable for the NiTPP oCVD coating, which shows a strong decrease and bathochromic shift of the Soret and Q bands (Figure 1c). UV/Vis/NIR spectroscopic analysis of the dichloromethane phase of this fully soluble coating revealed a broad absorption band with a pronounced maximum at 429 nm and weaker maxima at 462 and 514 nm (Supporting Information, Figure S3c and f). The two weaker maxima agree very well with literature reports for singly and doubly ring fused ZnTPP in DMF (471 and 532 nm, respectively).[28b] The bathochromic shift of the main band to 429 nm and the broadening are attributed to chlorination of the porphyrin.[27]

Atmospheric-pressure LDI-HRMS of all oCVD coatings (Figure 2) confirmed that, similar to solution-based approaches, a free *meso* position is required to promote the oxidative polymerisation of the porphyrin through oCVD.[14,30] Indeed, the mass spectrum of the oCVD NiTPP coating solely exhibits signals related to NiTPP monomers (Figure 2a), while peaks corresponding to oligomers are additionally observed for the oCVD NiP_3P and NiDPP coatings (Figure 2b and c). Besides signals of the expected NiP_3P dimers, weak signals of NiP_3P oligomers are detected as well (Figure 2b). This is in contrast to the reaction of NiP_3P and iron(III) salts in solution, which gives mainly doubly and triply linked dimers in a combined yield of 92%.[14] On the other hand, DFT calculations had suggested the possibility that in a CVD process tetraphenylporphyrins can undergo a free-radical polymerisation reaction through *exo*-pyrrole double bonds leading to a sterically congested β–β linked-staircase structure.[22] During the oCVD process discussed here, NiP_3P could possibly exhibit similar reactivity to form short oligomers through β–*meso* or β–β linkages at the less hindered side of the porphyrin (Figure 2b, inset). Clearly, linkages involving the β positions are possible in CVD processes, yet they

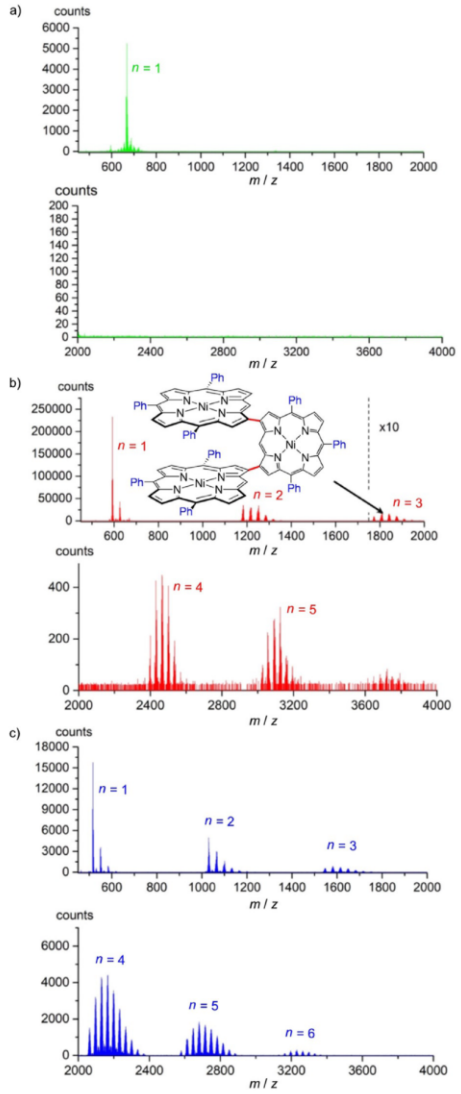

Figure 2. LDI-HRMS analysis of a) oCVD NiTPP, b) oCVD NiP_3P and c) oCVD NiDPP coatings. Peak distributions related to the chlorination of the porphyrin are present in all mass spectra. The spectra show the formation of oligomers for NiP_3P and NiDPP ($n > 1$). The m/z 500–2000 and 2000–4000 ranges were recorded in separate analyses and thus a meaningful comparison of intensities is not possible. b) The inset shows a conceivable structure of a β–β-linked NiP_3P trimer.

appear to be insignificant in solution processes involving NiP_3P. In such congested β–*meso* or β–β connections, the almost perpendicular arrangement of the monomeric units hampers π extension and conjugation compared with doubly or triply linked NiDPP. Less conjugation also explains the lower NIR absorbance of the oCVD NiP_3P coating compared to the oCVD NiDPP coating (Figure 1a and b). Further investigations on this intriguing reactivity pattern are ongoing but lie outside the scope of the present study.

Similar to previously reported data for NiDPP,[20] the LDI-HR mass spectra of oCVD NiP_3P and NiTPP coatings show signals related to the loss of an even number of hydrogen atoms ($-2n$H) for the monomer (Figure 3). Interestingly, the maximum number of 2H pairs eliminated from the porphyrin monomers is proportional to the number of phenyl substituents, that is, 4H for NiDPP, 6H for NiP_3P and 8H for NiTPP. This observation strongly supports the previously suggested intramolecular cyclisation between the phenyl substituent and the β position of the porphyrin (Scheme 2).

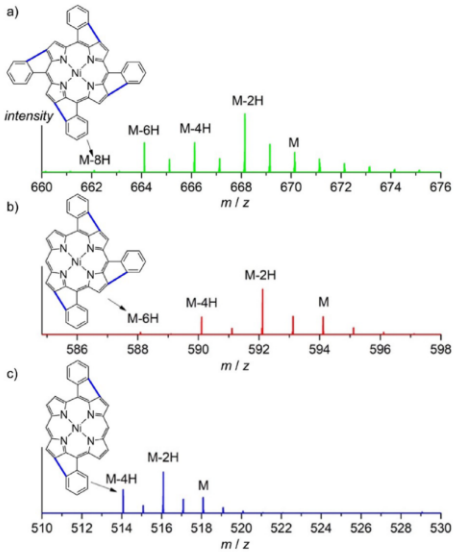

Figure 3. LDI-HR mass spectra of a) oCVD NiTPP, b) oCVD NiP_3P and c) oCVD NiDPP in the monomer range. The spectra show the loss of hydrogen atoms ($M-2n$H) attributed to the intramolecular cyclisation between the phenyl ring and the macrocycle. The coupling is drawn at arbitrary positions.

As already observed for oCVD NiDPP, the mass spectra of oCVD NiP_3P and NiTPP coatings show multiple chlorine-atom incorporation leading to several sets of peak clusters separated by 35 mass units (Figure 2). The mass spectra did not allow any preferential reactive site on the porphyrin for chlorination (Scheme 2) to be determined. This chlorination is likely due to a reaction between the porphyrin and iron(III) chloride or Cl_2 produced from $FeCl_3$ during sublimation.[27,31,32] Chlorinated by-products are also commonly observed in reactions of aromatic substrates and oxidizing metal halides.[33]

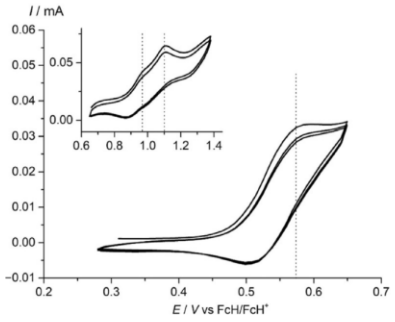

Figure 4. Cyclic voltammograms of NiDPP in $CH_2Cl_2/[n Bu_4N][PF_6]$ solution.

Mechanistic aspects of oCVD of nickel porphyrins

To gain a deeper understanding of the NiDPP/oxidant reactivity, electrochemical experiments were conducted (Figure 4). The cyclic voltammogram of NiDPP in $CH_2Cl_2/[n Bu_4N][PF_6]$ shows quasireversible waves at peak potentials of $E_p = 0.57$, 0.95 and 1.10 V versus the ferrocene/ferrocenium couple, assigned to the first, second and third oxidation of NiDPP, respectively. The first oxidation of NiP_3P has been reported at a very similar potential ($E_p \approx 0.55$ V vs. ferrocene/ferrocenium).[14] The quasireversibility suggests a follow-up reaction after the initial one-electron oxidation.

The oxidation potential of iron(III) triflate is high enough to promote the oxidative coupling of NiP_3P in CH_2Cl_2/CH_3NO_2 solution yielding triply and doubly linked dimers.[14] Furthermore, conjugated polyporphyrins have an even lower oxidation potential than their parent monomers, which favours extension of polymeric chains over initiation of new ones.[18] Similarly, $FeCl_3$ promotes oxidative polymerisation of NiDPP and NiP_3P in oCVD, as sublimation of $FeCl_3$(s) most probably yields $FeCl_3$(g), Fe_2Cl_6(g) and Cl_2(g) among other oxidizing/chlorinating species under the oCVD conditions.[34] We suggest that the formation of strongly oxidising species such as Cl_2 could be involved in the intramolecular cyclisation of the porphyrin. Indeed, it has been shown previously that a second oxidation of the porphyrin is needed to achieve electrochemical extension of the π system.[28b,c]

In all cases, the initial step of the oxidative polymerisation is most probably the one-electron oxidation of the nickel(II) porphyrins to $[NiDPP]^{\bullet+}$, $[NiP_3P]^{\bullet+}$ and $[NiTPP]^{\bullet+}$, respectively. In coordinating solvents or in the presence of coordinating ligands, $[NiTPP]^{\bullet+}$ is best described as a nickel(III) porphyrin, whereas a description as a nickel(II) porphyrin π cation radical is more appropriate in the absence of axial coordination.[35] To simulate the oCVD conditions, NiDPP (1 mM in CH_2Cl_2) was oxidised with one equivalent of WCl_6[36] under inert atmosphere and in the absence of coordinating ligands (apart from potentially dissociated chloride) in an EPR tube. The solution was rapidly frozen by immersing the EPR tube in liquid nitrogen and examined by X-band EPR spectroscopy. The corresponding EPR spectrum at 77 K (Figure 5a) shows a weakly anisotropic

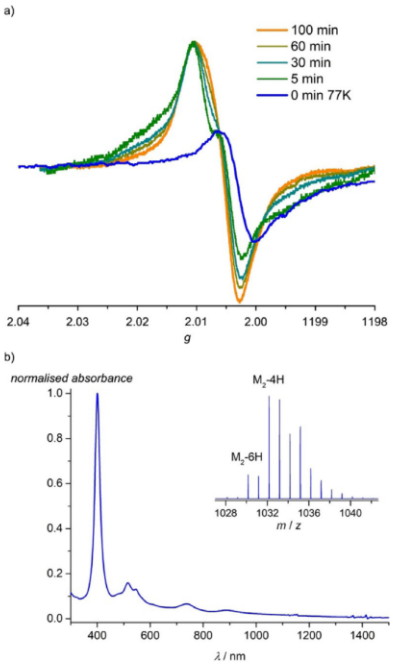

Figure 5. a) EPR spectrum of NiDPP/WCl_6 solution in CH_2Cl_2 rapidly frozen at 77 K (orange trace) and evolution of the EPR spectrum (normalised) upon thawing the solution and warming to room temperature over time. b) UV/Vis/NIR and MALDI-HR mass spectrum of the final NiDPP/WCl_6 solution (inset).

resonance at $g_{av} = 2.004$ $[NiDPP]^{\bullet+}$. No hyperfine coupling to ^{14}N nuclei was resolved. For $[Ni(TPP)]^{\bullet+}$, $g_{av} = 2.005$ ($g_x = 2.012$, $g_y \approx 2.004$, $g_z \approx 2.002$) has been reported, consistent with a nickel(II) porphyrin radical cation. On the other hand, nickel(III) porphyrins show highly anisotropic EPR patterns, for example, $g_x = 2.328$, $g_y = 2.305$ and $g_z = 2.093$ for $[Ni^{III}(TPP)(THF)_2]^{\bullet+}$.[35] Consequently, the electronic structure of $[NiDPP]^{\bullet+}$ is best described as nickel(II) porphyrin radical cation under these conditions. Upon warming the solution to room temperature, the isotropic EPR spectra evolved over time towards an isotropic value of $g_{iso} = 2.007$ suggesting an ongoing chemical reaction of the radical cations (Figure 5a). Persistent radical cations of aromatic molecules had been observed previously, for example, by using $MoCl_5$ or $FeCl_3$ with suitable aromatic substrates.[37,38]

UV/Vis/NIR spectroscopic analysis of the solution at the end of the EPR measurements (Figure 5b) showed new weak bands at 478, 615, 736 and 888 nm, which are consistent with porphyrin coupling reactions. LDI-HR mass spectra confirmed such coupling reactions. The mass spectrum in the *m/z* region of dimers shows a main peak at 1032.176 amu for $[C_{64}H_{36}N_8Ni_2]^+$, attributed to a doubly linked bis-porphyrin, and a five times less intense signal at 1030.160 amu for

$[C_{64}H_{34}N_8Ni_2]^{+}$ (inset of Figure 5b). The latter peak corresponds to the loss of 2H from the dimer, although it remains speculative whether a further porphyrin–porphyrin linkage or a phenyl cyclisation has occurred (Scheme 2). Clearly, WCl_6 promotes the dimerisation/oligomerisation of NiDPP in CH_2Cl_2 solution. Furthermore, the evolution of the EPR spectra demonstrates a radical chain growth mechanism with the EPR pattern of porphyrin oligomers varying with the oligomer length.

All obtained EPR data fit to essentially ligand-centred radicals without significant nickel contributions and are similar to literature data of $[NiTPP]^{\bullet+}$.[39,40] This electronic description of $[NiDPP]^{\bullet+}$ should apply for $[NiP_3P]^{\bullet+}$ as well, both for the solution (in the absence of axial ligands) and for the gas phase.

DFT calculations with B3LYP, TPSSH and PBE0 functionals converged to weakly distorted nickel(III) valence isomers as ground states, which are not observed under our conditions in the EPR spectra. Ambiguities and difficulties in assigning the correct valence isomeric descriptions have been noted before for $[NiTPP]^{\bullet+}$.[35,39,41] DFT calculations at the RIJCOSX-BP86-D3-ZORA/def2-TZVP level of theory [with and without solvent modelling by CPCM(CH_2Cl_2)] correctly describe $[NiDPP]^{\bullet+}$ and $[NiP_3P]^{\bullet+}$ as π radical cations with saddle-shaped macrocycles (Figure 6).[42]

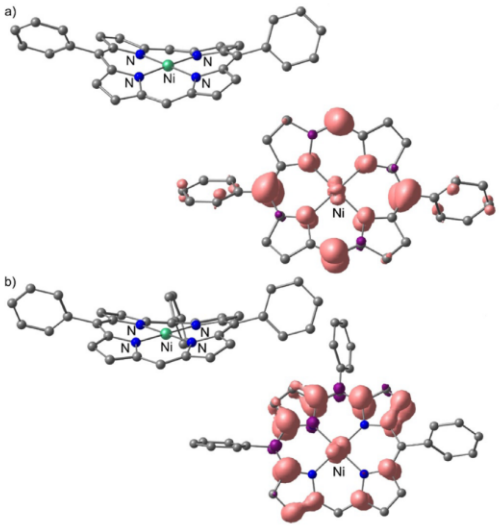

Figure 6. DFT calculated optimised geometries (approximately side view) and the respective spin densities (isosurface value 0.003 a.u.; approximately top view) of a) $[NiDPP]^{\bullet+}$ and b) $[NiP_3P]^{\bullet+}$ radical cations (side view). Hydrogen atoms omitted for clarity.

The actual symmetry of the spin density in the π radical (a_{1u} or a_{2u} in the idealised D_{4h} symmetry point group) is often ambiguous as well due to static and/or dynamic pseudo-Jahn–Teller effects which mix these states by appropriate vibrational modes.[42] According to the DFT calculations, $[NiDPP]^{\bullet+}$ features spin density at the *meso* positions (approximate a_{2u} symmetry), and $[NiP_3P]^{\bullet+}$ shows spin density at the pyrrole rings and nodal planes at the *meso* positions (approximate a_{1u} symmetry) at this level of theory (Figure 6). In fact, both descriptions may contribute to the true electronic structure of the π radical cations due to vibrationally induced mixing of the states. Considering the Jahn–Teller bistability of nickel porphyrin radical cations, spin density could be present at both *meso* and β positions of the radical cations and affect also the distribution of electrophilic sites within the macrocycle. Consequently, both sites are amenable to nucleophilic attack, that is, by a neutral nickel porphyrin with its *meso* positions having large orbital coefficients in the HOMO (a_{2u} symmetry; Supporting Information, Figure S5). Hence, both initial connections, β–*meso* and *meso*–*meso*, can in principle form. On oxidation with tris(4-bromophenyl)aminium hexachloroantimonate, NiDPP forms *meso*–β links in $CHCl_3$ (among other products),[17] while NiP_3P is reported to form both *meso*–β and *meso*–*meso* links.[14,17] In fact, the solvent/oxidant combination influences the *meso*–β/*meso*–*meso* link ratio.[14,17] We suggest that oxidant and environment may influence the actual spin density of the radical cations $[NiDPP]^{\bullet+}$ and $[NiP_3P]^{\bullet+}$ and consequently the regioselectivity of the initial C–C bond-forming reaction. The electron-deficient pyrrole rings of the radical cations might also be amenable to nucleophilic attack by the phenyl substituents leading to the intramolecular cyclisation. Such intramolecular dehydrogenative coupling reactions might be preferred under oCVD conditions, that is, in the gas phase, and by reactions of less-mobile porphyrins on the substrate surface.

Beyond the polymerization process, the observed diverse reactivity of nickel porphyrins in oCVD processes with $FeCl_3$ includes chlorination by highly reactive oxidants such as Cl_2 in the gas phase, formation of β–β linkages to form oligomers from NiP_3P and intramolecular cyclisation enabled by high dilution (gas phase), low mobility (surface) and the presence of strong oxidants (Cl_2).

Conclusion

The oCVD reaction of nickel(II) porphyrins with $FeCl_3$ requires free *meso* positions to form conjugated polyporphyrins. The first step in the polymerisation reaction is the one-electron oxidation of nickel(II) porphyrins to the respective π radical cations coordinated to nickel(II). In the gas phase and in non-coordinating solvents, the nickel(III) porphyrin isomer is less favourable. The pseudo-Jahn–Teller distortion of the π radical cations mixes states with different symmetry (a_{1u} and a_{2u}), and this allows for nucleophilic attack of the electron-rich *meso* position of neutral nickel(II) porphyrins at both the β and *meso* positions of the radical cations. This leads to both *meso*–β and *meso*–*meso* linkages in the growing polymer and gives doubly and triply linked units after further dehydrogenative coupling.

Compared to conventional solution-based methods, which mainly yield doubly and triply linked oligoporphyrins, the oCVD process of nickel(II) porphyrins and $FeCl_3$ shows an even broader reactivity pattern, including polymer formation, chlorination, formation of single β–β linkages and intramolecular

cyclisation. The diverse reactivity in the oCVD process is explained by the presence of chlorinating agents, the low porphyrin concentration in the gas phase and the low mobility on the substrate surface.

In addition to glass or silicon wafers as substrates, the reported oCVD process is also compatible with transparent, thermally stable[43] plastic foils (PEN). This could lead to the design of a new family of flexible optoelectronic devices thanks to the combination of the optical, electric and mechanical properties of the fused porphyrin thin films. Finally, the oxidant WCl_6[34,36,44] can also be used in the oxidative coupling of nickel porphyrins in solution and possibly also in oCVD processes.

Experimental Section

Materials

(5,15-Diphenylporphyrinato)nickel(II) (NiDPP) and (5,10,15,20-tetraphenylporphyrinato)nickel(II) (NiTPP) were prepared by metallation of 5,15-diphenylporphyrin (PorphyChem, 98%) (H_2DPP) and 5,10,15,20-tetraphenylporphyrin (PorphyChem, 98%), (H_2TPP), respectively, with $Ni(OAc)_2{\cdot}4H_2O$.[45] (5,10,15-Triphenylporphyrinato)-nickel(II) (NiP_3P) was obtained from PorphyChem and used without further purification (98%). Iron(III) chloride (97%; Sigma-Aldrich) and tungsten hexachloride (99.9%; ABCR) were used without further purification. Dichloromethane for EPR measurements was dried with CaH_2 and distilled prior to use.

oCVD experiments

oCVD experiments were performed in a custom-built oCVD reactor as described elsewhere.[20] The deposition experiments were carried out in argon (Air Liquide, 99.999%) at a pressure of 10^{-3} mbar. The evaporators, located at the bottom of the reaction chamber, were loaded with 10 mg of porphyrins and 150 mg of $FeCl_3$ and heated to 250 and 170 °C, respectively. The substrate holder, oriented face-down, was maintained at 130 °C. The deposition time was 30 min in all experiments. Microscope glass slides, silicon wafers and 125 μm PEN[43] foils (DuPont Teijin Films) were used as substrates.

Spectroscopy and film characterization

The optical absorbance of the films was measured in the range of 250–2000 nm with a UV/Vis/NIR spectrophotometer (PerkinElmer, Lambda 950) with a 150 mm-diameter integrating sphere. The absorption spectra were recorded directly on the glass substrates before and after rinsing the glass with dichloromethane and acetone. UV/Vis/NIR spectra of the soluble fractions of the coating in acetone or CH_2Cl_2 were measured in quartz cuvettes of 3.5 mL and 1 cm path length. The thin films thicknesses were measured using a KLA-Tencor P-17 Stylus profiler. Cyclic voltammetric measurements were carried out with a BioLogic SP-50 voltammetric potentiostat 1 mM in CH_2Cl_2 containing 0.1 M $[nBu_4N][PF_6]$ as supporting electrolyte with a platinum working electrode, a platinum wire as counter electrode and a 0.01 M $Ag/AgNO_3$ reference electrode. Cyclic voltammograms were recorded at 100 mV s^{-1} scan rate. Ferrocene was employed as an internal reference redox system. X-band CW EPR spectra were recorded with a Magnettech MS 300 spectrometer and a Hewlett Packard 5340A frequency counter at a microwave frequency of 9.39 GHz in CH_2Cl_2 solution (298 and 77 K). Mn^{2+} in ZnS was used as external standard ($g = 2.118$, 2.066, 2.027, 1.986, 1.946, 1.906). Atmospheric-pressure LDI-HRMS was employed for characterisation of the coatings. HRMS analyses were performed with an LTQ/Orbitrap Elite Hybrid Linear Ion Trap-Orbitrap Mass Spectrometer from Thermo Scientific (San Jose, CA) coupled with an AP-LDI (ng) UHR source from MassTech Inc (Columbia, MA) with a 355 nm Nd:YAG laser. The thin films were directly probed without any matrix deposition by the laser following a spiral motion during 30 s per sample. An in-source decay (ISD) of 70 V was applied to the samples in order to prevent any formation of non-covalent porphyrin clusters that could interfere with the distribution of the oligomers. A maximum injection time of 800 ms and a resolving power of 240000 at m/z 400 in the normal mass range (m/z 300–2000) and the high mass range (m/z 1800–4000) were employed for the HRMS analyses. The solution prepared for EPR analysis was studied by HR-MALDI mass spectrometry by using α-cyano-4-hydroxycinnamic acid as matrix.

Preparation of EPR samples

In an EPR tube, 0.5 mL of a 10^{-3} M CH_2Cl_2 solution of NiDPP was treated with 0.7 mL of a 10^{-3} M CH_2Cl_2 solution of WCl_6 under inert atmosphere. The solution was rapidly frozen by immersing the tube in liquid nitrogen. X-band EPR: $g_{av} = 2.004$ (77 K); $g_{iso} = 2.007$ (298 K); MALDI-HRMS (α-cyano-4-hydroxycinnamic acid): m/z = 518.103 $[M]^{\bullet+}$, 1030.160 $[M_2-6H]^{\bullet+}$, 1032.176 $[M_2-4H]^{\bullet+}$, 1542.217 $[M_3-12H]^{\bullet+}$, 1544.233 $[M_3-10H]^{\bullet+}$, 1546.252 $[M_3-8H]^{\bullet+}$; UV/Vis/NIR: λ_{max} = 478, 615, 736, 888 nm.

DFT calculations

DFT calculations were performed with the ORCA program package (Version 4.0.1).[46] All calculations were carried out by using the BP86[47,48] functional in combination with the D3[49,50] dispersion correction and the RIJCOX[51,52] approximation. A conductor-like screening solvation model (CPCM) modelling CH_2Cl_2 was used for the calculations unless noted otherwise.[53] Relativistic effects were included with the zeroth-order regular approximation (ZORA) level.[54] Geometry optimisations were performed by means of Ahlrichs' triple zeta valence basis set def2-TZVP[55–57] and Weigend's auxiliary basis set.[58] The optimised geometries were confirmed to be local minima on the respective potential energy surface by numerical frequency analyses that showed the absence of negative frequencies. Explicit counterions and/or solvent molecules were not taken into account.

Acknowledgements

We gratefully acknowledge the financial support of the Luxembourg National Research Fund (http://fnr.lu) through the POLYPORPH project (C15/MS/10340560/POLYPORH/Boscher). D. El Assad from LIST is acknowledged for insightful discussions and acquisition of the mass spectra. Parts of this research were conducted using the supercomputer MOGON and advisory services offered by Johannes Gutenberg University of Mainz (http://www.hpc.uni-mainz.de), which is a member of the AHRP and the Gauss Alliance e.V..

Conflict of interest

The authors declare no conflict of interest.

Keywords: chemical vapor deposition · nickel · polymerization · porphyrins · thin films

[1] J. Kesters, P. Verstappen, M. Kelchtermans, L. Lutsen, D. Vanderzande, W. Maes, *Adv. Energy Mater.* **2015**, *5*, 1500218.
[2] S. Mathew, A. Yella, P. Gao, R. Humphry-Baker, B. F. E. Curchod, N. Ashari-Astani, I. Tavernelli, U. Rothlisberger, M. K. Nazeeruddin, M. Grätzel, *Nat. Chem.* **2014**, *6*, 242 – 247.
[3] S. Lin, C. S. Diercks, Y.-B. Zhang, N. Kornienko, E. M. Nichols, Y. Zhao, A. R. Paris, D. Kim, P. Yang, O. M. Yaghi, C. J. Chang, *Science* **2015**, *349*, 1208 – 1213.
[4] a) W. Zhang, W. Lai, R. Cao, *Chem. Rev.* **2017**, *117*, 3717 – 3797; b) Y. Liu, Y. Han, Z. Zhang, W. Zhang, W. Lai, Y. Wang, R. Cao, *Chem. Sci.* **2019**, *10*, 2613 – 2622; c) B. L. Wadsworth, D. Khusnutdinova, G. F. Moore, *J. Mater. Chem. A* **2018**, *6*, 21654 – 21665; d) K. Rybicka-Jasińska, W. Shan, K. Zawada, K. M. Kadish, D. Gryko, *J. Am. Chem. Soc.* **2016**, *138*, 15451 – 15458.
[5] a) Y. Ding, W.-H. Zhu, Y. Xie, *Chem. Rev.* **2017**, *117*, 2203 – 2256; b) N. A. Rakow, K. S. Suslick, *Nature* **2000**, *406*, 710 – 713; c) P. Heier, N. D. Boscher, P. Choquet, K. Heinze, *Inorg. Chem.* **2014**, *53*, 11086 – 11095.
[6] S. Singh, A. Aggarwal, N. V. S. D. K. Bhupathiraju, G. Arianna, K. Tiwari, C. M. Drain, *Chem. Rev.* **2015**, *115*, 10261 – 10306.
[7] A. Tsuda, A. Osuka, *Science* **2001**, *293*, 79 – 82.
[8] M. Pawlicki, H. A. Collins, R. G. Denning, H. L. Anderson, *Angew. Chem. Int. Ed.* **2009**, *48*, 3244 – 3266; *Angew. Chem.* **2009**, *121*, 3292 – 3316.
[9] M. O. Senge, M. Fazekas, E. G. A. Notaras, W. J. Blau, M. Zawadzka, O. B. Locos, E. M. Ni Mhuircheartaigh, *Adv. Mater.* **2007**, *19*, 2737 – 2774.
[10] D. Khusnutdinova, B. L. Wadsworth, M. Flores, A. M. Beiler, E. A. R. Cruz, Y. Zenkov, G. F. Moore, *ACS Catal.* **2018**, *8*, 9888 – 9898.
[11] N. Yoshida, N. Aratani, A. Osuka, *Chem. Commun.* **2000**, 197 – 198.
[12] B. J. Brennan, J. Arero, P. A. Liddell, T. A. Moore, A. L. Moore, D. Gust, *J. Porphyrins Phthalocyanines* **2013**, *17*, 247 – 251.
[13] A. K. Sahoo, Y. Nakamura, N. Aratani, K. S. Kim, S. B. Noh, H. Shinokubo, D. Kim, A. Osuka, *Org. Lett.* **2006**, *8*, 4141 – 4144.
[14] C.-M. Feng, Y.-Z. Zhu, S.-C. Zhang, Y. Zang, J.-Y. Zheng, *Org. Biomol. Chem.* **2015**, *13*, 2566 – 2569.
[15] L. M. Jin, L. Chen, J. J. Yin, C. C. Guo, Q. Y. Chen, *Eur. J. Org. Chem.* **2005**, 3994 – 4001.
[16] K. Sugiura, T. Matsumoto, S. Ohkouchi, Y. Naitoh, T. Kawai, Y. Takai, K. Ushiroda, Y. Sakata, *Chem. Commun.* **1999**, 1957 – 1958.
[17] A. Tsuda, A. Nakano, H. Furuta, H. Yamochi, A. Osuka, *Angew. Chem. Int. Ed.* **2000**, *39*, 558 – 561; *Angew. Chem.* **2000**, *112*, 572 – 575.
[18] A. Tsuda, Y. Nakamura, A. Osuka, *Chem. Commun.* **2003**, 1096 – 1097.
[19] B. J. Brennan, M. J. Kenney, P. A. Liddell, B. R. Cherry, J. Li, A. L. Moore, T. A. Moore, D. Gust, *Chem. Commun.* **2011**, *47*, 10034 – 10036.
[20] G. Bengasi, K. Baba, G. Frache, J. Desport, P. Gratia, K. Heinze, N. D. Boscher, *Angew. Chem. Int. Ed.* **2019**, *58*, 2103 – 2108; *Angew. Chem.* **2019**, *131*, 2125 – 2130.
[21] M. Wang, X. Wang, P. Moni, A. Liu, D. H. Kim, W. J. Jo, H. Sojoudi, K. K. Gleason, *Adv. Mater.* **2017**, *29*, 1604606.
[22] M. Wang, N. D. Boscher, K. Heinze, K. K. Gleason, *Adv. Funct. Mater.* **2017**, *27*, 1606652.
[23] N. D. Boscher, W. Minghui, A. Perrotta, K. Heinze, M. Creatore, K. K. Gleason, *Adv. Mater.* **2016**, *28*, 7479 – 7485.
[24] K. M. Kadish, K. M. Smith, R. Guillard, *The Porphyrin Handbook: Inorganic, Organometallic and Coordination Chemistry, Vol. 3*, Academic Press, London, **2000**.
[25] *CRC Handbook of Chemistry and Physics*, 92nd ed. (Ed.: W. M. Haynes), CRC, Boca Raton, **2011**.
[26] M. H. Gharahcheshmeh, K. K. Gleason, *Adv. Mater. Interfaces* **2019**, *6*, 1801564.
[27] T. Wijesekera, A. Matsumoto, D. Dolphin, D. Lexa, *Angew. Chem. Int. Ed. Engl.* **1990**, *29*, 1028 – 1030; *Angew. Chem.* **1990**, *102*, 1073 – 1074.
[28] a) T. Ishizuka, Y. Saegusa, Y. Shiota, K. Ohtake, K. Yoshizawa, T. Kojima, *Chem. Commun.* **2013**, *49*, 5939 – 5941; b) P. Chen, Y. Fang, K. M. Kadish, J. P. Lewtak, D. Koszelewski, A. Janiga, D. T. Gryko, *Inorg. Chem.* **2013**, *52*, 9532 – 9538; c) Y. Fang, D. Koszelewski, K. M. Kadish, D. T. Gryko, *Chem. Commun.* **2014**, *50*, 8864 – 8867.
[29] Y. Saegusa, T. Ishizuka, K. Komamura, S. Shimizu, H. Kotani, N. Kobayashi, T. Kojima, *Phys. Chem. Chem. Phys.* **2015**, *17*, 15001 – 15011.
[30] T. Tanaka, A. Osuka, *Chem. Soc. Rev.* **2015**, *44*, 943 – 969.
[31] L. E. Wilson, N. W. Gregory, *J. Phys. Chem.* **1958**, *62*, 433 – 437.
[32] J. P. Lewtak, D. Gryko, D. Bao, E. Sebai, O. Vakuliuk, M. Ścigaj, D. T. Gryko, *Org. Biomol. Chem.* **2011**, *9*, 8178 – 8181.
[33] M. Schubert, J. Leppin, K. Wehming, D. Schollmeyer, K. Heinze, S. R. Waldvogel, *Angew. Chem. Int. Ed.* **2014**, *53*, 2494 – 2497; *Angew. Chem.* **2014**, *126*, 2527 – 2530.
[34] M. W. Chase, Jr., C. A. Davies, J. R. Downey, Jr., D. J. Frurip, R. A. McDonald, A. N. Syverud, *J. Phys. Chem. Ref. Data* **1985**, *14*, 903.
[35] J. Seth, V. Palaniappan, D. F. Bocian, *Inorg. Chem.* **1995**, *34*, 2201 – 2206.
[36] J. W. Herndon, M. E. Jung, *Encyclopedia of Reagents for Organic Synthesis*, Wiley, Hoboken, **2007**.
[37] J. Leppin, M. Schubert, S. R. Waldvogel, K. Heinze, *Chem. Eur. J.* **2015**, *21*, 4229 – 4232.
[38] T. Horibe, S. Ohmura, K. Ishihara, *J. Am. Chem. Soc.* **2019**, *141*, 1877 – 1881.
[39] D. Dolphin, T. Niem, R. H. Felton, I. Fujita, *J. Am. Chem. Soc.* **1975**, *97*, 5288 – 5290.
[40] D. Chatterjee, E. Balasubramanian, *J. Coord. Chem.* **1999**, *46*, 467 – 470.
[41] A. Wolberg, J. Manassen, *Inorg. Chem.* **1970**, *9*, 2365 – 2367.
[42] R. S. Czernuszewicz, K. A. Macor, X. Y. Li, J. R. Kincaid, T. G. Spiro, *J. Am. Chem. Soc.* **1989**, *111*, 3860 – 3869.
[43] L. D. Lillwitz, *Appl. Catal. A* **2001**, *221*, 337 – 358.
[44] M. Bortoluzzi, F. Marchetti, G. Pampaloni, C. Pinzino, S. Zacchini, *Inorg. Chem.* **2016**, *55*, 887 – 893.
[45] S. A. Yao, C. B. Hansen, J. F. Berry, *Polyhedron* **2013**, *58*, 2 – 6.
[46] F. Neese, *Wiley Interdiscip. Rev. Comput. Mol. Sci.* **2012**, *2*, 73 – 78.
[47] A. D. Becke, *Phys. Rev. A* **1988**, *38*, 3098 – 3100.
[48] J. P. Perdew, *Phys. Rev. B* **1986**, *33*, 8822 – 8824.
[49] S. Grimme, J. Antony, S. Ehrlich, H. Krieg, *J. Chem. Phys.* **2010**, *132*, 154104.
[50] S. Grimme, S. Ehrlich, L. Goerigk, *J. Comput. Chem.* **2011**, *32*, 1456 – 1465.
[51] F. Neese, F. Wennmohs, A. Hansen, U. Becker, *Chem. Phys.* **2009**, *356*, 98 – 109.
[52] R. Izsák, F. Neese, *J. Chem. Phys.* **2011**, *135*, 144105.
[53] V. Barone, M. Cossi, *J. Phys. Chem. A* **1998**, *102*, 1995 – 2001.
[54] D. A. Pantazis, X.-Y. Chen, C. R. Landis, F. Neese, *J. Chem. Theory Comput.* **2008**, *4*, 908 – 919.
[55] F. Weigend, R. Ahlrichs, *Phys. Chem. Chem. Phys.* **2005**, *7*, 3297.
[56] A. Schäfer, H. Horn, R. Ahlrichs, *J. Chem. Phys.* **1992**, *97*, 2571 – 2577.
[57] A. Schäfer, C. Huber, R. Ahlrichs, *J. Chem. Phys.* **1994**, *100*, 5829 – 5835.
[58] F. Weigend, *Phys. Chem. Chem. Phys.* **2006**, *8*, 1057 – 1065.

Manuscript received: February 20, 2019
Revised manuscript received: March 22, 2019
Accepted manuscript online: April 2, 2019
Version of record online: May 24, 2019

5.4 Molecular Flattening Effect to Enhance the Conductivity of Fused Porphyrin Tapes Thin Films

Giuseppe Bengasi, Jessica S. Desport, Kamal Baba, João P. Cosas Fernandes, Olivier De Castro, Katja Heinze, Nicolas D. Boscher

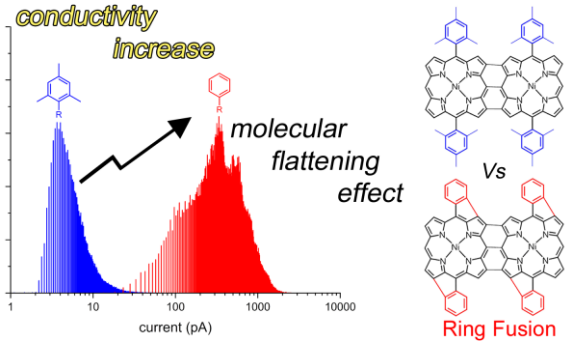

The oCVD of porphyrins allows the straightforward formation of porphyrin tapes films without solubilizing agents. This make possible studying the conductivity of porphyrin tapes films according to their substituent. We observed that the flattening of the *meso* substituents improves the film conductivity of several orders of magnitude.

Authors contributions

Giuseppe Bengasi performed the deposition experiments with contribution from Kamal Baba. Giuseppe Bengasi performed the DFT calculations. Jessica Desport performed GPC analysis, Joao Paulo Cosas Fernandes the C-AFM analysis and Olivier de Castro acquired the HIM images. Giuseppe Bengasi made the interpretation of the results with contributions of all co-authors. Giuseppe Bengasi wrote the manuscript with contribution from Katja Heinze and Nicolas Boscher.

Supporting Information

Supporting information can be found at page 130.

Reprinted from permission from:

Giuseppe Bengasi, Jessica S. Desport, Kamal Baba, Joao P. Cosas Fernandes, Olivier De Castro, Katja Heinze and Nicolas D. Boscher, *RSC Adv.,* **10**, 7048-7057

RSC Advances

ROYAL SOCIETY OF CHEMISTRY

PAPER

View Article Online
View Journal | View Issue

Check for updates

Cite this: *RSC Adv.*, 2020, **10**, 7048

Molecular flattening effect to enhance the conductivity of fused porphyrin tape thin films†

Giuseppe Bengasi,[ab] Jessica S. Desport,[a] Kamal Baba,[a] João P. Cosas Fernandes,[a] Olivier De Castro,[a] Katja Heinze *[b] and Nicolas D. Boscher *[a]

Received 20th November 2019
Accepted 7th February 2020

DOI: 10.1039/c9ra09711b

rsc.li/rsc-advances

The straightforward synthesis of directly fused porphyrins (porphyrin tapes) from 5,15-diphenyl porphyrinato nickel(II) complexes with different substituents on the phenyl rings is achieved while processing from the gas phase. The porphyrin tapes, exhibiting NIR absorption, are readily obtained in thin film form. The gas phase approach cuts the need for solubilizing groups allowing for the first time the study of their conductivity according to the substituent. 2-Point probe and conductivity AFM measurements evidence that reducing the size of the *meso* substituents, phenyl < mesityl < di(3,5-*tert*-butyl)phenyl < di(2,6-dodecyloxy)phenyl, improves the thin film conductivity by several orders of magnitude. Density functional theory and gel permeation chromatography, correlate this improvement to changes in the intermolecular distances and molecular geometry. Furthermore, the oCVD of porphyrins with free *ortho*-phenyl positions causes intramolecular dehydrogenative side reactions inducing a complete planarization of the molecule. This molecular flattening drastically affects the π–π stacking between the porphyrins further enhancing the electronic properties of the films.

Introduction

Porphyrins are versatile compounds that are used in a broad range of applications such as catalysis,[1–7] photovoltaics[8–10] or photodynamic therapy.[11–14] They have fascinating optical and electronic properties, which can be tuned by structural modifications affecting electronic and steric properties.[15–18] Particularly, the extension of the porphyrin π-system plays an important role in the enhancement of their optical properties yielding NIR absorbers.[19–23] One application of these materials is the production of bulk heterojunction solar cells.[24]

The extension of the porphyrin π-conjugation generally increases the absorption in the Q-band region and widens the fraction of the solar spectrum that can be used for the conversion of energy.[24] The direct fusion of porphyrinic cores with free *β* and *meso* positions into conjugated polymers further pushes the optoelectronic boundaries of the porphyrins yielding chromophores with very low HOMO–LUMO gaps (oligomers) or bandgaps (polymers) reaching the infrared region.[16] These highly conjugated porphyrin-based systems exhibit interesting chemical and physical properties such as two-photon absorption,[25] increased electro-catalytic activities,[5] low conductance attenuation factors[26,27] and switchable carrier species in liquid crystalline semiconductors.[28]

The unique properties of fused porphyrins fostered the development of a wide series of synthetic strategies aiming to obtain directly fused porphyrins (porphyrin tapes) (Scheme 1). The main synthetic route towards directly fused porphyrins involves the solution-based dehydrogenative coupling of metalloporphyrins with transition metal salts such as AgX,[29] CuX_2,[30,31] FeX_3,[32] WCl_6 [33] or organic oxidants such as $[(p\text{-}Br\text{-}C_6H_4)_3N][SbCl_6]$,[34] or a mixture of 2,3-dichloro-5,6-dicyano-1,4-benzoquinone and $Sc(OTf)_3$.[16] Solution-based methods have enabled the preparation of fused porphyrin tapes from several metalloporphyrin complexes such as zinc(II), nickel(II), palladium(II) and copper(II).[16,30,35,36] However, porphyrinoids, and more particularly π-extended porphyrins, usually experience very low solubility and solubilizing substituents are required to allow both their synthesis and integration into optoelectronic devices.

Although the introduction of substituents such as long alkyl chains increases the solubility and hence processability of such planar chromophores, their effect on π–π stacking adversely affects the device performance.[24,37] Fused porphyrin tapes require side chains to retain the solubility necessary to achieve high degree of polymerization.[29] The difficult processability, strongly dependent on the substituents, of porphyrin tapes in thin film form has hindered the study of the electrical properties of the bulk materials and their application in advanced devices. We recently developed a gas phase approach for the

[a]*Materials Research and Technology, Luxembourg Institute of Science and Technology (LIST), 5 Avenue des Hauts-Fourneaux, L-4362 Esch/Alzette, Luxembourg. E-mail: nicolas.boscher@list.lu*

[b]*Institute of Inorganic Chemistry and Analytical Chemistry, Johannes Gutenberg University of Mainz, Duesbergweg 10-14, 55128 Mainz, Germany. E-mail: Katja.heinze@uni-mainz.de*

† Electronic supplementary information (ESI) available. See DOI: 10.1039/c9ra09711b

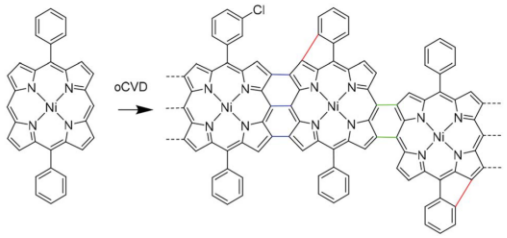

Scheme 1 oCVD reaction for NiDPP. The products are characterized by the incorporation of chlorine (the position of the Cl atom in the structure is merely representative). We also observed double (green) and triple (blue) links between the monomer units and the dehydrogenative cyclization of the phenyl substituent and the porphyrin macrocycle (red).

simultaneous synthesis and deposition of fused porphyrin thin films.[38] This approach relies on the oxidative chemical vapour deposition (oCVD)[39,40] reaction of porphyrins with free *meso* and *β* positions using a suitable volatile oxidant (preferentially $FeCl_3$) for dehydrogenative coupling. The oCVD technique is been mainly used for the synthesis of poly(3,4-ethylenedioxythiophene) (PEDOT)[41–43] and polyaniline (PANI)[44] finding application in organic electronics,[45] volatile compound detectors[46–48] and supercapacitors.[49,50]

Furthermore, the oxidant acts as doping agent directly yielding conductive thin films on virtually any substrates including sensitive substrates such as paper and polymers.[38] In addition of allowing the deposition of patterned, smooth and thickness-controlled fused porphyrin thin films, this oCVD approach does not require solubilizing substituents. Consequently, substituents can be used to implement advanced functionalities in the material beyond mere solubility.

In contrast to solution-based approaches, further dehydrogenative couplings (loss of 2H) were detected in both the porphyrin units and fused porphyrin oligomers as evidenced by laser desorption ionisation high-resolution mass spectrometry (LDI-HRMS).[33] Cyclization of phenyl rings on the porphyrin macrocycle accounts for these coupling reactions (Scheme 1). The $Cl_{2(g)}$ produced during the reaction leading to a second oxidation of the porphyrin could account for this reaction.[33,51,52] The fusion of aromatic rings on the porphyrin core was already observed in presence of iron oxidants, yet electron-donating groups on the phenyl rings are usually required.[20,21,53] However, so far the poor solubility of the oligomeric and polymeric products of the oCVD process hindered an unequivocal assignment and a proper characterization of the cyclization reaction.

In this study, we investigate the intramolecular cyclization reaction in the fused porphyrin thin films obtained *via* oCVD, their impact on the π–π stacking interactions and the resulting effect on conductivity. To this end, 5,15-diphenyl porphyrinato nickel(II) complexes with different substituents on the phenyl rings were employed in the oCVD process, namely 5,15-(diphenyl) porphyrinato nickel(II) (**NiDPP**), 5,15-(di-3,5-di-*tert*-butylphenyl) porphyrinato nickel(II) (**NiD*t*-BuPP**), 5,15-(dimesityl)porphyrinato nickel(II) (**NiDMP**) and 5,15-(di-2,6-dodecyloxyphenyl) porphyrinato nickel(II) (**NiDDOPP**) (Scheme 2). Nickel(II) complexes were chosen due to the already proven high stability of the Ni^{2+} in the porphyrin core during the oCVD process.[33,38,54] **NiDPP** and **NiD*t*-BuPP** possess free *ortho* positions on the phenyl rings, potentially allowing an intramolecular cyclization reaction. In **NiDMP** and **NiDDOPP** these positions are blocked preventing intramolecular dehydrogenative coupling reactions. Furthermore, the size of the porphyrin substituent R increases in the order phenyl < mesityl < di(*tert*-butyl)phenyl < di(alkoxy)phenyl in **NiDPP**, **NiDMP**, **NiD*t*-BuPP** and **NiDDOPP**, respectively. This steric aspect likely affects the intermolecular π–π stacking interaction in oCVD films. Finally, the substituents should modify the electronic properties, especially the redox potential for the Ni(P)/$[Ni(P)]^{+\cdot}$ oxidation of the monomer, which initiates the intra- and intermolecular dehydrogenative coupling reactions of the nickel porphyrins.[33,34]

Hence, steric and electronic effects on the resulting film properties (absorptivity, homogeneity, morphology and conductivity) imposed by the substituents are addressed employing High Resolution Mass Spectrometry (HRMS), Gel Permeation Chromatography (GPC), UV/Vis/NIR spectroscopy, 2-point probe *I*/*V* measurements, Conductive Atomic Force Microscopy (C-AFM) and Helium Ion Microscopy (HIM). Furthermore, Density Functional Theory (DFT) calculations on pairs of nickel porphyrins with different *meso* substituents deliver information on the conceivable porphyrin–porphyrin interactions in the film. Finally, we correlate the obtained structural information on the oCVD films to their conductivity.

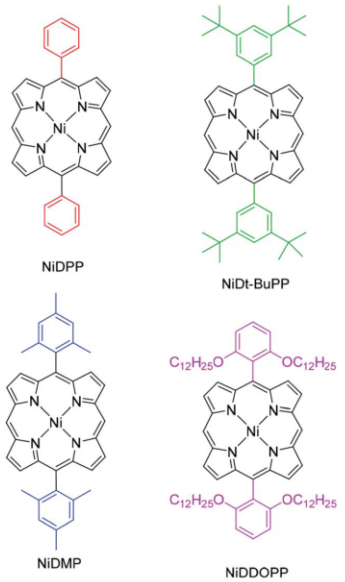

Scheme 2 Structure of the porphyrins employed in the experiments.

Results and discussion

Prior to sublimation under oxidative conditions, the thermal stability of each porphyrin was controlled by thermogravimetry (Fig. S1†). All the porphyrins are thermally stable up to at least 300 °C confirming their suitability for oCVD processing. The first oxidation potentials of **NiDPP**, **NiDMP**, **NiDD*t*-BuPP** and **NiDDOPP** were determined by cyclic voltammetry in CH_2Cl_2/$[^nBu_4N][PF_6]$ solution as E_p = 0.57, 0.60, 0.55 and 0.50 V *versus* ferrocene, respectively (Fig. S2†). This demonstrates the influence of the *meso* substituents on the potential of the Ni(P)/$[Ni(P)]^{\bullet+}$ redox couple. Particularly, a strong effect is observed for the **NiDDOPP** showing the lower value in the series thanks to the mesomeric effect of the two alkoxy substituents on the phenyl rings. In a custom built reactor (Fig. S3†),[38] we performed the oCVD reaction of the differently substituted nickel porphyrins using $FeCl_3$ as oxidant and silicon wafers or microscope slides as substrates for the deposition of the films. For the sake of comparison, the porphyrin/oxidant molar ratio was kept constant for each deposition varying the sublimation temperature of the porphyrin (Table S1 ESI†). The thickness of the oCVD coatings was 169, 520, 355 and 560 nm for **NiDPP**, **NiDMP**, **NiDD*t*-BuPP** and **NiDDOPP**, respectively, according to profilometry (Table S2†). All oCVD coatings exhibit a clearly visible colour change when compared to the reference coatings obtained from mere sublimation of the respective monomer (Fig. S4†). The sublimed reference coatings are pink (**NiDDOPP**), orange (**NiDMP** and **NiDPP**) and yellow (**NiD*t*-BuPP**), while all oCVD coatings exhibit a green, intense coloration. This is consistent with previous studies on oCVD polymerization of porphyrins[33,38,54] hinting to retention of the porphyrin macrocycle upon sublimation and oxidative dehydrogenation and polymerization. The colour changes are also reflected in the UV/Vis/NIR spectra (Fig. 1). All oCVD films absorb up to the NIR region as expected by fused porphyrin tapes. **NiDPP** and **NiD*t*-BuPP** exhibit a significant broadening of the absorption in the Soret band region (Fig. 1a and b). As we already observed, this is consistent with the formation of fused porphyrins with intramolecular dehydrogenative cyclizations (Scheme 1) causing a redshift of the Soret band and, consequently, a general broadening of the spectrum.[38,54–56] Differently, the oCVD film of the mesityl derivative **NiDMP** shows several well defined absorption bands between 800 nm and 1500 nm in addition to a weakly broadened Soret band. This points to the formation of oligomers/polymers lacking intramolecular dehydrogenative cyclizations which is rationalized by the blocked *ortho* positions of the mesityl substituents. Similarly, **NiDDOPP** lacks free *ortho* positions on the phenyl ring preventing the cyclization. Consequently, the **NiDDOPP** oCVD film exhibits well-defined Soret bands. Unexpectedly, the Soret band of the **NiDDOPP** oCVD coating is red-shifted from 407 to 448 nm. This bathochromic shift might be related to ring chlorination of the porphyrin[57] or to a further coupling of the aryl rings (see below).

The **NiDPP** oCVD coating is insoluble contrarily to **NiDMP** and **NiD*t*-BuPP** oCVD coatings thanks to their solubilizing substituents (Fig. S5†). Surprisingly, even with the long alkoxy substituents, the **NiDDOPP** oCVD coating, is completely insoluble in THF or toluene even at boiling temperatures. This indicates a particularly high degree of polymerization or a high degree of chlorination of the polymer (*cf.* red-shift of Soret bands) that is known to significantly reduce the solubility of the porphyrins.[58] Furthermore, alkoxy substituted aryl groups are quite electron rich and easy to oxidize (see above). Consequently, biaryl formation between $OC_{12}H_{25}$-substituted aryl groups (Scheme S2†) is conceivable and has been observed with simpler OCH_3 substituted arenes, *e.g.* using molybdenum(v) oxidants or iron(iii) chloride.[59–63] This additional intermolecular

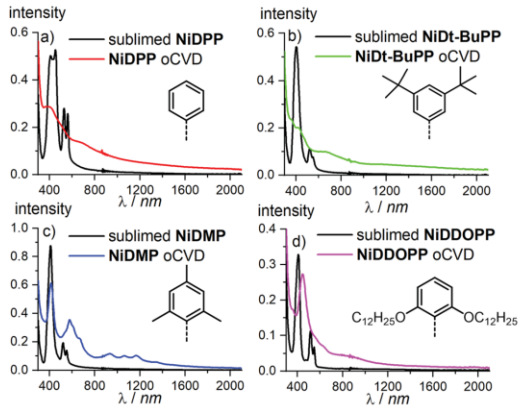

Fig. 1 UV/VIS/NIR spectra of (a) **NiDPP**, (b) **NiD*t*-BuPP**, (c) **NiDMP** and (d) **NiDDOPP** oCVD coatings and their respective references.

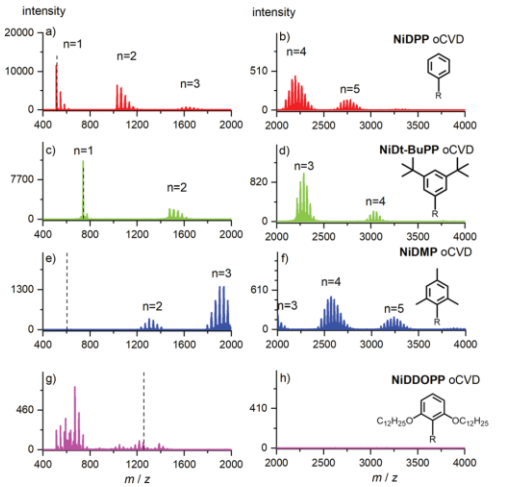

Fig. 2 LDI-HRMS of the (a and b) **NiDPP** (c and d) **NiD*t*BuPP** (e and f) **NiDMP** (g and h) **NiDDOPP** oCVD coatings. The expected mass of the monomer is evidenced from the dashed line. Ions are detected as radical cations $[M]^{\bullet+}$. Two scan events were used to acquire spectra within a broad mass range (400–2000 and 2000–4000 *m*/*z*).

C–C coupling *via* the aryl substituents might lead to cross-linking of the porphyrin oligomers and polymers thus reducing their solubility. The resulting different (biaryl) substituents furthermore could account for the shifted Soret bands of the **NiDDOPP** oCVD film.

High resolution mass spectrometry (HRMS) was used to assess both the effective oligomerization and the intramolecular ring fusion M_n–*x*2H reactions occurring during oCVD deposition. The analysis confirmed the presence of oligomers for all oCVD coatings, except for the film derived from $OC_{12}H_{25}$-substituted **NiDDOPP**. Its mass spectrum seems to only reveal low molecular weight fragments with low intensity (Fig. 2). This is consistent with the above suggested additional cross-linking *via* the alkoxy-substituted aryl substituents. Indeed samples with a high level of entanglement are well known to be rather difficult to ionize in their intact form. As a result, the energy provided by the laser most likely induces fragmentation of the chains, explaining the presence of small ions (<800 *m*/*z*), with no consistent molecular formula identification. To ensure that the absence of signal is not related to the limitation of the HRMS analyser (*m*/*z* < 4000), the range of detection was extended to high masses by performing both solvent-free MALDI-TOF and LDI-TOF without any success. This strongly supports the idea of a highly entangled/crosslinked insoluble system. In addition to polymerization, chlorination of the poly(porphyrins) is observed for **NiDPP**, **NiD*t*-BuPP** and **NiDMP** as evidenced by the family of peak distributions related to the repeating increment of a chlorine atom mass for each oligomer (Fig. 2). This reaction was known for chlorine-containing oxidants (*i.e.* $FeCl_3$, $CuCl_2$ and $Cu(ClO_4)_2 \cdot 6H_2O$)[54] in the oCVD of porphyrins.

Due to the lack of monomer and oligomer signals of the **NiDDOPP** film, the extent of chlorine incorporation is unavailable from mass spectrometry in this case. Yet, as chlorination has been observed in all cases so far using $FeCl_3$ as oxidant,[33,38,54] we suspect that this is likely also the case for **NiDDOPP** films. To confirm this idea, we performed a new oCVD deposition of **NiDDOPP** decreasing the substrate temperature to 50 °C to reduce the reactivity and avoid a deep reticulation of the system, favouring its ease of ionization *via* LDI-HRMS.

As expected, the new MS spectrum allowed the discrimination of several species. Particularly, this experiment confirmed the formation of highly chlorinated monomers and dimers singly, doubly and triply linked (Fig. S6 & S7†). Interestingly, signals related to the cleavage of one or two ether groups with subsequent formation of phenols are observed (Fig. S6 and Scheme S2†). It is not clear if this reaction is related to the laser irradiation or to the HCl formed during the oxidative polymerization.[64] All these experiments hint undeniably to a polymerization process occurring for all nickel porphyrins irrespective of the substituent.

Parts of the **NiD*t*-BuPP** and **NiDMP** oCVD coatings are sufficiently soluble allowing solution based studies. For this reason, the two oCVD coatings were investigated by Gel Permeation Chromatography coupled to Electrospray Ionization High resolution Mass Spectrometry (GPC × ESI-HRMS). As opposed to LDI, ESI ionization allows for the formation of multiply charged ions (*z* > 1), thus permitting to detect higher masses. For instance, the **NiDMP** oCVD film mass spectrum shows soluble oligomers up to a degree of polymerization of 7 (Fig. S8†). An advantage of the online GPC × ESI-HRMS analysis is the possibility to report specific *m*/*z* as function of elution time. The results are plotted in the Extracted Ion Chromatograms (EIC) (Fig. S9 and S10†). In addition to an MS coupling, the GPC analyses of the soluble samples were also combined with differential refractive index detection, which typically provides a fairly representative picture of the sample in terms of relative abundance of the species. The intensity of the unreacted monomer signal (retention time determined from the **NiDMP** and **NiD*t*-BuPP** reference chromatogram) confirms the higher conversion of **NiDMP** compared to **NiD*t*-BuPP** (Fig. 3 and 4). This might be ascribed to the absence of the intramolecular dehydrogenative cyclization in **NiDMP** and a thus preferred polymerization. Interestingly, the GPC analysis of **NiD*t*-BuPP** (Fig. 4) gives rise to an intense monomer signal (8.9 minutes)

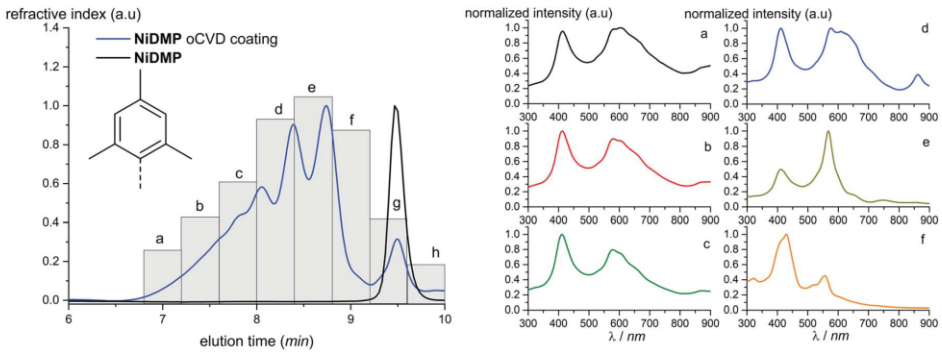

Fig. 3 Chromatogram obtained from the GPC analysis of **NiDMP**. UV-Vis spectra in the range 300–900 nm were recorded with regular time (indicated with the letters *a*–*h*). The corresponding spectra are reported on the right (*a*–*f*). The spectra of the monomeric region (*g* and *h*) are reported in the ESI.†

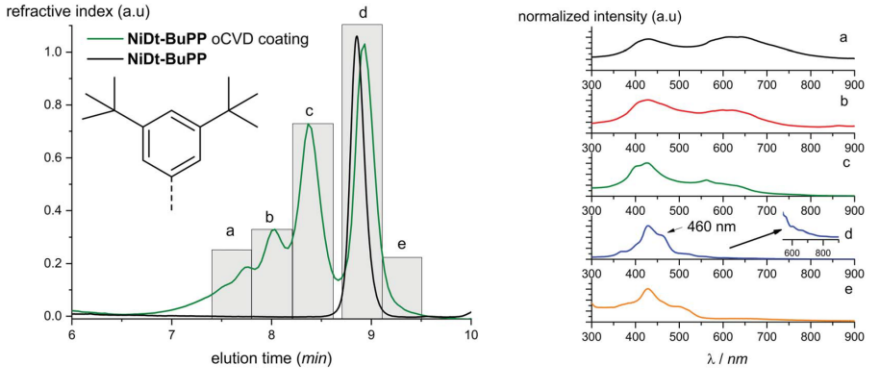

Fig. 4 Chromatogram obtained from the GPC analysis of **NiD*t*-BuPP** oCVD coating and from **NiD*t*-BuPP**. UV-Vis spectra in the range 300–900 nm were recorded with at specific time (indicated with the letters *a*–*e*). The corresponding spectra are reported on the right.

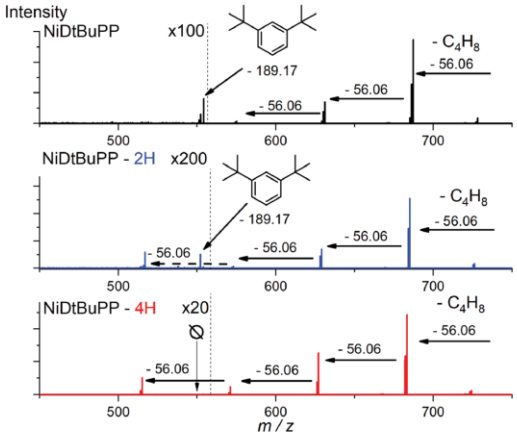

Fig. 5 Collision Induced Dissociation (CID) MS/MS analysis of **NiD*t*-BuPP** (*m*/*z* = 743.36), **NiD*t*-BuPP-2H** (*m*/*z* = 741.35) and **NiD*t*BuPP-4H** (*m*/*z* = 739.33). Normalized CID energy was set to 70. With ESI-HRMS, parent ions are detected as proton adducts $[M + H]^+$.

shifted as compared to the chromatogram of the non-polymerized reference (8.8 minutes).

Thanks to the online MS, we assigned the chromatographic peak to the protonated fused monomers **NiD*t*-BuPP-2H** (741.35 *m*/*z*) and **NiD*t*-BuPP-4H** (739.33 *m*/*z*) with elution time of 8.9 and 9.0 minutes respectively (Fig. S11†). The shift towards smaller hydrodynamic volume can be rationalized with the direct impact of the ring fusion on the molecular shape as shown by DFT calculations (see below). To undoubtedly demonstrate that the 2H elimination is related to a cyclization between the phenyl and porphyrinic ring, a structural MS/MS analysis of the ions with *m*/*z* = 743.36, 741.35 and 739.33 assigned to **NiD*t*-BuPP**, **NiD*t*-BuPP-2H** and **NiD*t*-BuPP-4H** respectively, was included in the GPC × ESI-HRMS method (Fig. 5).

Because of their new C–C bond between the phenyl substituent and the porphyrin, fused monomers are less likely to lose a phenyl ring. Indeed, while the loss of a phenyl ring is observed in the MS/MS spectra of **NiD*t*-BuPP** and **NiD*t*-BuPP-2H**, no phenyl ring is eliminated from **NiD*t*-BuPP-4H** (Fig. 5). A detailed list of the fragments is given Table S3.† Both EIC and MS/MS confirm the dehydrogenative ring fusion reaction occurring during the oCVD deposition of phenyl substituted porphyrins with free *ortho* positions and its effect on the porphyrin geometry. Finally, the UV/Vis spectra (Fig. 4d) exhibit a red-shifted shoulder (460 nm), and an increased number of Q-bands. This agrees with the spectra reported for phenyl fused porphyrins.[51,55,65] Contrarily to **NiD*t*-BuPP**, **NiDMP** should not undergo internal cyclisation, making it a good candidate for the in-depth investigation of oligomerization. To obtain information on the kind of links between the units, rapid UV-Vis scans from 300 to 900 nm were acquired at regular time intervals during the GPC × ESI-HRMS analysis (Fig. 3). It is important to note that the UV-Vis detector scans the full spectra in about 24 seconds and during this time, elution continues. As a result, UV-Vis spectra are only partially representative of the eluted species and a sharp feature assignment remains complicated. Nevertheless, the resulting UV-Vis spectra may be used to draw a trend and further correlation with the MS data ensures a reliable identification. Particularly, it is known that triply linked (*β*–*β*/*meso*–*meso*/*β*–*β*) porphyrins own smaller HOMO–LUMO gaps shifting the absorption more in the NIR compared to the (*β*–*meso*/*meso*–*β*) doubly linked porphyrins. As expected, the molecules with highest degrees of polymerization elute at shorter retention times from fraction *a* to *d* (EIC in Fig. S9†) and exhibit a broadened but unshifted Soret band I at 410 nm together with a widened, red-shifted band II around 574 nm. Because of instrumental limits, it was not possible to detect with precision the position of the band III typical of fused porphyrins. On the other hand, these fractions exhibit an intense absorption around 900 nm. Fraction *e* mainly corresponds to the elution of dimers. The presence of triply and doubly linked species was addressed by isotopic pattern simulations and comparison to

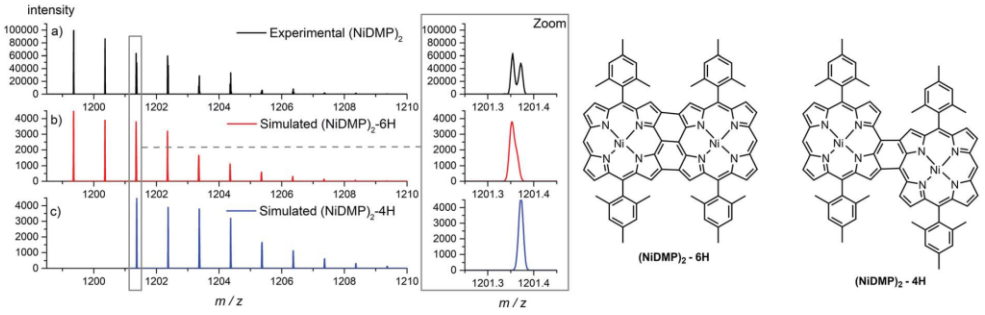

Fig. 6 Isotopic pattern peaks corresponding to NiDMP dimers, (a) experimental spectrum, (b) theoretical isotopic pattern of triply linked dimers (A + 2 isotopic contribution = 1201.352), (c) theoretical isotopic pattern of doubly linked dimers (m/z = 1201.372). The corresponding structures are shown on the right.

HRMS (Fig. 6). Both **(NiDMP)$_2$-6H** and **(NiDMP)$_2$-4H** isotopic contributions are identified in the experimental spectrum.

Unfortunately, because of instrumental limitations, only the **(NiDMP)$_2$-4H** can be observed in the UV-Vis spectra of fraction *e*. Particularly, doubly linked (*β–meso*/*meso–β*) porphyrin dimers show absorption maxima around 750 nm while triply linked porphyrins exhibit broader absorptions generally over 900 nm.[16,32,66] These observations confirm that the synthesis of both triply and doubly linked porphyrins is possible in oCVD. We previously suggested that the initial formation of *meso–meso* or *β–meso* singly linked diporphyrins leading to triply or doubly linked dimers, respectively, is enabled by a dynamic Jahn–Teller distortion of the initially formed nickel(II) porphyrin radical cation generating different electrophilic sites for the first C–C bond formation.[33]

Surprisingly, the formation of **NiDMP-2H** was observed in traces (Fig. 3 fraction *h* and Fig. S12†). This species displays an absorption spectrum similar to the one attributed to the cyclization of **NiD*t*-BuPP** (an intense shoulder at 463 nm and the presence of multiple Q-bands). The small amount obtained suggests a different reactivity of the molecule and/or a different reaction mechanism. It was shown that dimesityl groups on porphyrins can undergo dehydrogenative coupling on Cu(110) surfaces.[67] We suggest that a similar reaction could be stimulated by the iron species deposited on the surface forming a six membered ring on the **NiDMP** molecule between the methyl group and the pyrrole ring. This new arrangement should modify the hydrodynamic volume and the symmetry of the molecule explaining the increase in the number of Q-bands and the higher retention time observed. However, the intensity of the signal of the refractive index detector evidences that this reaction is only marginal for **NiDMP**.

The GPC experiments showed that the substituents and the cyclization affect the reactivity and the geometry of the molecule. To investigate the effects of these structural modifications on the electrical and morphological properties of the obtained coatings, we analyzed the samples by C-AFM (yielding information on the local conductivity of the samples) and Helium Ion Microscopy (HIM) (where contrast in the image is created mainly by composition and topography). HIM images show that the **NiDPP** oCVD coating exhibits a rather smooth surface. Contrarily, **NiDMP**, **NiDDOPP** and **NiD*t*-BuPP** oCVD coatings exhibit a rugged surface (Fig. S13†). This strongly contrasts the smooth surface obtained from the respective sublimed monomers (Fig. S14†). Consequently, it can be assumed that the polymerization induces a different homogeneity of the surface, which relates to the polymer structure. Interestingly, the sublimed **NiDDOPP** monomer film shows the formation of small islands and holes (Fig. S14d†), which might be an effect of the long side chains assisting supramolecular aggregation of the monomers. It is known that the side groups affect the supramolecular aggregation of porphyrins both on surface and in solutions.[68,69] Fig. S15† shows representative C-AFM images relative to the topography while Fig. S16† and 7 show the respective local conductivity acquired simultaneously and the respective representative histograms. We imaged areas of 2 × 2 μm^2 avoiding the oxidant inclusions that could affect the measured conductivity. The measured roughness (R_a) (Table S4†) of the samples was calculated considering the average of at least 4 different locations on the samples. Ra varied from 1 to 20 nm. **NiDDOPP** with its bulky $OC_{12}H_{25}$ groups presents the highest roughness (21 ± 3 nm) average of (4.0 ± 1.0 pA) and the lowest conductivity. Coherently, **NiD*t*-BuPP** and **NiDPP**, undergoing the cyclization reaction, possess the highest conductivity (averages of 77 ± 15 pA and 440 ± 120 pA, respectively) and lowest roughness (Ra of 1.2 ± 0.2 nm and 4.6 ± 0.7) in the series (Table S4†). Finally, **NiDMP** exhibit lower conductivity (6.5 ± 0.6 pA) than **NiD*t*-BuPP** and higher roughness (10 ± 2 nm).

2-Point probe conductivity measurements confirm this trend showing an increase in conductivity by several orders of magnitude by decreasing the size of the substituents (from 0.7 S cm^{-1} for **NiDPP** to 10^{-7} S cm^{-1} for **NiDDOPP**) (Fig. S17 & S18†). Obviously, larger substituents reduce the conductivity. This relation might be based on a simple steric effect preventing the π–π stacking, which is required for efficient electron transfer across porphyrin chains. Besides, this effect may also be ascribed to a dilution of the conjugated porphyrin moiety in the film. A similar relation was observed between field effect

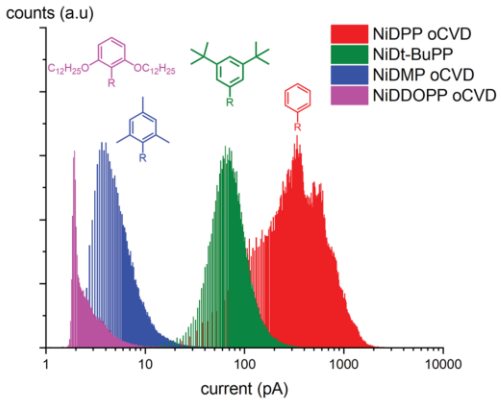

Fig. 7 Histograms obtained from the C-AFM measurements. The graph shows the distribution of current measured while imaging different points of the image in the oCVD samples.

mobility and intermolecular distance in porphyrin crystals.[70] Consequently, the smallest phenyl substituent in **NiDPP** gives rise to the highest conductivity in the series. Furthermore, the intramolecular cyclization reaction occurring in **NiDPP** might further enhance the planarization of the individual moieties and hence the π–π stacking. On the other hand, the very poor conductivity of **NiDDOPP** might be ascribed to the suggested extra cross linking *via* the substituents, which further prevents efficient π–π stacking by forming reticular networks. The electrical conductivity of oCVD films is drastically increased compared to solution-based films. Particularly, *meso–meso* singly and *β–β*/*meso–meso*/*β–β* triply linked porphyrins of 48 and 8 repetitive units respectively with long alkyl chains exhibit resistances between 125–670 MΩ and 50 MΩ, respectively.[71] While the **NiDDOPP** oCVD coating exhibits a resistance of 400 MΩ, **NiDPP**, **NiD*t*-BuPP** and **NiDMP** show much smaller resistances of 100 Ω, 230 KΩ and 400 KΩ, respectively (Fig. S17†). Obviously, the oCVD of porphyrins allows obtaining coatings with increased conductivity compared to solution based approaches. This effect may be ascribed to both the reduction of the substituent size enabling a better π–π stacking and to the doping of the coatings due to the excess oxidant. C-AFM and 2-point probe measurements provide complementary insights into the film properties. While C-AFM probes the film on the nanoscale excluding the effect of oxidant residuals, the 2-point probe measurements take place on the microscale and are more affected by the film homogeneity and the iron salt inclusions.

In order to obtain deeper insight into conceivable π–π stacking interactions of nickel(II) porphyrins, DFT calculations (RIJCOSX-BP86-D3BJ-ZORA/def2-SVP) were performed on model aggregates consisting of two porphyrins, namely **(NiDPP)$_2$**, **(NiDMP)$_2$** and **(NiD*t*-BuPP)$_2$** as well as on two porphyrins with complete intramolecular dehydrogenative cyclization **(NiDPP-4H)$_2$** and **(NiD*t*-BuPP-4H)$_2$** (Fig. S19–S22† and 8). Expectedly, the **(NiDPP)$_2$** aggregate consists of two saddle shaped porphyrins[33] in an offset face to face arrangement. The phenyl substituents display torsional angles between 59° and 64° with the porphyrin plane (Fig. S19†). To avoid steric interactions, the phenyl substituents point to different directions in the two monomers (staggered arrangement of the **NiDPP** entities).

On the other hand, the complete dehydrogenative cyclization in **(NiDPP-4H)$_2$** almost completely planarizes the entire molecules including the *meso*-phenyl substituents. This structural modification facilitates π–π stacking interactions between the planarized entities (Fig. 8). Increasing ring-fusion and concomitant planarization enables better π–π stacking as shown by Ishizuka and Kojima on zinc porphyrins[55] and this effect appears to be valid for the nickel porphyrins as well. Similarly, the *tert*-butyl substituted nickel porphyrin **NiD*t*-BuPP** shows a saddle distortion with non-coplanar *meso*-aryl substituents (dihedral angles between ~55° and 66°; Fig. S20†). Again, the two porphyrins orient with the *meso*-substituents pointing towards four different directions limiting the steric hindrance between the peripheral groups.

Dehydrogenative cyclization of the aryl substituents flattens the chromophore, allowing a better stacking interaction in **(NiD*t*-BuPP-4H)$_2$** (Fig. S21†). With respect to π–π stacking, the situation is worse for the **(NiDMP)$_2$** aggregate with mesityl substituents. These bulky *meso*-substituents are essentially orthogonal to the porphyrin plane (dihedral angle ~91°)

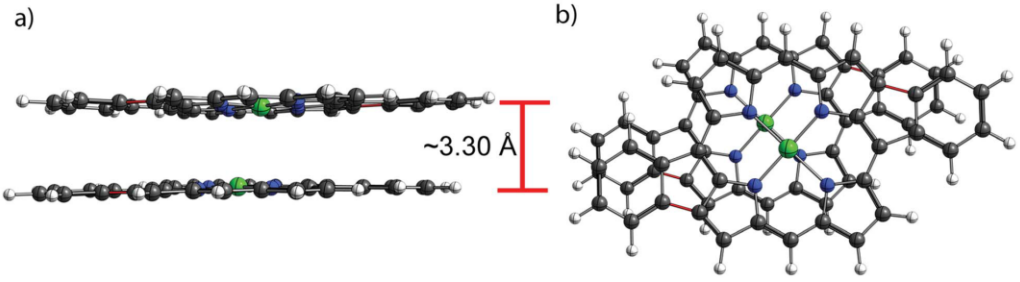

Fig. 8 DFT calculated geometry for two NiDPP molecules which have undergone the cyclization reaction of both the phenyl rings. (a) side view, (b) top view. The cyclization induces planarization of the molecule with phenyl rings co-planar to the porphyrin macrocycle. The cyclization is highlighted in red.

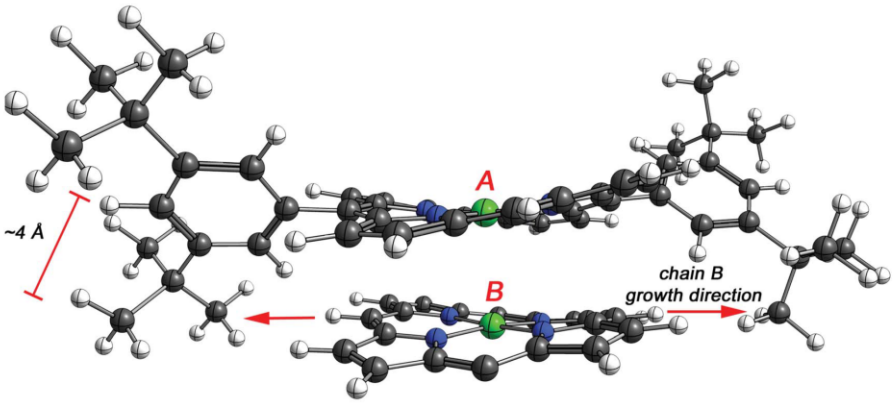

Fig. 9 DFT model of two NiDt-BuPP porphyrins (indicated with A and B). 3,5-Di(*tert*-butyl)phenyl substituents of porphyrin B are omitted for clarity. The *tert*-butyl groups of porphyrin A point out of the porphyrin plane hindering the growth reaction of porphyrin B.

preventing any close contact of the porphyrin planes or stacking interactions (Fig. S22†). As **NiDMP** is unable to planarize by intramolecular dehydrogenative cyclization, this unfavourable situation with respect to π–π stacking will be realized in the oCVD films of **NiDMP** as well.

To assess the effect of the cyclization, the distance between the porphyrins plane was estimated by DFT for **NiDPP**, **NiDt-BuPP** and their respective fused counterparts (details in ESI†). The estimated distance between the porphyrinic units are 3.39 Å ± 0.2 (**NiDPP**), 3.30 Å ± 0.1 (**NiDPP-4H**), 3.44 Å ± 0.2 (**NiDt-BuPP**) 3.26 Å ± 0.02 (**NiDt-BuPP-4H**), which are in good agreement with the experimental data obtained by Ishizuka and Kojima.[55] However, this small model doesn't take into account that advancing polymerization causes an overlap between the growing chain and the substituents on the surrounding porphyrin chains (Fig. 9). Particularly, the di(*tert*-butyl)phenyl and mesityl substituents point out of the porphyrin plane by *ca.* 4 and 3.5 Å, respectively (see **NiDt-BuPP** example in Fig. 9). Contrarily, in **NiDt-BuPP-4H**, thanks to the ring fusion forcing the co-planarity of the phenyl rings to the plane, the di(*tert*-butyl)phenyl groups point out of the plane by only ~2 Å (Fig. S21†). Since the size of the groups exceeds the average distance between the porphyrins calculated in the small model (3.4–3.2 Å), it can be speculated that the intermolecular distance in the polymeric structure will increase. For example, in **NiDt-BuPP**, the offset arrangements between the porphyrins yield substituents hindering the growth of the neighbouring porphyrin tape chain (Fig. 9).

This likely causes an increase of the interplanar distances for porphyrin tapes not undergoing cyclization. On the other hand, ring fusion flattens the porphyrins minimizing this effect. Considering the ring fusion, the interplanar distance between the units increases in the following order: **NiDPP** < **NiDt-BuPP** < **NiDMP** < **NiDDOPP** in the oCVD coatings. The different conductivity observed is then related to increasing interchain distances hindering the electron transport process in the material. All the experiments strongly point towards the advantages of the oCVD of porphyrins for the integration into devices of porphyrin tapes. Particularly, the technique allows the synthesis of conjugated porphyrins tapes without any solubilizing agent on the molecule, which is crucial to ensure more compact arrangements that improve the electron transfer and the conductivity in the coatings. This is particularly true for **NiDPP**. In fact, solution based approaches induce low polymerisation yields, solely forming short oligomers, which are insoluble over five repetitive units.[66] On the other hand, the oCVD approach directly yields smooth coatings that, thanks to a completely flat structure, exhibit the best performances in the studied series.

Conclusions

In conclusion, we demonstrated that unlike solution-based approaches, oCVD does not require specific solubilizing substituents attached to the porphyrin to form fused porphyrin tapes. Thin films of fused porphyrin tapes were readily obtained from nickel(II) porphyrins bearing phenyl, mesityl, di(*tert*-butyl)phenyl or di(alkoxy)phenyl *meso*-substituents, overcoming the difficulties related to the processability these materials into advanced devices. The decoupling of the porphyrin substituents from the synthesis requirement allows the formation of dense and homogeneous thin films with conductivity as high as 0.7 S cm^{-1} for the oCVD coatings prepared from **NiDPP**. The substituent size was shown to severely affect the arrangement of the molecules and consequently the conductivity of the oCVD films. Large substituents increase the intermolecular distance, weakening the π–π interactions and hindering the interchain electron transfer. This effect highlights a main advantage of the oCVD of porphyrins that allows obtaining porphyrin tapes starting from porphyrins with small substituents. Furthermore, the oCVD approach causes a cyclization between *meso*-phenyl rings and porphyrin macrocycle improving the electrical performance of the material thanks to enhanced π–π interactions (molecular flattening effect). Nonetheless, it is possible to

use the free *meso*-positions on the porphyrins to increase the functionality of the material. Furthermore, we undoubtedly demonstrated that the formation of *β–β/meso–meso/β–β* triply linked nickel porphyrins is possible by oCVD.

Experimental section

Experimental procedures, cyclic voltammograms, *I–V* curves, HIM, AFM images, DFT calculations, extracted ion chromatograms and TGA are provided in the ESI†

Conflicts of interest

There are no conflicts to declare.

Acknowledgements

We gratefully acknowledge the financial support of the Luxembourgish "Fonds National de la Recherche" through the CORE project POLYPORPH (C15/MS/10340560/POLYPORH/Boscher). Parts of this research were conducted using the supercomputer Mogon and advisory services offered by Johannes Gutenberg University Mainz (http://www.hpc.uni-mainz.de), which is a member of the AHRP and the Gauss Alliance e. V.

References

1 K. Rybicka-Jasińska, W. Shan, K. Zawada, K. M. Kadish and D. Gryko, *J. Am. Chem. Soc.*, 2016, **138**, 15451–15458.
2 K. Ladomenou, M. Natali, E. Iengo, G. Charalampidis, F. Scandola and A. G. Coutsolelos, *Coord. Chem. Rev.*, 2015, **304–305**, 38–54.
3 M. Zhao, S. Ou and C. De Wu, *Acc. Chem. Res.*, 2014, **47**, 1199–1207.
4 W. Liu and J. T. Groves, *Acc. Chem. Res.*, 2015, **48**, 1727–1735.
5 D. Khusnutdinova, B. L. Wadsworth, M. Flores, A. M. Beiler, E. A. Reyes Cruz, Y. Zenkov and G. F. Moore, *ACS Catal.*, 2018, **8**, 9888–9898.
6 E. Rose, B. Andrioletti, S. Zrig and M. Quelquejeu-Ethève, *Chem. Soc. Rev.*, 2005, **34**, 573–583.
7 W. Zhang, W. Lai and R. Cao, *Chem. Rev.*, 2017, **117**, 3717–3797.
8 S. Mathew, A. Yella, P. Gao, R. Humphry-Baker, B. F. E. Curchod, N. Ashari-Astani, I. Tavernelli, U. Rothlisberger, M. K. Nazeeruddin and M. Grätzel, *Nat. Chem.*, 2014, **6**, 242–247.
9 L.-L. Li and E. Wei-Guang Diau, *Chem. Soc. Rev.*, 2013, **42**, 291–304.
10 B. Li, C. Zheng, H. Liu, J. Zhu, H. Zhang, D. Gao and W. Huang, *ACS Appl. Mater. Interfaces*, 2016, **8**, 27438–27443.
11 S. Singh, A. Aggarwal, N. V. S. D. K. Bhupathiraju, G. Arianna, K. Tiwari and C. M. Drain, *Chem. Rev.*, 2015, **115**, 10261–10306.
12 M. Ethirajan, Y. Chen, P. Joshi and R. K. Pandey, *Chem. Soc. Rev.*, 2011, **40**, 340–362.
13 A. E. O'Connor, W. M. Gallagher and A. T. Byrne, *Photochem. Photobiol.*, 2009, **85**, 1053–1074.
14 Y. Zhang and J. F. Lovell, *Theranostics*, 2012, **2**, 905–915.
15 M. O. Senge, M. Fazekas, E. G. A. Notaras, W. J. Blau, M. Zawadzka, O. B. Locos and E. M. Ni Mhuircheartaigh, *Adv. Mater.*, 2007, **19**, 2737–2774.
16 A. Tsuda and A. Osuka, *Science*, 2001, **293**, 79–82.
17 H. L. Anderson, *Chem. Commun.*, 1999, 2323–2330.
18 W. Jentzen, M. C. Simpson, J. D. Hobbs, X. Song, J. A. Shelnutt, T. Ema, N. Y. Nelson, C. J. Medforth, K. M. Smith, M. Veyrat, M. Mazzanti, R. Ramasseul, J. C. Marchon, T. Takeuchi and W. A. Goddard, *J. Am. Chem. Soc.*, 1995, **117**, 11085–11097.
19 C. Jiao, N. Zu, K. W. Huang, P. Wang and J. Wu, *Org. Lett.*, 2011, **13**, 3652–3655.
20 N. K. S. Davis, M. Pawlicki and H. L. Anderson, *Org. Lett.*, 2008, **10**, 3945–3947.
21 N. K. S. Davis, A. L. Thompson and H. L. Anderson, *Org. Lett.*, 2010, **12**, 2124–2127.
22 S. Banala, K. Wurst and B. Kräutler, *Chempluschem*, 2016, **81**, 477–488.
23 L. Si, H. He and K. Zhu, *New J. Chem.*, 2014, **38**, 1565–1572.
24 J. Kesters, P. Verstappen, M. Kelchtermans, L. Lutsen, D. Vanderzande and W. Maes, *Adv. Energy Mater.*, 2015, **5**, 1500218.
25 D. Y. Kim, T. K. Ahn, J. H. Kwon, D. Kim, T. Ikeue, N. Aratani, A. Osuka, M. Shigeiwa and S. Maeda, *J. Phys. Chem. A*, 2005, **109**, 2996–2999.
26 N. Algethami, H. Sadeghi, S. Sangtarash and C. J. Lambert, *Nano Lett.*, 2018, **18**, 4482–4486.
27 E. Leary, B. Limburg, A. Alanazy, S. Sangtarash, I. Grace, K. Swada, L. J. Esdaile, M. Noori, M. T. González, G. Rubio-Bollinger, H. Sadeghi, A. Hodgson, N. Agraït, S. J. Higgins, C. J. Lambert, H. L. Anderson and R. J. Nichols, *J. Am. Chem. Soc.*, 2018, **140**, 12877–12883.
28 S. Ha, K. Kato, T. Sakurai, A. Saeki, M. Takata, M. Uchiyama, A. Osuka, J. Kim, Y. Honsho, K. Tashiro, T. Aida, S. Seki and A. Muranaka, *J. Am. Chem. Soc.*, 2011, **133**, 6537–6540.
29 N. Yoshida, N. Aratani and A. Osuka, *Chem. Commun.*, 2000, 197–198.
30 B. J. Brennan, M. J. Kenney, P. A. Liddell, B. R. Cherry, J. Li, A. L. Moore, T. A. Moore and D. Gust, *Chem. Commun.*, 2011, **47**, 10034–10036.
31 B. J. Brennan, J. Arero, P. A. Liddell, T. A. Moore, A. L. Moore and D. Gust, *J. Porphyrins Phthalocyanines*, 2013, **17**, 247–251.
32 C.-M. Feng, Y.-Z. Zhu, S.-C. Zhang, Y. Zang and J.-Y. Zheng, *Org. Biomol. Chem.*, 2015, **13**, 2566–2569.
33 G. Bengasi, K. Baba, O. Back, G. Frache, K. Heinze and N. D. Boscher, *Chem.–Eur. J.*, 2019, **25**, 8313–8320.
34 A. Tsuda, A. Nakano, H. Furuta, H. Yamochi and A. Osuka, *Angew. Chem., Int. Ed.*, 2000, **39**, 558–561.
35 A. Tsuda, Y. Nakamura and A. Osuka, *Chem. Commun.*, 2003, 1096–1097.
36 Y. Nakamura, N. Aratani, A. Tsuda, A. Osuka, K. Furukawa and T. Kato, *J. Porphyrins Phthalocyanines*, 2003, **7**, 264–269.
37 H. Qin, L. Li, F. Guo, S. Su, J. Peng, Y. Cao and X. Peng, *Energy Environ. Sci.*, 2014, **7**, 1397–1401.

38 G. Bengasi, K. Baba, G. Frache, J. Desport, P. Gratia, K. Heinze and N. D. Boscher, *Angew. Chem., Int. Ed.*, 2019, **58**, 2103–2108.
39 M. Heydari Gharahcheshmeh and K. K. Gleason, *Adv. Mater. Interfaces*, 2019, **6**, 1801564.
40 M. Wang, X. Wang, P. Moni, A. Liu, D. H. Kim, W. J. Jo, H. Sojoudi and K. K. Gleason, *Adv. Mater.*, 2017, **29**, 1604606.
41 H. Goktas, X. Wang, N. D. Boscher, S. Torosian and K. K. Gleason, *J. Mater. Chem. C*, 2016, **4**, 3403–3414.
42 H. Goktas, X. Wang, A. Ugur and K. K. Gleason, *Macromol. Rapid Commun.*, 2015, **36**, 1283–1289.
43 J. P. Lock, S. G. Im and K. K. Gleason, *Macromolecules*, 2006, **39**, 5326–5329.
44 S. Nejati and K. K. S. Lau, *Langmuir*, 2011, **27**, 15223–15229.
45 P. Kovacik, G. del Hierro, W. Livernois and K. K. Gleason, *Mater. Horiz.*, 2015, **2**, 221–227.
46 X. Wang, S. Ermez, H. Goktas, S. Gradečak and K. K. Gleason, *Macromol. Rapid Commun.*, 2017, **38**, 1700055.
47 X. Wang, A. Ugur, H. Goktas, N. Chen, M. Wang, N. Lachman, E. Kalfon-Cohen, W. Fang, B. L. Wardle and K. K. Gleason, *ACS Sens.*, 2016, **1**, 374–383.
48 X. Wang, S. Hou, H. Goktas, P. Kovacik, F. Yaul, A. Paidimarri, N. Ickes, A. Chandrakasan and K. K. Gleason, *ACS Appl. Mater. Interfaces*, 2015, **7**, 16213–16222.
49 Y. Y. Smolin, K. L. Van Aken, M. Boota, M. Soroush, Y. Gogotsi and K. K. S. Lau, *Adv. Mater. Interfaces*, 2017, **4**, 1601201.
50 S. Nejati, T. E. Minford, Y. Y. Smolin and K. K. S. Lau, *ACS Nano*, 2014, **8**, 5413–5422.
51 Y. Fang, D. Koszelewski, K. M. Kadish and D. T. Gryko, *Chem. Commun.*, 2014, **50**, 8864–8867.
52 P. Chen, Y. Fang, K. M. Kadish, J. P. Lewtak, D. Koszelewski, A. Janiga and D. T. Gryko, *Inorg. Chem.*, 2013, **52**, 9532–9538.
53 J. P. Lewtak, B. Koszarna, M. K. Charyton and D. T. Gryko, *J. Porphyrins Phthalocyanines*, DOI: 10.1142/S1088424619501530.
54 K. Baba, G. Bengasi, D. El Assad, P. Grysan, E. Lentzen, K. Heinze, G. Frache and N. D. Boscher, *Eur. J. Org. Chem.*, 2019, 2368–2375.
55 T. Ishizuka, Y. Saegusa, Y. Shiota, K. Ohtake, K. Yoshizawa and T. Kojima, *Chem. Commun.*, 2013, **49**, 5939.
56 Y. Saegusa, T. Ishizuka, K. Komamura, S. Shimizu, H. Kotani, N. Kobayashi and T. Kojima, *Phys. Chem. Chem. Phys.*, 2015, **17**, 15001–15011.
57 T. Wijesekera, A. Matsumoto, D. Dolphin and D. Lexa, *Angew. Chem., Int. Ed. Engl.*, 1990, **29**, 1028–1030.
58 M. O. Senge, O. Flögel and K. Ruhlandt-Senge, *J. Porphyrins Phthalocyanines*, 2001, **5**, 503–506.
59 M. Schubert, P. Franzmann, A. Wünsche von Leupoldt, K. Koszinowski, K. Heinze and S. R. Waldvogel, *Angew. Chem., Int. Ed.*, 2016, **55**, 1156–1159.
60 M. Schubert, J. Leppin, K. Wehming, D. Schollmeyer, K. Heinze and S. R. Waldvogel, *Angew. Chem., Int. Ed.*, 2014, **53**, 2494–2497.
61 J. Leppin, M. Schubert, S. R. Waldvogel and K. Heinze, *Chem.–Eur. J.*, 2015, **21**, 4229–4232.
62 T. C. Jempty, K. A. Z. Gogins, Y. Mazur and L. L. Miller, *J. Org. Chem.*, 1981, **46**, 4545–4551.
63 A. A. O. Sarhan and C. Bolm, *Chem. Soc. Rev.*, 2009, **38**, 2730–2744.
64 R. L. Burwell, *Chem. Rev.*, 1954, **54**, 615–685.
65 J. P. Lewtak, D. Gryko, D. Bao, E. Sebai, O. Vakuliuk, M. Ścigaj and D. T. Gryko, *Org. Biomol. Chem.*, 2011, **9**, 8178–8181.
66 A. Tsuda, Y. Nakamura and A. Osuka, *Chem. Commun.*, 2003, 1096–1097.
67 M. In't Veld, P. Iavicoli, S. Haq, D. B. Amabilino and R. Raval, *Chem. Commun.*, 2008, 1536–1538.
68 V. Villari, P. Mineo, E. Scamporrino and N. Micali, *Chem. Phys.*, 2012, **409**, 23–31.
69 T. Yokoyama, S. Yokoyama, T. Kamikado, Y. Okuno and S. Mashiko, *Nature*, 2001, **413**, 619–621.
70 T. Minari, M. Seto, T. Nemoto, S. Isoda, K. Tsukagoshi and Y. Aoyagi, *Appl. Phys. Lett.*, 2007, **91**, 123501.
71 D. H. Yoon, S. B. Lee, K. H. Yoo, J. Kim, J. K. Lim, N. Aratani, A. Tsuda, A. Osuka and D. Kim, *J. Am. Chem. Soc.*, 2003, **125**, 11062–11064.

5.5 Metal Ion Effect on Regioselectivity in the Synthesis of Porphyrin Tapes in oCVD.

Giuseppe Bengasi, Louise Quétu, Kamal Baba, Alexander Ost, João P. Cosas Fernandes, Patrick Grysan, Katja Heinze, Nicolas D. Boscher.

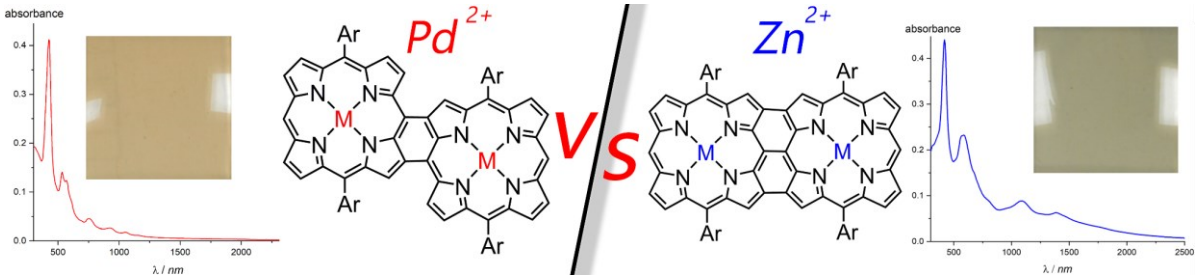

Triply-linked porphyrins films: The effect of the metal center on the oCVD of porphyrins was unclear. We investigate the effect of different metal cations (M=Ni^{II}, Cu^{II}, Zn^{II}, Co^{II}, Pd^{II}, $Fe^{III}Cl$, 2H). In oCVD, zinc(II) porphyrins are highly regioselective leading to the synthesis, deposition and doping of triply-linked porphyrin tapes thin films in a single step with improved electrical properties.

Authors contributions

Louise Quétu performed the deposition experiments under the supervision of Giuseppe Bengasi and Nicolas Boscher. Kamal Baba performed the UV/Vis/NIR analyses. Giuseppe Bengasi performed the cyclic voltammetry analyses. Joao P. Cosas Fernandes and Patrick Grysan performed the AFM measurements and Alexander Ost acquired the HIM images. Giuseppe Bengasi made the interpretation of the results. Giuseppe Bengasi wrote the manuscript with contribution from Katja Heinze and Nicolas Boscher.

Supporting Information

Supporting information can be found at page 179.

Metal Ion Effect on Regioselectivity in the Synthesis of Porphyrin Tapes in oCVD.

Giuseppe Bengasi,[a][b] Louise Quétu,[a] Kamal Baba,[a] Alexander Ost,[a] João P. Cosas Fernandes, [a] Patrick Grysan, [a] Katja Heinze,* [b] Nicolas D. Boscher*[a].

Abstract: Solvent-free oxidative chemical vapour deposition of nickel(II) porphyrins yields thin films of nickel(II) porphyrin tapes. Up to date, the effect of the metal center on the oCVD of porphyrins remained unclear. By means of high resolution mass spectrometry, UV/Vis/NIR/ spectroscopy, X-ray photoelectron spectroscopy, cyclic voltammetry and helium ion microscopy we investigate the effect of different metal cations (M=Ni^{II}, Cu^{II}, Zn^{II}, Co^{II}, Pd^{II}, $Fe^{III}Cl$, 2H) on the oCVD of M-5,15-(dimesityl)porphyrins. Through cyclic voltammetry we study the effect of the metal center on the frontier orbitals and on the reaction regioselectivity. In oCVD, zinc(II) porphyrins are highly regioselective towards the formation of triply-linked (*β–β /meso-meso/β–β)* porphyrin tapes. This lead to the synthesis, deposition and doping of triply-linked porphyrin tapes thin films in a single step. Conductive atomic force microscopy studies show that triply-linked zinc porphyrins exhibit the best electric performance in the series. Palladium(II) porphyrins exhibit higher regioselectivity towards doubly linked porphyrin tapes. The synthesis of doubly and triply-linked cobalt(II) porphyrin tapes is also obtained for the first time.

Introduction

Porphyrin tapes (Scheme 1) are promising materials for applications as NIR absorbers,[1] non linear optics[2,3] and molecular wires.[4,5] However, their integration in optoelectronic devices is hindered by their complex synthesis and poor solubility. The synthesis of porphyrin tapes relies on the oxidative coupling of porphyrins bearing free *β* and *meso* positions. This can lead to the formation of doubly or triply-linked porphyrins. The regioselectivity towards the formation of doubly or triply-linked porphyrin tapes (Scheme 1) is related to the porphyrin metal center.[6–8] Up to date, directly fused porphyrins bearing Zn^{II},[1] Ni^{II},[7,9] Pd^{II}[6,7,10] or Cu^{II}[7,11,12] as central metal ions have been achieved via solution-based approaches. Yet, only Zn^{II} porphyrins showed high regioselectivity for the formation of triply-linked porphyrin tapes, exhibiting the most interesting properties for optoelectronic device fabrication.[1,4,13] Contrarily, other cations induce lower regioselectivity or regioselectivity towards doubly-linked (*β-meso*, *meso-β*) porphyrin tapes. Therefore, the careful selection of the metal cation provides an easy pathway for tuning porphyrins' optical, electronic and catalytic properties.[14–18] The synthesis of triply-linked porphyrin tapes is usually achieved in a two-step reaction. In a first step, a *meso-meso* connection is formed between porphyrin units employing Ag^{+} oxidants.[19] Subsequently, a second oxidation step is carried out to obtain triply-linked porphyrin tapes.[1] During the last two decades, a significant effort has been undertaken to investigate numerous porphyrin/oxidant/solvent combinations in order to develop an efficient synthetic route for the formation of multiply-linked porphyrin tapes in one-step.[7,11,12,20–22] Yet, although the single-step synthesis of doubly-linked porphyrins has been successfully achieved,[7,21] the direct synthesis of triply-linked porphyrin tapes remains elusive up-to date.

We recently investigated the gas phase reaction of nickel(II) porphyrins and iron(III) chloride for the simultaneous synthesis, deposition and doping of nickel porphyrin tapes directly in thin film form.[23] The approach, known as oxidative chemical vapour deposition (oCVD),[24] circumvents the need for long alkyl substituents used to ensure the solubility in solution-based methods. Furthermore, compared to on-substrate synthesis yielding merely monolayers,[25–28] the oCVD approach allow the deposition of thin smooth layers on virtually any substrate.[23,29]

Operating from the gas phase, the oCVD of porphyrins allows the incorporation of new substituents, including smaller substituents that can enhance the electrical properties of the thin films. Indeed, reducing the substituent size decreases the intermolecular distances and improves the π–π stacking in the film facilitating the electron transfer.[30] Moreover, in oCVD the use of the substituents that possess free *ortho* positions on the phenyl rings, allows condensation of the phenyl ring on the macrocycle.[22,31] Intramolecular cyclization forces co-planarity between the phenyl ring and the porphyrin macrocycle increasing the conductivity of the porphyrin tapes thin film, further highlighting the importance of the substituent selection. However, the effect of the porphyrin's metal cation on the chemistry and properties of the porphyrin tapes thin film obtained by oCVD is an open question. Up to date, only nickel(II) porphyrins have been studied in oCVD.

In order to investigate the influence of the metal center on the reactivity of porphyrins in oCVD, we study for the first time in this work the oCVD reaction of several M-5,15-(dimesityl)porphyrins (M = 2H, $Fe^{III}Cl$, Co^{II}, Ni^{II}, Cu^{II}, Zn^{II} and Pd^{II}) (M-(DMP)). Mesityl groups were selected as substituents due to their blocked *ortho* positions on the phenyl ring that prevent the cyclization between the phenyl ring and the porphyrin *β*-position[30,31], ensuring the easier discrimination of the number of bonds formed between the porphyrinic units. Indeed, intramolecular cyclization causes the elimination of one to multiple 2H pairs, which generates a series of isobaric species that hinder a straightforward identification of the connections between porphyrinic

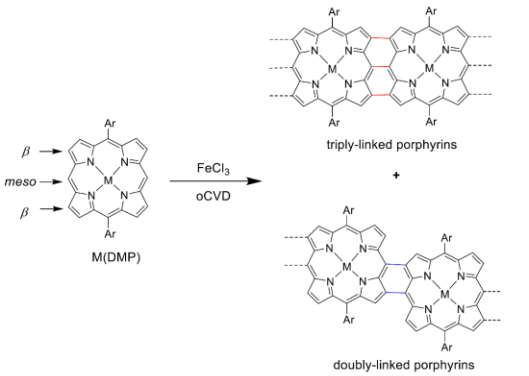

Scheme 1. *Oxidative coupling of dimesityl porphyrins with $FeCl_3$ in oCVD. The oxidative coupling yields doubly (blue lines) and/or triply-linked (red lines) porphyrin tapes.*

[a] G. Bengasi, L. Quétu, Dr. K. Baba, A. Ost, Dr. J. P. Cosas Fernandes, Dr. P. Grysan, Dr. N. D. Boscher
Materials Research and Technology
Luxembourg Institute of Science and Technology (LIST)
5 Avenue des Hauts-Fourneaux, L-4362 Esch/Alzette, Luxembourg
E-mail: nicolas.boscher@list.lu

[b] G. Bengasi, Prof. Dr. K. Heinze,
Department of Inorganic Chemistry and Analytical Chemistry
Johannes Gutenberg University of Mainz
Duesbergweg 10-14, 55128 Mainz, Germany
E-mail: Katja.heinze@uni-mainz.de

Supporting information for this article is given via a link at the end of the document

Porphyrin	$E_{1/2}$ / V	*Thickness* / nm	*Roughness Ra* / nm
FeCl(DMP)	0.62	38 ± 7	8.8 ± 5.3
Pd(DMP)	0.58	19 ± 4	2.7 ± 0.3
H_2DMP	0.54	55 ± 3	4.6 ± 1.4
Ni(DMP)	0.54	133 ± 27	8.6 ± 2.6
Cu(DMP)	0.46	118 ± 26	19.0 ± 8.7
Zn(DMP)	0.40	344 ± 51	41.0 ± 2.0
Co(DMP)	0.30 (irr.)	424 ± 53	20.7 ± 14.5

***Table 1**. Measured oxidation potential for the studied porphyrins (vs FcH/FcH$^+$ in CH_2Cl_2 employing [nBu4N][PF6] as supporting electrolyte), thickness of the film and arithmetic average roughness of the respective oCVD films.*

units by mass spectrometry. $FeCl_3$ was chosen as oxidant due to its proven efficiency to initiate the oxidative coupling in solution and in oCVD.[22,24,32] The composition, connectivity, morphology and electrical conductivity of the obtained thin films is elucidated by ultraviolet-visible-near infrared (UV/Vis/NIR) spectroscopy, laser desorption ionization high resolution mass spectrometry (LDI-HRMS), X-ray photoelectron spectroscopy (XPS), helium ion microscopy (HIM) and conductive atomic force microscopy (C-AFM). Supported by cyclic voltammetry (CV) measurements, we elucidate the dependence of the oCVD reaction of dimesityl metalloporphyrins on their central metal ion.

Results and discussion

Oxidative chemical vapour deposition reaction

The thermal stability of the free-base and metallated 5,15-(dimesityl)porphyrins was studied by thermogravimetric analysis (TGA). For all the investigated porphyrins, TGA shows a good thermal stability, up to 350°C, confirming their suitability for the oCVD process (Figure S1). Interestingly, different metal cations in the porphyrin core affect the sublimation temperature. Preliminary experiments, not reported in this work for brevity, allowed to determine the sublimation temperature (from 220°C to 260°C) of each porphyrin in order to sublime similar amounts and maintain the porphyrin/oxidant ratio as constant as possible (Table S1). For all oCVD experiments, $FeCl_3$ was used in excess in the present study to ensure sufficient reactivity. Following, the $E_{1/2}$ of all the porphyrins in CH_2Cl_2 was investigated by cyclic voltammetry employing [nBu$_4$N][PF$_6$] as supporting electrolyte (Table 1).

Irrespective of the central metal ions, the oCVD reaction of the M(DMP) porphyrins yields the formation of macroscopically homogeneous thin films. The film colours range from orange/dark green of the Co, Ni, Cu, Zn and Pd DPMs, to the light green of the FeCl(DMP) and H_2DMP films. Helium ion microscopy of the oCVD films evidences the formation of smooth and uniform thin films covering the whole surface of the substrates (Figure S2). As previously reported, iron chloride particles are present on the surface of the oCVD films.[22] Nevertheless, the oCVD films present higher uniformity compared to the reference films obtained by sublimation (Figure S3). The lower roughness of the oCVD films is confirmed by AFM measurements (Figure S4), revealing a roughness between 2.7 and 20.7 nm depending on the starting porphyrin (Table 1). Interestingly, the higher roughness of the Co(DMP), Zn(DMP) and Cu(DMP) oCVD films correlates with their higher thickness.

Although similar amounts of porphyrin were sublimed during the oCVD process, drastic changes in the thickness of the different oCVD films are observed (Table 1). Particularly, the oCVD films obtained from H_2DMP, Pd(DMP) and FeCl(DMP) exhibit a lower thicknesses (ranging from 19 to 55 nm), while the oCVD films obtained from Co(DMP) and Zn(DMP) exhibit thicknesses in the range of several hundreds of nanometers. Interestingly, both higher thickness and higher roughness seem to correlate with lower oxidation potentials (Figure S6 and S7). The drastic colour change observed between the oCVD films and their respective reference films obtained by sublimation evidence the occurrence of reactions at the porphyrin macrocycle that will be identified in the following sections.

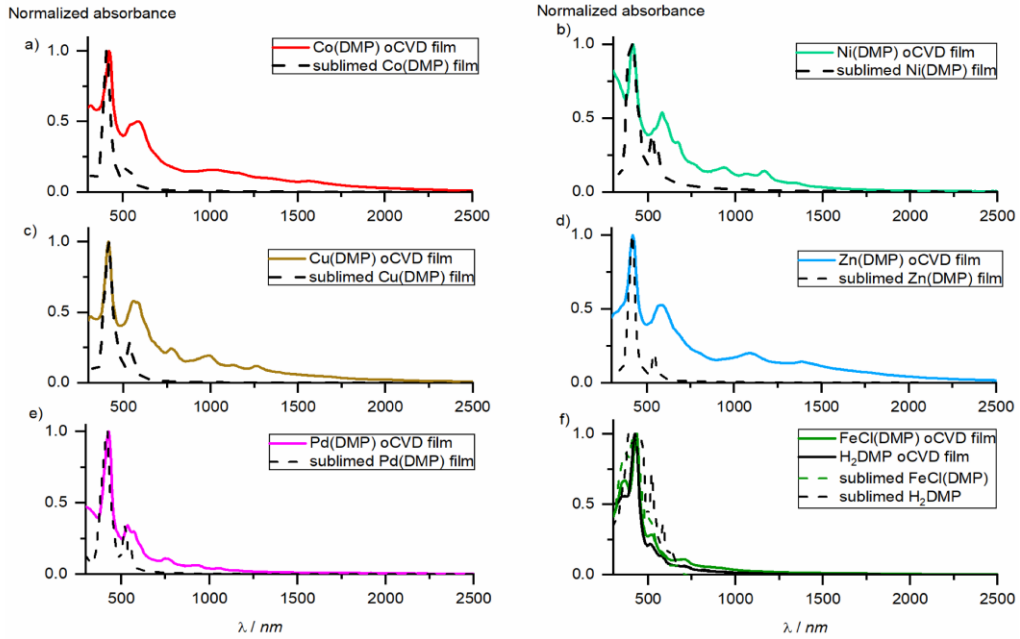

***Figure 1.** Normalized UV/Vis/NIR absorption spectra of the oCVD films and their respective reference films obtained from the different M(DMP)s.*

Dehydrogenative coupling of porphyrins

UV/Vis/NIR spectroscopy of the thin films on glass reveals more intense Q bands and absorption in the NIR for the oCVD films prepared from Co, Ni, Cu, Zn and Pd (DMP)s (Figure 1a-e), pointing towards the formation of porphyrin tapes for all the M^{II} porphyrins. This contrasts with the FeCl(DMP) and H_2DMP oCVD films that exhibit very weak absorptions in the NIR (Figure 1f). Tsuda et al. calculated that doubly-linked Ni^{II} porphyrin tapes exhibit effective conjugation length (ECL) effect around 1480 nm.[9] Contrarily, triply-linked zinc porphyrin tapes do not exhibit any ECL effect below to 2800 nm.[33] Consequently, UV/Vis/NIR spectroscopy suggests that Co(DMP), Cu(DMP) and Zn(DMP) films showing absorption over 1500 nm form triply-linked porphyrin tapes. We recently demonstrated that Ni(DMP) forms both doubly and triply-linked porphyrin tapes.[30] The lower NIR absorption could then be related to the formation of shorter oligomers. Contrarily, Pd(DMP) UV/Vis/NIR spectrum showing absorption far below 1500 nm is compatible with the formation of doubly-linked porphyrin tapes. It is interesting to note that the films showing a lower absorption in the NIR range also exhibit a lower thickness and roughness in the series while possessing higher $E_{1/2}$ (Table 1). A lower reactivity towards the oxidative coupling due to the higher oxidation potential could account for these differences: Oligomers are probably less volatile than monomers. During the oCVD, H_2DMP, Pd(DMP) and FeCl(DMP) forming shorter chains or not polymerizing, resublime from the hot substrate yielding thinner oCVD films. On the contrary, higher reactivity of Co(DMP), Cu(DMP) and Zn(DMP) lead to thicker films. Furthermore, $HCl_{(g)}$ is produced during the oxidative coupling. Bubbling of this gaseous product during the deposition could vary the film porosity explaining the different roughness observed in the films. A similar behaviour was observed for the oCVD of 3,4-ethylenedioxythiophene employing $CuCl_2$ as oxidant.[34]

LDI-HRMS provides an insight into the reactivity of the different metallo-porphyrins. LDI-HRMS analysis of the H_2DMP oCVD (Figure 2a) film shows that: i) H_2DMP doesn't exhibit signals of oligomers; ii) the monomers are detected as protonated adducts $[H_2DMP]+H^+$; iii) FeCl(DMP) is formed during the oCVD of H_2DMP. The latter observation explains the similarity between the UV/Vis/NIR spectra of the H_2DMP and FeCl(DMP) oCVD films. These reactions could be ascribed to the formation of Fe^{II} and Cl_2 during sublimation of $FeCl_3$:[35]

$$2Fe^{III}Cl_{3(g)} \leftrightarrow 2Fe^{II}Cl_{2(g)} + Cl_{2(g)}$$

While the Fe^{II} formed is probably responsible for the metalation of the porphyrin, the Cl_2 causes chlorination of the porphyrin in the presence of $FeCl_3$.[36] The chlorination reaction also yields HCl accounting for the formation of protonated adducts. Furthermore, protonation increases the

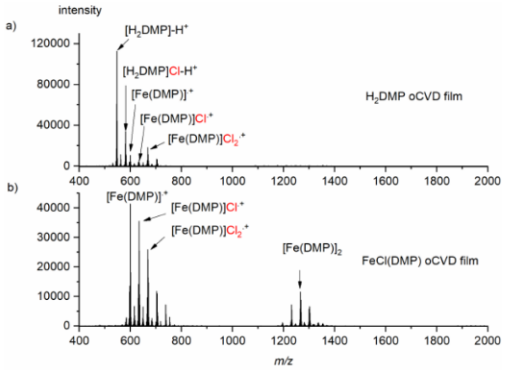

Figure 2. *LDI-HRMS of H_2DMP and FeCl(DMP) oCVD films. H_2DMP spectrum shows the formation of FeCl(DMP) due to metalation by $FeCl_3$.*

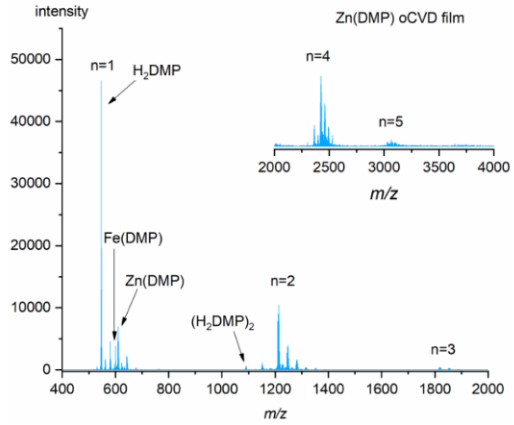

Figure 3. *LDI-HRMS spectra of the Zn(DMP) oCVD film in the 400-2000 and 2000-4000* m/z. The two spectra are acquired in separate scanning events. The analysis highlight the demetalation of the porphyrin and the substitution of the zinc with the iron.

oxidation potential hindering the polymerization reaction. XPS analysis confirms also the metalation/protonation of the porphyrin core for H_2DMP. H_2DMP possesses two inequivalent nitrogen atoms while $[H_4DMP]^{2+}$ or the metalated FeCl(DMP) possess four equivalent nitrogen atoms. The two XPS signals observed for sublimed H_2DMP (400.4 eV and 398.4 eV) converge to one single signal (399.1 eV) for the oCVD H_2DMP film (Figure S15). This confirms the formation of H_4DMP^{2+} and FeCl(DMP) (FeCl(DMP) oCVD film N_{1s} signal at 399.2 eV) (Figure S16).

The mass spectrum of FeCl(DMP) oCVD film shows the formation of dimeric species (Figure 2b). Simulation of the isotopic pattern allows to assign the peak to doubly and triply-linked porphyrins (Figure S8a). The low polymerization degree could be rationalized with the higher oxidation potential of FeCl(DMP) compared to the other cations (Table 1) and with the formation of both $[Fe^{III}Cl(DMP^{\bullet})]^+$ porphyrin radical cation and $[Fe^{IV}(DMP)]^+$ (vide infra).

The LDI-HRMS spectrum of Pd(DMP) exhibits signals related to the formation of oligomers up to pentamers attributed, on the basis of the isotopic pattern simulation, to be exclusively doubly-linked. (Figure S9 and S10). On the other hand, Ni(DMP), Co(DMP) and Cu(DMP) exhibit the formation of both doubly and triply-linked oligomers (Figure S8 and S9).

Finally, Zn(DMP) oCVD film exhibit signals of oligomeric species (Figure 3) but a slightly different reactivity when compared to the other metallo-porphyrins. The mass spectra confirm the regioselectivity of zinc porphyrins in oCVD exhibiting the formation of pure triply-linked porphyrin tapes (Figure S11). Secondly, the zinc porphyrin is subject to demetalation of the core yielding H_2DMP that is detected as main ion in the monomer mass range (Figure 3). Although the intensity of the signal in the mass spectra is proportional to the concentration of the species, it also depends on the species ionizability. Considering the different nature of the two ionization processes (protonation vs radical cation formation) the LDI-HRMS spectrum does not provide an accurate description of the concentration of the species in the film. The spectrum also suggests the presence of FeCl(DMP). HCl produced during the oCVD process might cause the demetalation of zinc porphyrins. Following, similarly to the H_2DMP case, Fe^{II} ions can react to form iron porphyrin complexes. Analogous reactions are observed in the oligomeric range. Demetalation of Zn(DMP) is confirmed by XPS analysis that reveals a general broadening of the Zn 2p peaks in the Zn(DMP) oCVD film, while the N 1s peak exhibits both a broadening and a new peak at higher binding energy (400.3 eV) assigned to the partial demetalation of the porphyrin core (Figure S14).

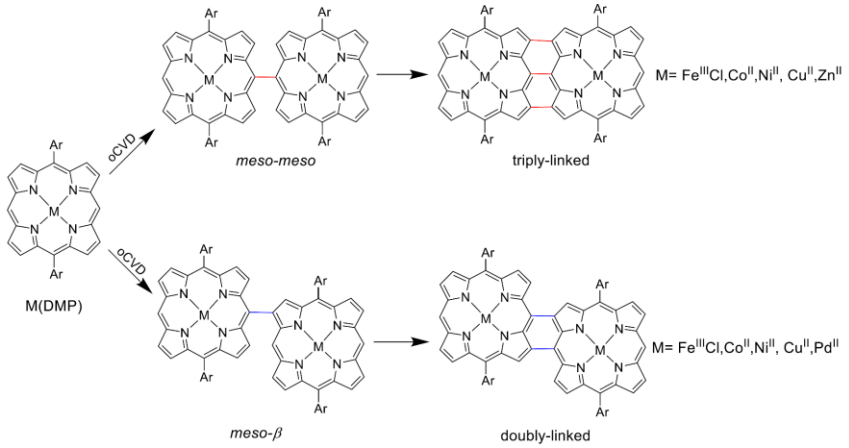

***Figure 4**. Products obtained by oCVD of porphyrins. The formation of doubly or triply-linked porphyrin tapes is dependent on the first step of the oxidative coupling leading to the formation meso-meso or meso-β bonds. The regioselectivity of the reaction varies with the metal center.*

Character of the radical cation and regioselectivity

The generally accepted reaction mechanism consists of a nucleophilic attack from a neutral porphyrin to a porphyrin radical cation.[6,7,10,19,31] In most cases, the porphyrin's *meso* position is the most electron-rich site, causing the *meso*-position to act as nucleophilic site in the coupling reaction. Thus, the regioselectivity depends on the symmetry of the SOMO of the radical cation defining the location of the electrophilic site. Porphyrins possess two types of occupied frontier orbitals: a_{1u} orbitals bearing large orbital coefficients on the β positions and a_{2u} orbitals with large orbital coefficients in the *meso* position. Thus, the selection between an attack to the *meso* or β position (leading to triply and doubly linked porphyrin tapes respectively) (Figure 4) depends on the relative energy of the a_{2u} and a_{1u} orbitals defining the character of the radical cation.[6,7] Unfortunately, the attribution of the product of oxidation of metalloporphyrins is not trivial, highly debated in literature and depending on the nature of the cation, substituents, ligands and physical state (solution, gas or solid).[37–42] Finally, in case of redox active metal cations, also the oxidation of the metal center can occur.[39–41,43]

Zheng, Zhu and co-workers suggested that the character of the frontier orbitals could be indirectly observed from the oxidation potential reflecting the position of the frontier orbital.[7] Particularly, once the porphyrin substituents pattern is fixed, the metal cations interact exclusively with the a_{2u} orbitals since a_{1u} orbitals possess a node on the four nitrogen atoms.[44] As a result, a decrease of the oxidation potential should corresponds to higher energy of the a_{2u} compared to the a_{1u} orbitals, while an increase of the oxidation potential relates a lowering in the energy of the a_{2u} orbital. Therefore, to gain information on the position of the frontier orbitals of the different DMPs, is interesting to observe the of the first oxidation potential ($E_{1/2}$) of the monomers measured by cyclic voltammetry in CH_2Cl_2/[^{n}Bu$_4$N][PF_6] (Figure S12).

The Zn^{II} porphyrin exhibits a low oxidation potential, i.e. 0.40 V (Table 1). Zn^{II} diphenyl porphyrins radical cation are also known to host the unpaired electron in the a_{2u} orbital.[8] Contrarily, the more electronegative Pd^{II} ion increase the oxidation potential of the porphyrins (0.58 V). Pd^{II} diphenyl porphyrins radical cation are known to host their unpaired electron in the a_{1u} orbital.[6,45] Our experiments are in agreement with these results showing the formation of pure doubly and triply-linked porphyrin tapes respectively for Pd(DMP) and Zn(DMP).

Cu^{II} and Ni^{II} porphyrins possess intermediate oxidation potential suggesting a_{1u} and a_{2u} orbitals closer in energy (Table 1). Based on resonance Raman spectroscopy evidences, Spiro and co-workers suggested that Cu^{II}, Ni^{II} and $Fe^{III}Cl$ tetraphenyl porphyrins are subject to pseudo-Jahn-Teller distortions upon oxidation.[40] As a result the distortion, the symmetry is lowered and the A_{2u} and A_{1u} states are mixed yielding mixed a_{1u}/a_{2u} radical cations character.[40] This is only possible when the a_{1u} and a_{2u} orbitals are close in energy. We recently proved that this effect is responsible for the formation of both doubly and triply-linked porphyrin tapes in the oCVD of Ni^{II} diphenyl porphyrins.[31] We suggest a similar effect on Cu^{II} diphenyl porphyrins since both solution based [11,12,45] and oCVD experiments shows the formation of both doubly and triply-linked porphyrin tapes.

Co(DMP) and FeCl(DMP) oxidation product in the gas phase

The cobalt porphyrin exhibiting the lowest oxidation potential of the series (Table 1), yields both doubly and triply-linked porphyrin tapes. The reason of this discrepancy might be found in the product of the first oxidation of the porphyrin. Indeed, Co(DMP) cyclic voltammogram shows a distance between the anodic and cathodic peak around 200 mV suggesting irreversible first oxidation products. In Co^{II} porphyrins the first oxidation is usually attributed to the oxidation of the cobalt metal center from Co^{II} to Co^{III}. Kadish, Sankar et al. recently observed an equilibrium between the Co^{III} porphyrin and the porphyrin radical cation $[Co^{II}P^{\bullet}]^+$ in the presence of non-coordinating solvents.[43] This equilibrium suggests that the cobalt *d* orbitals and the porphyrin frontier orbitals are close in energy. Due to the vacuum operating conditions used in oCVD, any coordinating ligand effect can be neglected during the dehydrogenative coupling of Co^{II}(DMP). Consequently, the existence of an equilibrium between $[Co^{III}(DMP)]^+$ and $[Co^{II}(DMP^{\bullet})]^+$ provides a suitable description of the oxidized states of the Co(DMP) during the deposition. Furthermore, the mere formation of $[Co^{III}(DMP)]^+$ would be incompatible with the oxidative coupling observed by UV/Vis/NIR and LDI-HRMS for Co(DMP). XPS analysis of the Co_{2p} peak of the Co(DMP) oCVD film reveals a broadening and a shift towards higher binding energy (780.9 to 781.7 eV) compared the sublimed Co^{II}(DMP) (Figure S13). We attributed this change to the presence of both Co^{II} and Co^{III} porphyrins supporting the valence isomeric nature of the Co(DMP) first oxidation products (Co^{III}(DMP) / $[Co^{II}(DMP)^{\bullet}]^+$) in the gas phase.

In addition, the N 1s signal exhibits a new contribution at higher binding energy confirming the presence of nitrogen atoms with increased positive charge (Figure S13). Similarly to Co^{II} porphyrins, the nature of the oxidation products of Fe^{III} porphyrins is debated in the literature.[41]

The oxidation product of iron(III) chlorido *meso*-tetraphenyl porphyrin ($Fe^{III}Cl$(TPP)) is the $[Fe^{III}Cl(TPP^{\bullet})]^+$ radical cation valence isomer.[46] Differently, an equilibrium between $[Fe^{IV}(N_3)_2(P^{Mes})]^+$ and the $[Fe^{III}(P^{Mes\bullet})]^+$ radical cation was reported for cationic iron *meso*-tetramesityl porphyrins bearing two axial azido ligands. [41] Furthermore, the $[Fe^{IV}(N_3)_2(P^{C6H4CF3})]^+$ valence isomer is favoured over the

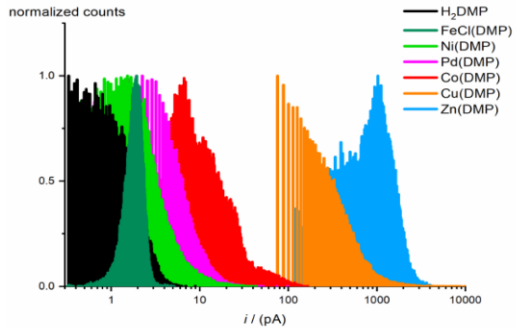

***Figure 5**. Histograms of the current obtained from the C-AFM measurements (Logarithmic scale). Cu(DMP) and Zn(DMP) exhibit the highest currents in the series.*

$[Fe^{III}(N_3)_2(P^{C6H4CF3\bullet})]^+$ radical cation with an electron-deficient 5,10,15,20-(4-trifluoromethylphenyl) porphyrin as a result of lower energy a_{2u} orbitals. [41]. A similar equilibrium could also be expected in 5,15-(dimesityl)porphyrins possessing only two substituents on the *meso* positions (i.e. lower a_{2u} orbital).

Consequently, the poor degree of polymerization achieved in the oCVD of FeCl(DMP) could be ascribed to an isomer valence equilibrium favouring the formation of the $[Fe^{IV}Cl(DMP)]^+$ valence isomer and/or to the high oxidation potential of the monomer. In contrast to the Co(DMP) case, XPS does not provide information on the distribution of Fe^{III} and Fe^{IV} porphyrins since the iron region is dominated by the contribution related to the employed oxidant. In spite of the lower and higher oxidation potential respectively, Co(DMP) and FeCl(DMP) exhibit a behaviour similar to Cu(DMP) and Ni(DMP). This is probably related to the equilibrium between $[Co^{III}(DMP)]^+/[Co^{II}(DMP^\bullet)]^+$ and $[Fe^{IV}(DMP)]^+/[Fe^{III}(DMP^\bullet)]^+$ yielding a situation similar to the Cu^{II} and Ni^{II} case.

Regioselectivity and electronic conductivity

Conductivity atomic force microscopy measurements evidenced a strong influence of the central metal cation on the electrical properties of the oCVD thin films obtained from porphyrins bearing an identical substituent pattern. Analysis of the current obtained by C-AFM notably a higher conductivity for the Zn(DMP) oCVD film (Figure 5 & S5). Porphyrins yielding both doubly and triply-linked porphyrin tapes, i.e. Cu(DMP) and Co(DMP), exhibit intermediate values, followed by Pd(DMP) that solely yields doubly-linked porphyrins. As expected from the poor or absent polymerisation observed by LDI-HRMS, low currents are obtained by H_2DMP and FeCl(DMP) oCVD films. On the other hand, Ni(DMP), shown to form both doubly and triply-linked porphyrin tapes, exhibits a conductivity in the order the one achieved from Pd(DMP). We related these differences in conductivity between the different porphyrins to two aspects: i) different regioselectivity towards triply-linked porphyrin tapes and ii) different chain lengths. In fact, several reports showed that triply-linked porphyrin tapes exhibit outstanding electrical properties.[4,5,47,48] In triply-linked porphyrin tapes the conductance attenuation factor decreases with length leading to improved conductivity in longer tapes.[4,47] This aspect was related to the decrease of the HOMO-LUMO gap compensating for the increasing tunnelling distance. Accordingly, it is not surprising that Co(DMP), Cu(DMP) and Zn(DMP) oCVD films that exhibit more intense absorption in the NIR due to formation of longer triply linked tapes, also present higher conductivities. Contrarily, Ni(DMP) and Pd(DMP), exhibiting lower NIR absorption attributed to shorter and doubly-linked chains, show lower conductivities. Finally, in spite of its strong NIR absorption, Co(DMP) films exhibit lower conductivity compared to Cu(DMP) and Zn(DMP) films. This could be rationalized, with i) different doubly/triply-linked porphyrin ratios in the film and ii) Co^{II}/Co^{III} redox activity acting as "electron trap" due to the higher positive charge of the Co^{III} species. Furthermore, the different conductivities in the oCVD film can be rationalized in terms of axial ligation. Cu(DMP) and Zn(DMP) favour 5-coordinate complexes over the 6-coordinate Co(DMP).[49] The formation of 6-coordinate complexes with axial ligands (e.g. H_2O in ambient condition) would lead to an increase of the intermolecular distances in the film, which was previously shown to negatively affect the conductivity in porphyrin tapes thin films.[30] Similarly, 4-coordinate Pd(DMP) complexes should present smaller intermolecular distances with respect to the 6-coordinate Ni(DMP) complexes.

Conclusions

In conclusion, we showed that several M^{II} cations, i.e. Co^{II}, Ni^{II}, Cu^{II}, Zn^{II} and Pd^{II}, in porphyrins with free *meso* and *β* positions readily yields multiply-linked porphyrin tapes thin films via oxidative chemical vapour deposition. The metal center affects the regioselectivity of the reaction. Zn(DMP) yields triply-linked porphyrin tapes during the oCVD process. On the contrary, Pd(DMP) yields only doubly-linked porphyrin tapes. Both Zn^{II} Pd^{II} and Cu^{II} porphyrins exhibit in oCVD a regioselectivity similar to solution based approaches.[1,10-12] For the first time we also report the formation of cobalt porphyrin tapes. The formation of porphyrin tapes is possible thanks to the equilibrium between Co^{III}(DMP) and $[Co^{II}(DMP^\bullet)]^+$ favouring the radical cation valence isomer in the gas phase. On the contrary, the high redox potential of Fe^{III} porphyrins and the equilibrium between the $[Fe^{III}(DMP^\bullet)]^+$ radical cation and $[Fe^{IV}(DMP)]^+$ yields low degree of polymerization. Probably because of its basicity, the free-base porphyrins H_2DMP does not yield porphyrin tapes in oCVD. Zn(DMP) and its films are more sensible to the presence of the HCl produced during the oxidative coupling causing the demetalation of the porphyrin core. Finally, C-AFM measurements show improved electrical conductivity for Zn(DMP) probably because of the higher conversion into triply-linked porphyrin tapes, which are known to exhibit higher conductivity with longer chain length.

Experimental Section

Materials. All the 5,15-(dimesityl) metalloporphyrins were obtained by PorphyChem and used without further purifications (98%). Iron(III) chloride (97%) was obtained by Sigma-Aldrich and used without further purifications. Dichloromethane used for the cyclic voltammetry experiments was dried with CaH_2 and distilled prior to use.

Preparation of the films. The films were prepared in a custom built oCVD reactor (Scheme S1). The deposition experiments were carried out in argon (Air Liquide, 99.999 %) at a pressure of 10^{-3} mbar. The evaporators, located at the bottom of the reaction chamber, were loaded with 10 mg of porphyrins and 150 mg of $FeCl_3$. The deposition time was 30 minutes in all experiments and microscope glass slides and silicon wafers were used as substrates. Further details are provided in table S1.

UV/Vis/NIR and thickness. The optical absorbance of the films was measured in the range of 250–2500 nm with a UV/Vis/NIR spectrophotometer (PerkinElmer, Lambda 950) with a 150 mm-diameter integrating sphere. The absorption spectra were recorded directly on the glass substrates. The thin films thicknesses were measured using a KLA-Tencor P-17 Stylus profiler.

C-AFM. Images of the topography and conductivity of the samples were simultaneously acquired using the C-AFM mode of an Innova AFM (Bruker). Conductive AFM tips ElectriMulti75-G from BudgetSensors coated with a layer of 5 nm chromium and 25 nm of platinum with nominal spring constants of 3 N/m and nominal radius <25 nm were used. Images of a 2x2 µm² area with a resolution of 256x256 pixels were taken at a scan rate of 0.5 Hz. Samples were deposited on monocrystalline silicon wafers coated with platinum and connected to the conductive stage via a silver colloidal ink. The topography was obtained by maintaining the tip deflection constant (0.25 V) via the feedback loop of the AFM acting on the piezo Z direction. A bias of +4 V was applied to the back

electrode of the samples while the grounded conductive tip was collecting electrons for the current measured by an amplifier (DLPCA-200, Femto). A 109 VA-1 amplification was used for the pA current range and a 107 VA-1 for the ones in nA range and the signal output was then transmitted to the AFM electronic and recorded. The reported average and standard deviation values of conductivity and roughness (Ra) consider at least 4 images in each sample for reliable results. Noise on current detection is appearing at low values, this is close to the limit of noise of the amplifier. A 80 nm wavelength filter is apply before to remove this noise prior to roughness measurement

Helium Ion Microscopy. The images were acquired with a ZEISS ORION Nanofab Helium Ion Microscope (HIM). In a HIM, contrast is essentially due to topography and composition of the sample. He^+ or Ne^+ ions are produced in the Gas Field Ionization Source (GFIS). The upper part of the instrument contains a tungsten filament. Its tip consists only of three atoms (trimer) and is set under a positive high voltage with respect to the extraction electrode and cryo-cooled simultaneously. Surrounded by He or Ne gas atoms these become ionized at the tip apex and are accelerated in this case with 30 keV towards the sample. The trimer is emitting three beamlets whereas one atom is selected as the main emitter. While raster scanning over the surface secondary electrons (SE) are produced by impacting He^+ or Ne^+ primary ions and are detected by a Everhart-Thornley detector. A spatial resolution of down to 0.5 nm is achievable with the HIM. Advantages compared to a regular scanning electron microscope (SEM) are the high surface sensitivity and large depth of field favouring topographic imaging.[50,51] For this set of images, the primary ion current was varying between 0.1 and 0.6 pA. The working distance was at around 17 mm. Since a prototype instrument was used, higher sample stage positions and therefore smaller working distances were not feasible in the current prototype setup.

Mass spectrometry. Atmospheric-pressure LDI-HRMS was employed for characterisation of the coatings. HRMS analyses were performed with an LTQ/Orbitrap Elite Hybrid Linear Ion Trap-Orbitrap Mass Spectrometer from Thermo Scientific (San Jose, CA) coupled with an AP-LDI (ng) UHR source from MassTech Inc (Columbia, MA) with a 355 nm Nd:YAG laser. The thin films were directly probed without any matrix deposition by the laser following a spiral motion during 30 s per sample. An in-source decay (ISD) of 70 V was applied to the samples in order to prevent any formation of non-covalent porphyrin clusters that could interfere with the distribution of the oligomers. A maximum injection time of 800 ms and a resolving power of 240000 at m/z 400 in the normal mass range (m/z 300–2000) and the high mass range (m/z 1800–4000) were employed for the HRMS analyses.

Cyclic voltammetry. Cyclic voltammetric measurements were carried out with a BioLogic SP-50 voltammetric potentiostat. The porphyrins were dissolved (1 mM) in CH_2Cl_2 containing 0.1 M $[n\mathrm{Bu_4N}][PF_6]$ as supporting electrolyte. A platinum working electrode, a platinum wire counter electrode and a 0.01 M $Ag/AgNO_3$ reference electrode were used for the experiments. Cyclic voltammograms were recorded at 100 mVs^{-1} scan rate. Ferrocene was employed as an internal reference redox system. All the measurements are performed under inert atmosphere in a glove box.

Acknowledgment. We gratefully acknowledge the financial support of the Luxembourg National Research Fund (http://fnr.lu) through the POLYPORPH project (C15/MS/10340560/POLYPORH/ Boscher). D. El Assad and Dr. Gilles Frache and Dr. Jerome Guillot from LIST are acknowledged for insightful discussions and acquisition of the mass and XPS spectra.

References

[1] A. Tsuda, A. Osuka, *Science* **2001**, *293*, 79–82.
[2] M. O. Senge, M. Fazekas, E. G. A. Notaras, W. J. Blau, M. Zawadzka, O. B. Locos, E. M. Ni Mhuircheartaigh, *Adv. Mater.* **2007**, *19*, 2737–2774.
[3] H. S. Cho, D. H. Jeong, S. Cho, D. Kim, Y. Matsuzaki, K. Tanaka, A. Tsuda, A. Osuka, *J. Am. Chem. Soc.* **2002**, *124*, 14642–14654.
[4] E. Leary, B. Limburg, A. Alanazy, S. Sangtarash, I. Grace, K. Swada, L. J. Esdaile, M. Noori, M. T. González, G. Rubio-Bollinger, H. Sadeghi, A. Hodgson, N. Agraït, S. J. Higgins, C. J. Lambert, H. L. Anderson, R. J. Nichols, *J. Am. Chem. Soc.* **2018**, *140*, 12877–12883.
[5] G. Sedghi, L. J. Esdaile, H. L. Anderson, S. Martin, D. Bethell, S. J. Higgins, R. J. Nichols, *Adv. Mater.* **2012**, *24*, 653–657.
[6] Y. Nakamura, N. Aratani, A. Tsuda, A. Osuka, K. Furukawa, T. Kato, *J. Porphyrins Phthalocyanines* **2003**, *7*, 264–269.
[7] C.-M. Feng, Y.-Z. Zhu, S.-C. Zhang, Y. Zang, J.-Y. Zheng, *Org. Biomol. Chem.* **2015**, *13*, 2566–2569.
[8] N. Aratani, A. Osuka, *Chem. Rec.* **2003**, *3*, 225–234.
[9] A. Tsuda, Y. Nakamura, A. Osuka, *Chem. Commun.* **2003**, 1096–1097.
[10] A. Tsuda, A. Nakano, H. Furuta, H. Yamochi, A. Osuka, *Angew. Chem. Int. Ed.* **2000**, *39*, 558–561.
[11] B. J. Brennan, M. J. Kenney, P. A. Liddell, B. R. Cherry, J. Li, A. L. Moore, T. A. Moore, D. Gust, *Chem. Commun.* **2011**, *47*, 10034–10036.
[12] B. J. Brennan, J. Arero, P. A. Liddell, T. A. Moore, A. L. Moore, D. Gust, *J. Porphyrins Phthalocyanines* **2013**, *17*, 247–251.
[13] D. Y. Kim, T. K. Ahn, J. H. Kwon, D. Kim, T. Ikeue, N. Aratani, A. Osuka, M. Shigeiwa, S. Maeda, *J. Phys. Chem. A* **2005**, *109*, 2996–2999.
[14] K. Rybicka-Jasińska, W. Shan, K. Zawada, K. M. Kadish, D. Gryko, *J. Am. Chem. Soc.* **2016**, *138*, 15451–15458.
[15] D. Khusnutdinova, B. L. Wadsworth, M. Flores, A. M. Beiler, E. A. Reyes Cruz, Y. Zenkov, G. F. Moore, *ACS Catal.* **2018**, *8*, 9888–9898.
[16] E. Rose, B. Andrioletti, S. Zrig, M. Quelquejeu-Ethève, *Chem. Soc. Rev.* **2005**, *34*, 573–583.
[17] S. Lin, C. S. Diercks, Y.-B. Zhang, N. Kornienko, E. M. Nichols, Y. Zhao, A. R. Paris, D. Kim, P. Yang, O. M. Yaghi, C. J. Chang, *Science* **2015**, *349*, 1208–1213.
[18] S. Preiß, A. Päpcke, L. Burkhardt, L. Großmann, S. Lochbrunner, M. Bauer, T. Opatz, K. Heinze, *Chem. Eur. J.* **2019**, *25*, 5940–5949.
[19] A. Osuka, H. Shimidzu, *Angew. Chem. Int. Ed. Engl.* **1997**, *36*, 135–137 ; *Angew. Chem.* **1997**, *109*, 93–95;
[20] N. Yoshida, N. Aratani, A. Osuka, *Chem. Commun.* **2000**, 197–198.
[21] A. Tsuda, Y. Nakamura, A. Osuka, *Chem. Commun.* **2003**, *0*, 1096–1097.
[22] K. Baba, G. Bengasi, D. El Assad, P. Grysan, E. Lentzen, K. Heinze, G. Frache, N. D. Boscher, *Eur. J. Org. Chem.* **2019**, 2368–2375.
[23] G. Bengasi, K. Baba, G. Frache, J. Desport, P. Gratia, K. Heinze, N. D. Boscher, *Angew. Chem. Int. Ed.* **2019**, *58*, 2103–2108.
[24] J. P. Lock, S. G. Im, K. K. Gleason, *Macromolecules* **2006**, *39*, 5326–5329.
[25] L. M. Mateo, Q. Sun, S. Liu, J. J. Bergkamp, K. Eimre, C. A. Pignedoli, P. Ruffieux, S. Decurtins, G. Bottari, R. Fasel, T. Torres, *Angew.Chem. Int. Ed.* **2020**, *59*, 1334–1339; *Angew. Chem.* **2020**, *132*, 1350 – 1355.
[26] A. Wiengarten, K. Seufert, W. Auwärter, D. Ecija, K. Diller, F. Allegretti, F. Bischoff, S. Fischer, D. A. Duncan, A. C. Papageorgiou, F. Klappenberger, R. G. Acres, T. H. Ngo, J. V Barth, *J. Am. Chem. Soc.* **2014**, *136*, 9346–9354.
[27] B. Cirera, B. De La Torre, D. Moreno, M. Ondráček, R. Zbořil, R. Miranda, P. Jelínek, D. Écija, *Chem. Mater.* **2019**, *31*, 3248–3256.
[28] Y. He, M. Garnica, F. Bischoff, J. Ducke, M. Bocquet, M. Batzill, W. Auwärter, J. V Barth, *Nat. Chem.* **2017**, *9*, 33–38.
[29] M. Heydari Gharahcheshmeh, K. K. Gleason, *Adv. Mater. Interfaces* **2019**, *6*, 1801564.
[30] G. Bengasi, J. S. Desport, K. Baba, J. P. Cosas Fernandes, O. De

Castro, K. Heinze, N. D. Boscher, *RSC Adv.* **2020**, *10*, 7048–7057.
[31] G. Bengasi, K. Baba, O. Back, G. Frache, K. Heinze, N. D. Boscher, *Chem. Eur. J.* **2019**, *25*, 8313–8320.
[32] M. Grzybowski, B. Sadowski, H. Butenschön, D. Gryko, *Angew. Chem. Int. Ed.* **2020**, *59*, 2998–3027; *Angew. Chem.* **2020**, *132*, 3020 – 3050
[33] T. Ikeda, N. Aratani, A. Osuka, *Chem. Asian J.* **2009**, *4*, 1248–1256.
[34] S. G. Im, D. Kusters, W. Choi, S. H. Baxamusa, M. C. M. van de Sanden, K. K. Gleason, *ACS Nano* **2008**, *2*, 1959–1967.
[35] M. W. Chase Jr., C. A. Davies, J. R. Downey Jr., D. J. Frurip, R. A. McDonald, A. N. Syverud, *J. Phys. Chem. Ref. Data* **1985**, *14*, 903.
[36] T. Wijesekera, A. Matsumoto, D. Dolphin, D. Lexa, *Angew. Chem. Int. Ed. Engl.* **1990**, *29*, 1028–1030.
[37] A. Wolberg, J. Manassen, *Inorg. Chem.* **1970**, *9*, 2365–2367.
[38] D. Chatterjee, E. Balasubramanian, *J. Coord. Chem.* **1999**, *46*, 467–470.
[39] J. Seth, V. Palaniappan, D. F. Bocian, *Inorg. Chem.* **1995**, *34*, 2201–2206.
[40] R. S. Czernuszewicz, K. A. Macor, X. Y. Li, J. R. Kincaid, T. G. Spiro, *J. Am. Chem. Soc.* **1989**, *111*, 3860–3869.
[41] A. Ikezaki, M. Takahashi, M. Nakamura, *Chem. Commun.* **2013**, *49*, 3098–3100.
[42] W. F. Scholz, C. A. Reed, Y. J. Lee, W. R. Scheidt, G. Lang, *J. Am. Chem. Soc.* **1982**, *104*, 6791–6793.
[43] X. Ke, R. Kumar, M. Sankar, K. M. Kadish, *Inorg. Chem.* **2018**, *57*, 1490–1503.
[44] M. Gouterman, *J. Mol. Spectrosc.* **1961**, *6*, 138–163.
[45] M. Kamo, A. Tsuda, Y. Nakamura, N. Aratani, K. Furukawa, T. Kato, A. Osuka, *Org. Lett.* **2003**, *5*, 2079–2082.
[46] G. Buisson, A. Deronzier, E. Duee, P. Gans, J. C. Marchon, J. R. Regnard, *J. Am. Chem. Soc.* **1982**, *104*, 6793–6796.
[47] N. Algethami, H. Sadeghi, S. Sangtarash, C. J. Lambert, *Nano Lett.* **2018**, *18*, 4482–4486.
[48] D. H. Yoon, S. B. Lee, K. H. Yoo, J. Kim, J. K. Lim, N. Aratani, A. Tsuda, A. Osuka, D. Kim, *J. Am. Chem. Soc.* **2003**, *125*, 11062–11064.
[49] K. M. Kadish, K. M. Smith, R. Guilard, *The Porphyrin Handbook: Inorganic, Organometallic and Coordination Chemistry*, Academic Press, **2003**.
[50] T. Wirtz, O. De Castro, J.-N. Audinot, P. Philipp, *Annu. Rev. Anal. Chem.* **2019**, *12*, 523–543.
[51] G. Hlawacek, A. Gölzhäuser, *Helium Ion Microscopy*, Springer International Publishing, Cham, **2016**.

6 SUMMARY AND OUTLOOK

In this work, the synthesis of porphyrin tapes via oxidative chemical vapour deposition was performed for the first time. The study focused on five aspects of the oCVD of porphyrins:

- film characteristics,
- reaction mechanisms,
- role of the oxidant,
- role of the metal center,
- role of substituents.

First, the possibility to obtain porphyrin tapes by oCVD was demonstrated. This technique yields homogeneous nano-confined smooth films with extremely smooth surfaces. The obtained films can be deposited on virtually any thermostable substrate such as paper and polymers and exhibit NIR absorption and conductive behaviour.

The study also confirmed similarities between the reaction mechanisms of the oCVD and solution-based synthesis of porphyrin tapes. In both cases, the synthesis passes through the formation of a radical cation leading to nucleophilic attack of neutral porphyrins. However, vacuum conditions, i.e. the absence of solvents, seems to affect the regioselectivity of the reaction. In fact, the solvent can modify the order of the frontier orbitals yielding different regioselectivity. A key-role is played by the *meso*-position of the porphyrins that, being the most electron-rich position of the molecule, starts the nucleophilic attack. Tetraphenyl-*meso*-substituted porphyrins do not undergo oxidative polymerisation in oCVD. Finally, differently from solution-based approaches, the synthesis of porphyrin tapes in oCVD through $FeCl_3$ yields the cyclization of the phenyl ring on the porphyrin macrocycle.

This study showed that iron (III) chloride is an efficient oxidant for the formation of porphyrin tapes in oCVD. However, the oxidant exhibits a low selectivity towards dehydrogenative coupling yielding phenyl fused porphyrin and also chlorinated by-products. Although the cyclization can be easily avoided by means of *ortho*-phenyl

porphyrins (for instance mesityl groups), to date no solution to avoid formation of chlorinated products has been identified. Furthermore, increasing the amount of sublimed oxidant varies the unsaturation in the molecule, improving the molecular flattening and the electrical properties of the final film.

The influence of the molecular flattening was further elucidated by modifying the *meso*-substituent on the molecule. The presence of bulky substituents such as mesityl, di-*tert*-butyl-phenyl or dodecyl-oxyphenyl groups increases the distance between porphyrin tape chains hindering the electron transfer and reducing the electrical performances of the films. Contrarily, phenyl ring substituents containing free *ortho* positions further improve the conductivity thanks to the "molecular flattening effect", which decreases the intermolecular distances.

Finally, the effect of the metal center was evaluated. For the first time the synthesis of cobalt porphyrin tapes was reported. *Free base* porphyrins do not yield porphyrin tapes in oCVD. This was attributed to the acid-base activity of the pyrrolic rings modifying the oxidation potential of the porphyrins. All the other investigated metallo porphyrins (M= $Fe^{III}Cl$, Co^{II}, Ni^{II}, Cu^{II}, Zn^{II}, Pd^{II}) exhibited activity in oCVD. A higher oxidation potential decreases the reactivity in oCVD as observed for iron(III) porphyrins. Poor regioselectivity was observed for cobalt(II), nickel(II), copper(II) and iron(III) porphyrins while palladium(II) and zinc(II) porphyrins exhibited a good selectivity towards the formation of doubly and triply-linked porphyrin tapes, respectively.

This study highlights that the major advantage of the oCVD approach compared to solution-based synthesis is that bulky solubilizing substituents are unnecessary. As a result, phenyl rings can be used to achieve higher electrical performances thanks to the small substituents. Furthermore, the phenyl ring cyclization (occurring only in oCVD) seems to improve the electrical properties of the film thanks to enhanced π–π interactions.

In conclusion, the oCVD is a suitable technique for the synthesis of porphyrin tape thin films on sensitive substrates. Their electrical a1nd optical properties were tested and the effect of the metal center and the reaction mechanism were investigated. This study

paves the way to the production of a new class of technological devices such as sensors, catalysts and NIR absorbers that are already under investigation in the hosting laboratory.

7 APPENDIX

7.1 Supporting information: Conductive Fused Porphyrin Tapes on Sensitive Substrates by a Chemical Vapor Deposition Approach

---

Angewandte Chemie
Eine Zeitschrift der Gesellschaft Deutscher Chemiker

Supporting Information

Conductive Fused Porphyrin Tapes on Sensitive Substrates by a Chemical Vapor Deposition Approach

*Giuseppe Bengasi, Kamal Baba, Gilles Frache, Jessica Desport, Paul Gratia, Katja Heinze, and Nicolas D. Boscher**

anie_201814034_sm_miscellaneous_information.pdf

Author Contributions

G.B. Data curation: Lead; Formal analysis: Lead; Writing—original draft: Lead; Writing—review & editing: Lead
K.B. Data curation: Supporting; Formal analysis: Supporting; Writing—original draft: Supporting; Writing—review & editing: Supporting
G.F. Data curation: Supporting; Formal analysis: Supporting; Methodology: Supporting; Validation: Supporting; Writing—review & editing: Supporting
J.D. Data curation: Supporting; Formal analysis: Supporting; Methodology: Supporting; Writing—review & editing: Supporting
P.G. Data curation: Supporting; Formal analysis: Supporting; Methodology: Supporting; Writing—review & editing: Supporting
K.H. Data curation: Supporting; Methodology: Supporting; Supervision: Supporting; Validation: Supporting; Writing—review & editing: Supporting
N.B. Conceptualization: Lead; Data curation: Supporting; Formal analysis: Supporting; Funding acquisition: Lead; Investigation: Equal; Methodology: Lead; Project administration: Lead; Resources: Lead; Supervision: Lead; Validation: Lead; Writing—original draft: Supporting; Writing—review & editing: Equal.

Table of Contents

Experimental Procedures

Oxidative Chemical Vapor Deposition

The oCVD experiments described in this paper were performed in a custom-built oCVD reactor (Figure 1). The reactor body is a stainless steel cube of 41 cm on each side (Kurt J. Lesker Co.) equipped with a dry scroll pump (Varian) and a turbomolecular pump (Agilent) to achieve high vacuum. A butterfly type throttling valve (VAT) and a microleak valve fed with argon (Air Liquide, 99.999 %) were used to maintain the pressure to 10^{-3} mbar for all the deposition experiments. Pressure was monitored by means of a baratron vacuum gauge (MKS). At the bottom of the chamber are two low temperature evaporation (LTE) point sources (Kurt J. Lesker Co.) to supply the porphyrin and the oxidant to a temperature-controlled substrate holder (Thermocoax) located approximately 20 cm above. For the preparation of the oCVD NiDPP coating, the evaporators were loaded with 10 mg of nickel(II) 5,15-(diphenyl)porphyrin (NiDPP) and 150 mg of $FeCl_3$ and heated to 250 °C and 170 °C, respectively. For the preparation of the oCVD NiDD*t*-BuPP coating, the evaporators were loaded with 10 mg of nickel(II) 5,15-bis(di-3,5-tert-butylphenyl) porphyrin (NiDDt-BPP) and 150 mg of $FeCl_3$ and heated to 260 °C and 150 °C, respectively. Microscope glass slides, silicon wafers, printer paper sheets and organic field effect transistor chips (OFET) (Fraunhofer) were used as substrates. The substrate holder temperature was maintained at 130 °C and the deposition time was 30 minutes when coating the microscope glass slides, silicon wafers and OFET chips. The substrate holder temperature was maintained at 60 °C and the deposition time was 30 minutes when coating the printer paper sheets.

Materials and Reagents

NiDPP was prepared by metalation of 5,15-(diphenyl)porphyrin H_2DPP (PorphyChem, 98 %) with $Ni(OAc)_2 \times 4H_2O$.[1] NiDD*t*-BuPP was purchase from (PorphyChem, 98 %) and used as supply. The oxidant, iron(III) chloride ($FeCl_3$), was obtained from Sigma-Aldrich and used without further purification (97 %).

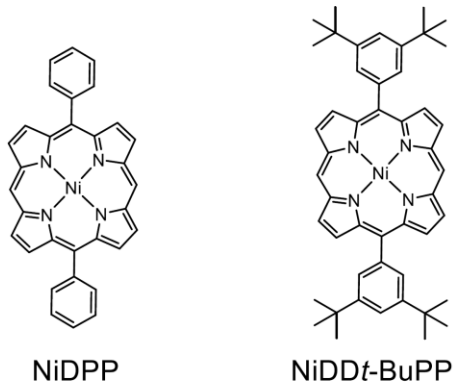

Scheme S1. Chemical structure for NiDPP and NiDD*t*-BuPP

Characterisation Methods

The thin films thicknesses were measured using a KLA-Tencor P-17 Stylus profiler.

The optical absorbance was measured in the range of 250–2000 nm using an UV-Vis-NIR spectrophotometer (Perkin Elmer, Lambda 950) with a 150 mm diameter integrating sphere. The absorption spectra were recorded directly on the glass substrates before and after rinsing the glass with dichloromethane (DCM), tetrahydrofuran (THF) and acetone. The coated glass substrates were rinsed by washing repeatedly with about 4 ml of solvent. The UV-Vis-NIR spectrum of the soluble phase of the coating in acetone or DCM was measured in quartz cuvettes of 3.5 mL and 1 cm light path.

X-ray photoelectron spectroscopy (XPS) analyses were performed on a Kratos Axis Ultra DLD instrument using a monochromatic Al Kα X-ray source ($h\upsilon$ = 1486.6 eV) at a power of 105 W. Charge calibration was accomplished by fixing the binding energy of carbon (C 1s) to 285.0 eV.

Laser desorption/ionization high-resolution mass spectra (LDI-HRMS) measurements were performed on an AP-MALDI UHR ion source from MassTech, Inc. coupled to an LTQ/Orbitrap Elite from Thermo Scientific. oCVD coated Si wafers were directly placed on the sample holder, adjusting the working distance to optimum. In source fragmentation (E = 70 V) was used to prevent the formation of clusters.

Gel permeation chromatography was performed using an Ultimate 3000 apparatus from ThermoFicher, equipped with an ERC differential refractive index detector and a UV detector. Samples were dissolved in tetrahydrofuran (THF) containing 1 vol.% of pyridine, as described elsewhere[2] and filtered over a 0.25 µm pore size membrane prior to injection. Flow rate was set to 1 $mL \cdot min^{-1}$. A mesopore column 3 µm (300 × 7.5 mm) from Agilent Technologies was used at 30°C.

Scanning electron microscopy images were recorded using a FEI Quanta 200F.

The 3D topographies were recorded in tapping mode at a scanning rate of 1 Hz with an atomic force microscope (AFM) MFP 3D Infinity.

Using a microprobe station (Cascade Microtech, PM8), 2-point current-voltage scans were recorded and the (lateral) thin-film conductivity was evaluated from a simple linear fit (Ohm's law). The measurements were performed at room temperature and under ambient atmosphere and the geometry of the channel was 2.5 µm (length) × 10 mm (total width) × 40 nm (height). The data were recorded using a Keithley (2401) sourcemeter by sweeping the voltage from –4 V to 4 V and back (hysteresis scan) at a scan rate of 500 mV s^{-1}. Contact resistance between the Au contacts and the thin film are neglected when using 2-point probe measurements (as opposed to 4-point probe measurements) because the film's conductivity was high enough to neglect this parameter.

Results and Discussion

NiDPP – UV-Vis-NIR spectrophotometry

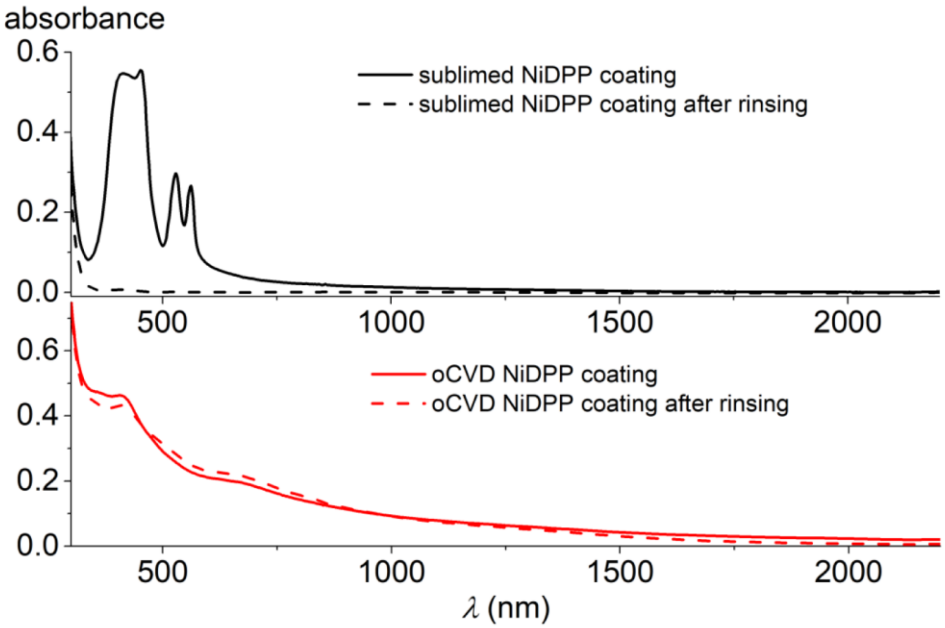

Figure S1. UV-Vis-NIR spectra of as-deposited (solid lines) and acetone rinsed (dashed lines) sublimed NiDPP coating (top) and oCVD NiDPP coating (bottom) on microscope glass slides.

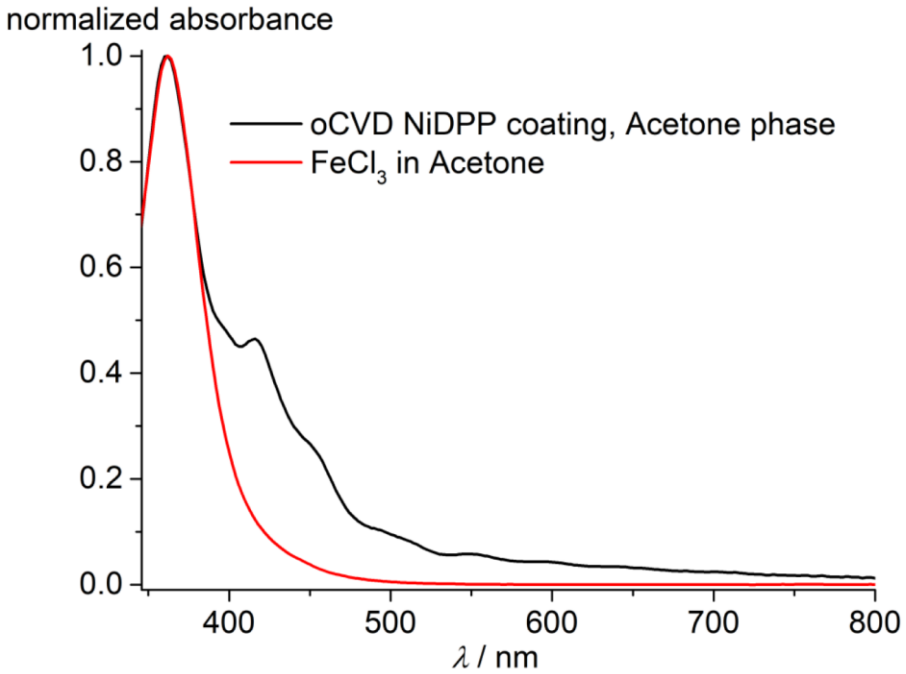

Figure S2. UV-Vis-NIR spectra of the soluble phase of the oCVD NiDPP coating in acetone (black) and its comparison to the spectrum of $FeCl_3$ in acetone (red). The analysis confirms the presence of unreacted $FeCl_3$ in the soluble phase of the oCVD NiDPP coating in acetone.

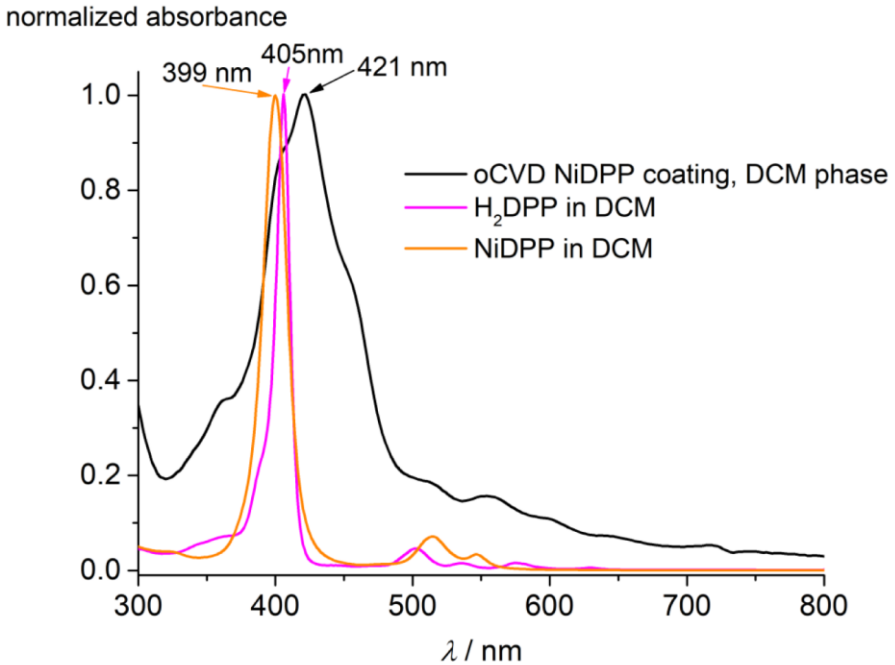

Figure S3. UV-Vis-NIR spectra of the soluble phase of the oCVD NiDPP coating in DCM (black) and its comparison to the spectra of NiDPP (orange) and H_2DPP (pink) in DCM. UV-Vis-NIR spectrum of the soluble phase of oCVD NiDPP coating in DCM exhibits a strong redshift and broadening and a change in the number of Q bands.

NiDPP – X-ray photoelectron spectroscopy

Table S1. Relative atomic concentration of the oCVD NiDPP coating and theoretical composition of NiDPP and fused NiDPP oligomers.

	Ni (%)	N (%)	C (%)	Cl (%)	Fe (%)
oCVD NiDPP coating	2.0	7.7	85.2	2.1	3.0
NiDPP & fused NiDPP oligomers	2.7	10.8	86.5	0.0	0.0

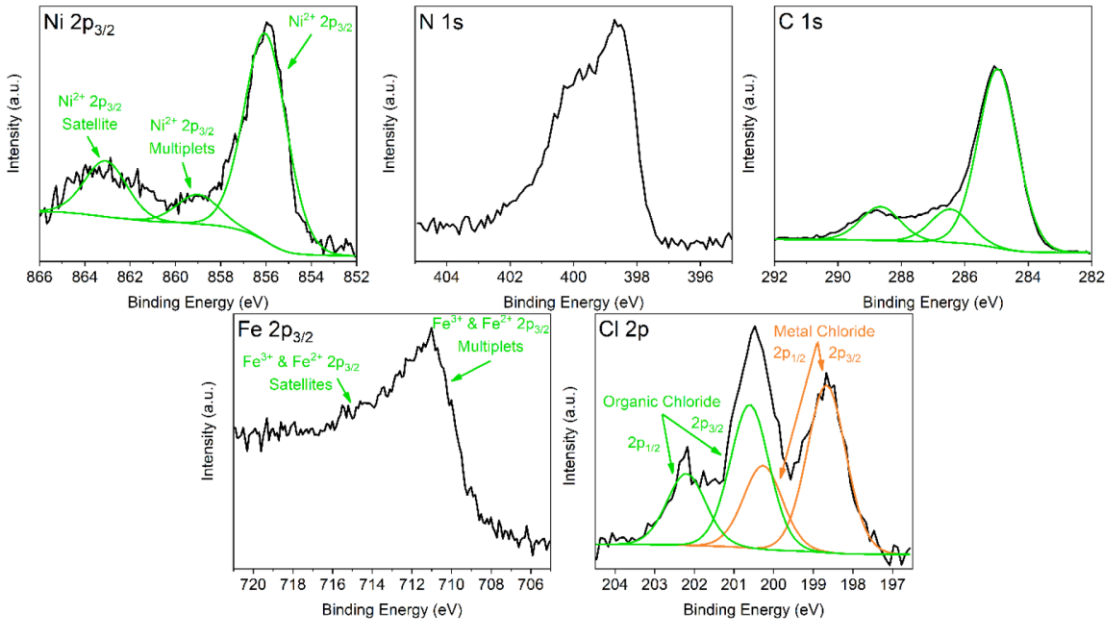

Figure S4. XPS spectra of the Ni $2p_{3/2}$, N 1s, C 1s, Fe $2p_{3/2}$ and Cl 2p core levels of the oCVD NiDPP coating. The binding energy of the main Ni $2p_{3/2}$ core level at 256.0 eV is consistent with the value reported for other nickel(II) porphyrins. Similarly to what observed for other nickel(II) porphyrins, the main Ni $2p_{3/2}$ peak is associated to weaker multiplets at higher binding energies (*ca.* 857.0 to 859.0 eV).[3] Interestingly, the Ni $2p_{3/2}$ XPS spectrum reveals the presence of a shake-up satellite at 863.1 eV, which has been reported for *β*-substituted nickel(II) porphyrins. This observation is consistent with the formation of triply linked *meso*-*meso*/*β*-*β*/*β*-*β* and doubly linked *meso*-*β*/*meso*-*β* linkages between the selected di-*meso*-subsituted nickel(II) porphyrin. The N 1s XPS spectrum shows a main peak at 399.1 eV, which is characteristic of the pyrrolic nitrogen in the nickel (II) porphyrins,[3] and a broadening towards higher binding energies that may arise from the multiplicity of bindings that affect the pyrrole rings (*i.e. meso*-*meso*, *β*-*β* and *meso*-*β* as well as chlorination at the *meso* and *β* positions). The C 1s XPS spectrum mainly shows three contributions associated to carbons pertaining to the phenyl rings (284.9 eV) and to the pyrrole rings (286.4 eV) and the pyrrole carbon shake-up transitions (288.6 eV) that is characteristic of porphyrins.[3] The Fe $2p_{3/2}$ reveal a main peak at 711.6 eV that can be attributed to unreacted ferric chloride ($FeCl_3$).[4] A second and poorly resolved contribution spreading around 716.0 eV is observed and associated to satellite peak.[4] The presence of ferrous chloride ($FeCl_2$) cannot be excluded, however, the Fe $2p_{3/2}$ multiplets that spread from 709.8 eV to 711.5 eV for $FeCl_2$ and from 711.3 eV to 714.2 eV for $FeCl_3$ complicate the attribution unreacted products and by-products.[4] Finally, the Cl 2p XPS spectrum reveals the presence of two chlorine environments associated to the metal chloride environment (Cl $2p_{3/2}$ = 198.7 eV and Cl $2p_{1/2}$ = 200.3 eV) related to the presence of unreacted $FeCl_3$ or $FeCl_2$ by-products in the oCVD NiDPP coating, and to organic chloride (Cl $2p_{3/2}$ = 200.6 eV and Cl $2p_{1/2}$ = 202.2 eV) related to the chlorination of the porphyrins.

NiDD*t*-BuPP – UV-Vis-NIR spectrophotometry

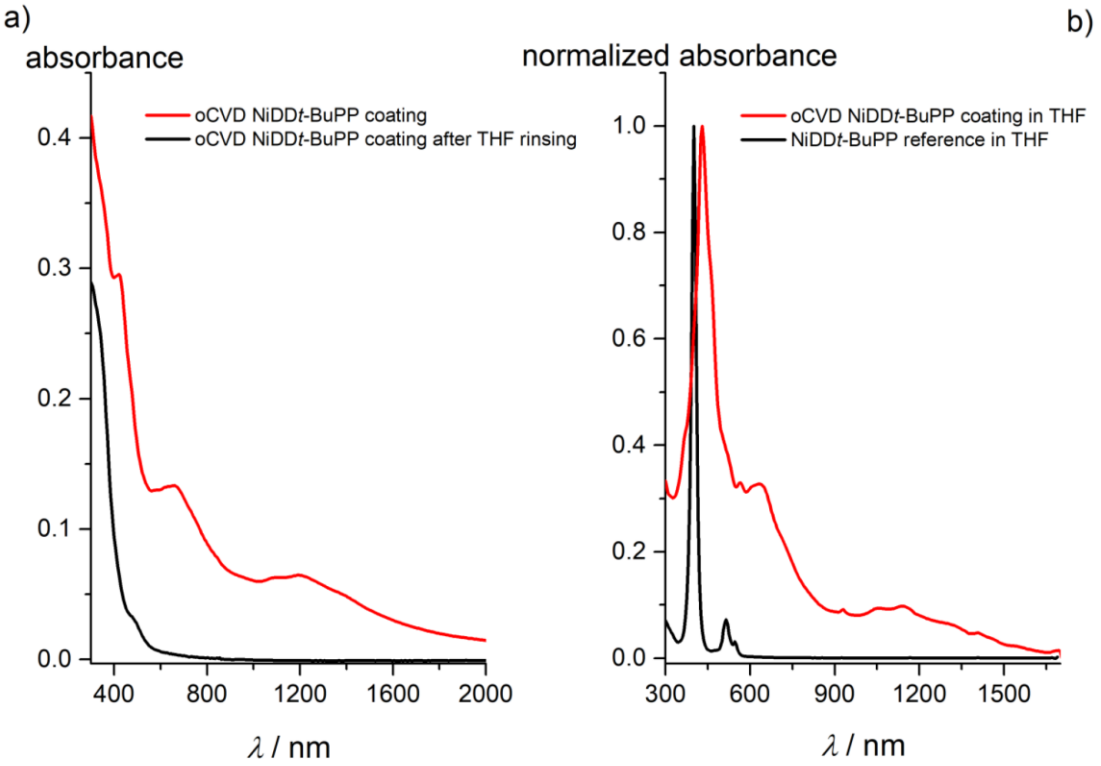

Figure S5. UV-Vis-NIR spectra of a) oCVD NiDD*t*-BuPP coating on glass as-deposited (red) and after rinsing with THF (black), b) the oCVD NiDD*t*-BuPP coating dissolved in THF (red) and NiDD*t*-BuPP monomer in THF (black). The oCVD NiDD*t*-BuPP coating exhibit NIR absorption similarly to the oCVD NiDPP coating. In contrast with the oCVD NiDPP coating, the oCVD NiDD*t*-BuPP coating is fully soluble in THF, exhibiting a strong redshift of the B-bands (30 nm) when compared to the pristine monomer dissolved in THF and a strong NIR absorption which is coherent with the formation of multiply fused porphyrin oligomers.

NiDD*t*-BuPP – Laser desorption ionization high-resolution mass spectrometry

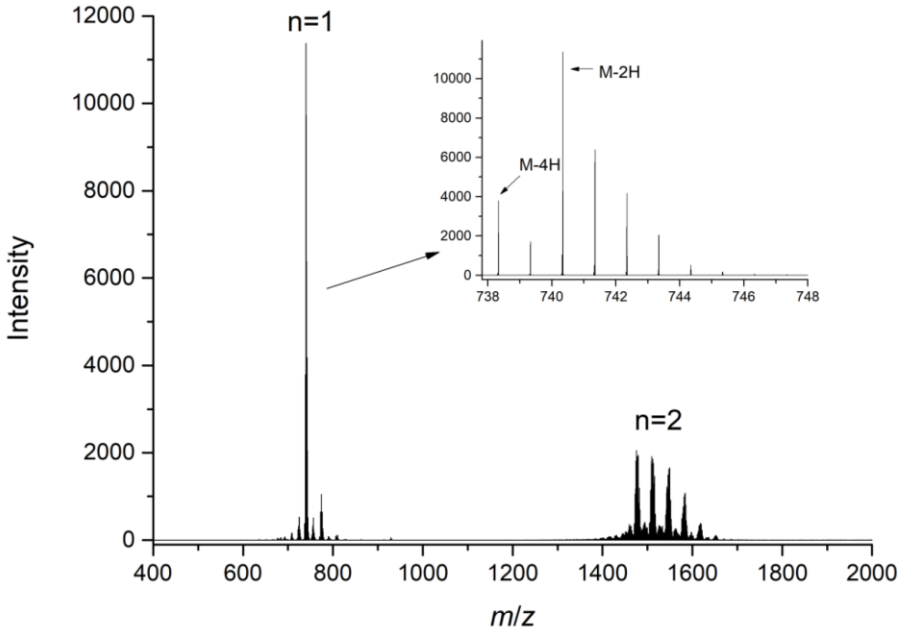

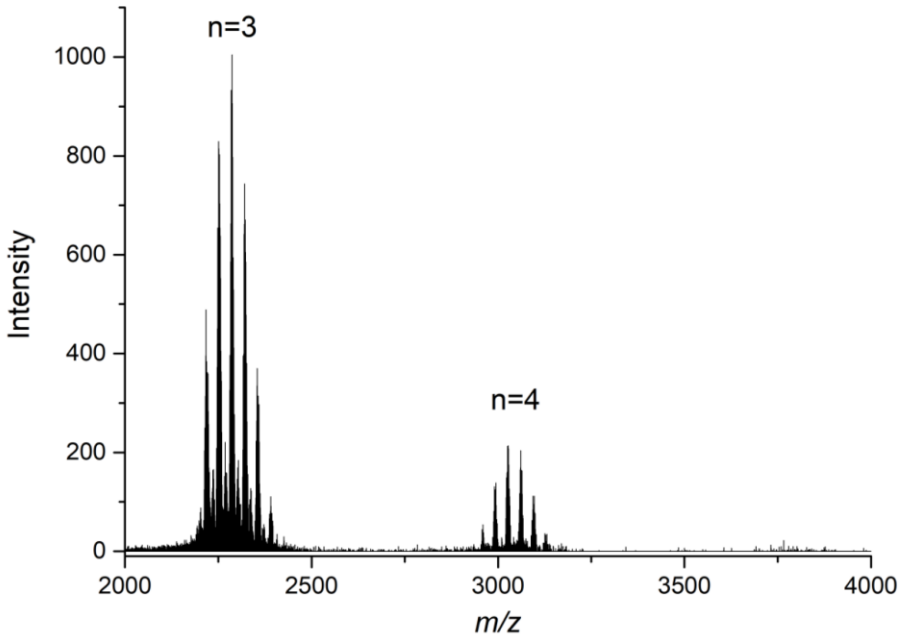

Figure S6. LDI-HRMS spectra of oCVD NiDD*t*-BuPP coating. It evidences the formation of oligomers. Similarly to the mass spectra of the oCVD NiDPP coating, the loss of 2H proportional to the number of phenyl rings is observed (inset). Chlorination of the NiDD*t*-BuPP monomer and P(NiDD*t*-BuPP) oligomers is observed.

NiDD*t*-BuPP – Gel permeation chromatography

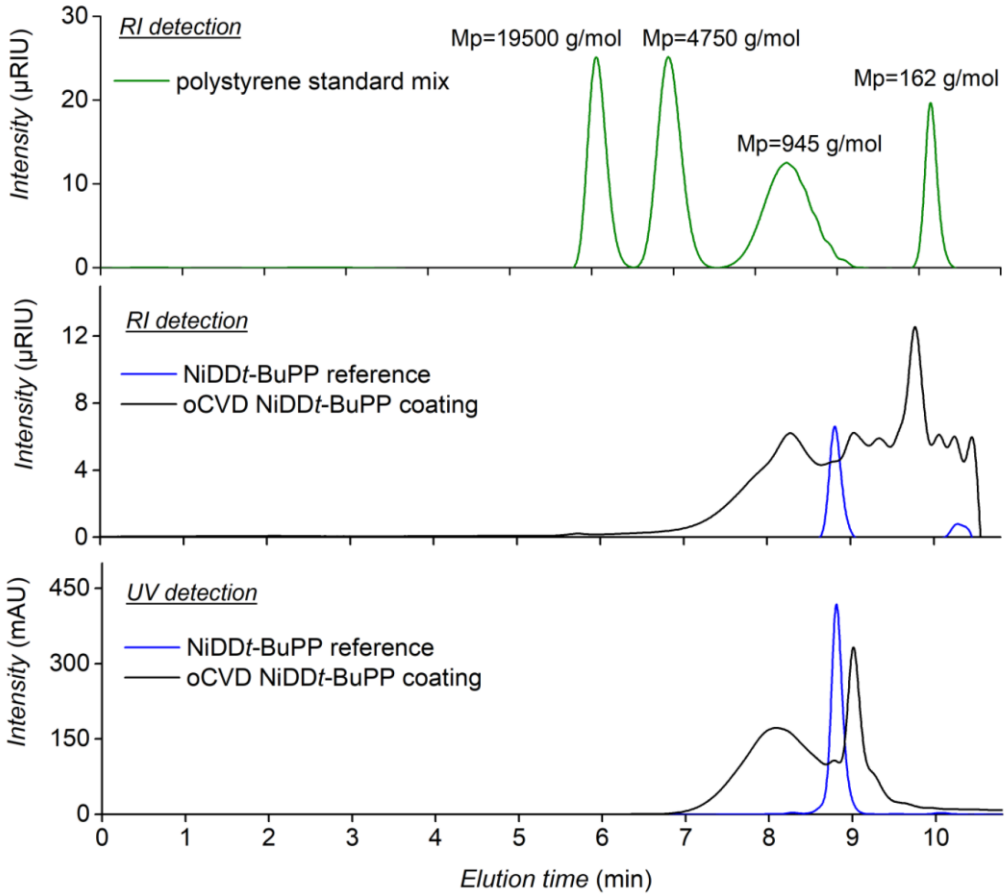

Figure S7. GPC chromatograms of NiDD*t*-BuPP monomer (blue) and its corresponding oCVD NiDD*t*-BuPP coating (black), with RI and UV (@ 430 nm) detection. The chromatogram of the oCVD NiDD*t*-BuPP coating shows a mass distribution up to 5,000 $g \cdot mol^{-1}$ when compared to polystyrene narrow standards. The UV-Vis detection allow the discrimination between the porphyrin-based components and the $FeCl_3$. It has to be noted that the comparison to polystyrene narrow standards yield an underestimation of the molecular weight of the NiDD*t*-BuPP monomer to a mass around 500 $g \cdot mol^{-1}$, while NiDDt-BuPP has a molecular weight of 743.67 $g \cdot mol^{-1}$. Interestingly, the GPC analysis highlighted the elution of porphyrinic compounds (evidenced from the UV-Vis detection at 430 nm) at higher retention times compared to the NiDD*t*-BuPP monomer. According to the LDI-HRMS analysis of the oCVD NiDD*t*-BuPP coating that does not reveal the presence of compounds with mass lower than $[(\text{NiDD}t\text{-BuPP}) - H_4]^+$ (Figure S6), the elution of porphyrinic compounds at higher retention times is unlikely to be related to formation of smaller porphyrin units, but might be related to the intramolecular cyclization between the phenyl ring and porphyrinic macrocycle that implies a more planar structure of the porphyrin. The new conformation could increase the interactions between the porphyrin units and the column stationary phase yielding an increase in the elution time despite the very similar hydrodynamic volume.

NiDPP – Laser desorption ionization high-resolution mass spectrometry

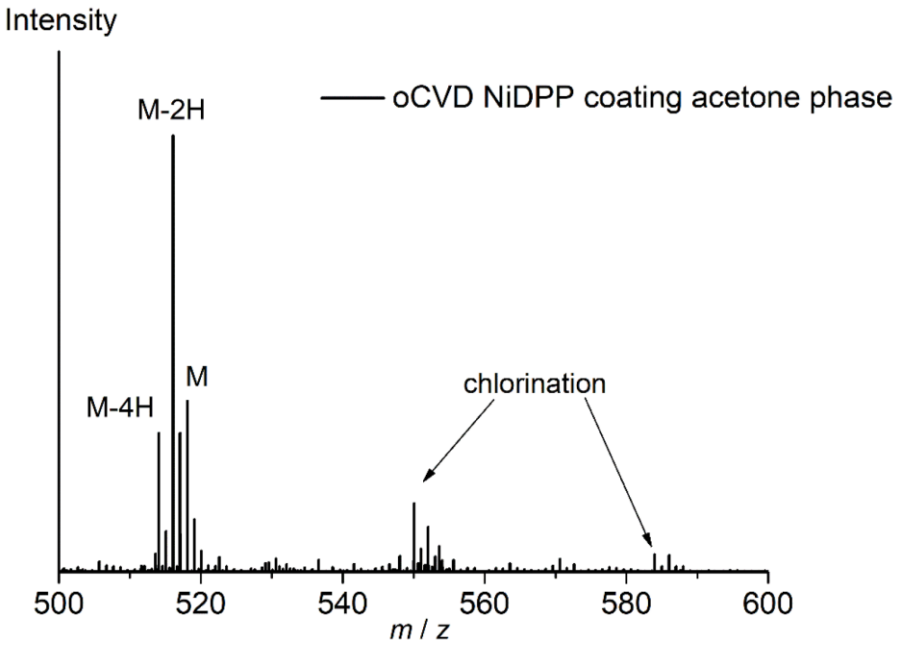

Figure S8. LDI-HRMS spectra of the soluble phase of the oCVD NiDPP coating in acetone. The spectrum displays signals related to the loss of two and four hydrogen atoms (M-2H $C_{32}H_{18}N_4Ni$ 516.088 *m*/z and M-4H $C_{32}H_{16}N_4Ni$ 514.072 *m*/*z*) from the monomer NiDPP. Signals related to the incorporation of one and two chlorine atoms are observed in the higher mass range ($C_{32}H_{17}N_4NiCl$ 550.049 *m*/*z*; $C_{32}H_{15}N_4NiCl$ 548.033 *m*/*z* and $C_{32}H_{16}N_4NiCl_2$ 584.010 *m*/*z*).

NiDD*t*-BuPP – Conductivity measurement

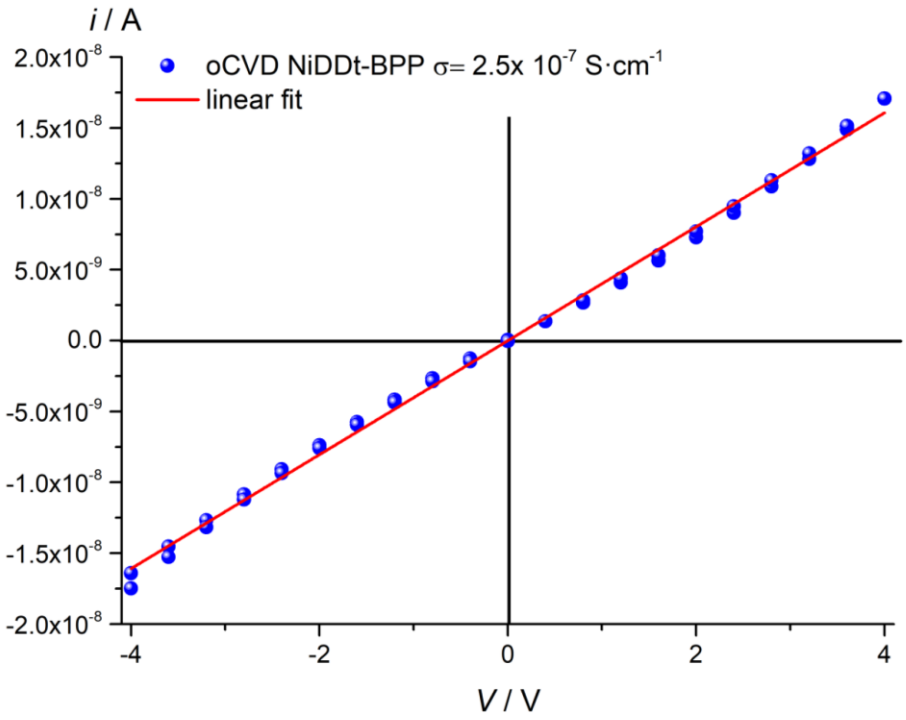

Figure S9. Lateral electrical conductivity measurement for the oCVD NiDD*t*-BuPP coating deposited on an OFET chip used to determine the conductivity. The conductivity measured for the oCVD NiDD*t*-BuPP coating is five orders of magnitude lower compared to the oCVD NiDPP coating.

NiDPP – Scanning electron microscopy and atomic force microscopy

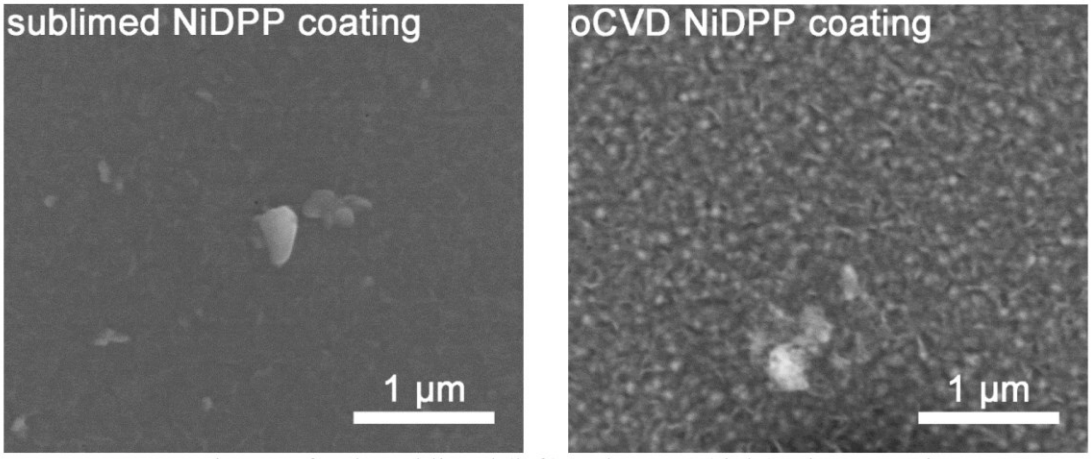

Figure S10. SEM images for the sublimed (left) and oCVD (right) NiDPP coating.

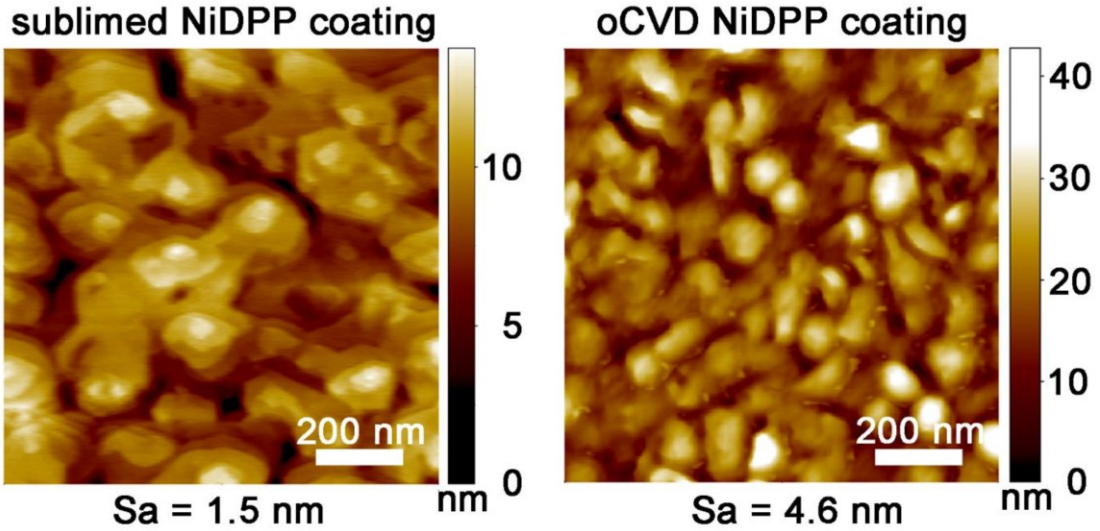

Figure S11. Atomic force microscopy (AFM) images of (left) a 50 nm thick sublimed NiDPP coating and (right) a 200 nm oCVD NiDPP coating deposited on a silicon wafer. The measured average roughnesses (Sa) of the thin films are 1.5 nm and 4.6 nm for the sublimed NiDPP coating and oCVD NiDPP coating, respectively.

References

[1] S. A. Yao, C. B. Hansen, J. F. Berry, *Polyhedron* **2013**, *58*, 2–6.
[2] N. Kamonsutthipaijit, H. L. Anderson, *Chem. Sci.* **2017**, *8*, 2729–2740.
[3] M. Rachele, G. Ricciardi, A. Rosa, *J. Porphyrins Phthalocyanines* **2017**, *21*, 371–380.
[4] A. P. Grosvenor, B. A. Kobe, M. C. Biesinger, N. S. Mcintyre, *Surf. Interface Anal.* **2004**, *36*, 1564–1574.

7.2 Supporting information: Conductive Directly Fused Poly(Porphyrin) Coatings by Oxidative Chemical Vapour Deposition – From Single- to Triple- Fused

Supporting Information

Conductive Directly Fused Poly(Porphyrin) Coatings by Oxidative Chemical Vapour Deposition – From Single- to Triple-Fused

Kamal Baba, Giuseppe Bengasi, Dana El Assad, Patrick Grysan, Esther Lentzen, Katja Heinze, Gilles Frache, and Nicolas D. Boscher*

ejoc201900045-sup-0001-SupMat.pdf

Table of Contents

1. Schematic of the oCVD reactor

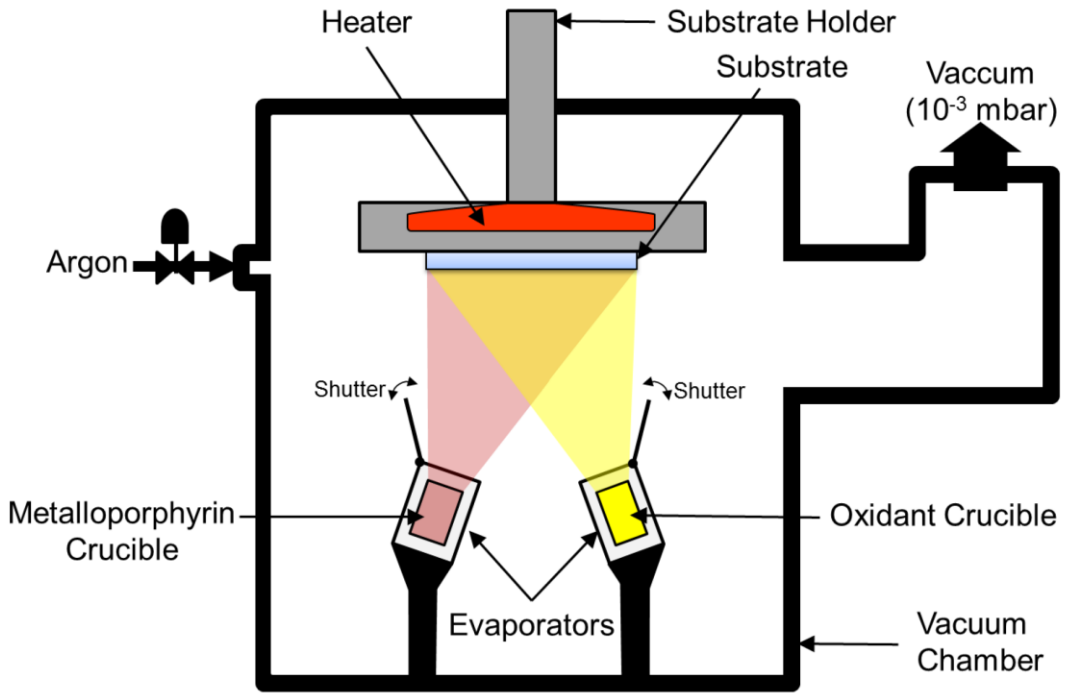

Figure S1. Scheme of the oCVD reactor employed for the simultaneous synthesis and deposition of directly fused poly(porphyrin) coatings using $FeCl_3$, $CuCl_2$ or $Cu(ClO_4)_2$ as oxidants.

2. Deposition conditions

Table S1. Deposition conditions

	NiDPP	$FeCl_3$	$CuCl_2$	$Cu(ClO_4)_2$
Sublimation temperatures	250°C	90°C 110°C 130°C 150°C 170°C	250°C 300°C 350°C	200°C 225°C 250°C

3. Optical photographs of NiDPP-based thin films

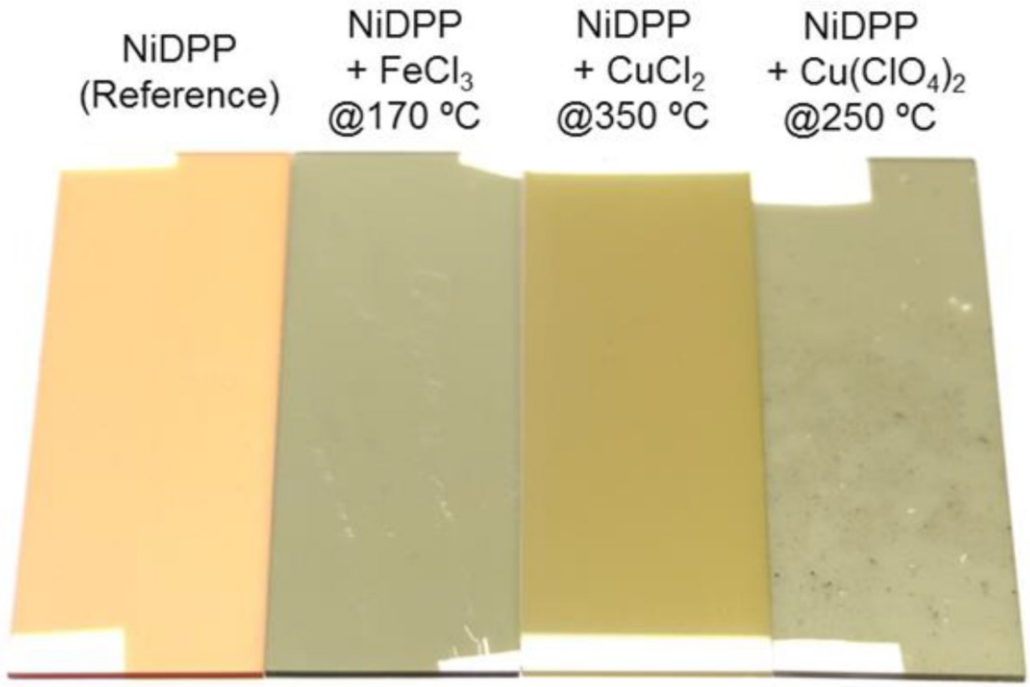

Figure S2. Photography of NiDPP-based thin films deposited on glass using different oxidants sublimed at different temperatures: $FeCl_3$ (170°C), $CuCl_2$ (350°C) and $Cu(ClO_4)_2$ (250°C). The reference NiDPP coating (sublimed in the absence of oxidant) is provided for comparison.

4. UV–Vis-NIR absorption spectra of the deposited NiDPP-based thin films

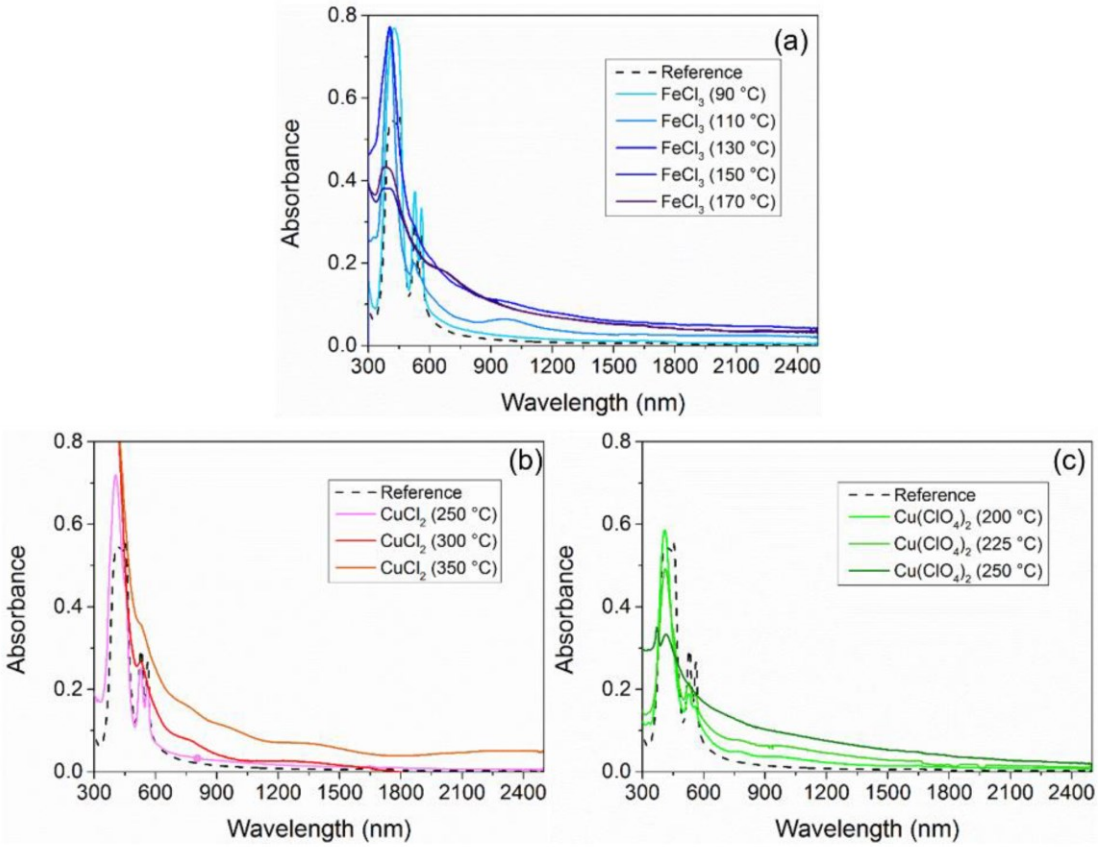

Figure S3. UV–Vis-NIR absorption spectra of the as-deposited NiDPP-based thin films deposited on glass using different oxidants sublimed at different temperatures (solid lines): (a) $FeCl_3$ (90-170°C), (b) $CuCl_2$ (250-350°C) and (c) $Cu(ClO_4)_2$ (200-250°C). The UV–Vis-NIR absorption spectrum of the reference NiDPP coating (sublimed in the absence of oxidant) is provided for comparison (dashed lines). The sharp and intense peak at 370 nm observed on (c) is related to the presence of the $Cu(ClO_4)_2$ in the NiDPP-based thin films.

5. XPS chemical composition of the NiDPP-based thin films

Table S2. XPS chemical composition of the NiDPP-based films formed using $FeCl_3$, $CuCl_2$ and $Cu(ClO_4)_2$ sublimed at 170°C, 300°C and 250°C, respectively.

% / NiDPP +	C 1s	Cl 2p	Fe 2p	N 1s	O 1s	Cu 2p	Ni 2p
$FeCl_3$	63.8	1.4	2.5	5.6	25.5	-	1.4
$CuCl_2$	35.6	28.9	-	1.7	12.6	20.6	0.7
$Cu(ClO_4)_2$	59.5	5.1	-	4.9	25.2	4.2	1.1

7.3 Supporting information: Reactivity of Nickel(II) Porphyrins in oCVD Processes— Polymerisation, Intramolecular Cyclisation and Chlorination

CHEMISTRY
A European Journal

Supporting Information

Reactivity of Nickel(II) Porphyrins in oCVD Processes— Polymerisation, Intramolecular Cyclisation and Chlorination

Giuseppe Bengasi,[a, b] Kamal Baba,[b] Oliver Back,[a] Gilles Frache,[b] Katja Heinze,*[a] and Nicolas D. Boscher*[b]

chem_201900793_sm_miscellaneous_information.pdf

Author Contributions

G.B., K.B. and N.D.B. carried out the deposition experiments. G.B. performed the CV measurements and DFT calculations. G.B. and O.B. collected and analysed the EPR data. K.B. performed the UV/Vis/NIR measurements. G.F. performed the HRMS measurements. K.H. and N.D.B. designed the experiments and supervised the project. G.B., K.H. and N.D.B. wrote the manuscript with input from all authors. All authors discussed the experiments.

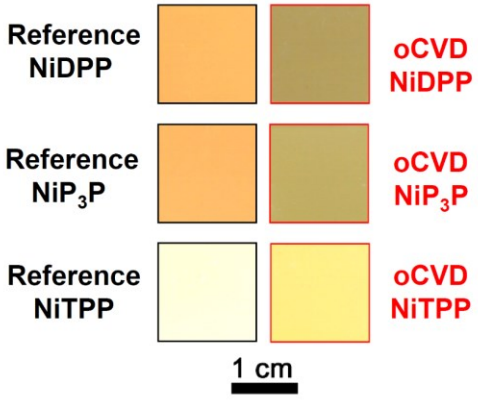

Figure S1. Optical images of reference and oCVD coatings of NiDPP, NiP_3P and NiTPP on glass.

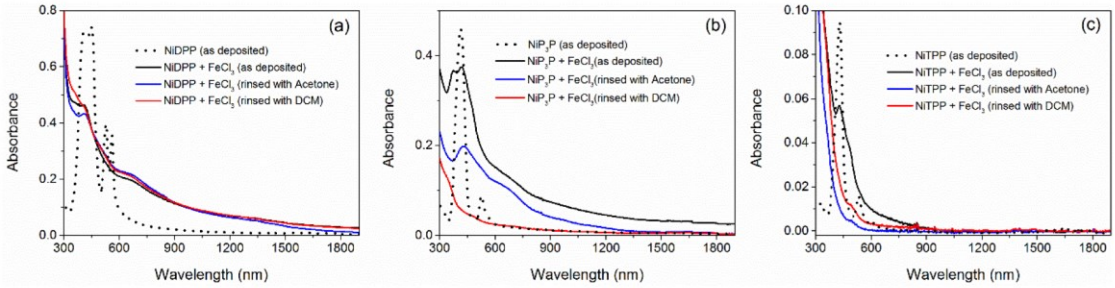

Figure S2. UV–Vis-NIR absorption spectra of the oCVD coatings on glass for (a) NiDPP, b) NiP_3P and (c) NiTPP before (black lines) and after rinsing with acetone (blue lines) or DCM (red lines). UV–Vis-NIR absorption spectra of the porphyrins sublimed in the absence of an oxidant are provided for comparison (dashed lines).

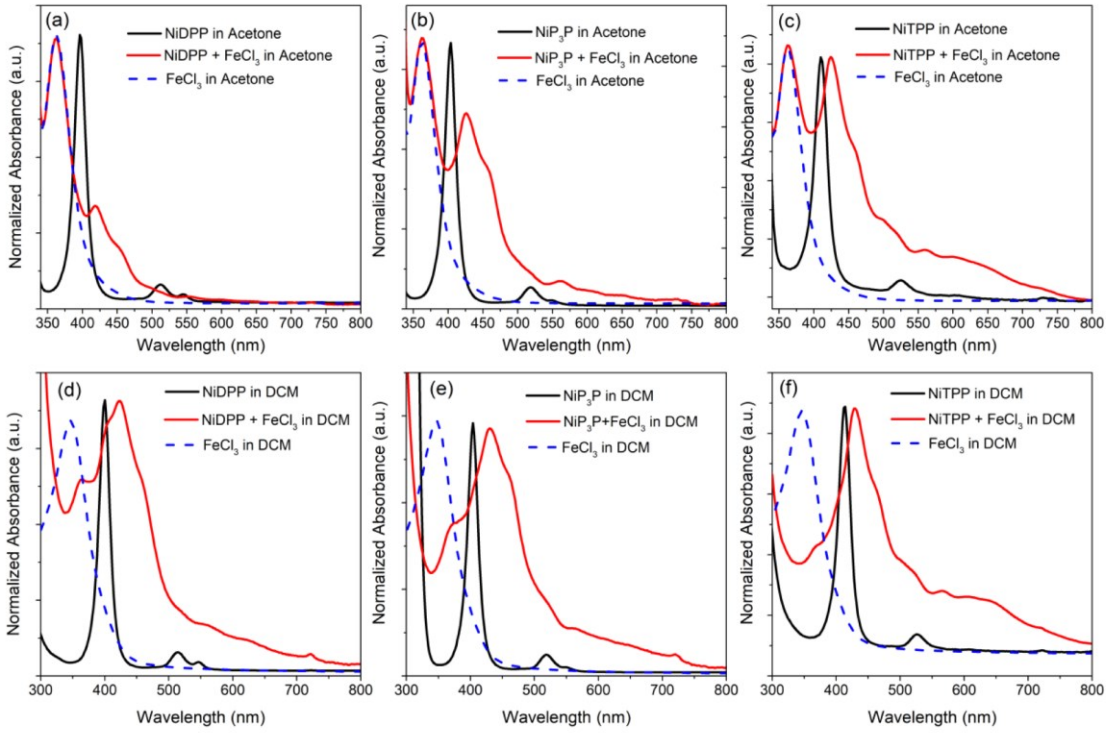

Figure S3. UV–Vis absorption spectra of the acetone and CH_2Cl_2 solutions of dissolved thin films formed by the oCVD reaction of (a, d) NiDPP, (b, e) NiP_3P and (c, f) NiTPP with $FeCl_3$ before and after rinsing with acetone or CH_2Cl_2. UV–vis absorption spectra of the dissolved sublimed porphyrins and $FeCl_3$ solutions are provided for comparison.

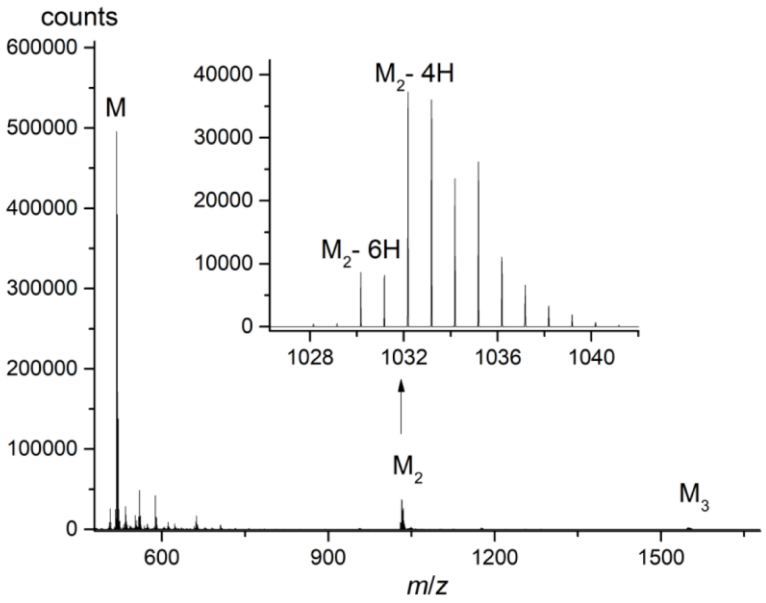

Figure S4. HR-MALDI mass spectrum of the NiDPP/WCl_6 mixture in CH_2Cl_2 solution at the end of the EPR measurements. Matrix α-cyano-4-hydroxycinnamic acid. The spectrum shows the formation of oligomers (M_2 – M_3). Inset: The dimer region (M_2) shows the sequential loss of 2H pairs.

film	$\lambda(CH_2Cl_2)$ / nm	λ(acetone) / nm
NiDPP	400	397
oCVD NiDPP	423	418
NiP_3P	404	404
oCVD NiP_3P	430	426
NiTPP	410	410
oCVD NiTPP	425	424

Table S1. Wavelength of the maximum absorption (Soret bands) of the washing solutions of reference and oCVD coatings (CH_2Cl_2 and acetone).

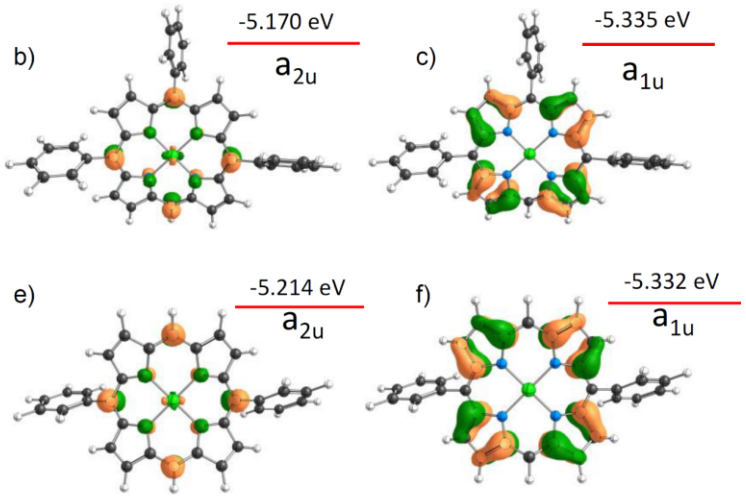

Figure S5. Illustration of a_{2u} and a_{1u} orbitals of NiP_3P and NiDPP and their respective energies (isosurface 0.006 and 0.004 a.u.) at the RIJCOSX-BP86-D3-ZORA/def2-TZVP/CPCM(CH_2Cl_2) level of theory.

Table S2. *DFT calculated Cartesian coordinates of* ***[NiDPP]***$^{\bullet+}$ *with and without solvent model.*

a) [NiDPP]$^{\bullet+}$ **with solvent model**

6	-1.346595000	-0.034744000	-3.072154000
6	-0.233812000	3.409784000	0.157009000
6	-1.347927000	0.108061000	3.534798000
6	-0.147391000	-3.306689000	0.305490000
7	-0.818594000	1.451635000	1.553986000
7	-0.795238000	1.402209000	-1.157976000
7	-0.782360000	-1.364164000	-1.091428000
7	-0.759832000	-1.314119000	1.620498000
6	-0.466560000	-2.691525000	-0.925127000
6	-1.168749000	-1.239060000	-2.418869000
6	-1.065532000	1.200682000	-2.493544000
6	-0.425097000	2.735692000	-1.053748000
6	-0.355355000	-2.637565000	1.516187000
6	-1.035020000	-1.119678000	2.956138000
6	-1.201396000	1.316572000	2.881483000
6	-0.536853000	2.786539000	1.387655000
6	-0.673856000	-3.417156000	-2.153427000
6	-1.142132000	-2.518786000	-3.071523000
6	-0.863606000	2.408376000	-3.242466000
6	-0.408451000	3.347420000	-2.358449000
6	-0.762562000	3.506659000	2.615943000
6	-1.207440000	2.596589000	3.534158000
6	-0.323037000	-3.248855000	2.820790000
6	-0.801641000	-2.321744000	3.705018000
1	-0.515692000	-4.482693000	-2.277509000
1	-1.416478000	-2.687316000	-4.108784000
1	-1.007560000	2.500081000	-4.315018000
1	-0.104605000	4.366619000	-2.566915000
1	-0.632147000	4.575952000	2.739831000
1	-1.485694000	2.758181000	4.571445000
1	0.006949000	-4.259993000	3.029169000
1	-0.942778000	-2.417243000	4.777607000
6	0.180373000	4.824743000	0.179214000
6	-0.546007000	5.818622000	-0.503986000
6	1.315764000	5.195633000	0.926268000
1	-1.454491000	5.547849000	-1.041433000
1	1.881723000	4.428892000	1.456158000
6	-0.137467000	7.150043000	-0.447873000
6	1.732007000	6.525055000	0.960215000
1	-0.718954000	7.914505000	-0.964044000
1	2.625050000	6.797051000	1.523612000
6	1.006143000	7.505848000	0.275210000
1	1.326858000	8.547487000	0.311408000
6	0.301379000	-4.711068000	0.283568000
6	1.445280000	-5.054700000	-0.463481000
6	-0.400766000	-5.721846000	0.967242000
1	1.993026000	-4.274740000	-0.993252000
1	-1.314994000	-5.472526000	1.505285000
6	1.892883000	-6.373893000	-0.497592000
6	0.039215000	-7.043226000	0.911019000
1	2.791916000	-6.624777000	-1.061266000
1	-0.523928000	-7.821189000	1.427359000
6	1.190624000	-7.371733000	0.187447000
1	1.535835000	-8.405495000	0.150522000
28	-0.763638000	0.044192000	0.231250000
1	-1.600607000	-0.057360000	-4.131331000
1	-1.602137000	0.124144000	4.594059000

b) [NiDPP]$^{\bullet+}$ **without solvent model**

6	-1.334166000	-0.032531000	-3.070161000
6	-0.227706000	3.412813000	0.158722000
6	-1.335204000	0.106325000	3.532886000
6	-0.142620000	-3.309947000	0.303748000
7	-0.806114000	1.451360000	1.554826000
7	-0.784304000	1.403905000	-1.157365000
7	-0.770628000	-1.363739000	-1.092239000
7	-0.749409000	-1.315692000	1.619967000
6	-0.456743000	-2.691820000	-0.926319000
6	-1.156124000	-1.238096000	-2.419286000
6	-1.054735000	1.202901000	-2.492965000
6	-0.417887000	2.737524000	-1.052235000

6	-0.349363000	-2.639599000	1.514742000
6	-1.024514000	-1.121597000	2.955642000
6	-1.188047000	1.316016000	2.881945000
6	-0.525950000	2.786938000	1.388837000
6	-0.664582000	-3.416851000	-2.154887000
6	-1.130493000	-2.517877000	-3.071917000
6	-0.854548000	2.412051000	-3.240442000
6	-0.400876000	3.350123000	-2.356213000
6	-0.751862000	3.506511000	2.617422000
6	-1.194703000	2.596044000	3.534556000
6	-0.316453000	-3.251549000	2.818725000
6	-0.793457000	-2.325245000	3.703083000
1	-0.510649000	-4.483037000	-2.276759000
1	-1.406264000	-2.689748000	-4.108124000
1	-0.995953000	2.507749000	-4.312871000
1	-0.092624000	4.368242000	-2.562545000
1	-0.624918000	4.576250000	2.739248000
1	-1.474544000	2.760923000	4.570803000
1	0.017537000	-4.261542000	3.024974000
1	-0.932043000	-2.424484000	4.775558000
6	0.176817000	4.830043000	0.179776000
6	-0.559775000	5.819219000	-0.499992000
6	1.311658000	5.211550000	0.922463000
1	-1.470086000	5.540979000	-1.030857000
1	1.887238000	4.449143000	1.448333000
6	-0.162998000	7.153148000	-0.444583000
6	1.717279000	6.543175000	0.953997000
1	-0.753926000	7.913856000	-0.955020000
1	2.611586000	6.822936000	1.511043000
6	0.980593000	7.517468000	0.272790000
1	1.292894000	8.561358000	0.307886000
6	0.296962000	-4.716703000	0.282771000
6	1.440916000	-5.070175000	-0.459793000
6	-0.415027000	-5.723670000	0.962647000
1	1.997615000	-4.293898000	-0.985708000
1	-1.331954000	-5.467883000	1.493413000
6	1.879218000	-6.391411000	-0.491169000
6	0.014509000	-7.047422000	0.907418000
1	2.780164000	-6.649131000	-1.048150000
1	-0.557529000	-7.822398000	1.417912000
6	1.166759000	-7.383503000	0.190130000
1	1.504729000	-8.419371000	0.155124000
28	-0.750071000	0.044278000	0.231280000
1	-1.589141000	-0.054714000	-4.129310000
1	-1.590434000	0.122037000	4.592089000

Table S3. *DFT calculated Cartesian coordinates of* ***[NiP$_3$P]$^{\bullet+}$*** *with and without solvent model.*

a) [NiP$_3$P]$^{\bullet+}$ with solvent model

6	0.691379072	0.163549108	-3.062418591
6	-1.186098415	3.496053946	-0.072535384
6	-0.914879200	0.130249042	3.435493844
6	-1.042922102	-3.245891223	-0.085369520
7	-0.984275504	1.499762938	1.377232475
7	-0.292848277	1.509350042	-1.264340976
7	-0.243241085	-1.239359576	-1.274477366
7	-0.913012791	-1.242905064	1.360443797
6	-0.561901570	-2.585845794	-1.213126672
6	0.337176926	-1.055348242	-2.517007772
6	0.323931090	1.366030322	-2.483806133
6	-0.634345406	2.862481668	-1.181297190
6	-1.108213049	-2.586676603	1.144359030
6	-0.929035749	-1.082961769	2.750671807
6	-1.035959188	1.337508726	2.752190017
6	-1.271747340	2.835329583	1.153943489
6	-0.211913263	-3.240081386	-2.460536093
6	0.389746452	-2.306384114	-3.242014470
6	0.408520603	2.645785172	-3.165833055
6	-0.215504260	3.558568301	-2.376522854
6	-1.550808433	3.508082674	2.412007364
6	-1.346254439	2.601865048	3.397880983
6	-1.258072871	-3.282444671	2.412940832
6	-1.114627736	-2.357261331	3.397988406
1	-0.397004118	-4.285707584	-2.679979548
1	0.801697711	-2.416057157	-4.240935484
1	0.877140924	2.789470554	-4.135271488
1	-0.359113969	4.619292454	-2.550067062
1	-1.833286953	4.550913229	2.502841697
1	-1.423220094	2.742328799	4.470240157
1	-1.424878007	-4.349839103	2.510241182
1	-1.158713492	-2.501537804	4.471712328
6	-1.564747491	4.930406872	-0.180128760
6	-2.672264673	5.298140609	-0.958827370
6	-0.815830448	5.925384457	0.466279770
1	-3.254796747	4.525430698	-1.462249562
1	0.059468410	5.644328894	1.053311968
6	-3.031757003	6.642569915	-1.079435332
6	-1.175865185	7.268603535	0.341110301
1	-3.898273636	6.917869087	-1.681579244
1	-0.583898410	8.035229495	0.842233747
6	-2.285440337	7.629504535	-0.429446388
1	-2.565849774	8.678966209	-0.525399982
6	-1.385452714	-4.690267295	-0.141588252
6	-0.407191839	-5.660054455	-0.411450128
6	-2.706065869	-5.097305672	0.106342931
1	0.625466870	-5.350859363	-0.577302216
1	-3.468409727	-4.345351680	0.315500768
6	-0.747594100	-7.014067690	-0.441244395
6	-3.044176264	-6.452057639	0.072597827
1	0.021894180	-7.759792736	-0.644727864
1	-4.074624071	-6.756251476	0.259647697
6	-2.066422340	-7.412745596	-0.202208152
1	-2.330433103	-8.470710620	-0.226011603
28	-0.608012488	0.131854037	0.050201458
1	1.161077327	0.179586354	-4.044024396
6	-0.895887557	0.112615269	4.923752468
6	-2.046817911	0.421011303	5.664023813
6	0.284191996	-0.237489987	5.596058933
6	-2.014067660	0.386806873	7.059889148
6	0.314199521	-0.268697686	6.992530705
6	-0.833671130	0.044039718	7.726398477
1	-2.971360945	0.673407154	5.142966260
1	1.178874616	-0.478681568	5.020371238
1	-2.915019973	0.623556011	7.627030631
1	1.237916510	-0.536159214	7.506902104
1	-0.809564460	0.018090983	8.816402537

***b) [NiP$_3$P]$^{\bullet+}$ without* solvent model**

6	-6.505044000	2.565616000	-1.316637000
6	-2.722732000	4.600981000	0.934035000

6	-2.377187000	0.414462000	3.406326000
6	-7.180790000	-0.060902000	2.700212000
7	-2.938170000	2.407195000	2.056271000
7	-4.624698000	3.269496000	0.087894000
7	-6.462389000	1.341371000	0.808382000
7	-4.759264000	0.473191000	2.741717000
6	-7.421285000	0.623766000	1.500396000
6	-7.057416000	1.695361000	-0.384598000
6	-5.390088000	3.346141000	-1.064231000
6	-3.788822000	4.361440000	0.046151000
6	-5.875668000	-0.190082000	3.211062000
6	-3.682305000	-0.096983000	3.396335000
6	-2.077725000	1.668072000	2.845097000
6	-2.293807000	3.615229000	1.832429000
6	-8.648255000	0.578510000	0.747264000
6	-8.400787000	1.192750000	-0.448719000
6	-4.995492000	4.478795000	-1.855239000
6	-4.024036000	5.131166000	-1.149859000
6	-1.039406000	3.642707000	2.534366000
6	-0.873099000	2.410060000	3.099307000
6	-5.493573000	-1.189409000	4.172194000
6	-4.130771000	-1.151159000	4.265843000
1	-9.572218000	0.126284000	1.087741000
1	-9.079354000	1.342585000	-1.283197000
1	-5.432955000	4.748805000	-2.811792000
1	-3.479949000	6.027941000	-1.424079000
1	-0.359695000	4.485840000	2.565230000
1	-0.020850000	2.043149000	3.658574000
1	-6.182233000	-1.856123000	4.678725000
1	-3.483895000	-1.750186000	4.896811000
6	-1.989761000	5.876761000	0.806794000
6	-2.682392000	7.087426000	0.996266000
6	-0.625344000	5.915482000	0.465215000
1	-3.740196000	7.062289000	1.260240000
1	-0.095114000	4.984333000	0.265215000
6	-2.016280000	8.305440000	0.879876000
6	0.030303000	7.137204000	0.327914000
1	-2.557586000	9.236013000	1.051325000
1	1.082032000	7.156199000	0.041591000
6	-0.659458000	8.333796000	0.544169000
1	-0.141919000	9.287885000	0.443011000
6	-8.275009000	-0.763762000	3.397685000
6	-9.042955000	-1.754432000	2.757792000
6	-8.540139000	-0.456599000	4.746013000
1	-8.810449000	-2.034456000	1.730402000
1	-7.949051000	0.311989000	5.244940000
6	-10.056418000	-2.413746000	3.449938000
6	-9.569862000	-1.103032000	5.425980000
1	-10.630478000	-3.195121000	2.951561000
1	-9.781343000	-0.840482000	6.462665000
6	-10.329111000	-2.083748000	4.780975000
1	-11.128203000	-2.595873000	5.317229000
28	-4.700662000	1.881169000	1.432415000
1	-7.052538000	2.738186000	-2.242812000
6	-1.335366000	-0.349684000	4.124311000
6	-0.687240000	0.169066000	5.259534000
6	-1.007193000	-1.643627000	3.679032000
6	0.273353000	-0.588244000	5.926891000
6	-0.030181000	-2.387833000	4.337475000
6	0.611263000	-1.863190000	5.462974000
1	-0.971183000	1.150688000	5.639286000
1	-1.508040000	-2.048958000	2.799206000
1	0.754468000	-0.185479000	6.818427000
1	0.231181000	-3.380670000	3.970916000
1	1.368875000	-2.449840000	5.982792000

Table S4. *DFT calculated Cartesian coordinates of* ***NiDPP*** *with and without solvent model.*

***a) NiDPP* with solvent model**

6	-1.129697000	-0.013433000	-3.108884000
6	-0.224672000	3.439840000	0.176873000
6	-1.132554000	0.092367000	3.571466000
6	-0.140471000	-3.337211000	0.286132000
7	-0.686294000	1.447754000	1.569949000
7	-0.677622000	1.408261000	-1.154099000
7	-0.650336000	-1.357433000	-1.107315000
7	-0.644355000	-1.317633000	1.616860000
6	-0.377480000	-2.705811000	-0.933505000
6	-0.949312000	-1.217300000	-2.454406000
6	-0.921374000	1.212067000	-2.504055000
6	-0.393978000	2.762415000	-1.028378000
6	-0.326904000	-2.664201000	1.491311000
6	-0.893406000	-1.127527000	2.966713000
6	-0.982016000	1.300286000	2.916952000
6	-0.446333000	2.802771000	1.396397000
6	-0.507610000	-3.408386000	-2.186786000
6	-0.893127000	-2.490614000	-3.120313000
6	-0.792239000	2.448282000	-3.227339000
6	-0.421351000	3.399823000	-2.321988000
6	-0.594389000	3.501826000	2.649650000
6	-0.957626000	2.574721000	3.582908000
6	-0.338382000	-3.301950000	2.784991000
6	-0.733348000	-2.360015000	3.690169000
1	-0.350416000	-4.474536000	-2.312463000
1	-1.099472000	-2.639506000	-4.176772000
1	-0.932685000	2.548270000	-4.300222000
1	-0.203505000	4.447766000	-2.497918000
1	-0.463566000	4.571522000	2.775330000
1	-1.167822000	2.718412000	4.639319000
1	-0.094160000	-4.343998000	2.961213000
1	-0.871429000	-2.463433000	4.763022000
6	0.095237000	4.893203000	0.177329000
6	-0.824752000	5.839269000	-0.301612000
6	1.326417000	5.338106000	0.684239000
1	-1.790801000	5.501445000	-0.679176000
1	2.044081000	4.606763000	1.059141000
6	-0.516630000	7.201278000	-0.280144000
6	1.635412000	6.700195000	0.702904000
1	-1.243606000	7.925849000	-0.649766000
1	2.598466000	7.031043000	1.094283000
6	0.715011000	7.635357000	0.220049000
1	0.955431000	8.699216000	0.235923000
6	0.216125000	-4.781952000	0.285600000
6	1.456852000	-5.195752000	-0.224488000
6	-0.678176000	-5.750944000	0.767410000
1	2.154582000	-4.446673000	-0.602004000
1	-1.651542000	-5.437729000	1.147367000
6	1.800244000	-6.549534000	-0.243615000
6	-0.335582000	-7.104691000	0.745672000
1	2.770241000	-6.856008000	-0.637676000
1	-1.042780000	-7.847227000	1.118010000
6	0.905259000	-7.507584000	0.242157000
1	1.172478000	-8.565022000	0.225509000
28	-0.664660000	0.045329000	0.231387000
1	-1.333859000	-0.033005000	-4.178674000
1	-1.337470000	0.106910000	4.641206000

***b) NiDPP* without solvent model**

6	-1.112116000	-0.012657000	-3.107197000
6	-0.221473000	3.439322000	0.176975000
6	-1.113042000	0.092083000	3.569912000
6	-0.136390000	-3.336478000	0.285640000
7	-0.676619000	1.447865000	1.570069000
7	-0.662649000	1.408832000	-1.155399000
7	-0.641463000	-1.357046000	-1.107412000
7	-0.628243000	-1.317684000	1.618045000
6	-0.374749000	-2.705500000	-0.933244000
6	-0.939342000	-1.216745000	-2.452727000
6	-0.900541000	1.212670000	-2.504555000
6	-0.381495000	2.761426000	-1.028476000

Table S4. *DFT calculated Cartesian coordinates of* ***NiDPP*** *with and without solvent model.*

***a) NiDPP* with solvent model**

6	-1.129697000	-0.013433000	-3.108884000
6	-0.224672000	3.439840000	0.176873000
6	-1.132554000	0.092367000	3.571466000
6	-0.140471000	-3.337211000	0.286132000
7	-0.686294000	1.447754000	1.569949000
7	-0.677622000	1.408261000	-1.154099000
7	-0.650336000	-1.357433000	-1.107315000
7	-0.644355000	-1.317633000	1.616860000
6	-0.377480000	-2.705811000	-0.933505000
6	-0.949312000	-1.217300000	-2.454406000
6	-0.921374000	1.212067000	-2.504055000
6	-0.393978000	2.762415000	-1.028378000
6	-0.326904000	-2.664201000	1.491311000
6	-0.893406000	-1.127527000	2.966713000
6	-0.982016000	1.300286000	2.916952000
6	-0.446333000	2.802771000	1.396397000
6	-0.507610000	-3.408386000	-2.186786000
6	-0.893127000	-2.490614000	-3.120313000
6	-0.792239000	2.448282000	-3.227339000
6	-0.421351000	3.399823000	-2.321988000
6	-0.594389000	3.501826000	2.649650000
6	-0.957626000	2.574721000	3.582908000
6	-0.338382000	-3.301950000	2.784991000
6	-0.733348000	-2.360015000	3.690169000
1	-0.350416000	-4.474536000	-2.312463000
1	-1.099472000	-2.639506000	-4.176772000
1	-0.932685000	2.548270000	-4.300222000
1	-0.203505000	4.447766000	-2.497918000
1	-0.463566000	4.571522000	2.775330000
1	-1.167822000	2.718412000	4.639319000
1	-0.094160000	-4.343998000	2.961213000
1	-0.871429000	-2.463433000	4.763022000
6	0.095237000	4.893203000	0.177329000
6	-0.824752000	5.839269000	-0.301612000
6	1.326417000	5.338106000	0.684239000
1	-1.790801000	5.501445000	-0.679176000
1	2.044081000	4.606763000	1.059141000
6	-0.516630000	7.201278000	-0.280144000
6	1.635412000	6.700195000	0.702904000
1	-1.243606000	7.925849000	-0.649766000
1	2.598466000	7.031043000	1.094283000
6	0.715011000	7.635357000	0.220049000
1	0.955431000	8.699216000	0.235923000
6	0.216125000	-4.781952000	0.285600000
6	1.456852000	-5.195752000	-0.224488000
6	-0.678176000	-5.750944000	0.767410000
1	2.154582000	-4.446673000	-0.602004000
1	-1.651542000	-5.437729000	1.147367000
6	1.800244000	-6.549534000	-0.243615000
6	-0.335582000	-7.104691000	0.745672000
1	2.770241000	-6.856008000	-0.637676000
1	-1.042780000	-7.847227000	1.118010000
6	0.905259000	-7.507584000	0.242157000
1	1.172478000	-8.565022000	0.225509000
28	-0.664660000	0.045329000	0.231387000
1	-1.333859000	-0.033005000	-4.178674000
1	-1.337470000	0.106910000	4.641206000

***b) NiDPP* without solvent model**

6	-1.112116000	-0.012657000	-3.107197000
6	-0.221473000	3.439322000	0.176975000
6	-1.113042000	0.092083000	3.569912000
6	-0.136390000	-3.336478000	0.285640000
7	-0.676619000	1.447865000	1.570069000
7	-0.662649000	1.408832000	-1.155399000
7	-0.641463000	-1.357046000	-1.107412000
7	-0.628243000	-1.317684000	1.618045000
6	-0.374749000	-2.705500000	-0.933244000
6	-0.939342000	-1.216745000	-2.452727000
6	-0.900541000	1.212670000	-2.504555000
6	-0.381495000	2.761426000	-1.028476000

Table S5. *DFT calculated Cartesian coordinates for* ***NiP_3P*** *with and without solvent model.*

a) NiP_3P with solvent model

6	1.139151000	0.041590000	-2.861041000
6	-0.410280000	3.383470000	0.294563000
6	0.139993000	0.002204000	3.757118000
6	-0.347497000	-3.358217000	0.261399000
7	-0.095671000	1.383779000	1.719371000
7	0.327745000	1.400949000	-0.981766000
7	0.361771000	-1.356996000	-0.994419000
7	-0.053171000	-1.362505000	1.701744000
6	0.039927000	-2.704703000	-0.905498000
6	0.835132000	-1.178235000	-2.284148000
6	0.839008000	1.250729000	-2.261587000
6	0.007641000	2.745167000	-0.870712000
6	-0.307422000	-2.711222000	1.496867000
6	0.053201000	-1.210766000	3.077143000
6	-0.013723000	1.218796000	3.096014000
6	-0.384808000	2.728732000	1.525316000
6	0.281587000	-3.358543000	-2.168500000
6	0.818523000	-2.422983000	-3.005004000
6	0.865619000	2.516204000	-2.945876000
6	0.318354000	3.435992000	-2.098851000
6	-0.518164000	3.395989000	2.794599000
6	-0.234456000	2.476226000	3.761782000
6	-0.370613000	-3.402608000	2.759035000
6	-0.114869000	-2.481746000	3.733159000
1	0.082096000	-4.405486000	-2.370246000
1	1.141179000	-2.538479000	-4.036186000
1	1.234235000	2.657953000	-3.958206000
1	0.162561000	4.497094000	-2.263616000
1	-0.765299000	4.444648000	2.919626000
1	-0.205850000	2.620905000	4.836327000
1	-0.557494000	-4.465490000	2.870619000
1	-0.072741000	-2.631560000	4.806903000
6	-0.778349000	4.824269000	0.223677000
6	-1.955882000	5.210964000	-0.435059000
6	0.044902000	5.814231000	0.782817000
1	-2.597310000	4.445157000	-0.873868000
1	0.971324000	5.521926000	1.279104000
6	-2.308841000	6.559667000	-0.523882000
6	-0.307031000	7.162695000	0.691722000
1	-3.230031000	6.845067000	-1.033876000
1	0.345005000	7.921927000	1.125967000
6	-1.485875000	7.539023000	0.040290000
1	-1.760411000	8.592385000	-0.029995000
6	-0.706722000	-4.801770000	0.224904000
6	0.247913000	-5.781785000	-0.089680000
6	-2.016841000	-5.202477000	0.531524000
1	1.272742000	-5.479225000	-0.309024000
1	-2.761809000	-4.444777000	0.779186000
6	-0.102765000	-7.133579000	-0.104556000
6	-2.367751000	-6.554294000	0.514160000
1	0.650962000	-7.884703000	-0.345092000
1	-3.391100000	-6.850334000	0.749182000
6	-1.411840000	-7.523530000	0.195069000
1	-1.685071000	-8.579507000	0.183491000
28	0.134590000	0.016737000	0.361785000
1	1.518849000	0.050548000	-3.881941000
6	0.286105000	-0.023554000	5.239147000
6	-0.782605000	0.322038000	6.080661000
6	1.503359000	-0.421759000	5.812777000
6	-0.634041000	0.277243000	7.468709000
6	1.652239000	-0.464598000	7.201195000
6	0.584246000	-0.114298000	8.032679000
1	-1.736837000	0.615219000	5.640705000
1	2.335737000	-0.694437000	5.162207000
1	-1.474458000	0.543851000	8.111163000
1	2.605744000	-0.771077000	7.633650000
1	0.699717000	-0.149110000	9.116806000

b) NiP_3P no solvent model

6	1.099828000	0.040061000	-2.871735000
6	-0.409437000	3.383704000	0.294678000

6	0.134336000	0.002285000	3.751866000
6	-0.348069000	-3.358967000	0.262900000
7	-0.099780000	1.384040000	1.716699000
7	0.309477000	1.400733000	-0.988183000
7	0.341549000	-1.358101000	-1.000826000
7	-0.057294000	-1.363139000	1.699554000
6	0.026304000	-2.705117000	-0.907244000
6	0.801891000	-1.179655000	-2.293369000
6	0.808020000	1.249667000	-2.270952000
6	-0.003577000	2.744632000	-0.873673000
6	-0.306491000	-2.711573000	1.496963000
6	0.049444000	-1.210678000	3.073187000
6	-0.016858000	1.218703000	3.091413000
6	-0.382965000	2.728703000	1.524274000
6	0.257645000	-3.361169000	-2.170927000
6	0.782168000	-2.425055000	-3.012785000
6	0.833348000	2.515296000	-2.954730000
6	0.298809000	3.436555000	-2.103231000
6	-0.511696000	3.397197000	2.793703000
6	-0.231046000	2.476454000	3.759312000
6	-0.365717000	-3.403410000	2.759429000
6	-0.113634000	-2.481442000	3.731692000
1	0.055921000	-4.408517000	-2.366853000
1	1.092657000	-2.541773000	-4.047337000
1	1.192680000	2.657880000	-3.970047000
1	0.146485000	4.498736000	-2.262166000
1	-0.756186000	4.446571000	2.915835000
1	-0.197016000	2.617381000	4.833988000
1	-0.546880000	-4.467300000	2.868317000
1	-0.070234000	-2.626610000	4.805756000
6	-0.763924000	4.827704000	0.228265000
6	-1.942307000	5.229747000	-0.418223000
6	0.074213000	5.808943000	0.779463000
1	-2.594532000	4.469889000	-0.850860000
1	1.001614000	5.503114000	1.265366000
6	-2.280411000	6.581521000	-0.503440000
6	-0.263368000	7.160535000	0.693694000
1	-3.202975000	6.877977000	-1.004396000
1	0.401222000	7.912226000	1.121870000
6	-1.442659000	7.550629000	0.053732000
1	-1.705982000	8.606921000	-0.013333000
6	-0.693059000	-4.805755000	0.229198000
6	0.272144000	-5.776807000	-0.078647000
6	-1.998674000	-5.221724000	0.531169000
1	1.293661000	-5.460553000	-0.293592000
1	-2.751036000	-4.469950000	0.773466000
6	-0.063047000	-7.131657000	-0.092321000
6	-2.334145000	-6.576568000	0.516663000
1	0.699846000	-7.875239000	-0.327145000
1	-3.354980000	-6.883698000	0.747994000
6	-1.367594000	-7.535393000	0.203373000
1	-1.629028000	-8.594227000	0.193113000
28	0.123065000	0.016258000	0.357544000
1	1.469593000	0.048716000	-3.896300000
6	0.273497000	-0.022590000	5.234158000
6	-0.800505000	0.317866000	6.070242000
6	1.487622000	-0.414779000	5.816792000
6	-0.660411000	0.274829000	7.458357000
6	1.627975000	-0.457524000	7.205158000
6	0.554783000	-0.111462000	8.029736000
1	-1.752117000	0.605764000	5.621516000
1	2.323555000	-0.683414000	5.169490000
1	-1.505937000	0.537087000	8.095820000
1	2.579963000	-0.759800000	7.643685000
1	0.663786000	-0.145660000	9.114418000

7.4 Supporting information: Molecular Flattening Effect to Enhance the Conductivity of Fused Porphyrin Tapes Thin Film

Molecular Flattening Effect to Enhance the Conductivity of Fused Porphyrin Tapes Thin Films

Supporting information.

Table of contents:

Contents

Experimental Section

Cyclic voltammetric measurements were carried out in a glovebox with a BioLogic SP-50 voltammetric analyzer in CH_2Cl_2 containing 0.1 M $[^nBu_4N]^-$ [PF6] as supporting electrolyte at a platinum working electrode, a platinum wire as counter electrode, and a 0.01 M $Ag/AgNO_3$ electrode as the reference electrode. All cyclic voltammetric measurements were recorded at 100 mV s^{-1} scan rate. Ferrocene was employed as an internal reference redox system. The thin films thicknesses were measured using a KLA-Tencor P-17 Stylus profiler.The optical absorbance of the films was measured in the range of 250–2000 nm using a UV-Vis-NIR spectrophotometer (Perkin Elmer, Lambda 950) with a 150 mm diameter integrating sphere. The absorption spectra were recorded directly on the glass substrates.

A model composed of two identical porphyrin was geometrically optimized by density functional theory (BP86/def2-SVP/RIJCOSX/ZORA level of theory). A centroid was placed in every pyrrolic ring and the interplanar distance was than calculated considering the angle formed between the pyrrolic ring, and the two centroid (β) (See scheme S1) using the law of sines:

$$\frac{a}{\sin\alpha} = \frac{b}{\sin\beta}$$

Assuming $\alpha = 90°$

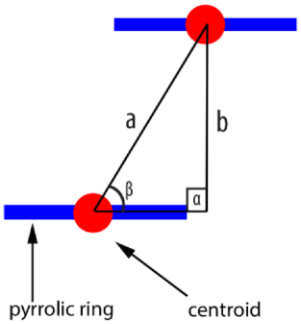

$$a \sin\beta = b$$

Scheme S1. Schematic of the method used to calculated the intramoleculra distance in the two porphyrins model.

The distances between all the four pyrrolic ring and the underlying one were calculated and the average assumed as intramolecular distance between the two porphyrins.

Images of the topography and conductivity of the samples were simultaneously acquired using the C-AFM mode of an Innova AFM (Bruker). Conductive AFM tips ElectriMulti75-G from BudgetSensors coated with a layer of 5 nm Chromium and 25nm of Platinum with nominal spring constants of 3 N/m and nominal radius <25 nm were used. Images of a 2x2 um^2 area with a resolution of 256x256 pixels were taken at a scan rate of 1Hz. Samples were deposited on monocrystalline silicon wafers and connected to the conductive stage via a colloidal carbon ink. The topography was obtained by maintaining the tip deflection constant via the feedback loop of the AFM acting on the piezo Z direction. A bias of 4V was applied to the back electrode of the samples while the grounded conductive tip was collecting electrons for the current measured by an amplifier (DLPCA-200, Femto). A 109 VA-1 amplification was used and the signal output was then transmitted to the AFM electronic and recorded. The reported average and standard deviation values of conductivity and roughness (Ra) consider at least 4 images in each sample for reliable results.

The Helium Ion Microscope images were recorded with an Orion Nanofab Instrument from Zeiss. The images were acquired from samples deposited on silicon wafers. Helium ions are generated using a gas field ionization

source (GFIS). Within the GFIS a sharp needle having an apex radius of approximately 100 nm is set to a positive high voltage with respect to an extraction electrode accelerating the ions. For the HIM images within this manuscript we used a landing energy of 30 keV, impinging ion currents in between 0.1 and 1 pA and a tilt angle of the substrate holder stage of 20°. The helium ion beam scans the sample surface creating secondary electrons (SE). Contrast in the images is created mainly by composition and topography. Compared to the standard secondary electron microscope (SEM), the HIM allows to probe specimens with a better surface sensitivity and a higher depth of field which makes it very suitable for topographic imaging. [1,2]

Using a microprobe station (Cascade Microtech, PM8), 2-point current-voltage scans were recorded and the (lateral) thin-film conductivity was evaluated from a simple linear fit approximating all the samples to ohmic materials. The measurements were performed at room temperature and under ambient atmosphere and the geometry of the channel was 2.5 µm (length), 10 mm (total width), 40 nm (height). The data were recorded using a Keithley (2401) sourcemeter by sweeping the voltage from −4 V to 4 V and back (hysteresis scan) at a scan rate of 500 mV s−1. DFT calculation were performed by mean of ORCA program package (Version 4.0.1) program suite.[3] All the calculation were carried out using the BP86[4,5] functional in combination with D3[6-7] correction and RIJCOX[8] approximation. Relativistic effects were calculated at the zeroth order regular approximation (ZORA) level.[9] Geometry optimizations were performed by mean of Ahlrichs' split valence basis set def2-SVP[10] and Weigend's auxiliary basis set[11]. The optimized geometries were confirmed to be local minima on the respective potential energy surface by numerical frequency analysis that shows the absence negative frequencies.

Laser desorption/ionization high-resolution mass spectrometry (LDI-HRMS) measurements were performed on an AP-MALDI UHR ion source from MassTech, Inc. coupled to an LTQ/Orbitrap Elite from Thermo Scientific. oCVD coated Si wafers were directly placed on the sample holder, adjusting the working distance to optimum. In source fragmentation (E = 70 V) was used to prevent the formation of clusters. Gel permeation chromatography was performed using an Ultimate 3000 apparatus from Thermo Scientific, equipped with an ERC differential refractive index detector and a UV detector in serie. The GPC was coupled online to an LTQ/Orbitrap Elite mass spectrometer with an Ion Max source, equipped with an electrospray (ESI) probe from Thermo Scientific. Samples were dissolved in THF containing 1 vol% of pyridine, as described elsewhere[12] and filtered over a 0.45 µm pore size membrane prior to injection. A mesopore column 3 µm (300 x 7.5 mm) from Agilent Technologies was used at 30°C. Flow rate was set to 1 mL·min-1 and split post-column towards the RI and UV detection on one hand and the ESI-HRMS detection on another hand methanol was added post-split to promote ionization. The spray voltage was set to 3.2 kV. A tandem mass spectrometry method was included in the GPCxESI-HRMS measurements. MS/MS was performed by Collision Induced Dissociation (CID) using a normalized energy of 70. Parent ion selection and fragmentation was performed in the ion trap (LTQ) while analysis of the fragment ions was done by the high resolution Orbitrap.

Thermogravimetric analyses were performed under inert atmosphere (Ar) with a ramp of 10K per minute.

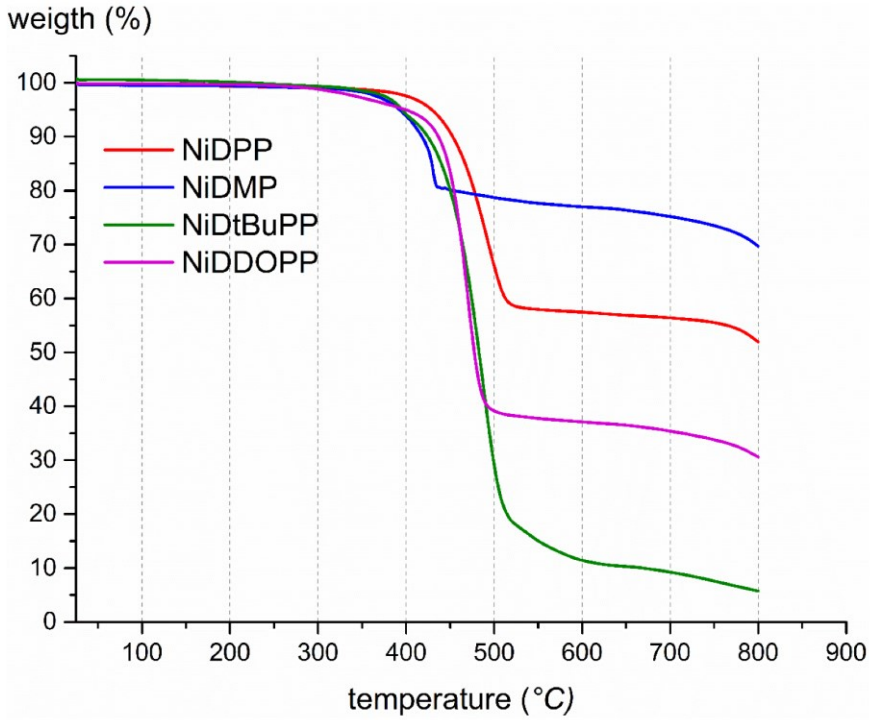

Figure S1. Thermo-gravimetric analysis of the monomer employed in the oCVD experiments. All the porphyrins exhibit a good thermal stability in the range of temperature used during the process.

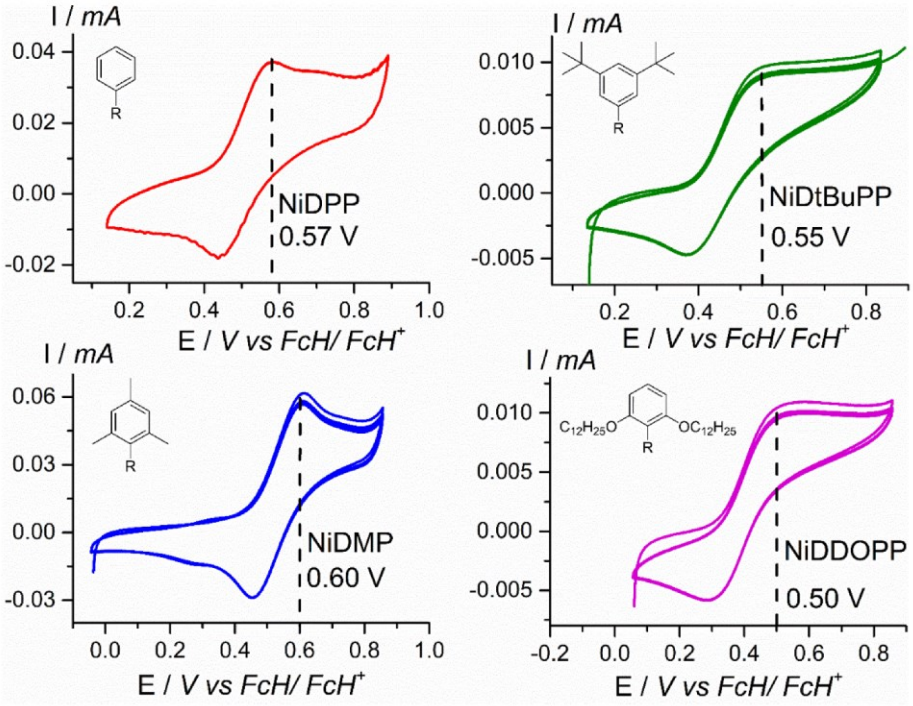

Figure S2. Cyclovoltammograms and respective oxidation potential obtained for of NiDPP (0.57 V), NiDtBuPP (0.55 V), NiDMP (0.60 V) and NiDDOPP (0.50 V) in $CH_2Cl_2/[^nBu_4N][PF_6]$.

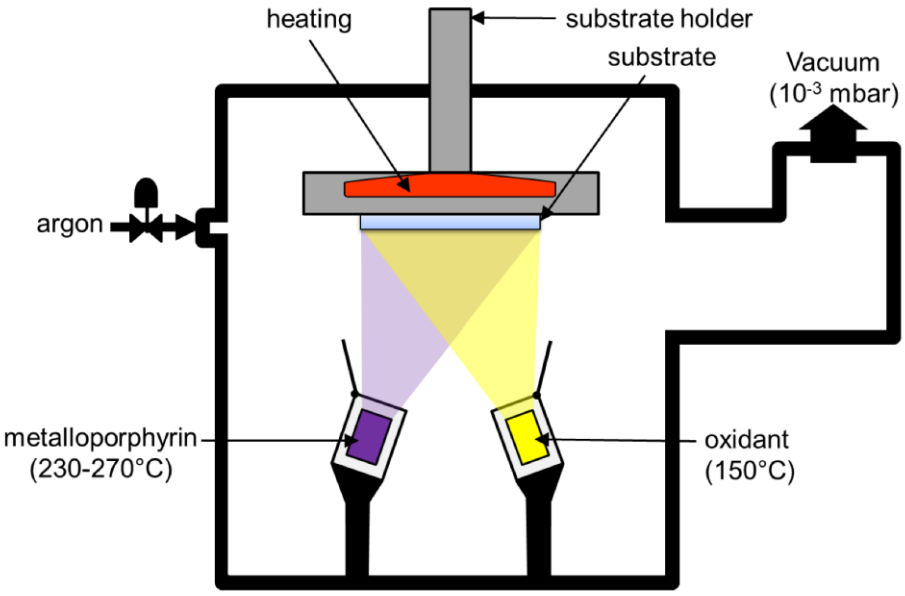

Figure S3. Schematic of the homemade built oCVD reactor used for the experiments. The porphyrins are sublimed under vacuum towards the substrate simultaneously to the oxidant ($FeCl_3$).

Substrate Temperature 150°C

NiDPP – Nickel(II) 5,15-(diphenyl)porphyrin	
Chemical formula:	$C_{32}H_{20}N_4Ni$
Molecular weight:	519.23 g·mol^{-1}
Sublimation temperature:	235°C
Sublimed amount (10^{-3} mbar & 235°C):	9.6 µmol

NiDMP – Nickel(II) 5,15-(dimesityl)porphyrin	
Chemical formula:	$C_{38}H_{32}N_4Ni$
Molecular weight:	603.40 g·mol^{-1}
Sublimation temperature:	230°C
Sublimed amount (10^{-3} mbar & 230°C):	13.1 µmol

NiDD*t*-BuPP – Nickel(II) 5,15-(di-3,5-di-tert-butylphenyl)porphyrin	
Chemical formula:	$C_{48}H_{52}N_4Ni$
Molecular weight:	743.67 g·mol^{-1}
Sublimation temperature:	260°C
Sublimed amount (10^{-3} mbar & 260°C):	9.7 µmol

NiDDOPP – Nickel(II) 5,15-(di-2,6-dodecyloxyphenyl)porphyrin	
Chemical formula:	$C_{80}H_{116}N_4NiO_4$
Molecular weight:	1256.53 g·mol^{-1}
Sublimation temperature:	270°C
Sublimed amount (10^{-3} mbar & 270°C):	8.8 µmol

$FeCl_3$ – Iron(III) Chloride	
Chemical formula:	Cl_3Fe
Molecular weight:	162.20 g·mol^{-1}
Sublimation temperature:	150°C
Sublimed amount (10^{-3} mbar & 150°C):	661.2 µmol

Table S1. Chemical formula, molecular weight, sublimation temperature and sublimed amount for the four porphyrins investigated and the oxidant.

Porphyrin	Film thickness
NiDPP	169 nm
NiDMP	520 nm
NiDDt-BuPP	355 nm
NiDDOPP	560 nm

Table S2. Thickness of the oCVD coating measured by profilometry.

Figure S4. Optical image of the different coating obtained by simple sublimation (left) and oCVD (right) for each porphyrin on microscope glass. A) NiDPP b) NiDtBuPP c) NiDMP d) NiDDOPP.

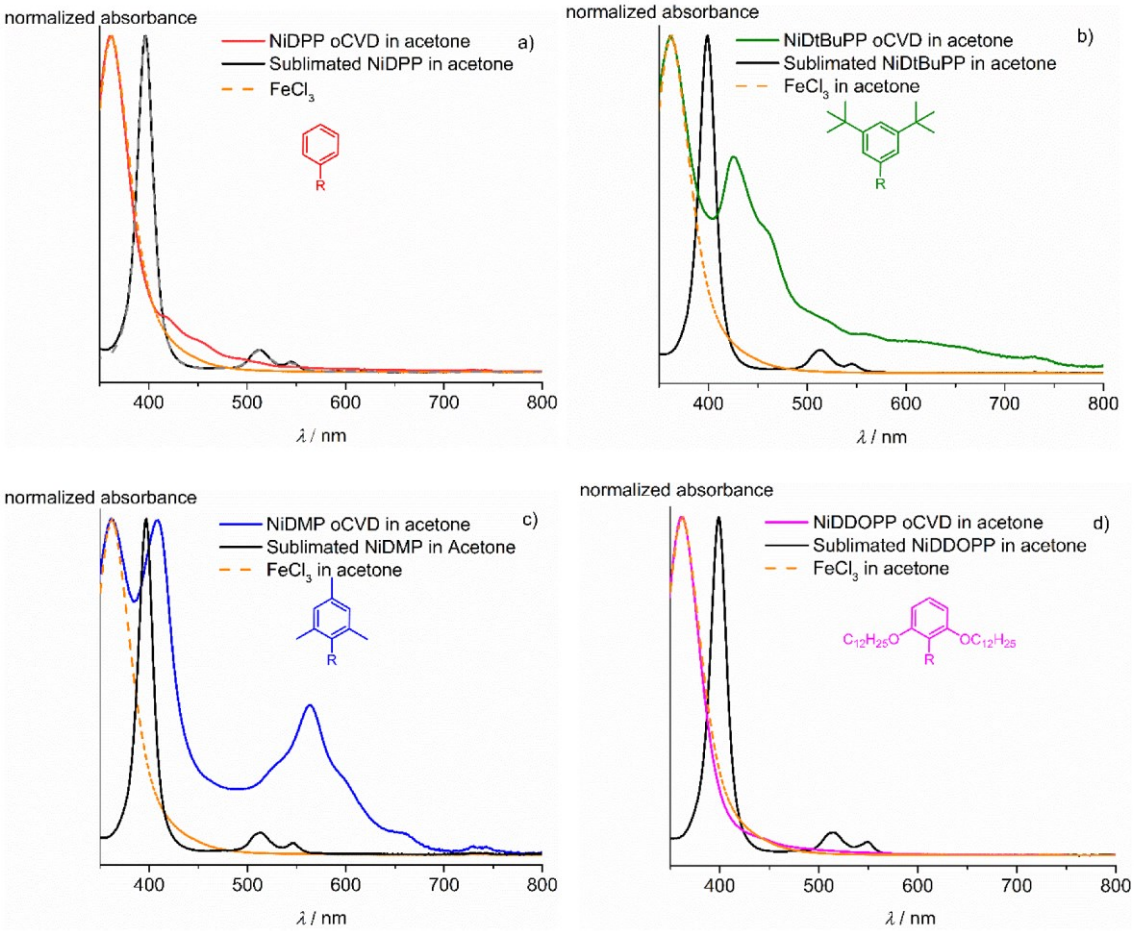

Figure S5. UV/Vis/ spectroscopy of the soluble fractions in acetone for the different oCVD coatings : a)NiDPP b) NiDtBuPP c) NiDMP d)NiDDOPP. For comparison the spectra of the sublimated porphyrin and of $FeCl_3$ solubilized in acetone are reported. All the samples exhibit residues of unreacted $FeCl_3$. The NiDPP and NiDDOPP coating are unsoluble and the only signal observed is related to the $FeCl_3$ residues.

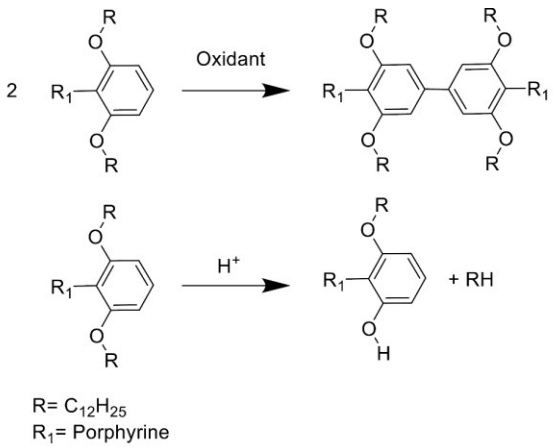

Scheme S3. Schematic of the suggested dehydrogenative coupling occurring on the NiDDOPP phenyl rings. The position of the coupling is merely representative.

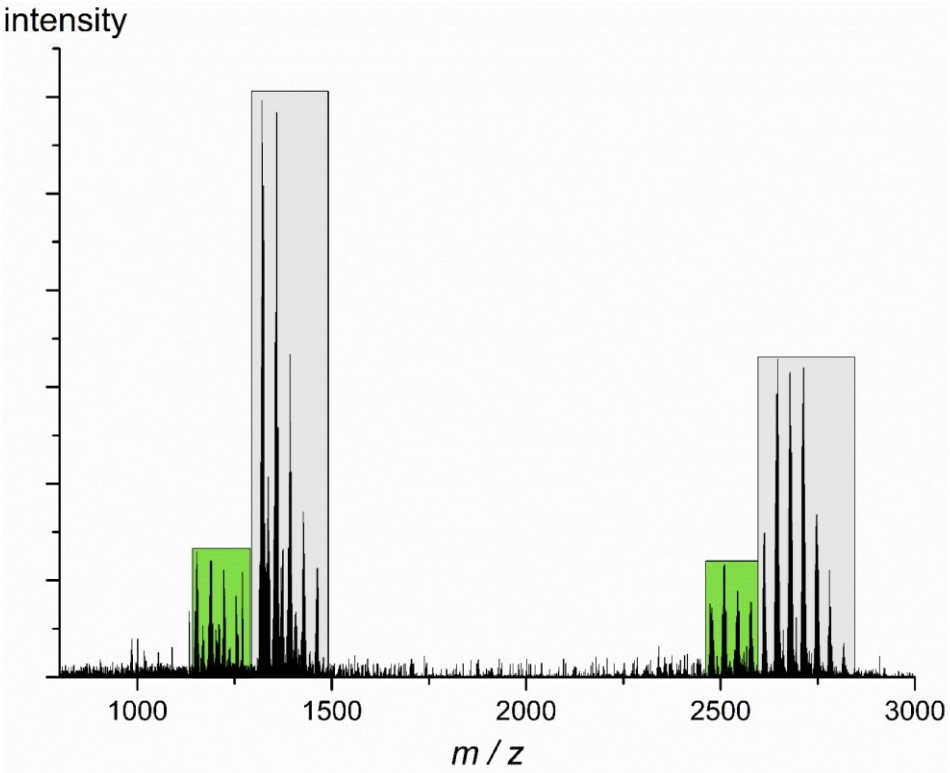

Figure S6. LDI-HRMS spectrum for the NiDDOPP oCVD coating synthesized in milder conditions (substrate temperature 50°C). The new spectrum evidence the presence of highly chlorinated monomer ($C_{80}H_{116}N_4NiO_4$)+nCl-nH (n= 2,3,4,5,6) and dimers ($C_{160}H_{232}N_8Ni_2O_8$)+ xCl –xH (x=3,4,5,6,7,8,9)-nH (n=2,4,6) (gray rectangles). The hydrolysis of the ether groups was observed both in the monomer ($C_{80}H_{116}N_4NiO_4$) + nCl – nH – $C_{12}H_{25}$ (n=2,3,4,5) and dimer region ($C_{160}H_{232}N_8Ni_2O_8$) + xCl – xH –nH – $C_{12}H_{25}$ (x=4,5,6,7,) (n=2,4,6) (green rectangles).

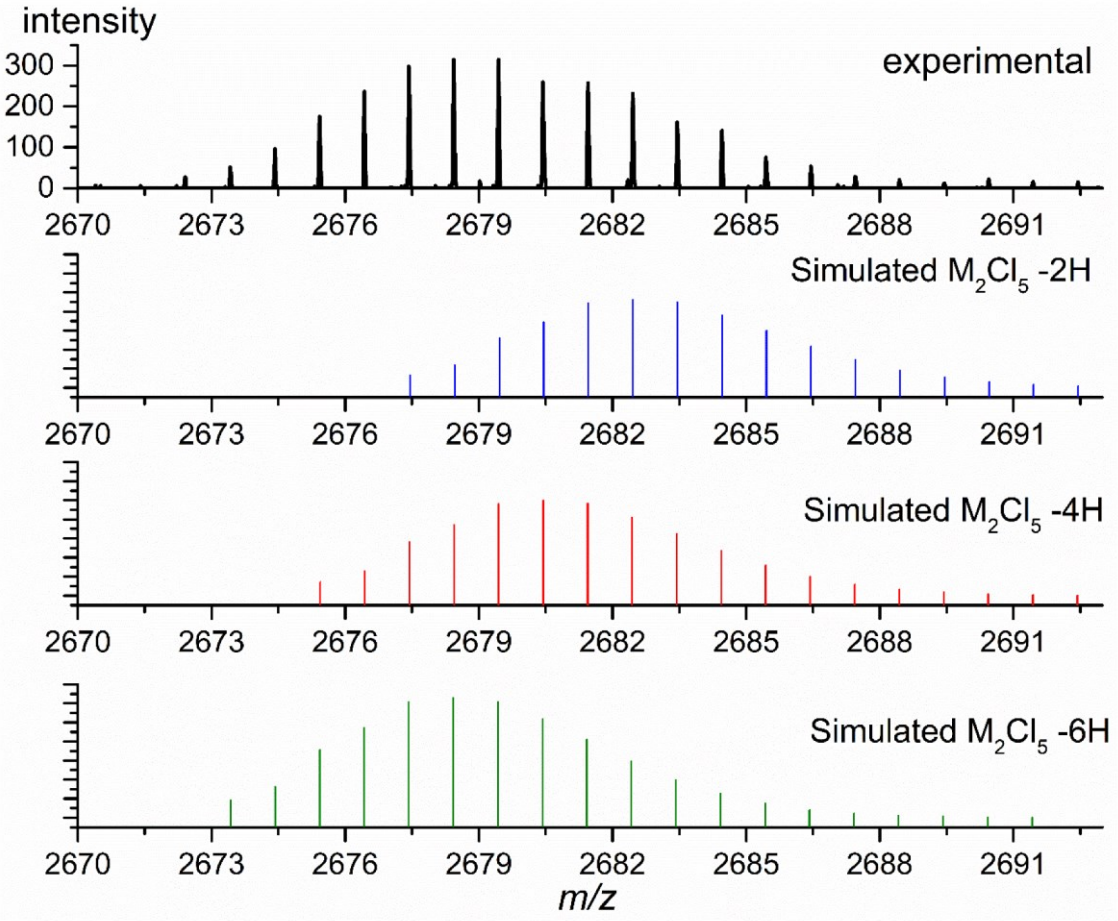

Figure S7. Experimental and simulated spectra for $(NiDDOPP)_2$+ 5Cl-xH. The spectra shows the existence of both triply, doubly and singly linked highly chlorinated dimers.

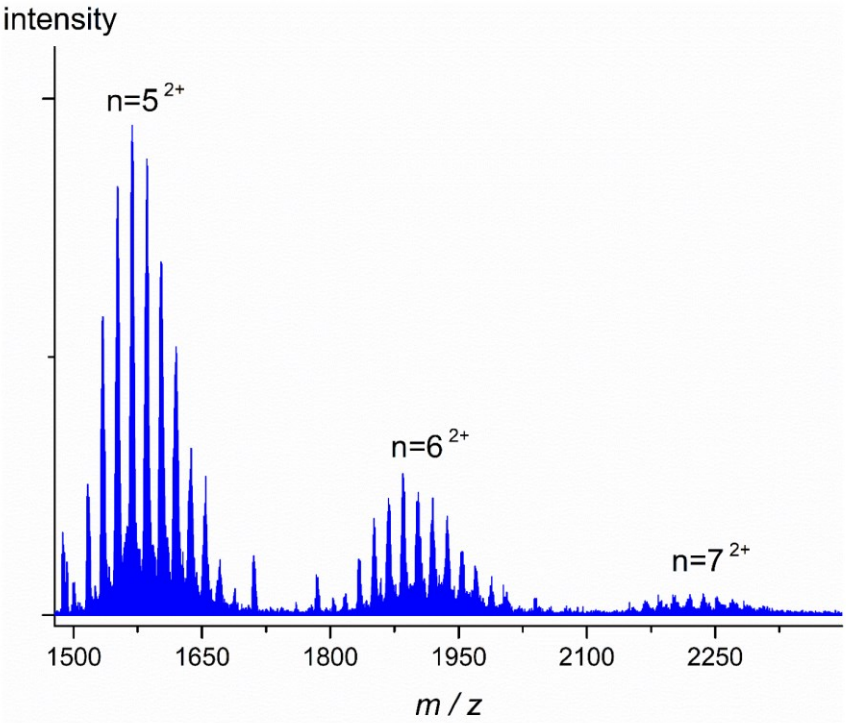

Figure S8. Sum of mass spectra recorded between 6.6 and 8.1 minutes of elution in GPCxESI-HRMS evidences the presence of doubly charged high oligomers (n= 5,6,7).

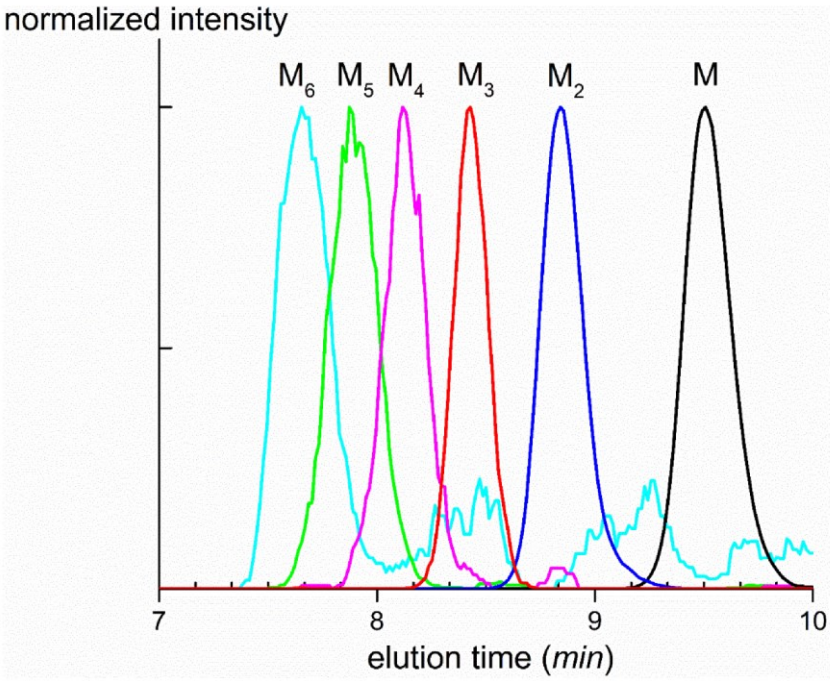

Figure S9. Extracted Ion Chromatogram (EIC) for the NiDMP oCVD coating different oligomers. The analysis clearly show different retention time for different *m/z* ratio going from hexamer (M_6) to monomer (M). The heptamer is omitted because of its low signal to noise ratio.

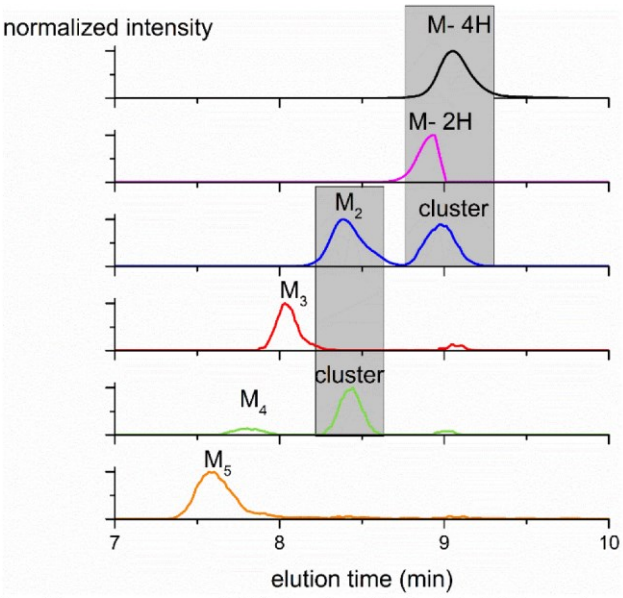

Figure S10. Extracted Ion Chromatograms (EIC) for the NiDtBuPP oCVD coating different oligomers. The analysis clearly show different retention time for different *m/z* going from pentamer (M_5) to the singly and doubly ring fused monomers (M-2H and M-4H). The signals around 8.5 minutes for M_4 and around 9 minutes for the M_2 (grey boxes) are attributed to the formation of clusters. Indeed, this signal is observed simoultaneously to the elution of M_2 and M-2H/M-4H that forming dimeric clusters yield the same *m/z* ratio.

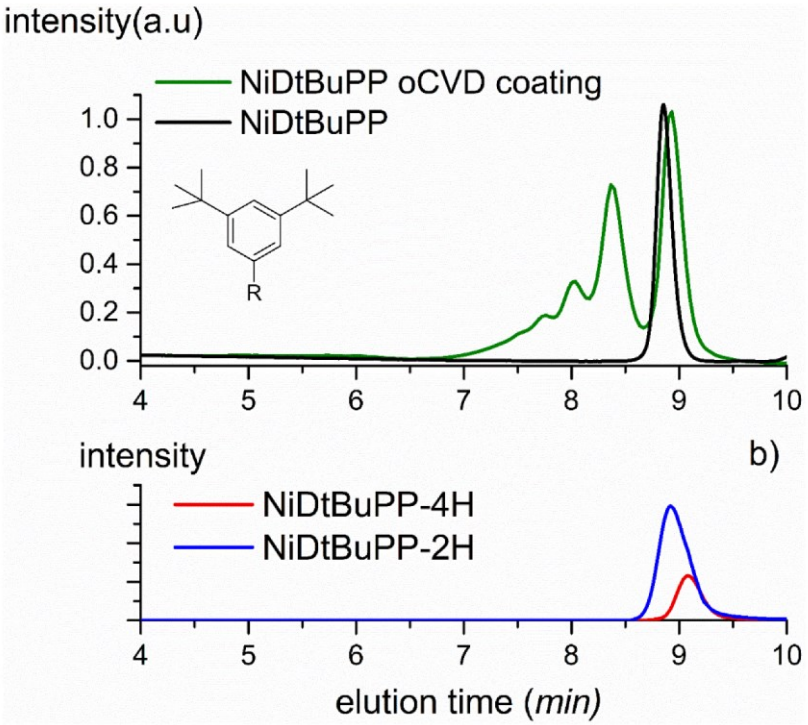

Figure S11. GPC analysis of the NiDtBUPP coating (a) and extracted ion chromatogram for *m/z = 741.35 (NiDtBuPP-2H)* and *739.33 (NiDtBuPP -4H)*. The analysis shows that the cyclization reaction affect the geometry of the molecule causing smaller hydrodinamic volume.

Monomer	NiDtBuPP	NiDtBuPP–2H	NiDtBuPP–4H
Parent ion (m/z)	743.36	741.35	739.33
Fragment ion exact mass (Da) **[Loss]**	728.3135 **[CH_3]**	726.3191 **[CH_3]**	724.3033 **[CH_3]**
	687.2797 **[C_4H_8]**	685.2844 **[C_4H_8]**	683.2683 **[C_4H_8]**
	631.2161 **[$(C_4H_8)_2$]**	629.2217 **[$(C_4H_8)_2$]**	627.2057 **[$(C_4H_8)_2$]**
	575.1540 **[$(C_4H_8)_3$]**	573.1586 **[$(C_4H_8)_3$]**	571.1432 **[$(C_4H_8)_3$]**
	554.1975 **[$C_{14}H_{21}$]**	552.1821 **[$C_{14}H_{21}$]**	-
	-	517.0756 **[$(C_4H_8)_4$]**	515.0806 **[$(C_4H_8)_4$]**

Table S3. List of fragment ions and corresponding molecular formula loss from the MS-MS structural analysis of NiDtBuPP monomer and its fused derivatives. Parent ions are detected as protonated adducts $[M+H]^+$.

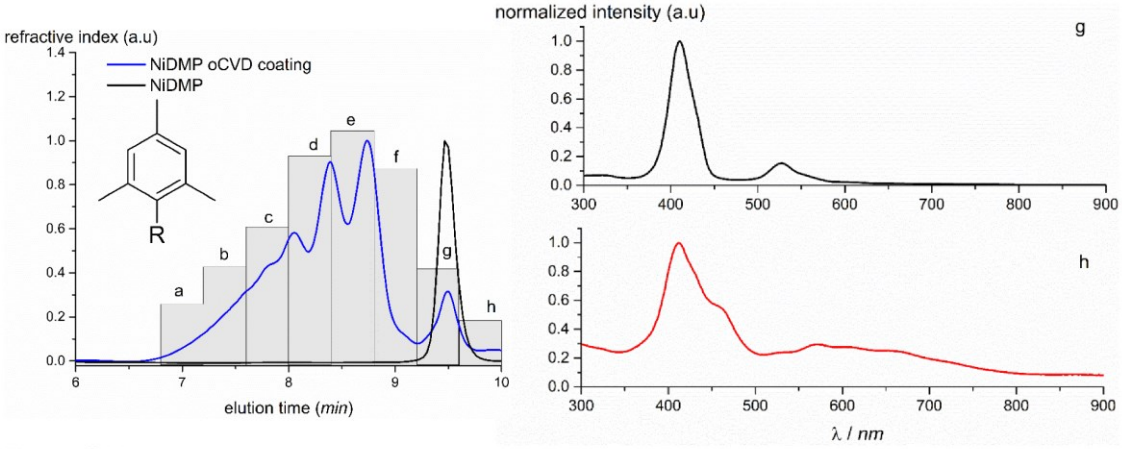

Figure S12. *GPC of the NiDMP oCVD coating and UV-Vis spectra acquired along the GPC elution of monomeric species for NiDMP oCVD coating* (indicated *as fraction g and h).*

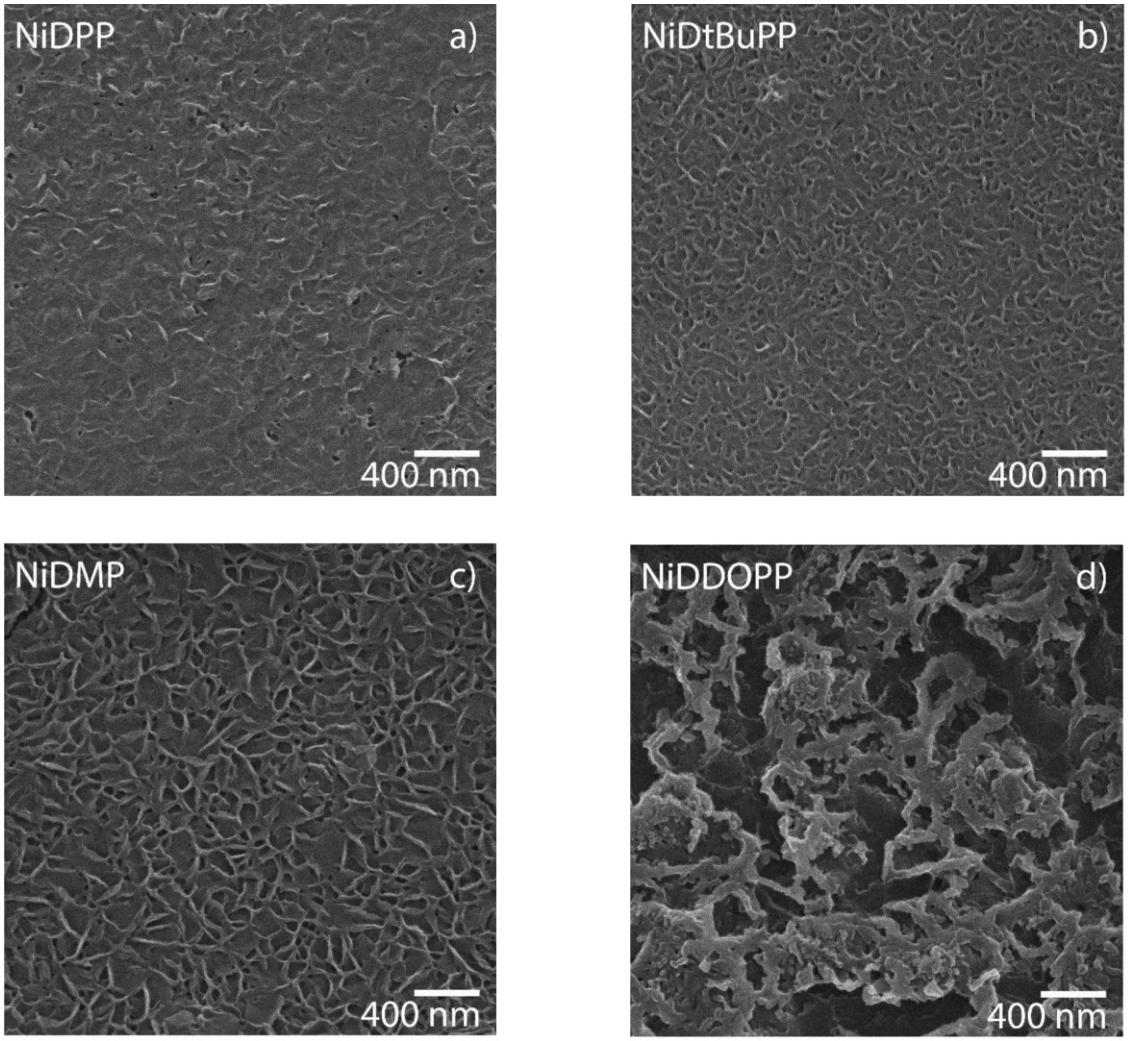

Figure S13. Helium ion microscope images of the a) NiDPP b) NiDtBuPP c) NiDMP d) NiDDOPP oCVD coatings deposited on silicon substrate. The images show the effect of the substituents on the morphology of the oCVD coatings. NiDPP (a) exhibit a smooth surface thanks to the intramolecular cyclization allowing more compact arrangements. Bigger substituents such as dimesity and di-tertbutyl cause a rugged surface (b,c). Finally, the long side chains of the NiDDOPP cause an even more rugged surface.

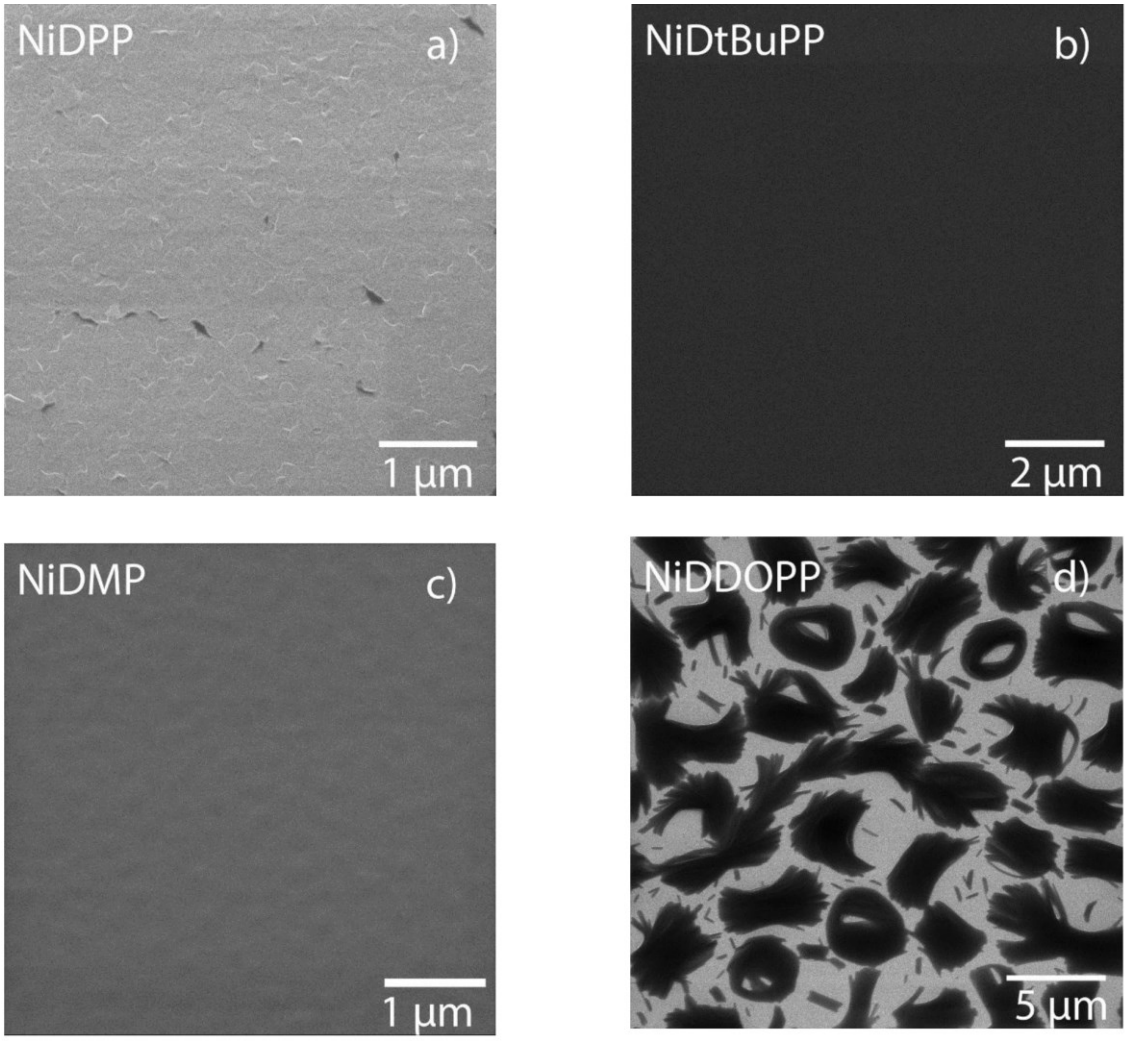

Figure S14. Helium ion microscope images of the sublimated porphyrins deposited on silicon substrate. All the porphyrins cover homogeneously and smoothly the surface. Only the NiDDOPP cover unomogenously the surface. This is probably related to the long chains inducing different interactions between the porphyrins.

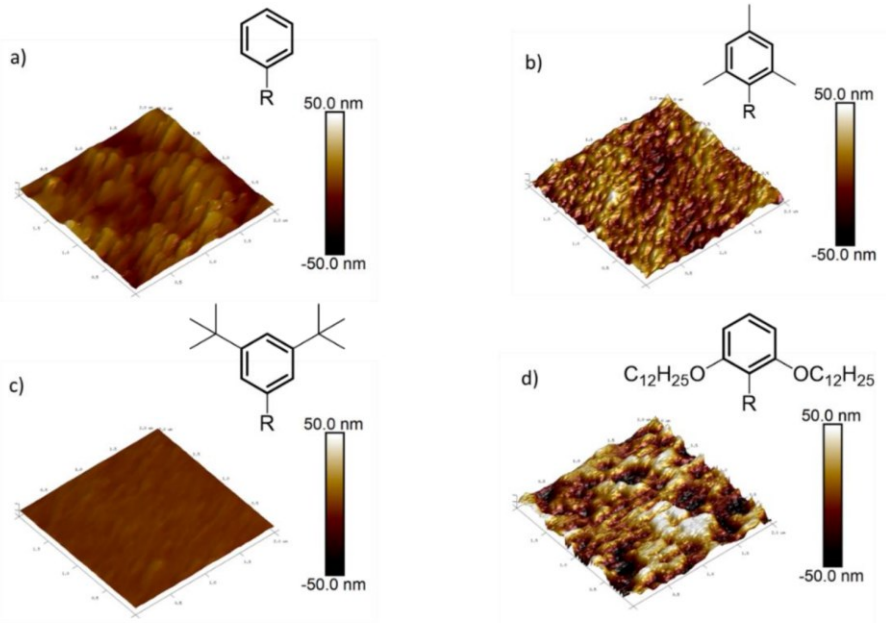

Figure S15. AFM Topography of the probed oCVD coatings on platinum substrate. The same scale used for the images to evidence differences in roughness between the coatings. a) NiDPP oCVD coating, b) NiDMP oCVD coating, c) NiDtBuPP oCVD coating, d) NiDDOPP oCVD coating.

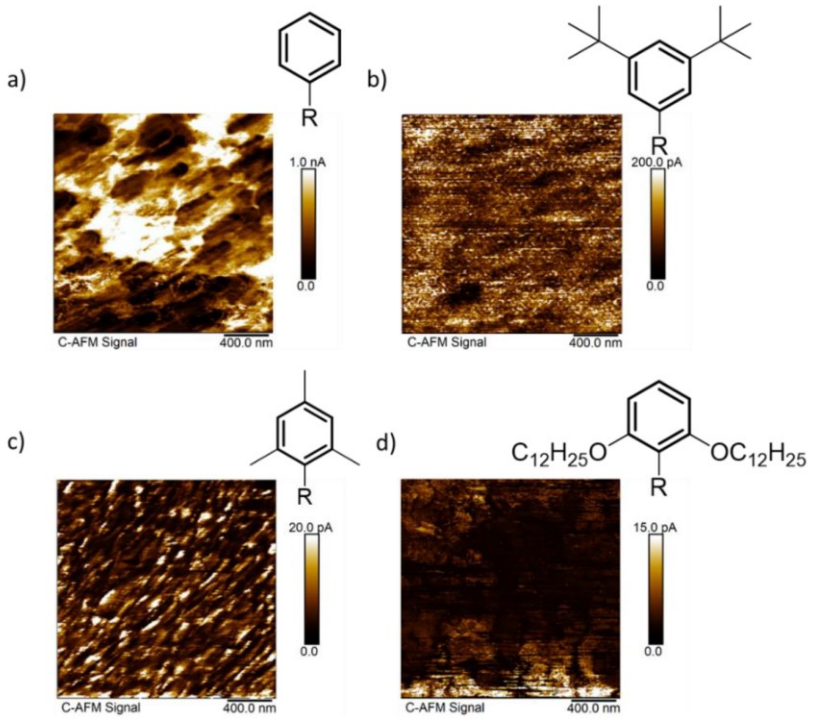

Figure S16. Conductivity AFM images of the probed oCVD coatings acquired simoultaneously to the topographic images. Due to their differences in conductivity, scales were adapted for contrast. a) NiDPP b) NiDMP c) NiDtBuPP and d) NiDDOPP oCVD coatings.

Porphyrin oCVD	Roughness (Ra / nm)	Current (pA)
NiDDOPP	21 ± 3	4.0 ± 1
NiDMP	10 ± 2	6.5 ± 0.6
NiDtBuPP	1.2 ± 0.2	77 ± 15
NiDPP	4.6 ± 0.7	440 ± 120

Table S4. Roughness and current of the different oCVD coatings obtained by C-AFM measurements.

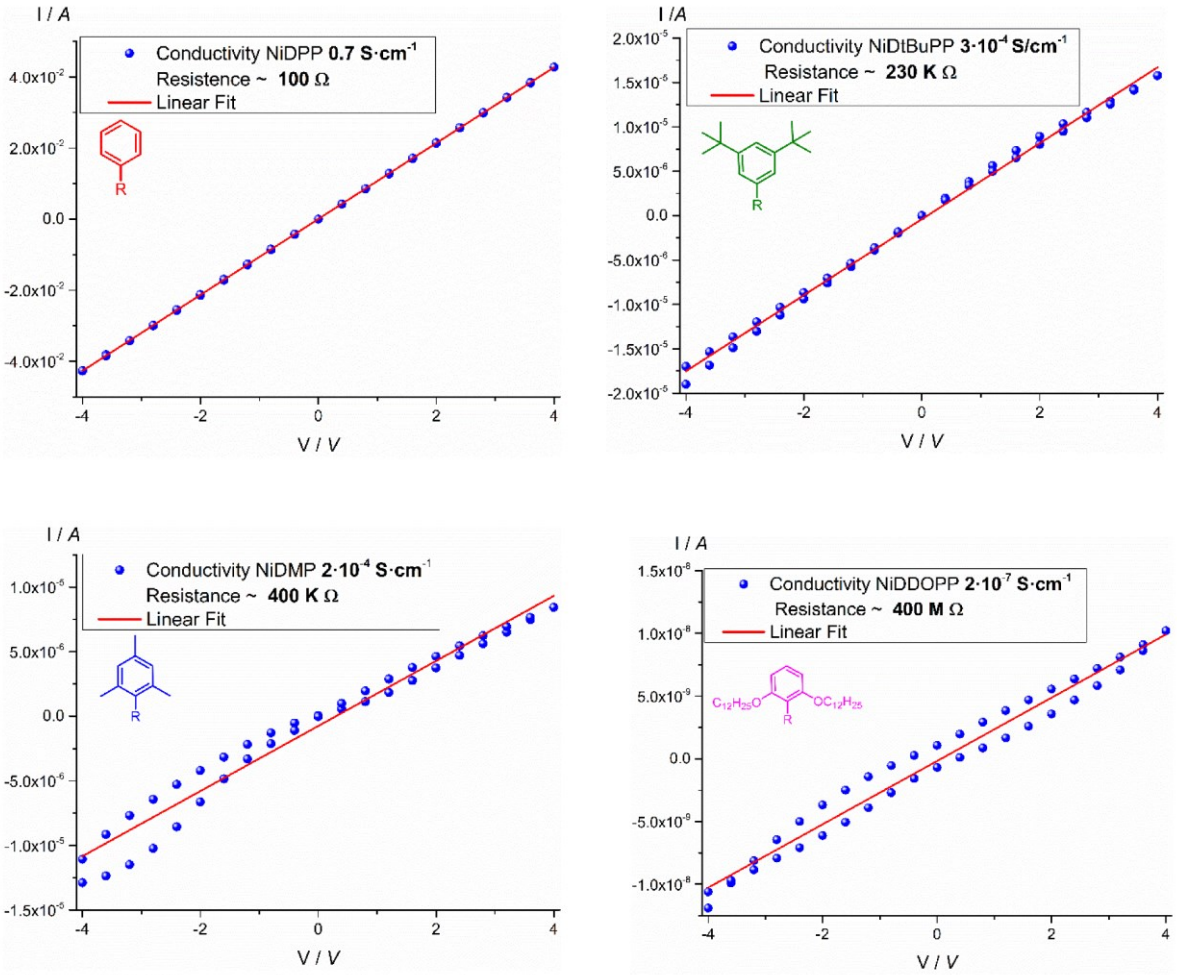

Figure S17. I-V curves obtained from 2-point-probes measurements. Only NiDPP present a perfectly ohmic behaviour. The conductivity is calculated assimilating the behaviour to ohmic also for the other compounds. The calculated conductivity is reported in each graph.

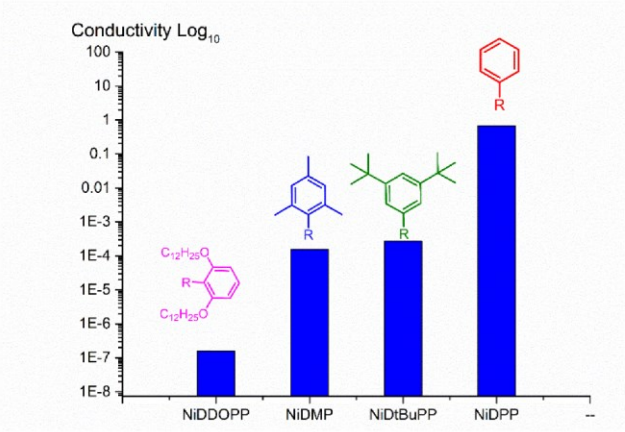

Figure S18. Conductivity calculated for the different oCVD coatings. The resulting conductivity is reported in logarithmic scale.

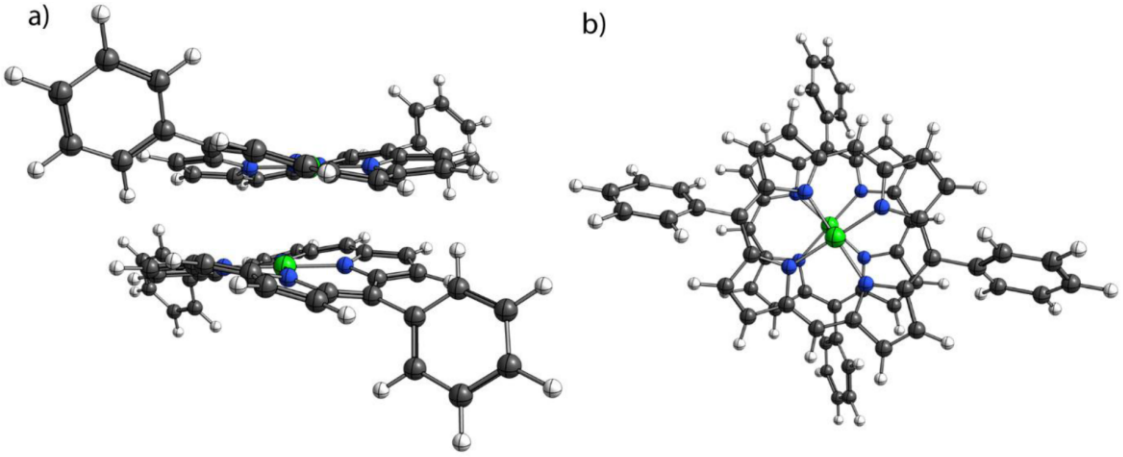

Figure S19. DFT calculated geometry for two NiDPP molecules. a) side view, b) top view. The NiDPP molecules present a saddle shape with the four substituents pointing to different direction to minimize the hindrance. RIJCOSX-BP86-D3BJ-ZORA/def2-SVP level of theory.

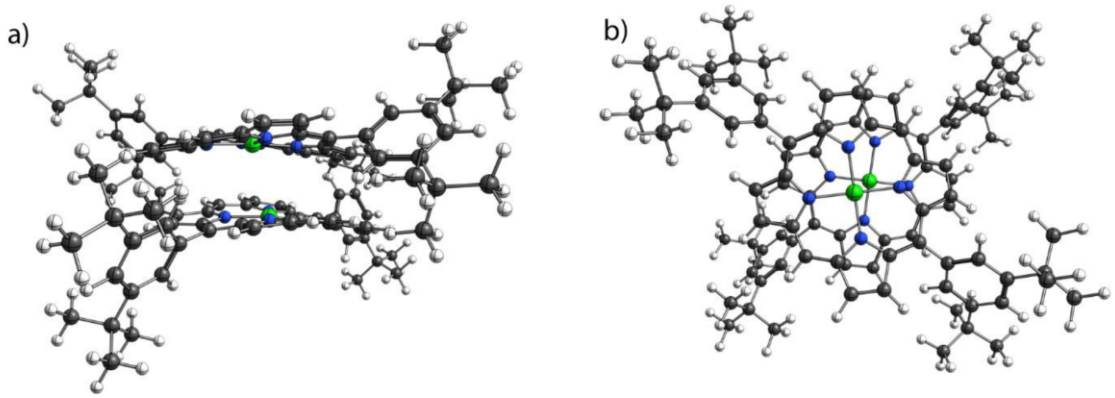

Figure S20. DFT calculated geometry for two NiDtBuPP molecules. a) side view, b) top view. The molecules adopt a saddled, staggered conformation with the *tertbutyl* groups pointing in different directions. RIJCOSX-BP86-D3BJ-ZORA/def2-SVP level of theory.

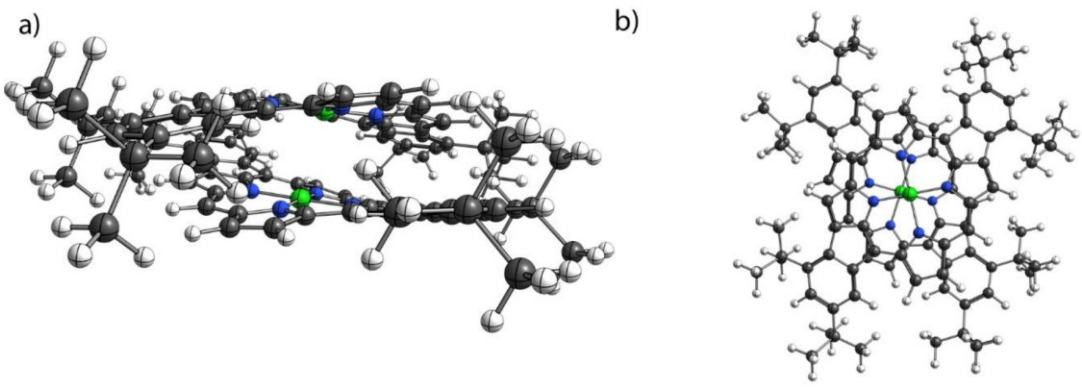

Figure S21. DFT calculated geometry for two NiDtBuPP molecules undergone to cyclization reaction between the phenyl and the porphyrin macrocycle (Fused NiDtBuPP).a) side view, b) top view. The porphyrin present an increase planarity if compared to NiDtBuPP. Only part of the *tert-butyl* group is pointing out of the plane. RIJCOSX-BP86-D3BJ-ZORA/def2-SVP level of theory.

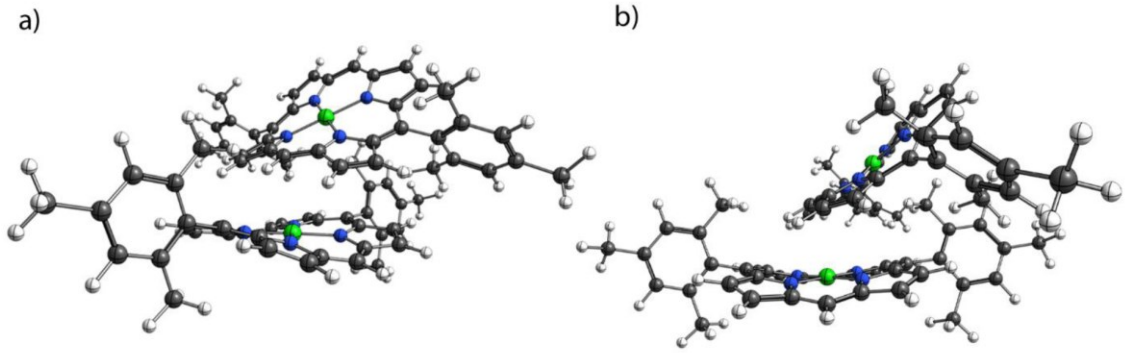

Figure S22. DFT calculated geometry for two NiDMP molecules. a),b) two different side view. Differently from NiDPP the molecules adopt a face to edge conformation. RIJCOSX-BP86-D3BJ-ZORA/def2-SVP level of theory.

Table S5. XYZ Coordinate calculated for two molecules of NiDPP.

	X	Y	Z
6	-0.556183000	-0.394667000	-3.256676000
6	0.199166000	3.395932000	-0.293014000
6	-0.818666000	0.380626000	3.399000000
6	0.351715000	-3.352484000	0.506012000
7	-0.273823000	1.541514000	1.293493000
7	-0.240932000	1.241712000	-1.438801000
7	-0.121520000	-1.525888000	-1.109518000
7	-0.310140000	-1.230184000	1.602419000
6	0.219272000	-2.832763000	-0.790575000
6	-0.338609000	-1.524615000	-2.479369000
6	-0.424844000	0.901801000	-2.769566000
6	0.031100000	2.604834000	-1.438211000
6	0.004181000	-2.583428000	1.626309000
6	-0.645730000	-0.905973000	2.908023000
6	-0.564554000	1.522188000	2.649059000
6	-0.006054000	2.871226000	0.991930000
6	0.238566000	-3.653505000	-1.986139000
6	-0.146063000	-2.847451000	-3.026373000
6	-0.274491000	2.063073000	-3.615903000
6	0.052194000	3.112630000	-2.794239000
6	-0.114509000	3.688426000	2.184455000
6	-0.485079000	2.851103000	3.206911000
6	-0.129315000	-3.105207000	2.971710000
6	-0.578938000	-2.072733000	3.754115000
1	0.464049000	-4.724315000	-1.999465000
1	-0.279338000	-3.105449000	-4.082969000
1	-0.343599000	2.050592000	-4.710129000
1	0.284242000	4.145737000	-3.070108000
1	0.041372000	4.771583000	2.210215000
1	-0.680990000	3.092073000	4.257768000
1	0.092433000	-4.133400000	3.269962000

1 -0.786092000 -2.068801000 4.829927000

6 0.520380000 4.845130000 -0.427381000

6 -0.367530000 5.738265000 -1.066551000

6 1.722189000 5.357212000 0.110340000

1 -1.311458000 5.349531000 -1.474807000

1 2.420072000 4.665979000 0.606406000

6 -0.061270000 7.103755000 -1.169713000

6 2.028590000 6.722574000 0.007678000

1 -0.768393000 7.785653000 -1.666602000

1 2.972490000 7.103006000 0.427407000

6 1.138381000 7.600607000 -0.633376000

1 1.378791000 8.671682000 -0.713741000

6 0.792907000 -4.766842000 0.662144000

6 2.058115000 -5.161735000 0.171469000

6 -0.027536000 -5.742894000 1.269986000

1 2.706112000 -4.406078000 -0.297486000

1 -1.016125000 -5.447528000 1.644705000

6 2.489490000 -6.491807000 0.285750000

6 0.404407000 -7.072853000 1.384716000

1 3.480701000 -6.778413000 -0.097969000

1 -0.252188000 -7.819808000 1.857110000

6 1.664223000 -7.453165000 0.892974000

1 2.002522000 -8.496685000 0.982816000

28 -0.267724000 0.007532000 0.086186000

1 -0.708120000 -0.534020000 -4.335188000

1 -1.069544000 0.502968000 4.460435000

6 -3.204531000 2.661225000 0.981529000

6 -3.898285000 -0.192921000 -2.897245000

6 -2.935035000 -3.971701000 0.021858000

6 -4.161529000 -1.182155000 3.821134000

7 -3.442765000 -1.826989000 -1.083022000

7 -3.465634000 0.881797000 -0.706144000

7 -3.674924000 0.489331000 2.047051000

7 -3.488060000 -2.229450000 1.676636000

23

6 -4.016307000 0.129527000 3.344919000

6 -3.485842000 1.862008000 2.082487000

6 -3.247837000 2.197227000 -0.325585000

6 -3.684404000 0.924822000 -2.077423000

6 -3.853187000 -2.287971000 3.016518000

6 -3.186161000 -3.533366000 1.318014000

6 -3.132305000 -3.178670000 -1.100684000

6 -3.714232000 -1.492700000 -2.402229000

6 -4.058215000 1.302136000 4.196542000

6 -3.705006000 2.373321000 3.414497000

6 -3.291137000 3.071392000 -1.472744000

6 -3.609316000 2.291279000 -2.554479000

6 -3.595653000 -2.662158000 -3.251942000

6 -3.196884000 -3.697912000 -2.447028000

6 -3.810823000 -3.656568000 3.488286000

6 -3.354580000 -4.422125000 2.444729000

1 -4.294927000 1.284349000 5.265082000

1 -3.606695000 3.428143000 3.694384000

1 -3.160880000 4.158179000 -1.426632000

1 -3.778075000 2.604159000 -3.588392000

1 -3.746007000 -2.658813000 -4.335940000

1 -2.974867000 -4.735352000 -2.721281000

1 -4.093462000 -3.978388000 4.495138000

1 -3.207550000 -5.508105000 2.409746000

6 -4.248268000 -0.023501000 -4.335526000

6 -3.404439000 0.665929000 -5.234375000

6 -5.447040000 -0.583369000 -4.832646000

1 -2.466518000 1.095899000 -4.859481000

1 -6.113251000 -1.116317000 -4.137678000

6 -3.749192000 0.792449000 -6.588527000

6 -5.791234000 -0.457246000 -6.186819000

1 -3.075374000 1.329059000 -7.274245000

1 -6.731999000 -0.895895000 -6.553447000

6 -4.943442000 0.231370000 -7.070651000

1 -5.213285000 0.330656000 -8.133088000

6 -4.573743000 -1.383027000 5.239396000

6 -5.844564000 -0.947237000 5.676301000

6 -3.707138000 -1.984893000 6.178184000

1 -6.526196000 -0.481135000 4.948960000

1 -2.711228000 -2.313663000 5.848401000

6 -6.238224000 -1.112497000 7.012884000

6 -4.100690000 -2.150746000 7.514781000

1 -7.234548000 -0.772077000 7.334291000

1 -3.409358000 -2.617139000 8.233427000

6 -5.368054000 -1.715488000 7.936740000

1 -5.676979000 -1.844986000 8.985194000

28 -3.485069000 -0.671180000 0.485295000

1 -3.040811000 3.733744000 1.147133000

1 -2.697601000 -5.032567000 -0.133114000

Table S6. XYZ Coordinate calculated for two molecules of fused NiDPP.

	X	Y	Z
6	6.041859000	-1.368733000	-2.177541000
6	8.397279000	0.970675000	1.364599000
6	5.878694000	-1.520056000	4.705722000
6	3.512151000	-3.848723000	1.160727000
7	6.863386000	-0.565688000	2.680057000
7	7.029467000	-0.415223000	-0.110165000
7	5.068534000	-2.331300000	-0.151989000
7	4.911033000	-2.494661000	2.637125000
6	4.095135000	-3.259977000	0.040179000
6	5.162694000	-2.226777000	-1.540551000
6	6.905002000	-0.516645000	-1.488911000
6	8.002458000	0.573770000	0.088939000
6	3.931010000	-3.470917000	2.438472000
6	5.031865000	-2.387705000	4.015716000
6	6.745184000	-0.645933000	4.070820000
6	7.808479000	0.387432000	2.488247000
6	3.537060000	-3.773425000	-1.187632000
6	4.215991000	-3.127166000	-2.198126000
6	7.794982000	0.404849000	-2.153584000
6	8.476162000	1.083367000	-1.172976000
6	8.317064000	0.952786000	3.714654000
6	7.643782000	0.299839000	4.727304000
6	3.446732000	-3.972855000	3.700038000
6	4.131260000	-3.298199000	4.681825000
1	4.122752000	-3.222645000	-3.286010000
1	7.880000000	0.507345000	-3.240838000
1	9.236888000	1.859009000	-1.292948000
1	7.715851000	0.419233000	5.815229000
1	4.040650000	-3.394445000	5.770346000
6	9.360410000	1.979587000	1.884839000
6	10.235303000	2.854971000	1.235744000

6 9.305416000 1.967464000 3.328755000

1 10.313133000 2.871524000 0.141085000

6 11.042111000 3.723465000 2.002620000

6 10.111924000 2.827059000 4.076647000

1 11.738700000 4.402596000 1.490470000

1 10.068795000 2.815239000 5.176103000

6 10.982284000 3.711863000 3.402783000

1 11.625976000 4.390131000 3.982645000

6 2.504740000 -4.813231000 0.640465000

6 1.629316000 -5.690865000 1.286358000

6 2.522965000 -4.761557000 -0.804933000

1 1.592975000 -5.753642000 2.382584000

6 0.776738000 -6.513132000 0.514583000

6 1.676351000 -5.576821000 -1.555142000

1 0.087861000 -7.203709000 1.024280000

1 1.701441000 -5.540743000 -2.653886000

6 0.797543000 -6.457321000 -0.885640000

1 0.128446000 -7.107144000 -1.469568000

28 5.994214000 -1.477439000 1.262767000

1 6.057583000 -1.344980000 -3.274658000

1 5.848746000 -1.531780000 5.803920000

1 2.675495000 -4.739679000 3.818094000

6 9.010380000 -2.800306000 -3.278690000

6 11.376114000 -0.469291000 0.265344000

6 8.847181000 -2.949170000 3.604276000

6 6.490467000 -5.288724000 0.063089000

7 9.820128000 -1.986828000 1.578492000

7 9.977773000 -1.824411000 -1.210350000

7 8.024535000 -3.752940000 -1.252917000

7 7.858999000 -3.903076000 1.537232000

6 7.079103000 -4.705638000 -1.060727000

6 8.143194000 -3.673678000 -2.643688000

6 9.857270000 -1.932577000 -2.588898000

6 10.957640000 -0.847907000 -1.012314000

6 6.885980000 -4.892112000 1.338630000

6 7.984169000 -3.801584000 2.915910000

6 9.725875000 -2.090777000 2.967103000

6 10.792909000 -1.057555000 1.386023000

6 6.570436000 -5.271367000 -2.286951000

6 7.244285000 -4.619347000 -3.299833000

6 10.758043000 -1.022590000 -3.255521000

6 11.442297000 -0.347058000 -2.274148000

6 11.350521000 -0.543244000 2.613704000

6 10.671869000 -1.189476000 3.624402000

6 6.413030000 -5.401854000 2.600763000

6 7.094550000 -4.723159000 3.581010000

1 7.172373000 -4.739332000 -4.387702000

1 10.848962000 -0.927284000 -4.344102000

1 12.213537000 0.419695000 -2.392649000

1 10.765043000 -1.093592000 4.712255000

1 7.010048000 -4.825686000 4.668307000

6 12.382812000 0.496065000 0.785321000

6 13.258048000 1.373656000 0.139131000

6 12.364246000 0.445171000 2.230754000

1 13.294649000 1.435778000 -0.957125000

6 14.110122000 2.196698000 0.910647000

6 13.210351000 1.261205000 2.980686000

1 14.798861000 2.887248000 0.400728000

1 13.184982000 1.225799000 4.079445000

6 14.088975000 2.141675000 2.310890000

1 14.757662000 2.792085000 2.894633000

6 5.527349000 -6.297797000 -0.456801000

6 4.652490000 -7.172946000 0.192643000

6 5.582062000 -6.285902000 -1.900725000

1 4.574972000 -7.189365000 1.287326000

6 3.845330000 -8.041400000 -0.573923000

6 4.775080000 -7.145324000 -2.648300000

1 3.148763000 -8.720356000 -0.061515000

1 4.817917000 -7.133675000 -3.747770000

6 3.904709000 -8.029872000 -1.974102000

1 3.260691000 -8.708018000 -2.553744000

28 8.894186000 -2.841094000 0.164064000

1 9.040898000 -2.789267000 -4.376882000

1 8.831581000 -2.972894000 4.701395000

1 5.652523000 -6.177651000 2.721131000

29

Table 7. XYZ Coordinate calculated for two molecules of NiDtBuPP.

	X	Y	Z
6	-4.065303000	0.280229000	-2.533904000
6	-2.922297000	2.653473000	1.553882000
6	-2.897160000	-1.616216000	3.861173000
6	-3.022146000	-3.963546000	-0.387767000
7	-2.870522000	0.288648000	2.298991000
7	-3.514353000	1.065336000	-0.261561000
7	-3.464490000	-1.614199000	-1.077198000
7	-3.155666000	-2.400094000	1.535378000
6	-3.244239000	-2.961097000	-1.340572000
6	-3.788353000	-1.058047000	-2.307477000
6	-3.929832000	1.266300000	-1.569665000
6	-3.363358000	2.344941000	0.263852000
6	-3.082524000	-3.675713000	0.983482000
6	-3.101619000	-2.601444000	2.909365000
6	-2.725636000	-0.275168000	3.556655000
6	-2.675668000	1.651382000	2.498646000
6	-3.415959000	-3.238421000	-2.753288000
6	-3.768693000	-2.056301000	-3.349189000
6	-4.078343000	2.672186000	-1.858112000
6	-3.704962000	3.347397000	-0.725047000
6	-2.350951000	1.925327000	3.883706000
6	-2.393081000	0.723946000	4.542421000
6	-3.017939000	-4.676988000	2.028478000
6	-3.068781000	-4.009034000	3.223142000
1	-3.330963000	-4.232044000	-3.201915000
1	-4.022141000	-1.865446000	-4.397770000
1	-4.394794000	3.072242000	-2.828192000
1	-3.643700000	4.427313000	-0.559075000
1	-2.163631000	2.923948000	4.289913000
1	-2.232975000	0.511788000	5.605986000
1	-2.927786000	-5.752634000	1.858663000

1 -3.026316000 -4.421716000 4.237277000

6 -2.830727000 4.079735000 1.976060000

6 -3.999270000 4.861627000 2.040569000

6 -1.603651000 4.655695000 2.351393000

1 -4.951899000 4.396492000 1.749841000

1 -0.697595000 4.034824000 2.290489000

6 -3.966467000 6.200807000 2.469053000

6 -1.528582000 5.990926000 2.794036000

6 -2.720376000 6.743343000 2.843207000

1 -2.676579000 7.783417000 3.184436000

6 -2.669088000 -5.334040000 -0.856347000

6 -1.537770000 -5.497707000 -1.689354000

6 -3.401525000 -6.471108000 -0.479976000

1 -0.966891000 -4.601053000 -1.961670000

1 -4.290678000 -6.329082000 0.144549000

6 -1.143426000 -6.765113000 -2.144284000

6 -3.020509000 -7.764739000 -0.892276000

6 -1.896195000 -7.886400000 -1.725784000

1 -1.585092000 -8.883156000 -2.065485000

28 -3.280947000 -0.666097000 0.627989000

1 -4.331006000 0.593388000 -3.551194000

1 -2.809161000 -1.916181000 4.912392000

6 -0.163976000 6.573762000 3.206713000

6 0.801691000 6.507686000 1.999317000

6 0.406903000 5.734378000 4.375194000

1 -0.271258000 5.767264000 5.252374000

1 0.539476000 4.671351000 4.091471000

1 1.396769000 6.126172000 4.689579000

1 0.949693000 5.467376000 1.647806000

1 1.796512000 6.916475000 2.273938000

1 0.408624000 7.098358000 1.146929000

6 -5.278169000 7.005581000 2.516134000

6 -6.273243000 6.297051000 3.466672000

6 -5.879203000 7.068040000 1.091157000

1 -5.181990000 7.570893000 0.390275000

1 -6.087819000 6.056038000 0.689668000

1 -6.834230000 7.633713000 1.094246000

1 -6.506662000 5.268347000 3.126278000

1 -7.229640000 6.857909000 3.518728000

1 -5.857649000 6.226084000 4.492390000

6 -3.840904000 -8.977949000 -0.415381000

6 -3.224192000 -10.312823000 -0.872517000

6 -5.274880000 -8.879014000 -0.986347000

1 -5.787315000 -7.961387000 -0.635949000

1 -5.260703000 -8.855895000 -2.095004000

1 -5.887193000 -9.747344000 -0.665472000

1 -3.195112000 -10.396751000 -1.977768000

1 -3.830333000 -11.159383000 -0.490980000

1 -2.191143000 -10.439741000 -0.490062000

6 0.073431000 -6.969392000 -3.065689000

6 -0.397902000 -7.636628000 -4.380120000

6 1.100941000 -7.884839000 -2.358272000

1 1.447957000 -7.428177000 -1.409160000

1 0.670060000 -8.877184000 -2.117175000

1 1.986597000 -8.050169000 -3.006775000

1 -0.872657000 -8.620858000 -4.194661000

1 0.461161000 -7.799718000 -5.064021000

1 -1.138852000 -6.998102000 -4.903014000

6 -0.270567000 8.039714000 3.666410000

1 -0.654725000 8.697978000 2.860917000

1 -0.935015000 8.148961000 4.547501000

1 0.731317000 8.416713000 3.955666000

6 -5.060750000 8.444386000 3.019700000

1 -4.370952000 9.011342000 2.362150000

1 -6.027227000 8.987658000 3.037204000

1 -4.648538000 8.462591000 4.048945000

6 -3.903469000 -8.969895000 1.131040000

1 -4.381334000 -8.047554000 1.518473000

1 -4.491799000 -9.834604000 1.502723000

1 -2.886115000 -9.030918000 1.568277000

6 0.763974000 -5.638187000 -3.416199000

1 1.150223000 -5.123827000 -2.513198000

1 1.625905000 -5.826542000 -4.088005000

1 0.076806000 -4.942675000 -3.939211000

6 -6.381071000 1.626015000 0.872762000

6 -6.123035000 -1.875120000 4.226403000

6 -6.375769000 -5.170813000 0.667302000

6 -7.109466000 -1.679640000 -2.609550000

7 -6.344005000 -3.194277000 2.137733000

7 -6.187415000 -0.442623000 2.198314000

7 -6.757915000 -0.357414000 -0.540478000

7 -6.545986000 -3.100627000 -0.653834000

6 -7.156014000 -0.493606000 -1.866431000

6 -6.782687000 1.009186000 -0.302371000

6 -6.066213000 0.932980000 2.029076000

6 -5.984059000 -0.652024000 3.557523000

6 -6.732876000 -2.889132000 -2.015111000

6 -6.371549000 -4.473533000 -0.530969000

6 -6.426729000 -4.560411000 1.910215000

6 -6.340146000 -3.065191000 3.521611000

6 -7.516338000 0.792820000 -2.425797000

6 -7.254352000 1.729803000 -1.459217000

6 -5.707687000 1.577714000 3.268623000

6 -5.653857000 0.594854000 4.220833000

6 -6.503698000 -4.358661000 4.155498000

6 -6.536551000 -5.289401000 3.149785000

6 -6.565978000 -4.126249000 -2.751034000

6 -6.345348000 -5.111680000 -1.825635000

1 -7.904021000 0.942905000 -3.437779000

1 -7.369831000 2.818610000 -1.502589000

1 -5.519039000 2.650953000 3.380023000

1 -5.399007000 0.688529000 5.279498000

1 -6.580156000 -4.516421000 5.235372000

1 -6.633967000 -6.379107000 3.221479000

1 -6.608335000 -4.208151000 -3.840957000

1 -6.176788000 -6.181585000 -1.987318000

6 -5.991377000 -1.907535000 5.708392000

6 -6.801966000 -1.093836000 6.523577000

6 -5.030760000 -2.734219000 6.322909000

1 -7.565088000 -0.468914000 6.037410000

1 -4.406759000 -3.367362000 5.679768000

6 -6.651553000 -1.073538000 7.922825000

6 -4.856469000 -2.752879000 7.717807000

6 -5.672553000 -1.909404000 8.498578000

1 -5.543863000 -1.904252000 9.586534000

6 -7.435004000 -1.658640000 -4.062257000

6 -6.710278000 -0.832490000 -4.943745000

6 -8.459654000 -2.478496000 -4.577293000

1 -5.918302000 -0.206065000 -4.522229000

1 -9.023282000 -3.102542000 -3.872389000

6 -6.982216000 -0.814654000 -6.322405000

6 -8.759636000 -2.492522000 -5.951966000

6 -8.007842000 -1.654407000 -6.800599000

1 -8.232236000 -1.655202000 -7.878156000

28 -6.418994000 -1.772282000 0.780378000

1 -6.341180000 2.722492000 0.894268000

1 -6.389074000 -6.268069000 0.631886000

6 -3.789222000 -3.681589000 8.325789000

6 -2.403635000 -3.316587000 7.741219000

6 -4.133366000 -5.145420000 7.959491000

1 -5.123410000 -5.432353000 8.368797000

1 -4.168029000 -5.294991000 6.861473000

1 -3.373451000 -5.841379000 8.372194000

1 -2.373487000 -3.448111000 6.640987000

1 -1.613185000 -3.964306000 8.173932000

1 -2.144967000 -2.261148000 7.962619000

6 -7.549063000 -0.145609000 8.762632000

6 -9.029683000 -0.538913000 8.544681000

6 -7.326254000 1.315802000 8.303329000

1 -6.268980000 1.618035000 8.449503000

1 -7.569768000 1.451858000 7.230812000

1 -7.967082000 2.009938000 8.886172000

1 -9.324774000 -0.454336000 7.479984000

1 -9.698783000 0.121847000 9.134506000

1 -9.210426000 -1.586089000 8.862026000

6 -9.866667000 -3.383662000 -6.545614000

6 -9.239091000 -4.340580000 -7.587335000

6 -10.925733000 -2.488996000 -7.232627000

1 -11.384836000 -1.790739000 -6.503598000

1 -10.484807000 -1.881965000 -8.048500000

1 -11.733871000 -3.109847000 -7.672689000

1 -8.749989000 -3.787113000 -8.413727000

1 -10.017300000 -4.994485000 -8.033360000

1 -8.472429000 -4.988860000 -7.116046000

6 -6.198143000 0.079078000 -7.300369000

6 -7.181232000 1.051802000 -7.994225000

6 -5.508607000 -0.810314000 -8.362022000

1 -4.803290000 -1.520368000 -7.884028000

1 -6.244104000 -1.404853000 -8.939874000

1 -4.937392000 -0.187730000 -9.081862000

1 -7.966423000 0.508658000 -8.557019000

1 -6.642787000 1.706345000 -8.711023000

1 -7.687999000 1.698508000 -7.249231000

6 -3.718939000 -3.561857000 9.859257000

1 -3.454484000 -2.533839000 10.180152000

1 -4.680847000 -3.835354000 10.338154000

1 -2.942037000 -4.246243000 10.256213000

6 -7.235625000 -0.236878000 10.267574000

1 -6.188709000 0.053942000 10.489359000

1 -7.899144000 0.449075000 10.832188000

1 -7.400445000 -1.259905000 10.662480000

6 -10.567214000 -4.230839000 -5.466866000

1 -11.061081000 -3.598075000 -4.702164000

1 -11.349639000 -4.862862000 -5.933772000

1 -9.857366000 -4.905614000 -4.947121000

6 -5.116029000 0.908711000 -6.582689000

1 -4.359661000 0.262988000 -6.091755000

1 -4.581182000 1.546732000 -7.314793000

1 -5.551799000 1.576642000 -5.811977000

Table S8. XYZ Coordinate calculated for two molecules of fused NiDtBuPP.

	X	Y	Z
6	5.977339000	-1.085407000	-2.422983000
6	9.659072000	0.457704000	0.332783000
6	7.419111000	-1.285100000	4.272475000
6	4.475992000	-3.777770000	1.336607000
7	8.176507000	-0.672887000	2.029113000
7	7.643784000	-0.436183000	-0.705210000
7	5.603995000	-2.192662000	-0.278567000
7	6.037941000	-2.303419000	2.484759000
6	4.790942000	-3.205678000	0.105813000
6	5.320339000	-2.016075000	-1.632357000
6	7.072218000	-0.347478000	-1.969065000
6	8.808486000	0.328025000	-0.770379000
6	5.030153000	-3.268826000	2.512951000
6	6.343365000	-2.050565000	3.814204000
6	8.328471000	-0.686722000	3.413860000
6	9.280870000	-0.029469000	1.579606000
6	3.994610000	-3.753393000	-0.968172000
6	4.308345000	-2.972360000	-2.069851000
6	7.855633000	0.519306000	-2.815948000
6	8.937542000	0.931783000	-2.074564000
6	10.204245000	0.365639000	2.626763000
6	9.571457000	-0.026123000	3.795977000
6	4.674165000	-3.582766000	3.876258000
6	5.477438000	-2.812301000	4.684018000
1	3.926133000	-3.008749000	-3.096308000
1	7.625562000	0.734788000	-3.865796000
1	9.754064000	1.586357000	-2.391738000
1	9.866534000	0.086193000	4.841708000
1	5.515496000	-2.777935000	5.777898000
6	10.973702000	1.100983000	0.538562000
6	11.821353000	1.629954000	-0.429846000

6 11.345007000 1.035377000 1.942275000

1 11.509028000 1.622055000 -1.478178000

6 13.097547000 2.106047000 -0.067185000

6 12.620980000 1.516236000 2.319080000

6 13.451712000 2.032820000 1.287599000

1 14.447956000 2.396763000 1.577047000

6 3.510881000 -4.862812000 1.035913000

6 2.983379000 -5.835245000 1.879147000

6 3.219128000 -4.867829000 -0.382726000

1 3.248877000 -5.834191000 2.944198000

6 2.150960000 -6.854226000 1.355794000

6 2.390524000 -5.872635000 -0.921720000

6 1.875514000 -6.843473000 -0.021304000

1 1.235443000 -7.632453000 -0.428458000

28 6.881924000 -1.420441000 0.877841000

1 5.680079000 -0.972348000 -3.473767000

1 7.594139000 -1.231713000 5.355352000

1 3.890717000 -4.285622000 4.175692000

6 12.170969000 -2.218790000 1.808376000

6 9.886496000 -2.313300000 -2.471723000

6 6.770209000 -5.590816000 -0.705770000

6 8.358585000 -4.531686000 3.749711000

7 8.483259000 -3.888217000 -1.090962000

7 10.761899000 -2.535477000 -0.207864000

7 10.071403000 -3.370973000 2.293653000

7 7.885886000 -4.870245000 1.384951000

6 9.468602000 -3.742925000 3.448902000

6 11.259834000 -2.763898000 2.701726000

6 11.922400000 -2.124864000 0.437956000

6 10.888995000 -2.084952000 -1.522127000

6 7.640804000 -5.158268000 2.728479000

6 7.004108000 -5.668274000 0.670174000

6 7.435112000 -4.693859000 -1.527660000

6 8.823604000 -3.163053000 -2.184419000

6 10.206115000 -3.370922000 4.635822000

6 11.362553000 -2.773572000 4.156614000

6 12.805933000 -1.463647000 -0.490737000

6 12.160809000 -1.429536000 -1.705401000

6 7.999227000 -3.424082000 -3.348355000

6 7.140218000 -4.428676000 -2.931698000

6 6.628283000 -6.180937000 2.845298000

6 6.245777000 -6.510717000 1.565856000

1 12.225451000 -2.367986000 4.696650000

1 13.779903000 -1.040671000 -0.220183000

1 12.523021000 -1.006027000 -2.646931000

1 6.359578000 -4.972174000 -3.469355000

1 5.487480000 -7.232550000 1.243838000

6 9.674939000 -1.868895000 -3.865923000

6 10.382912000 -0.894845000 -4.564690000

6 8.498017000 -2.518006000 -4.419477000

1 11.238793000 -0.407306000 -4.087040000

6 9.951923000 -0.492791000 -5.845587000

6 8.059555000 -2.126889000 -5.706037000

6 8.812997000 -1.121207000 -6.370595000

1 8.468137000 -0.805986000 -7.365673000

6 8.285234000 -4.568801000 5.230651000

6 7.309848000 -5.122681000 6.053380000

6 9.410382000 -3.846528000 5.787379000

1 6.450433000 -5.637378000 5.605716000

6 7.403273000 -4.983939000 7.459075000

6 9.520798000 -3.699453000 7.185828000

6 8.499886000 -4.280573000 7.984088000

1 8.573147000 -4.169726000 9.070427000

28 9.284721000 -3.637051000 0.598349000

1 13.104796000 -1.790001000 2.194355000

1 5.980255000 -6.221919000 -1.134195000

1 6.269269000 -6.605485000 3.787437000

6 13.613386000 2.981194000 4.115343000

1 14.051428000 3.009237000 5.134843000

1 14.353575000 3.423315000 3.419872000

1 12.714554000 3.630494000 4.108436000

1 12.806179000 1.016828000 5.803483000

6 12.299519000 0.987201000 4.817586000

1 11.379665000 1.597074000 4.893364000

1 12.013955000 -0.060853000 4.616075000

6 13.239639000 1.527039000 3.734405000

6 14.513258000 0.645550000 3.735070000

1 15.270355000 0.997130000 3.006839000

1 14.983494000 0.647402000 4.740424000

1 14.263265000 -0.404406000 3.478788000

6 14.095179000 2.655645000 -1.101556000

6 13.512271000 2.633343000 -2.527545000

1 14.254612000 3.032357000 -3.247807000

1 12.598396000 3.255851000 -2.609480000

1 13.256523000 1.603657000 -2.849848000

6 14.456508000 4.115409000 -0.738684000

1 15.177733000 4.533599000 -1.471714000

1 14.918568000 4.184477000 0.266360000

1 13.552014000 4.756882000 -0.737705000

6 15.374012000 1.784314000 -1.086395000

1 16.116921000 2.166997000 -1.817064000

1 15.854660000 1.777888000 -0.087861000

1 15.138857000 0.734336000 -1.355555000

6 1.614689000 -7.939756000 2.304674000

6 2.815132000 -8.689246000 2.933461000

1 2.462613000 -9.474678000 3.634183000

1 3.476063000 -8.003779000 3.500987000

1 3.429923000 -9.177554000 2.149916000

6 0.778962000 -7.271579000 3.422778000

1 0.392141000 -8.035293000 4.129417000

1 -0.086271000 -6.725224000 2.995628000

1 1.378880000 -6.545651000 4.007235000

6 0.725907000 -8.965527000 1.577498000

1 0.360155000 -9.725317000 2.297555000

1 -0.161654000 -8.486713000 1.116516000

1 1.281347000 -9.500945000 0.781105000

6 2.067820000 -5.941812000 -2.426756000

6 1.151636000 -7.129907000 -2.781188000

1 0.949009000 -7.127281000 -3.871386000

1 0.174230000 -7.070581000 -2.261179000

1 1.618258000 -8.104570000 -2.532543000

6 1.336207000 -4.644596000 -2.846841000

1 1.158695000 -4.635052000 -3.942656000

1 1.904737000 -3.734866000 -2.580823000

1 0.352646000 -4.576619000 -2.339466000

6 3.386017000 -6.117312000 -3.220079000

1 3.187321000 -6.118647000 -4.312039000

1 4.111765000 -5.311611000 -3.006405000

1 3.867264000 -7.082173000 -2.959557000

6 10.691036000 -2.938061000 7.837103000

6 10.584976000 -2.890356000 9.374294000

1 11.449879000 -2.331875000 9.786221000

1 10.599070000 -3.903384000 9.824646000

1 9.663965000 -2.373327000 9.711930000

6 12.016602000 -3.652484000 7.480142000

1 12.884491000 -3.082898000 7.873561000

1 12.148482000 -3.773772000 6.389445000

1 12.039644000 -4.666406000 7.928307000

6 10.694605000 -1.478273000 7.324617000

1 11.560277000 -0.920430000 7.738171000

1 10.750829000 -1.425516000 6.222804000

1 9.768625000 -0.955251000 7.639937000

6 6.301827000 -5.591945000 8.344590000

6 4.942646000 -4.952999000 7.968905000

1 4.124579000 -5.385335000 8.581994000

1 4.689250000 -5.121932000 6.903192000

41

1 4.959364000 -3.857650000 8.143357000

6 6.239504000 -7.118570000 8.097116000

1 5.444341000 -7.582078000 8.717723000

1 7.204752000 -7.599641000 8.354763000

1 6.019954000 -7.354346000 7.036600000

6 6.556221000 -5.350185000 9.843815000

1 5.741428000 -5.804935000 10.442849000

1 7.510639000 -5.805286000 10.177461000

1 6.586304000 -4.268869000 10.087528000

6 6.824569000 -2.645982000 -6.475860000

6 5.851855000 -1.465134000 -6.718821000

1 4.957086000 -1.809876000 -7.277823000

1 6.319714000 -0.646913000 -7.300547000

1 5.507372000 -1.035652000 -5.755644000

6 7.282454000 -3.231368000 -7.834945000

1 6.407824000 -3.612288000 -8.402419000

1 7.986761000 -4.073731000 -7.680440000

1 7.791564000 -2.478682000 -8.468306000

6 6.050358000 -3.742497000 -5.734208000

1 5.185039000 -4.068265000 -6.346585000

1 6.685354000 -4.629441000 -5.550213000

1 5.660872000 -3.379734000 -4.765608000

6 10.658035000 0.617916000 -6.642653000

6 11.876216000 1.181370000 -5.886458000

1 12.363292000 1.974021000 -6.489467000

1 12.635941000 0.398861000 -5.686391000

1 11.585716000 1.633960000 -4.916745000

6 11.139201000 0.049945000 -7.998787000

1 11.647422000 0.837224000 -8.593928000

1 10.294716000 -0.337321000 -8.603191000

1 11.853668000 -0.784237000 -7.845997000

6 9.659167000 1.774785000 -6.886752000

1 10.141348000 2.593860000 -7.460281000

1 8.772881000 1.437183000 -7.460109000

42

1 9.298758000 2.193398000 -5.924774000

43

Table S8. XYZ Coordinate calculated for two molecules of NiDMP.

	X	Y	Z
6	-0.668769000	-0.511084000	-3.517404000
6	-2.275878000	2.262464000	0.153887000
6	-0.852718000	-1.316061000	3.133479000
6	-1.089150000	-4.401674000	-0.622848000
7	-1.535612000	0.191596000	1.302672000
7	-1.466097000	0.517584000	-1.419966000
7	-0.909259000	-2.185607000	-1.727260000
7	-1.001026000	-2.514817000	0.986421000
6	-0.952491000	-3.574073000	-1.743771000
6	-0.629605000	-1.813328000	-3.033493000
6	-1.116253000	0.565401000	-2.763167000
6	-1.932026000	1.789445000	-1.118584000
6	-1.048578000	-3.867507000	0.669866000
6	-0.789377000	-2.467492000	2.356302000
6	-1.284166000	-0.092517000	2.637094000
6	-2.061142000	1.478029000	1.294047000
6	-0.710879000	-4.073933000	-3.080829000
6	-0.469967000	-2.977729000	-3.873786000
6	-1.359951000	1.881504000	-3.307812000
6	-1.885305000	2.638287000	-2.291053000
6	-2.183727000	1.980413000	2.647993000
6	-1.665597000	1.020521000	3.477495000
6	-0.894587000	-4.673617000	1.862404000
6	-0.690081000	-3.801843000	2.904210000
1	-0.701541000	-5.136513000	-3.347107000
1	-0.239771000	-2.942928000	-4.945209000
1	-1.166758000	2.166480000	-4.348545000
1	-2.197436000	3.687956000	-2.300176000
1	-2.589242000	2.961849000	2.906468000
1	-1.579639000	1.035477000	4.570166000
1	-0.908392000	-5.768999000	1.869009000
1	-0.520460000	-4.026741000	3.963905000

6 -2.706068000 3.687736000 0.307248000

6 -4.019381000 4.079335000 -0.054235000

6 -1.782107000 4.650948000 0.794023000

6 -4.409898000 5.417540000 0.136589000

6 -2.216069000 5.978060000 0.968471000

1 -5.438882000 5.709627000 -0.129616000

1 -1.497971000 6.724658000 1.345942000

6 -3.530107000 6.380482000 0.661782000

6 -1.111308000 -5.886271000 -0.806639000

6 0.112173000 -6.602738000 -0.851626000

6 -2.346636000 -6.566046000 -0.945407000

6 0.074838000 -7.997483000 -1.034544000

6 -2.337227000 -7.961408000 -1.127063000

1 1.026163000 -8.553216000 -1.073507000

1 -3.299108000 -8.488281000 -1.238844000

6 -1.138493000 -8.697542000 -1.172347000

28 -1.250853000 -0.995819000 -0.216096000

1 -0.432395000 -0.340553000 -4.576374000

1 -0.679415000 -1.406335000 4.214391000

6 -3.986947000 7.798581000 0.908644000

1 -4.770394000 8.106683000 0.187889000

1 -4.421453000 7.904650000 1.926635000

1 -3.146994000 8.517931000 0.836431000

6 -0.348140000 4.276340000 1.088008000

1 -0.261192000 3.663880000 2.009650000

1 0.082144000 3.665396000 0.268653000

1 0.279522000 5.178972000 1.218889000

6 -4.982728000 3.082874000 -0.637700000

1 -4.800300000 2.923302000 -1.721391000

1 -4.875233000 2.086580000 -0.163573000

1 -6.033277000 3.407887000 -0.523264000

6 -3.648959000 -5.804487000 -0.901790000

1 -3.696773000 -5.033310000 -1.697735000

1 -4.517318000 -6.478850000 -1.027915000

1 -3.769922000 -5.267537000 0.061476000

6 1.428684000 -5.876933000 -0.711729000

1 1.487755000 -5.333135000 0.253740000

1 2.283362000 -6.578058000 -0.768007000

1 1.553365000 -5.111879000 -1.505798000

6 -1.155750000 -10.199309000 -1.333158000

1 -0.229149000 -10.569409000 -1.815185000

1 -1.235556000 -10.705029000 -0.346186000

1 -2.019775000 -10.535072000 -1.940632000

6 -9.394645000 2.069561000 -0.916503000

6 -6.252809000 0.984694000 2.643960000

6 -4.202392000 -2.118515000 -0.498635000

6 -5.939044000 0.703305000 -4.068460000

7 -5.460487000 -0.411184000 0.755433000

7 -7.608123000 1.284730000 0.588087000

7 -7.464018000 1.191982000 -2.175028000

7 -5.315867000 -0.508384000 -1.996736000

6 -7.077568000 1.293895000 -3.502711000

6 -8.707063000 1.804064000 -2.098531000

6 -8.836692000 1.882231000 0.345865000

6 -7.344904000 1.500127000 1.931421000

6 -5.154935000 -0.201605000 -3.341654000

6 -4.486799000 -1.594720000 -1.757304000

6 -4.612658000 -1.506005000 0.682239000

6 -5.413557000 0.015835000 2.076651000

6 -8.089030000 1.990804000 -4.269400000

6 -9.117715000 2.274098000 -3.403128000

6 -9.371133000 2.446227000 1.565816000

6 -8.426382000 2.243163000 2.543331000

6 -4.497256000 -0.813814000 2.833213000

6 -4.057290000 -1.798644000 1.984712000

6 -4.186448000 -1.095543000 -3.944329000

6 -3.821209000 -1.997449000 -2.976363000

1 -8.012658000 2.198991000 -5.342392000

1 -10.065365000 2.786024000 -3.609033000

1 -10.335803000 2.962100000 1.641804000

1 -8.451512000 2.533558000 3.599584000

1 -4.253667000 -0.658797000 3.888839000

1 -3.368700000 -2.623220000 2.193222000

1 -3.867218000 -1.045573000 -4.990706000

1 -3.131545000 -2.843198000 -3.059686000

6 -6.033690000 1.419241000 4.056723000

6 -6.413404000 0.587795000 5.142507000

6 -5.451825000 2.690544000 4.296988000

6 -6.134488000 1.016973000 6.453171000

6 -5.184794000 3.075583000 5.624183000

1 -6.430831000 0.371701000 7.296723000

1 -4.719005000 4.057846000 5.808330000

6 -5.502488000 2.247706000 6.716337000

6 -5.636019000 0.949333000 -5.511791000

6 -4.914155000 2.113097000 -5.876657000

6 -6.083456000 0.040826000 -6.504219000

6 -4.618669000 2.332642000 -7.234566000

6 -5.767587000 0.300192000 -7.851206000

1 -4.054763000 3.237233000 -7.516468000

1 -6.117425000 -0.404710000 -8.623420000

6 -5.028335000 1.434071000 -8.237769000

28 -6.462107000 0.382948000 -0.709714000

1 -10.371685000 2.567548000 -0.984545000

1 -3.520944000 -2.974398000 -0.431526000

6 -5.170913000 2.660595000 8.131006000

1 -5.075177000 3.760526000 8.224426000

1 -5.944318000 2.318930000 8.848168000

1 -4.205739000 2.217808000 8.460772000

6 -5.171914000 3.632931000 3.152844000

1 -4.775715000 3.101994000 2.268634000

1 -6.104225000 4.132326000 2.812769000

1 -4.454000000 4.428037000 3.434027000

6 -7.143919000 -0.712485000 4.901006000

1 -7.999729000 -0.563797000 4.211121000

1 -6.492026000 -1.472869000 4.423574000

1 -7.528009000 -1.136925000 5.848700000

6 -6.902588000 -1.168898000 -6.122515000

1 -7.794811000 -0.875429000 -5.531799000

1 -7.243606000 -1.722929000 -7.018214000

1 -6.324172000 -1.866897000 -5.482407000

6 -4.492083000 3.102367000 -4.818716000

1 -3.928313000 2.601834000 -4.006464000

1 -3.855767000 3.903650000 -5.242097000

1 -5.374327000 3.578582000 -4.341997000

6 -4.667190000 1.669449000 -9.685577000

1 -4.587259000 2.750561000 -9.916377000

1 -3.684916000 1.210252000 -9.932115000

1 -5.415504000 1.224154000 -10.371090000

References

1 T. Wirtz, O. De Castro, J.-N. Audinot and P. Philipp, *Annu. Rev. Anal. Chem.*, 2019, **12**, 523–543.

2 G. Hlawacek and A. Gölzhäuser, *Helium Ion Microscopy*, Springer International Publishing, Cham, 2016.

3 F. Neese, *Wiley Interdiscip. Rev. Comput. Mol. Sci.*, 2012, **2**, 73–78.

4 A. D. Becke, *Phys. Rev. A*, 1988, **38**, 3098–3100.

5 J. P. Perdew, *Phys. Rev. B*, 1986, **33**, 8822–8824.

6 S. Grimme, J. Antony, S. Ehrlich and H. Krieg, *J. Chem. Phys.*, 2010, **132**, 154104.

7 L. G. S. Grimme, S. Ehrlich, *J. Comput. Chem.*, 2011, **7**, 1456–1465.

8 F. Neese, F. Wennmohs, A. Hansen and U. Becker, *Chem. Phys.*, 2009, **356**, 98–109.

9 D. A. Pantazis, X.-Y. Chen, C. R. Landis and F. Neese, *J. Chem. Theory Comput.*, 2008, **4**, 908–919.

10 F. Weigend and R. Ahlrichs, *Phys. Chem. Chem. Phys.*, 2005, **7**, 3297.

11 F. Weigend, *Phys. Chem. Chem. Phys.*, 2006, **8**, 1057–1065.

12 N. Kamonsutthipaijit and H. L. Anderson, *Chem. Sci.*, 2017, **8**, 2729–2740.

7.5 Supporting information: Metal Ion Effect on Regioselectivity in the Synthesis of Porphyrin Tapes in oCVD.

Metal Ion Effect Regioselectivity in the Synthesis of Porphyrin Tapes in oCVD.

Giuseppe Bengasi, Louise Quétu, Kamal Baba, Alexander Ost, Joao Paulo Cosas Fernandes, Patrick Grysan, Katja Heinze,* Nicolas D. Boscher*

Supporting Information

Contents

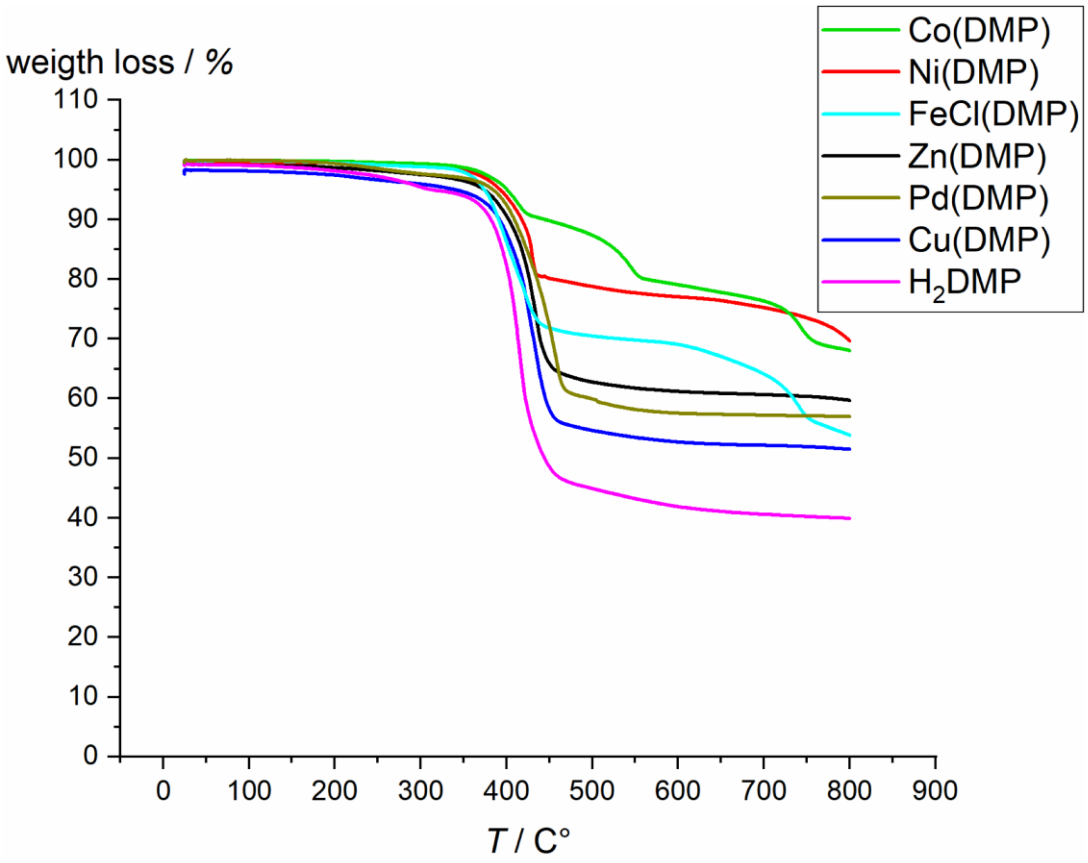

Figure S1. Thermogravimetric analysis of 5,15-(dimesityl)porphyrinato metal complexes (M = 2H, $Fe^{III}Cl$, Co^{II}, Ni^{II}, Cu^{II}, Zn^{II} and Pd^{II}). Measurements performed in argon atmosphere and a temperature ramp of 10 K min^{-1}.

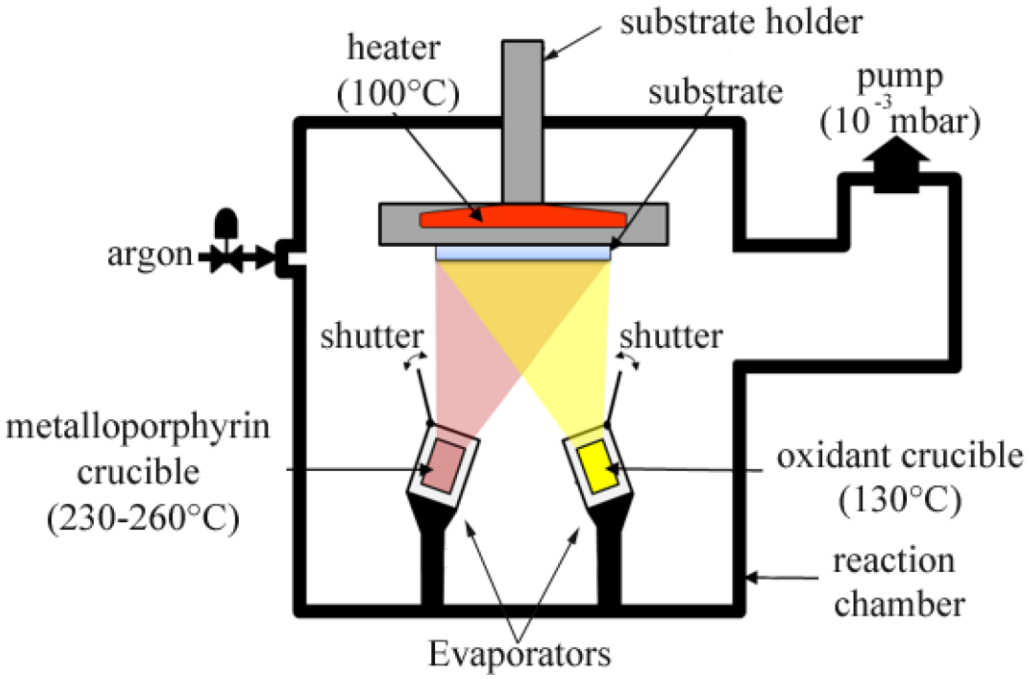

Scheme S1. Schematic of the oCVD reactor used for the experiments. The porphyrins and oxidants placed in the crucibles are sublimed under reduced pressure (10^{-3} mbar). The substrate holder is heated at 100°C to facilitate the reaction. Argon is introduced in the chamber to tune the pressure inside the chamber.

Monomer	Sublimation Temperature	Sublimed monomer (mg)	Sublimed monomer (µmol)	Sublimed $FeCl_3$ (mg)	Sublimed $FeCl_3$ (µmol)	$FeCl_3$/porhyrin Ratio
H_2DMP	245 °C	4.3	7.9	60.5	224	28.5
Ni(DMP)	230 °C	4.9	8.1	54.2	201	24.7
Pd(DMP)	260 °C	5.1	7.8	60.2	223	28.4
Zn(DMP)	245 °C	5.1	8.3	48.0	178	21.2
Co(DMP)	220 °C	5.0	8.3	45.5	168	20.3
Cu(DMP)	230 °C	3.9	6.4	48.0	178	27.7
FeCl(DMP)	235 °C	4.7	7.4	42.0	155	21.0

Table S1. Deposition reaction conditions for the preparation of the oCVD coatings from different 5,15-(dimesityl)porphyrin metal complexes (M = 2H, $Fe^{III}Cl$, Co^{II}, Ni^{II}, Cu^{II}, Zn^{II} and Pd^{II}). The table reports the sublimation temperature used for each of the studied porphyrins and the sublimed amount. The substrate temperature was kept constant at 100°C for all depositions. The oxidant crucible temperature was set to 130°C for the preparation of the oCVD coatings. The amount of iron(III) chloride sublimed is reported for each experiments. The values are obtained from the difference in the weight of the crucibles before and after the deposition. The reference coatings were obtained under the same conditions (substrate temperature of 100°C and pressure of 10^{-3} mbar) without supplying oxidant.

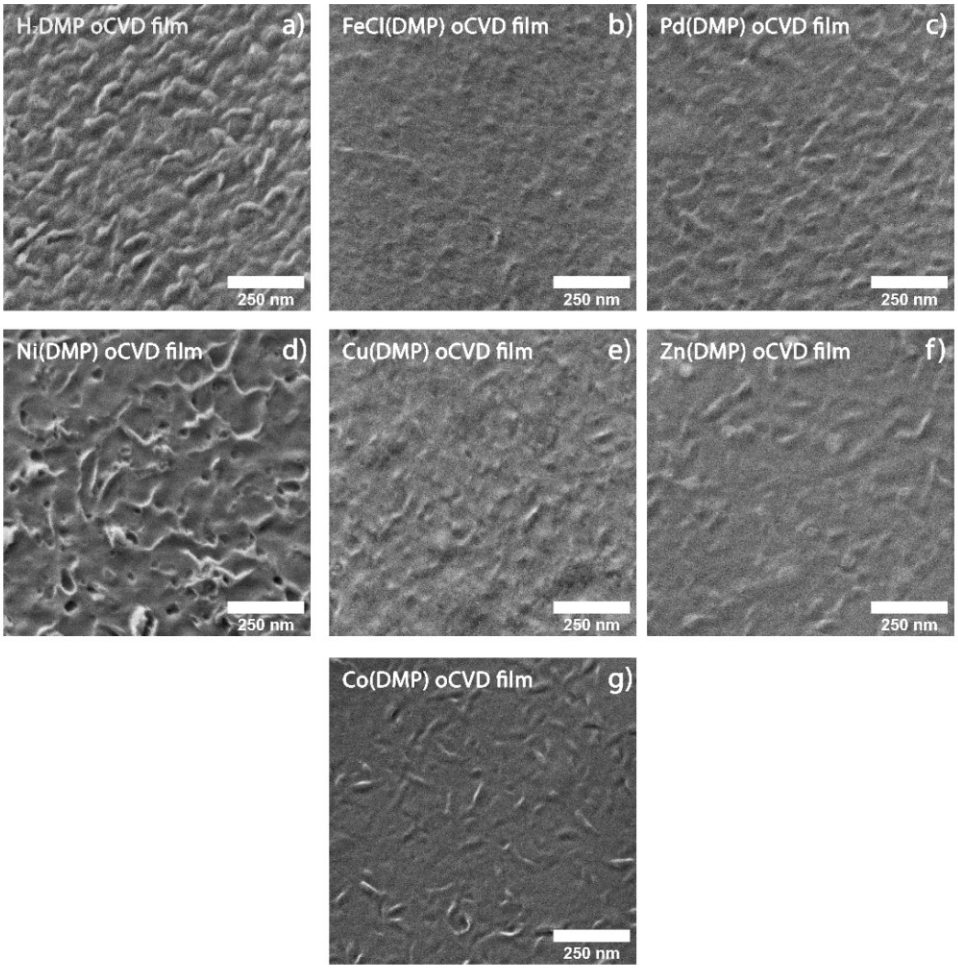

Figure S2. HIM images of the oCVD porphyrin films prepared from a) H_2DMP, b) FeCl(DMP), c) Pd(DMP), d) Ni(DMP), e) Cu(DMP), f) Zn(DMP) and g) Co(DMP).

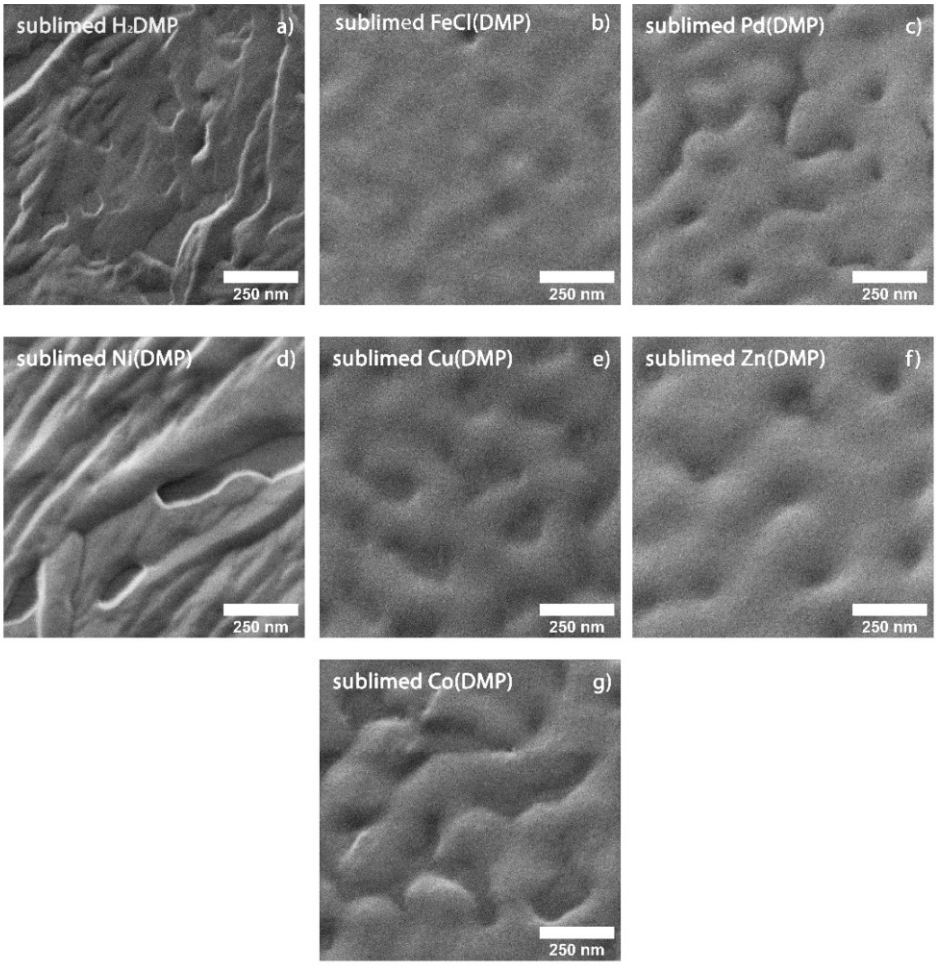

Figure S3. HIM images of the sublimed porphyrin films prepared from a) H_2DMP, b) FeCl(DMP), c) Pd(DMP), d) Ni(DMP), e) Cu(DMP), f) Zn(DMP) and g) Co(DMP).

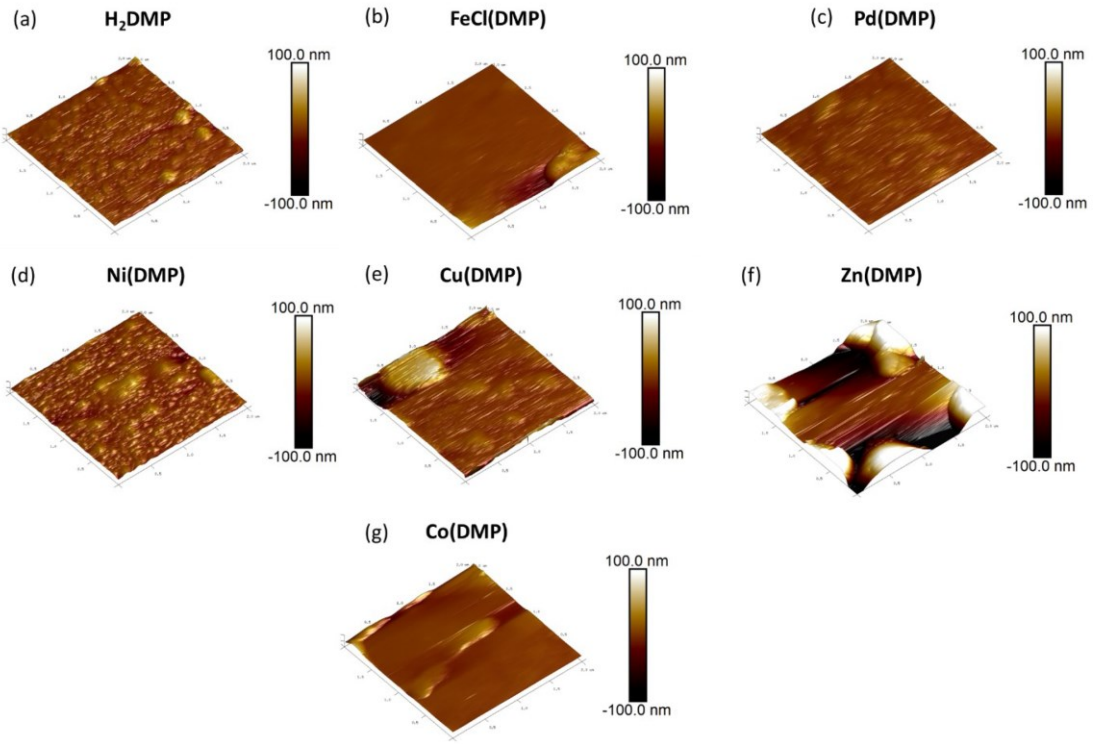

Figure S4. AFM images of the oCVD porphyrin films show the formation of smooth coatings for a) H_2DMP (Ra 4.6 ± 1.4 nm), b) FeCl(DMP) (Ra 8.8 ± 5.3 nm), c) Pd(DMP) (Ra 2.7 ± 0.3 nm), d) Ni(DMP) (Ra 8.6 ± 2.6 nm). Higher roughness are observed for e) Cu(DMP) (Ra 19.0 ± 8.7 nm), f) Zn(DMP) (Ra 41.0 ± 2.0 nm) and g) Co(DMP) (Ra 20.7 ± 14.5 nm).

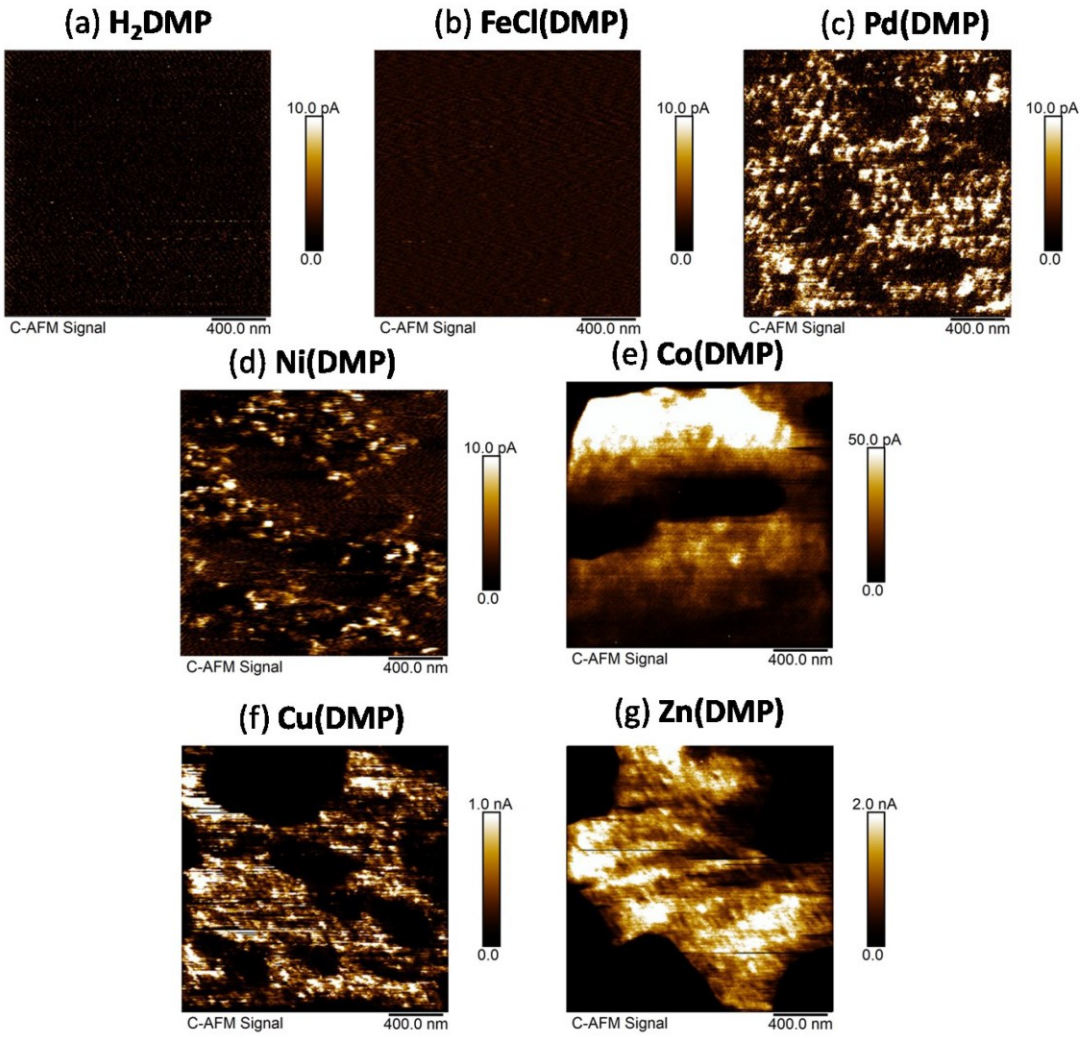

Figure S5. C-AFM images of the oCVD films prepared from a) H_2DMP, b) FeCl(DMP), c) Pd(DMP), d) Ni(DMP), e) Co(DMP), f) Cu(DMP) and g) Zn(DMP). The images of H_2DMP and FeCl(DMP) oCVD films show the poor conductivity of these two films which is attributed to the essentially absent polymerization.

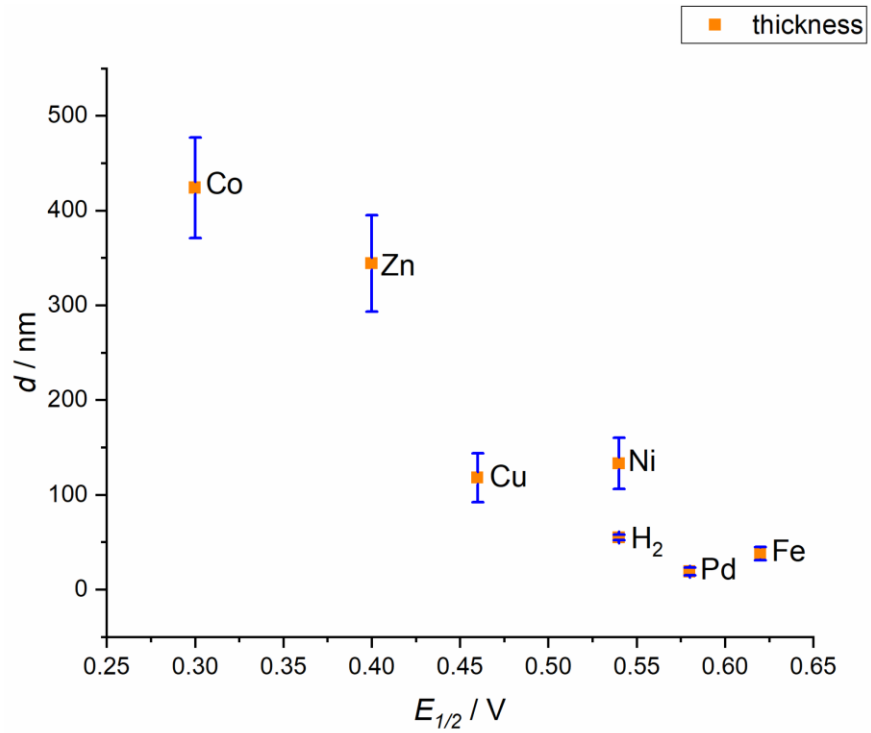

Figure S6. Relationship between the thickness and the $E_{1/2}$ of the oCVD films prepared from M(DMP) (M = 2H, $Fe^{III}Cl$, Co^{II}, Ni^{II}, Cu^{II}, Zn^{II} and Pd^{II}). A decrease of the oxidation potential of the monomer correlates to an increase of the thickness the film.

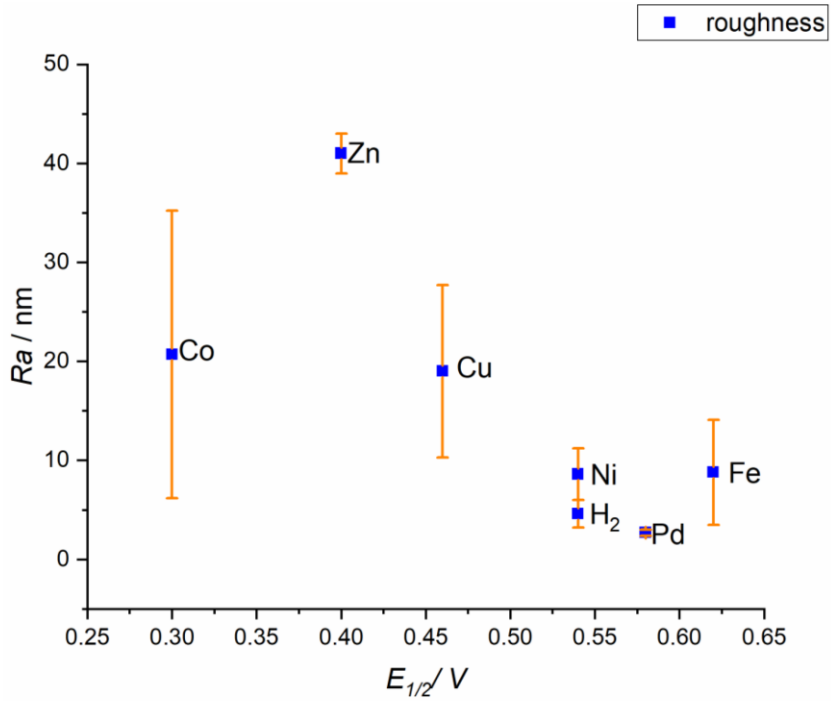

Figure S7. Relationship between the roughness and the $E_{1/2}$ of the oCVD films prepared from M(DMP) (M = 2H, $Fe^{III}Cl$, Co^{II}, Ni^{II}, Cu^{II}, Zn^{II} and Pd^{II}). A decrease of the oxidation potential of the monomer correlates to an increase of the roughness the film.

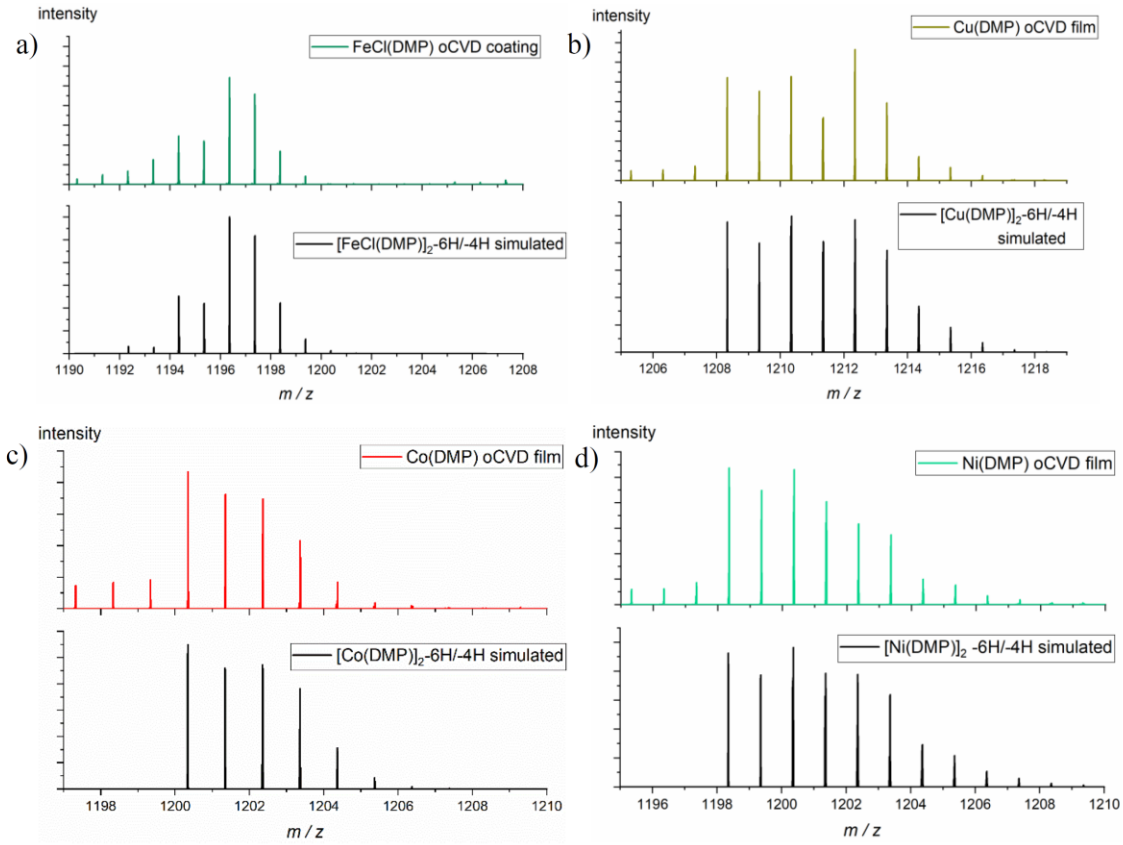

Figure S8. LDI-HR mass spectra of a) FeCl(DMP), b) Cu(DMP), c) Co(DMP) and d) Ni(DMP) oCVD films in the dimer region and the corresponding simulated pattern. All the spectra are simulated considering contributions from triply and doubly linked species [(M(DMP)$_2$]- 6H / -4H) (calculated for $C_{76}H_{58}N_8M_2$ and $C_{76}H_{60}N_8M_2$. M=Fe, Cu, Co, Ni).

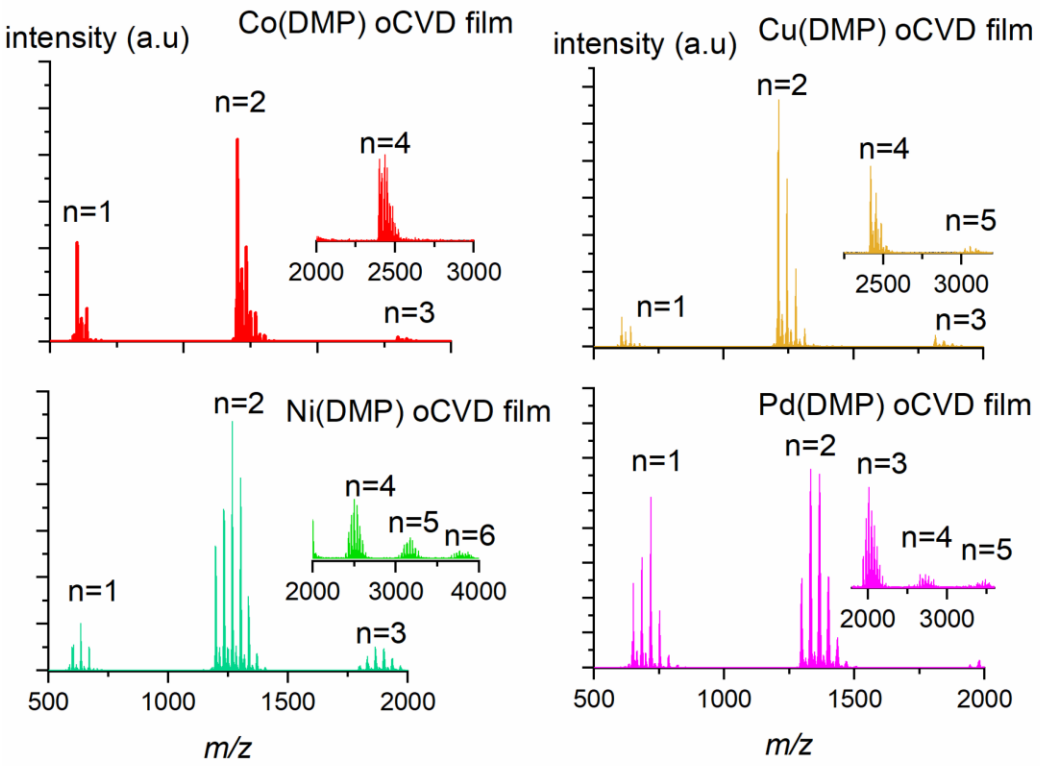

Figure S9. LDI-HRMS spectra of the oCVD films (M=Co^{II}, Ni^{II}, Pd^{II}, Cu^{II}) (n= degree of polymerization). The spectra are acquired in two separate experiments in the 400-2000 and 2000-4000 range.

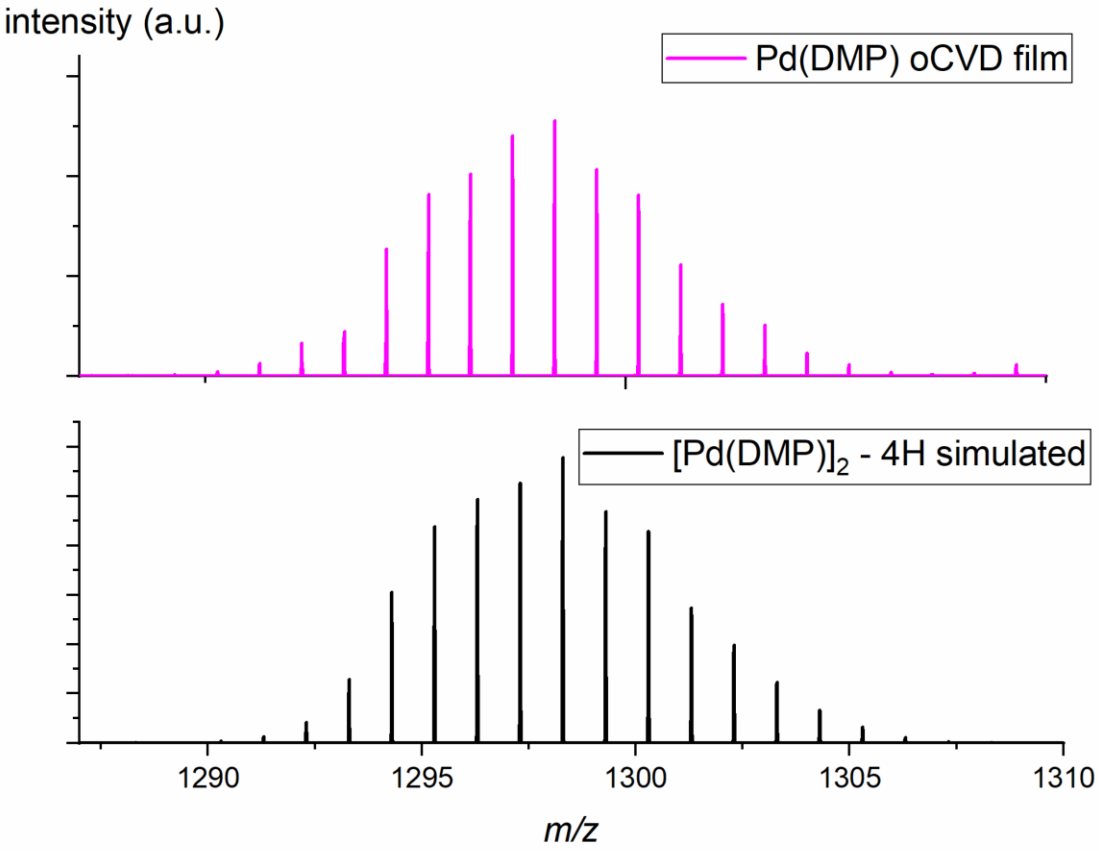

Figure S10. LDI-HR mass spectrum of the Pd(DMP) oCVD film in the dimer region and the simulated pattern of Pd(DMP) dimer doubly linked $[Pd(DMP)]_2$-4H (calculated for $C_{76}H_{60}N_8Pd_2$)

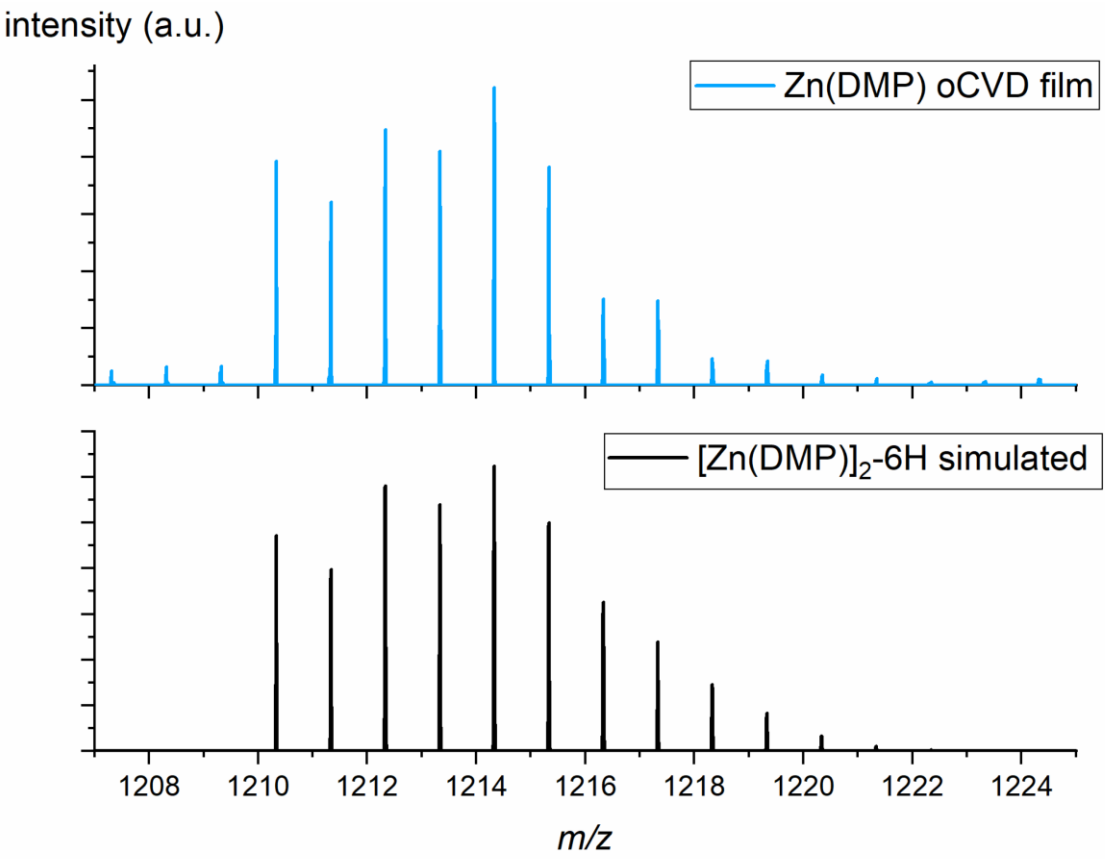

Figure S11. LDI-Hr mass spectrum of the Zn(DMP) oCVD film in the dimer region and the simulated spectrum of Zn(DMP) dimer triply linked [Zn(DMP)$_2$]-6H (calculated for $C_{76}H_{58}N_8Zn_2$)

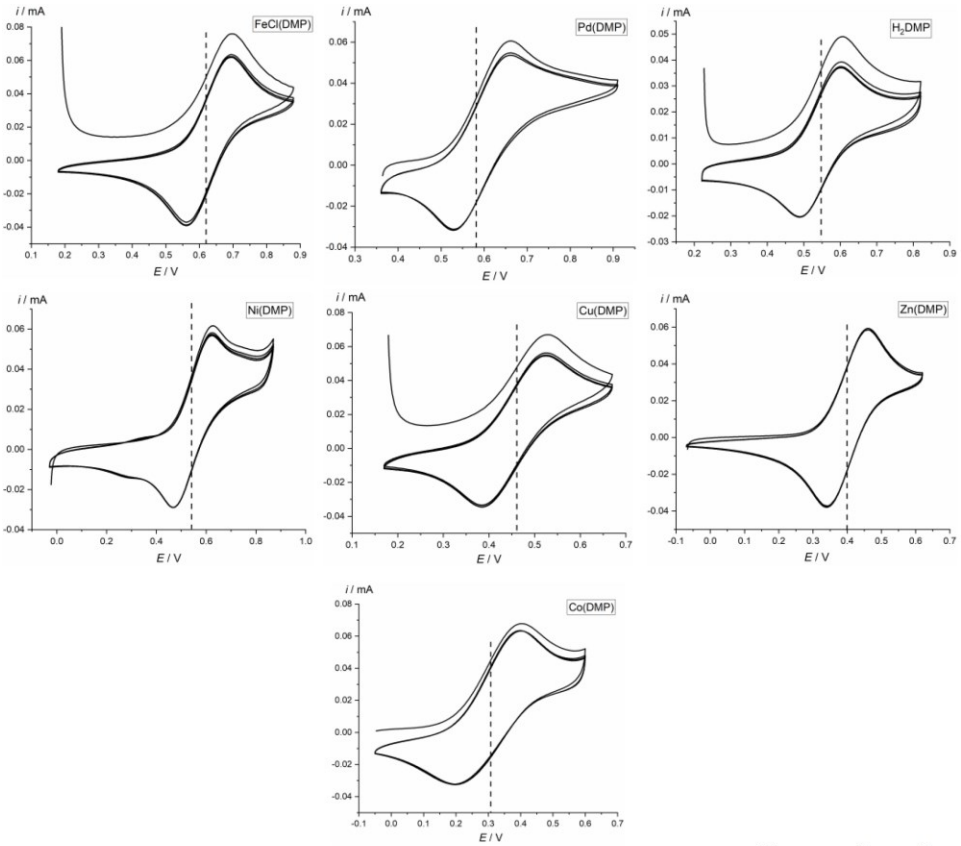

Figure S12. Cyclic voltammograms of M(DMP) (M = 2H, $Fe^{III}Cl$, Co^{II}, Ni^{II}, Cu^{II}, Zn^{II} and Pd^{II}) 1mM in CH_2Cl_2 using [nBu$_4$N][PF_6] (0.1 M) as supporting electrolyte. Potentials given Vs FcH/FcH^+.

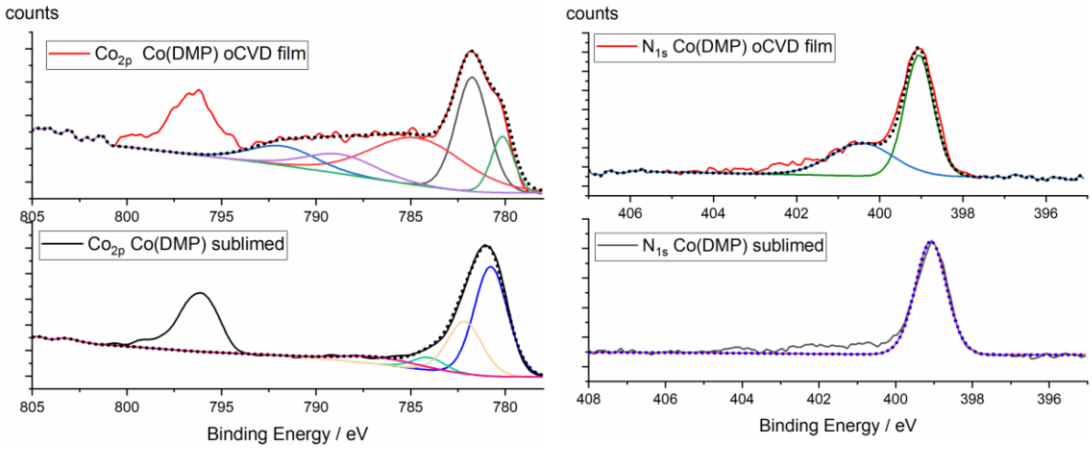

Figure S13. XPS spectra of the Co(DMP) oCVD film and sublimed Co(DMP) film in the region of the Co_{2p} and N_{1s} peaks.

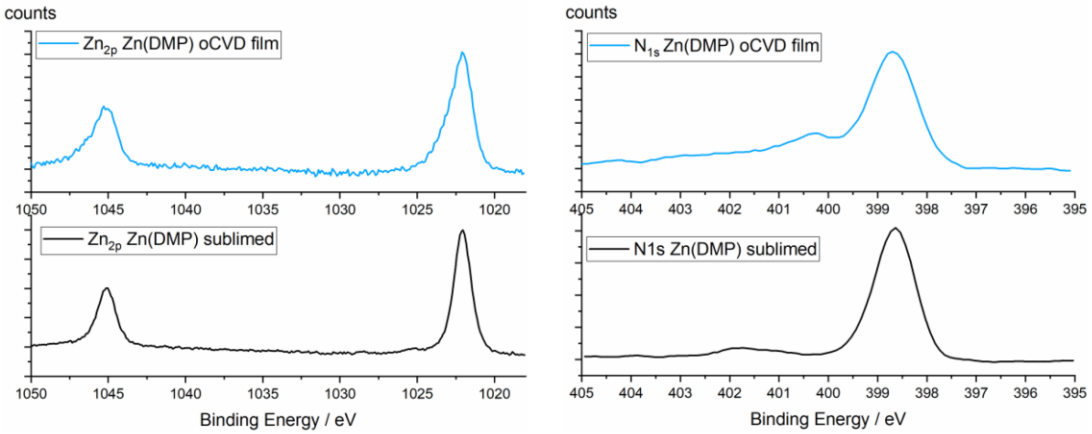

Figure S14. XPS spectra of the Zn(DMP) oCVD film and sublimed Zn(DMP) film in the region of the Zn 2p and N 1s peaks.

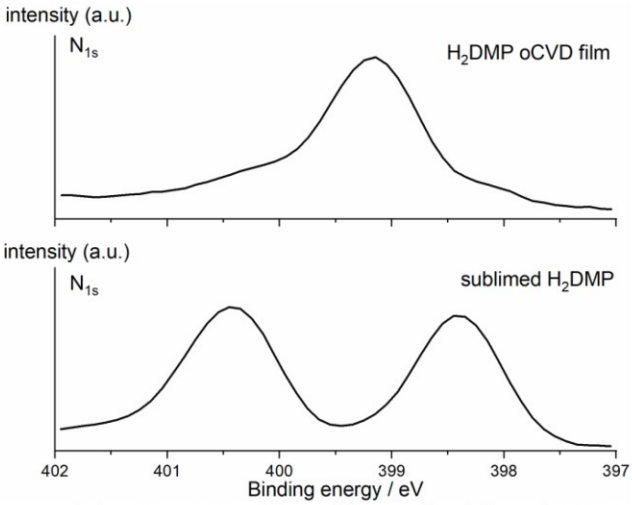

Figure S15. XPS spectra of the H_2DMP oCVD film and sublimed H_2DMP film in the N_{1S} region. Two signals are present in the spectrum of sublimed H_2DMP due to the non-equivalent 4 nitrogen atoms.

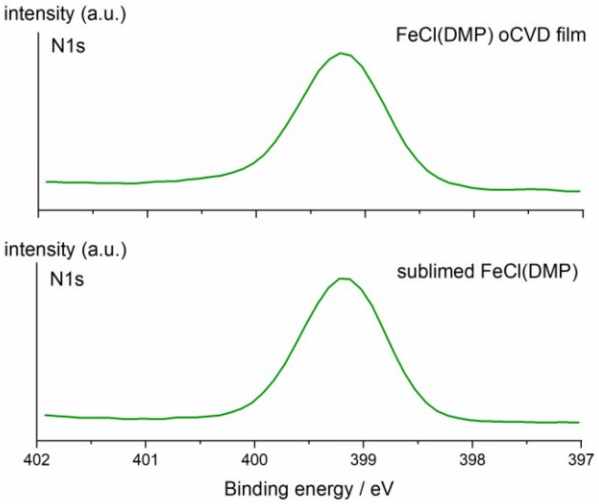

Figure S16. XPS spectra of the FeCl(DMP) oCVD film and sublimed FeCl(DMP) film in the N_{1S} region.

8 REFERENCES

[1] S. Lin, C. S. Diercks, Y.-B. Zhang, N. Kornienko, E. M. Nichols, Y. Zhao, A. R. Paris, D. Kim, P. Yang, O. M. Yaghi, C. J. Chang, *Science* **2015**, *349*, 1208–1213.

[2] E. Rose, B. Andrioletti, S. Zrig, M. Quelquejeu-Ethève, *Chem. Soc. Rev.* **2005**, *34*, 573–583.

[3] K. Rybicka-Jasińska, W. Shan, K. Zawada, K. M. Kadish, D. Gryko, *J. Am. Chem. Soc.* **2016**, *138*, 15451–15458.

[4] K. Ladomenou, M. Natali, E. Iengo, G. Charalampidis, F. Scandola, A. G. Coutsolelos, *Coord. Chem. Rev.* **2015**, *304–305*, 38–54.

[5] J. Kesters, P. Verstappen, M. Kelchtermans, L. Lutsen, D. Vanderzande, W. Maes, *Adv. Energy Mater.* **2015**, *5*, 1500218.

[6] S. Mathew, A. Yella, P. Gao, R. Humphry-Baker, B. F. E. Curchod, N. Ashari-Astani, I. Tavernelli, U. Rothlisberger, M. K. Nazeeruddin, M. Grätzel, *Nat. Chem.* **2014**, *6*, 242–247.

[7] M. E. El-Khouly, E. El-Mohsnawy, S. Fukuzumi, *J. Photochem. Photobiol. C Photochem. Rev.* **2017**, *31*, 36–83.

[8] R. Ye, M. Zhu, J. Chen, Y.-F. Han, L. Huang, J. Xu, *Angew. Chemie Int. Ed.* **2019**, 1–6.

[9] K. Rybicka-Jasińska, W. Shan, K. Zawada, K. M. Kadish, D. Gryko, *J. Am. Chem. Soc.* **2016**, *138*, 15451–15458.

[10] W. Jentzen, M. C. Simpson, J. D. Hobbs, X. Song, J. A. Shelnutt, T. Ema, N. Y. Nelson, C. J. Medforth, K. M. Smith, M. Veyrat, M. Mazzanti, R. Ramasseul, J. C. Marchon, T. Takeuchi, W. A. Goddard, *J. Am. Chem. Soc.* **1995**, *117*, 11085–11097.

[11] M. E. Ragoussi, G. De La Torre, T. Torres, *European J. Org. Chem.* **2013**, 2832–2840.

[12] G. Sedghi, L. J. Esdaile, H. L. Anderson, S. Martin, D. Bethell, S. J. Higgins, R. J. Nichols, *Adv. Mater.* **2012**, *24*, 653–657.

[13] H. Mori, T. Tanaka, A. Osuka, *J. Mater. Chem. C* **2013**, *1*, 2500.

[14] M. Gouterman, *J. Mol. Spectrosc.* **1961**, *6*, 138–163.

[15] N. K. S. Davis, A. L. Thompson, H. L. Anderson, *Org. Lett.* **2010**, *12*, 2124–2127.

[16] N. K. S. Davis, M. Pawlicki, H. L. Anderson, *Org. Lett.* **2008**, *10*, 3945–3947.

[17] J. P. Lewtak, B. Koszarna, M. K. Charyton, D. T. Gryko, *J. Porphyrins Phthalocyanines* **2019**, DOI 10.1142/S1088424619501530.

[18] C. Jiao, N. Zu, K. W. Huang, P. Wang, J. Wu, *Org. Lett.* **2011**, *13*, 3652–3655.

[19] E. Leary, B. Limburg, A. Alanazy, S. Sangtarash, I. Grace, K. Swada, L. J. Esdaile, M. Noori, M. T. González, G. Rubio-Bollinger, H. Sadeghi, A. Hodgson, N. Agraït, S. J. Higgins, C. J. Lambert, H. L. Anderson, R. J. Nichols, *J. Am. Chem. Soc.* **2018**, *140*,

12877–12883.

[20] N. Algethami, H. Sadeghi, S. Sangtarash, C. J. Lambert, *Nano Lett.* **2018**, *18*, 4482–4486.

[21] M. Pawlicki, H. A. Collins, R. G. Denning, H. L. Anderson, *Angew. Chemie - Int. Ed.* **2009**, *48*, 3244–3266.

[22] M. O. Senge, M. Fazekas, E. G. A. Notaras, W. J. Blau, M. Zawadzka, O. B. Locos, E. M. Ni Mhuircheartaigh, *Adv. Mater.* **2007**, *19*, 2737–2774.

[23] J. P. Lewtak, D. Gryko, D. Bao, E. Sebai, O. Vakuliuk, M. Ścigaj, D. T. Gryko, *Org. Biomol. Chem.* **2011**, *9*, 8178–8181.

[24] T. Ishizuka, Y. Saegusa, Y. Shiota, K. Ohtake, K. Yoshizawa, T. Kojima, *Chem. Commun.* **2013**, *49*, 5939.

[25] Y. Saegusa, T. Ishizuka, K. Komamura, S. Shimizu, H. Kotani, N. Kobayashi, T. Kojima, *Phys. Chem. Chem. Phys.* **2015**, *17*, 15001–15011.

[26] A. Osuka, H. Shimidzu, *Angew. Chemie Int. Ed. English* **1997**, *36*, 135–137.

[27] N. Aratani, A. Takagi, Y. Yanagawa, T. Matsumoto, T. Kawai, Z. S. Yoon, D. Kim, A. Osuka, *Chem. - A Eur. J.* **2005**, *11*, 3389–3404.

[28] D. H. Yoon, S. B. Lee, K. H. Yoo, J. Kim, J. K. Lim, N. Aratani, A. Tsuda, A. Osuka, D. Kim, *J. Am. Chem. Soc.* **2003**, *125*, 11062–11064.

[29] A. Tsuda, Y. Nakamura, A. Osuka, *Chem. Commun.* **2003**, *0*, 1096–1097.

[30] A. Tsuda, Y. Nakamura, A. Osuka, *Chem. Commun.* **2003**, 1096–1097.

[31] A. Tsuda, A. Osuka, *Science* **2001**, *293*, 79–82.

[32] T. Ikeda, N. Aratani, A. Osuka, *Chem. Asian J.* **2009**, *4*, 1248–1256.

[33] D. Y. Kim, T. K. Ahn, J. H. Kwon, D. Kim, T. Ikeue, N. Aratani, A. Osuka, M. Shigeiwa, S. Maeda, *J. Phys. Chem. A* **2005**, *109*, 2996–2999.

[34] Y. Nakamura, N. Aratani, A. Tsuda, A. Osuka, K. Furukawa, T. Kato, *J. Porphyrins Phthalocyanines* **2003**, *7*, 264–269.

[35] C.-M. Feng, Y.-Z. Zhu, S.-C. Zhang, Y. Zang, J.-Y. Zheng, *Org. Biomol. Chem.* **2015**, *13*, 2566–2569.

[36] B. J. Brennan, J. Arero, P. A. Liddell, T. A. Moore, A. L. Moore, D. Gust, *J. Porphyrins Phthalocyanines* **2013**, *17*, 247–251.

[37] B. J. Brennan, M. J. Kenney, P. A. Liddell, B. R. Cherry, J. Li, A. L. Moore, T. A. Moore, D. Gust, *Chem. Commun.* **2011**, *47*, 10034–10036.

[38] A. Tsuda, A. Nakano, H. Furuta, H. Yamochi, A. Osuka, *Angew. Chemie Int. Ed.* **2000**, *39*, 558–561.

[39] R. S. Czernuszewicz, K. A. Macor, X. Y. Li, J. R. Kincaid, T. G. Spiro, *J. Am. Chem. Soc.* **1989**, *111*, 3860–3869.

[40] N. Aratani, A. Osuka, *Chem. Rec.* **2003**, *3*, 225–234.

[41] G. Bengasi, K. Baba, O. Back, G. Frache, K. Heinze, N. D. Boscher, *Chem. Eur. J.* **2019**, *25*, 8313–8320.

[42] A. Giraudeau, H. J. Callot, M. Gross, *Inorg. Chem.* **1979**, *18*, 201–206.

[43] X. Ke, R. Kumar, M. Sankar, K. M. Kadish, *Inorg. Chem.* **2018**, *57*, 1490–1503.

[44] A. Giraudeau, I. Ezhar, M. Gross, H. J. Callot, J. Jordan, *J. Am. Chem. Soc.* **1979**, *101*, 3857–3862.

[45] A. Giraudeau, D. Schaming, J. Hao, R. Farha, M. Goldmann, L. Ruhlmann, *J. Electroanal. Chem.* **2010**, *638*, 70–75.

[46] N. G. Connelly, W. E. Geiger, *Chem. Rev.* **1996**, *96*, 877–910.

[47] P. Mineo, E. Scamporrino, D. Vitalini, *Macromol. Rapid Commun.* **2002**, *23*, 681–687.

[48] R. F. Pasternack, P. R. Huber, P. Boyd, G. Engasser, L. Francesconi, E. Gibbs, P. Fasella, G. C. Venturo, L. D. Hinds, *J. Am. Chem. Soc.* **1972**, *94*, 4511–4517.

[49] A. Mammana, A. D'Urso, R. Lauceri, R. Purrello, *J. Am. Chem. Soc.* **2007**, *129*, 8062–8063.

[50] T. Yokoyama, S. Yokoyama, T. Kamikado, Y. Okuno, S. Mashiko, *Nature* **2001**, *413*, 619–621.

[51] N. Yoshida, N. Aratani, A. Osuka, *Chem. Commun.* **2000**, 197–198.

[52] T. business research Company, *Plastics And Polymers Global Market Briefing 2018*, **2018**.

[53] H. W. Starkweather, G. E. Moore, J. E. Hansen, T. M. Roder, R. E. Brooks, *J. Polym. Sci.* **1956**, *21*, 189–204.

[54] M. Gahleitner, P. Jääskeläinen, E. Ratajski, C. Paulik, J. Reussner, J. Wolfschwenger, W. Neißl, *J. Appl. Polym. Sci.* **2005**, *95*, 1073–1081.

[55] M. M. Green, R. A. Gross, F. C. Schilling, K. Zero, C. Crosby, *Macromolecules* **1988**, *21*, 1839–1846.

[56] G. Perego, G. D. Cella, C. Bastioli, *J. Appl. Polym. Sci.* **1996**, *59*, 37–43.

[57] G. Natta, P. Pino, G. Mazzanti, U. Giannini, *J. Inorg. Nucl. Chem.* **1958**, *8*, 612–619.

[58] K. Ziegler, E. Holzkamp, H. Breil, H. Martin, *Angew. Chemie* **1955**, *67*, 426–426.

[59] C. K. Chiang, Y. W. Park, A. J. Heeger, H. Shirakawa, E. J. Louis, A. G. MacDiarmid, *J. Chem. Phys.* **1978**, *69*, 5098–5104.

[60] R. Mehta, V. Kumar, H. Bhunia, S. N. Upadhyay, *J. Macromol. Sci. - Polym. Rev.* **2005**, *45*, 325–349.

[61] P. M. Beaujuge, J. R. Reynolds, *Chem. Rev.* **2010**, *110*, 268–320.

[62] J. Pan, S. Lu, Y. Li, A. Huang, L. Zhuang, J. Lu, *Adv. Funct. Mater.* **2010**, *20*, 312–319.

[63] H. Shirakawa, J. Louis, A. G. Macdiarmid, *J. C. S. Chem. Comm* **1977**, 578–580.

[64] Y. Y. Smolin, M. Soroush, K. K. S. Lau, *Beilstein J. Nanotechnol.* **2017**, *8*, 1266–1276.

[65] S. Nejati, K. K. S. Lau, *Langmuir* **2011**, *27*, 15223–15229.

[66] J. L. Bredas, G. B. Street, *Acc. Chem. Res.* **1985**, *18*, 309–315.

[67] D. Kumar, R. C. Sharma, *Eur. Polym. J.* **1998**, *34*, 1053–1060.

[68] A. G. MacDiarmid, *Angew. Chem. Int. Ed. Engl.* **2001**, *40*, 2581–2590.

[69] K. K. S. Lau, K. K. Gleason, *Macromolecules* **2006**, *39*, 3688–3694.

[70] C. E. Knapp, J. B. Chemin, S. P. Douglas, D. A. Ondo, J. Guillot, P. Choquet, N. D. Boscher, *Adv. Mater. Technol.* **2018**, *3*, 1–6.

[71] P. Ghamgosar, F. Rigoni, S. You, I. Dobryden, M. G. Kohan, A. L. Pellegrino, I. Concina, N. Almqvist, G. Malandrino, A. Vomiero, *Nano Energy* **2018**, *51*, 308–316.

[72] A. L. Pellegrino, P. Cortelletti, M. Pedroni, A. Speghini, G. Malandrino, *Adv. Mater. Interfaces* **2017**, *4*, 2–7.

[73] B. H. Lee, K. R. Min, S. Y. Choi, K. H. Lee, S. Im, M. M. Sung, *J. Am. Chem. Soc.* **2007**, *129*, 16034–16041.

[74] K. E. Kim, S. R. Jang, J. Park, R. Vittal, K. J. Kim, *Sol. Energy Mater. Sol. Cells* **2007**, *91*, 366–370.

[75] M. Wang, N. D. Boscher, K. Heinze, K. K. Gleason, *Adv. Funct. Mater.* **2017**, *27*, 1606652.

[76] C. A. Dorval Dion, J. R. Tavares, *Powder Technol.* **2013**, *239*, 484–491.

[77] W. E. Tenhaeff, K. K. Gleason, *Adv. Funct. Mater.* **2008**, *18*, 979–992.

[78] H. Zhou, S. F. Bent, *CVD Polym. Fabr. Org. Surfaces Devices* **2015**, *40801*, 133–170.

[79] M. Heydari Gharahcheshmeh, K. K. Gleason, *Adv. Mater. Interfaces* **2019**, *6*, 1801564.

[80] P. W. Loscutoff, H. B. R. Lee, S. F. Bent, *Chem. Mater.* **2010**, *22*, 5563–5569.

[81] N. D. Boscher, M. Wang, A. Perrotta, K. Heinze, M. Creatore, K. K. Gleason, *Adv. Mater.* **2016**, *28*, 7479–7485.

[82] D. Abessolo Ondo, F. Loyer, J.-B. Chemin, S. Bulou, P. Choquet, N. D. Boscher, *Plasma Process. Polym.* **2017**, e1700172.

[83] S. Das, D. P. Chatterjee, R. Ghosh, A. K. Nandi, *RSC Adv.* **2015**, *5*, 20160–20177.

[84] J. P. Lock, S. G. Im, K. K. Gleason, *Macromolecules* **2006**, *39*, 5326–5329.

[85] H. Coskun, A. Aljabour, P. De Luna, D. Farka, T. Greunz, D. Stifter, M. Kus, X. Zheng, M. Liu, A. W. Hassel, W. Schöfberger, E. H. Sargent, N. S. Sariciftci, P. Stadler, *Sci. Adv.* **2017**, *3*, 1–9.

[86] H. Coskun, A. Aljabour, L. Uiberlacker, M. Strobel, S. Hild, C. Cobet, D. Farka, P. Stadler, N. S. Sariciftci, *Thin Solid Films* **2018**, *645*, 320–325.

[87] A. Castro-Carranza, J. C. Nolasco, S. Bley, M. Rückmann, F. Meierhofer, L. Mädler, T. Voss, J. Gutowski, *J. Polym. Sci. Part B Polym. Phys.* **2016**, *54*, 1537–1544.

[88] S. Vaddiraju, K. Seneca, K. K. Gleason, *Adv. Funct. Mater.* **2008**, *18*, 1929–1938.

[89] H. Goktas, X. Wang, N. D. Boscher, S. Torosian, K. K. Gleason, *J. Mater. Chem. C* **2016**, *4*, 3403–3414.

[90] S. G. Im, D. Kusters, W. Choi, S. H. Baxamusa, M. C. M. van de Sanden, K. K. Gleason, *ACS Nano* **2008**, *2*, 1959–1967.

[91] S. Nejati, T. E. Minford, Y. Y. Smolin, K. K. S. Lau, *ACS Nano* **2014**, *8*, 5413–5422.

[92] M. W. Chase Jr., C. A. Davies, J. R. Downey Jr., D. J. Frurip, R. A. McDonald, A. N. Syverud, *J. Phys. Chem. Ref. Data* **1985**, *14*, 903.

[93] M. Tosi, *Annu. Rev. Phys. Chem.* **1993**, *44*, 173–211.

[94] L. Edwards, D. H. Dolphin, M. Gouterman, A. D. Adler, *J. Mol. Spectrosc.* **1971**, *38*, 16–32.

[95] T. Zambelli, Y. Boutayeb, F. Gayral, J. Lagoute, N. K. Girdhar, A. Gourdon, S. Gauthier, M. J. Blanco, J. C. Chambron, V. Heitz, J. P. Sauvage, *Int. J. Nanosci.* **2004**, *3*, 331–341.

[96] M. Tonezzer, G. Maggioni, E. Dalcanale, *J. Mater. Chem.* **2012**, *22*, 5647.

[97] E. V. Antina, E. V. Balantseva, M. B. Berezin, *Russ. J. Gen. Chem.* **2011**, *81*, 1222–1230.

[98] S. Preiß, C. Förster, S. Otto, M. Bauer, P. Müller, D. Hinderberger, H. Hashemi Haeri, L. Carella, K. Heinze, *Nat. Chem.* **2017**, *9*, 1249–1255.

[99] L. Zajac, L. Bodek, B. Such, *Appl. Surf. Sci.* **2018**, *443*, 452–457.

[100] F. Buchner, K. Comanici, N. Jux, H. P. Steinrück, H. Marbach, *J. Phys. Chem. C* **2007**, *111*, 13531–13538.

[101] A. Resta, R. Felici, M. Kumar, M. Pedio, *J. Non. Cryst. Solids* **2010**, *356*, 1951–1954.

[102] J. Otsuki, *Coord. Chem. Rev.* **2010**, *254*, 2311–2341.

[103] Y. He, M. Garnica, F. Bischoff, J. Ducke, M. Bocquet, M. Batzill, W. Auwärter, J. V Barth, *Nat. Chem.* **2017**, *9*, 33–38.

[104] B. Cirera, B. De La Torre, D. Moreno, M. Ondráček, R. Zbořil, R. Miranda, P. Jelínek, D. Écija, *Chem. Mater.* **2019**, *31*, 3248–3256.

[105] M. In't Veld, P. Iavicoli, S. Haq, D. B. Amabilino, R. Raval, *Chem. Commun.* **2008**, 1536–1538.

[106] L. Lafferentz, V. Eberhardt, C. Dri, C. Africh, G. Comelli, F. Esch, S. Hecht, L. Grill, *Nat. Chem.* **2012**, *4*, 215–220.

[107] A. Wiengarten, K. Seufert, W. Auwärter, D. Ecija, K. Diller, F. Allegretti, F. Bischo, S. Fischer, D. A. Duncan, A. C. Papageorgiou, F. Klappenberger, R. G. Acres, T. H. Ngo, J. V Barth, *J. Am. Chem. Soc.* **2014**, *136*, 9346−9354.

[108] K. Nakamura, M. Watanabe, M. Zhou, M. Fujishima, M. Tsuchiya, T. Handa, S. Ishii, H. Noguchi, K. Kashiwagi, Y. Yoshida, *Thin Solid Films* **1999**, *345*, 99–103.

[109] G. Maggioni, S. Carturan, M. Tonezzer, M. Buffa, A. Quaranta, E. Negro, G. Della Mea, *Eur. Polym. J.* **2008**, *44*, 3628–3639.

[110] N. D. Boscher, M. Wang, K. K. Gleason, *J. Mater. Chem. A* **2016**, *4*, 18144–18152.